10-5-2017

Development of an adaptive cutting device for improved crashworthiness performance

Peter Shery
University of Windsor

Recommended Citation
Shery, Peter, "Development of an adaptive cutting device for improved crashworthiness performance" (2017). *Electronic Theses and Dissertations*. 7298.
https://scholar.uwindsor.ca/etd/7298

Development of an adaptive cutting device for improved crashworthiness performance

By

Peter Shery

A Thesis
Submitted to the Faculty of Graduate Studies
through the Department of **Mechanical, Automotive, and Materials Engineering**
in Partial Fulfillment of the Requirements for
the Degree of **Master of Applied Science**
at the University of Windsor

Windsor, Ontario, Canada

2017

Development of an adaptive cutting device for improved crashworthiness performance

by

Peter Shery

APPROVED BY:

V. Stoilov
Department of Mechanical, Automotive, and Materials Engineering

D. Green
Department of Mechanical, Automotive, and Materials Engineering

W. Altenhof, Advisor
Department of Mechanical, Automotive, and Materials Engineering

July 7, 2017

DECLARATION OF CO-AUTHORSHIP / PREVIOUS PUBLICATION

I. Co-Authorship Declaration

I hereby declare that this thesis incorporates material that is result of joint research, as follows:

Chapter 2 contains material published in an SAE conference paper that I developed in a collaborative effort. Experiments were performed with Ryan Smith, Thomas Gruenheid and Professor William Altenhof. Specimens for testing were supplied by Elmar Beeh and Phillip Strassburger. I certify that I analyzed and interpreted all the data, and had the role of lead author in preparing and writing the SAE conference paper.

I am aware of the University of Windsor Senate Policy on Authorship and I certify that I have properly acknowledged the contribution of other researchers to my thesis, and have obtained written permission from each of the co-author(s) to include the above material(s) in my thesis.

I certify that, with the above qualification, this thesis, and the research to which it refers, is the product of my own work.

II. Declaration of Previous Publication

This thesis includes 1 original paper that has been submitted for a conference publication, as follows:

Thesis Chapter	Publication title/full citation	Publication status*
Chapter 2	P. Shery, W. Altenhof, R. Smith, E. Beeh, P. Strassburger, and T. Gruenheid, "Experimental observations on the mechanical response of AZ31B magnesium and AA6061-T6 aluminum extrusions subjected to compression and cutting modes of deformation," SAE Technical Paper 2017-01-0377, 2017.	*Published*

I certify that I have obtained a written permission from the copyright owner(s) to include the above published material(s) in my thesis. I certify that the above material describes work completed during my registration as graduate student at the University of Windsor.

I declare that, to the best of my knowledge, my thesis does not infringe upon anyone’s copyright nor violate any proprietary rights and that any ideas, techniques, quotations, or any other material from the work of other people included in my thesis, published or otherwise, are fully acknowledged in accordance with the standard referencing practices. Furthermore, to the extent that I have included copyrighted material that surpasses the bounds of fair dealing within the meaning of the Canada Copyright Act, I certify that I have obtained a written permission from the copyright owner(s) to include such material(s) in my thesis.

I declare that this is a true copy of my thesis, including any final revisions, as approved by my thesis committee and the Graduate Studies office, and that this thesis has not been submitted for a higher degree to any other University or Institution.

ABSTRACT

A circular cutting device, referred to as the quadrotor, that adaptively changes configuration to either 4, 6, or 8 equally spaced blades and endures axially cutting through a 3.175 mm thick AA6061-T6 aluminum extrusion under impact has been developed to a manufacture-ready stage. The device comprises a pair of uniquely shaped 3-bladed cutters and 4-bladed cutters. Finite element simulations of both cutters during deployment as well as during dynamic axial cutting were generated to evaluate the device performance. Virtually, all the parts during the deployment stage of either cutter have negligible stresses. During cutting, the device was found to endure 36,000 cycles, which should equate to decades of testing. A simplified apparatus which replicates each cutter deployment was also constructed to validate the numerical models of each cutter's deployment dynamics. As was assumed in the simulations, the neodymium magnet was necessary to catch the blade upon impact with the end stop. Also, compared to the simulations, the angular rotation of the 3-bladed cutter and 4-bladed cutter geometries with respect to time had acceptable validation metrics of 0.78 and 0.70, respectively. Friction associated with the experimental setup was more significant than expected and caused both cutters to deploy slightly slower than predicted. Nonetheless, the apparatus demonstrated a successful deployment of both cutters. The slower cutter had a total response time of 47 ms, allowing the electronic system that controls the device configuration to trigger when the impacting entity is still within close range, which is desirable. Overall, based on the findings of this thesis, the complete quadrotor is worth constructing to perform dynamic axial cutting experiments in the future.

DEDICATION

To my parents Robert Shery and Carol Ann Burton, and to my sister Nicole Ann Shery: for their love and encouragement

ACKNOWLEDGEMENTS

I would first like to thank my advisor Dr. Altenhof for his moral and financial support throughout my two years at the University of Windsor. At each stage of this project, he was devoted to guiding me in the best possible direction. His guidance has not only improved my engineering design skills, but also my redesign skills. Whether designing a geometric model or a numerical model, I have learned to better recognize the challenges in every design approach considered, and to devise multiple approaches. I must also thank him for his excellent tips and teaching of finite element analysis, which I have discovered through this project to be an interesting and valuable tool that will greatly benefit my mechanical engineering career.

The technicians at the University of Windsor have also assisted in this project: I thank Patrick Seguin for constructing the solenoid driver module as well as advising me on the most economic options for the control system of the adaptive cutting device. Andrew Jenner, Dean Poublon, and Matt St. Louis also deserve my thanks for machining the parts for the cutter deployment apparatus as well as providing their insights on the manufacturing of the device.

Finally, I want to acknowledge the financial support provided by the Natural Sciences and Engineering Research Council (NSERC), the Ontario Graduate Scholarship (OGS), and the top up scholarship by the University of Windsor.

TABLE OF CONTENTS

NOTE ON UNITS

Best attempts are made to follow and implement the S.I. system of units. However, in the minority of cases, U.S. Imperial units are used for appropriate description of bolts and other mechanical elements.

LIST OF TABLES

LIST OF FIGURES

LIST OF APPENDICES

LIST OF ABBREVIATIONS

AC	Alternating Current
AISI	American Iron and Steel Institute
ALE	Arbitrary Lagrangian Eulerian
CAD	Computer Aided Design
CFE	Crush Force Efficiency
CNC	Computer Numeric Controlled
CPU	Central Processing Unit
DC	Direct Current
EDM	Electric Discharge Machining
FBD	Free Body Diagram
FE	Finite Element
GDP	Gross Domestic Product
HCF	High Cycle Fatigue
IEPE	Integrated Electronic Piezoelectric
IHSA	Infrastructure Health and Safety Association
LCF	Low Cycle Fatigue
MRD	Magnetorheological Damper
SAE	Society of Automotive Engineers
SEA	Specific Energy Absorption
TTL	Transistor-Transistor Logic
VDC	Viscous Damping Coefficient

NOMENCLATURE

A	Cross-sectional area of bolt shaft
d	Diameter of thread portion on bolt
E	Modulus of elasticity
$E_{loss\ i}$	Instantaneous experimental energy loss in cutter rotation
F	Axial force representing tensile preload in bolt
F_c	Axial cutting force
$I_{bolt\ axis}$	Mass moment of inertia of cutter about axis passing through bolt
K	Torque coefficient
$KE_{rot\ i}$	Experimental instantaneous rotational kinetic energy of cutter
k	Stiffness of discrete linear spring
k_t	Torsional stiffness of torsion spring
L	Axial length of bolt below head
l	Axial length of cut in AA6061-T6 aluminum extrusion
m_c	Mass of droptower crosshead (carriage)
n	Number of tests performed constituting the sample size
$T_{cutter\ i}$	Experimental instantaneous inertia torque of cutter
$T_{frict\ i}$	Experimental instantaneous frictional torque
t	Wall thickness of the AA6061-T6 aluminum extrusion
$\bar{t}$	Mean response time
V	Validation metric
v	Velocity of crosshead immediately before impact with extrusion
$Z_{\alpha/2}$	Z-score for a normally distributed population
α_i	Experimental instantaneous angular acceleration of cutter
ϑ_i	Experimental instantaneous angular position of cutter
$\vartheta_{preload}$	Angle of torsion spring at the initial, preloaded position
σ	Standard deviation
ω_i	Experimental instantaneous angular velocity of cutter

1.0 INTRODUCTION

Unintentional injuries resulting from impact, namely automobile crashes, falling, and blunt trauma, among other examples, place not only an emotional burden on the lives of the victims and their families, but an economic burden associated with medical care. In 2004, injuries classified as unintentional accounted for 81% of all injury costs in Canada at 16 billion dollars, whereas intentional injuries only accounted for 17% [1]. Two leading causes of unintentional injuries are transport, followed by falling, both of which are impact-related injuries. Vehicle accidents are the leading cause of death worldwide in people aged between 15 and 29 and cost governments approximately 3% of the Gross Domestic Product GDP [2]. In 2014, motor vehicle accidents in the United States claimed 32,675 lives (i.e. about 1 in every 10,000 people living in the United States) and 2.34 million injuries [3]. In the same year in Canada, 1,834 deaths and 149,900 injuries resulted from motor vehicle accidents [4], which are also high compared to the nation’s total population of 36 million. Unintentional injuries from falls are a frequent occurrence in people aged 65 and over [5]. Among this age group in the United States, the rate of falls resulting in death has been steadily increasing from 41 to 57 people per 100,000 between 2003 and 2013, with direct medical costs of 34 billion dollars annually [6]. The top three unintentional injury types are impact-related, namely motor accidents, falling from scaffolding or ladders, and struck-bys from machinery or other objects [7]. Struck-bys are also a significant cause of impact injury in the military; traumatic brain injuries being one of them. Between 2000 and 2015, a total of 327,299 traumatic brain injuries in the U.S. military have been reported, 8,287 of which were classified as severe or penetrating [8]. The staggering number of deaths and injuries associated with impacts each year are a harsh reminder that society is in need of energy dissipating devices that can allow victims to walk away alive and unharmed from impact-related accidents.

Impacts involving high kinetic energy of the nature mentioned previously often result in a significant energy transfer to the occupant. For enhanced safety, the devices that dissipate that energy may need to be sacrificial. For example, automobiles are designed with sacrificial structures such as crash boxes so that as little energy as possible is absorbed by the passengers. In construction, workers standing in high places are equipped with restraint devices to prevent from falling. However, the cable itself does not absorb much of the kinetic energy in the event of a fall, which results in high forces to the wearer. Audysho [9] had studied a novel material combination, namely stainless steel braided tubing wrapped around pucks of aluminum foam, which could serve as an effective sacrificial energy dissipater at the end of a harness cable by significantly reducing the forces as a falling worker loads the cable axially. To mitigate head and body strikes, military personnel and athletes in some sports wear padding, which is typically made of a non-sacrificial material for reusable purposes, but as a result has limited protection. A material reaches its highest energy dissipating potential when deformation is beyond its elastic limit and enters the regime of plastic deformation.

The effectiveness of a structure designed to deform plastically under impact is defined by its crashworthiness. Two important metrics that quantify the crashworthiness are the specific energy absorption (SEA) and crush force efficiency (CFE). The SEA is the energy absorption capability of a material per unit mass, and the CFE is the ratio of the average load to the peak load throughout the entire crushing distance. An ideal energy dissipating device should not only possess a high SEA and CFE, but also be stable, repeatable, and have a constant load/displacement curve.

A novel energy dissipating device developed by Altenhof, Jin, and Majumder [10] involving axial cutting of tubular extrusions has the characteristics of stability, repeatability, constant load/displacement, and high CFE. However, because the cutting tools have a fixed number of blades, each tool is optimized for a pre-defined impact situation. There are two extreme cases that render cutting an ineffective deformation mechanism: (1) In a high energy impact, if a cutter with few blades was selected, the SEA of the sacrificial tube may be significantly lower than can be achieved by a conventional deformation mechanism known as progressive folding. (2) In a low energy impact, if a cutter with many blades was selected, the kinetic energy is converted into deformation with a high cutting force and limited cutting distance.

The objective of this thesis is to redesign the cutting tool such that immediately preceding an impact, the tool can adaptively change for a desired load/displacement response, depending on energy dissipation requirements. This thesis is an expansion of the studies by Jin [11], and aims to demonstrate the benefit of controlling the load/displacement curve. Such a tool would optimize the SEA and still produce a deformation that is stable and repeatable, with a constant load/displacement response and high CFE.

2.0 LITERATURE REVIEW

The literature review for the purpose of this thesis is divided into two major categories, namely passive energy dissipation, in section 2.1, and adaptive energy dissipation, in section 2.2. Within passive energy dissipation, conventional deformation mechanisms for a ductile metal and brittle metal are first introduced. Deformation mechanisms that produce constant load/deflection responses, namely axial inversion, axial splitting, and axial cutting will follow. This last topic will provide a transition to section 2.2, which reviews literature examining adaptive energy dissipation. Although this area of research is limited, adaptive energy dissipation was found to be applied in two broad ways: (1) modifying the geometry of the sacrificial structure, and (2) incorporating dampers into the structure.

2.1 Passive Energy Dissipation

Structures that must be sacrificed in the event of an impact are often designed with axially loaded members. A desired mode of deformation under axial loading is progressive folding [12] because it results in a high specific energy absorption and a high crush force efficiency. Another possible mode of deformation is global bending, which is much less effective at absorbing energy as it essentially produces a single fold. After the initial kink in the member, the load supported by the tube drops steeply and results in a low SEA and a low CFE, which is an ineffective use of material. The appearance of these two deformation types are shown in Figure 2.1 [11] and the corresponding load/displacement responses are shown in Figure 2.2 [11]. Although one may try to design a structure to fail by progressive folding, a slight off-axis disturbance in the load can cause the mode of deformation to switch to global bending [13]. Changes in velocity can also produce the same transition from one mode to the other [14], resulting in inefficient energy dissipation. Even if progressive folding could be designed to be stable and repeatable, a disadvantage of this deformation mode is that the load magnitude oscillates throughout the tube’s crushing distance. An on-board occupant would sense these oscillations as accelerations acting on their body and may lead to serious injury or death.

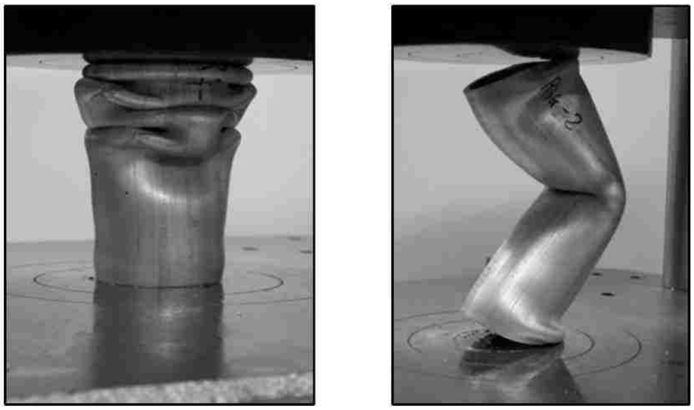

Figure 2.1 Axial crushing of circular AA6061-T6 aluminum tubes by progressive folding (left) and global bending (right) [11].

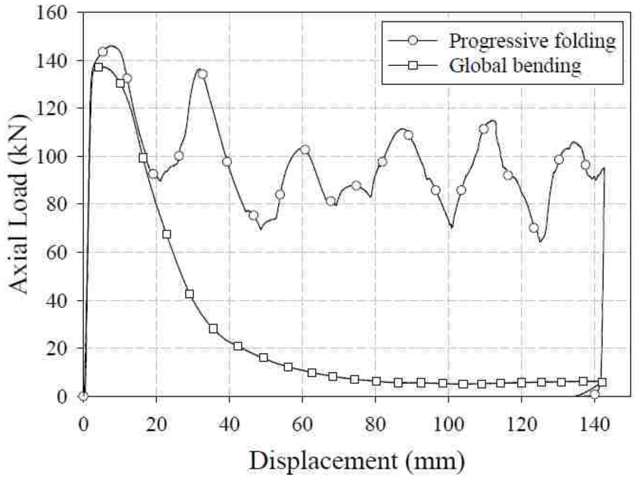

Figure 2.2 Typical load/displacement responses of progressive folding and global bending [11].

If one considers a brittle metal rather than a ductile metal subjected to axial loading, these oscillations would actually amplify because brittle metals can undergo significant fracturing. For example, AZ31B magnesium extrusions under axial load revealed sharding [15], which is the formation of sharp mulch-shaped fragments. Shown in Figure 2.3 [16] is the segmented fracturing mechanism of AZ31B and resulting shards. In addition to the general oscillatory response, rapid fluctuations of the load/displacement response were observed as presented in Figure 2.4 [16]. Therefore, an occupant would sense more violent changes in acceleration with axial loading of a brittle metal than a ductile one.

Figure 2.3 Shards produced by an AZ31B Mg extrusion 3.175 mm thick and 65 mm outer diameter subjected to quasi-static axial crushing [16].

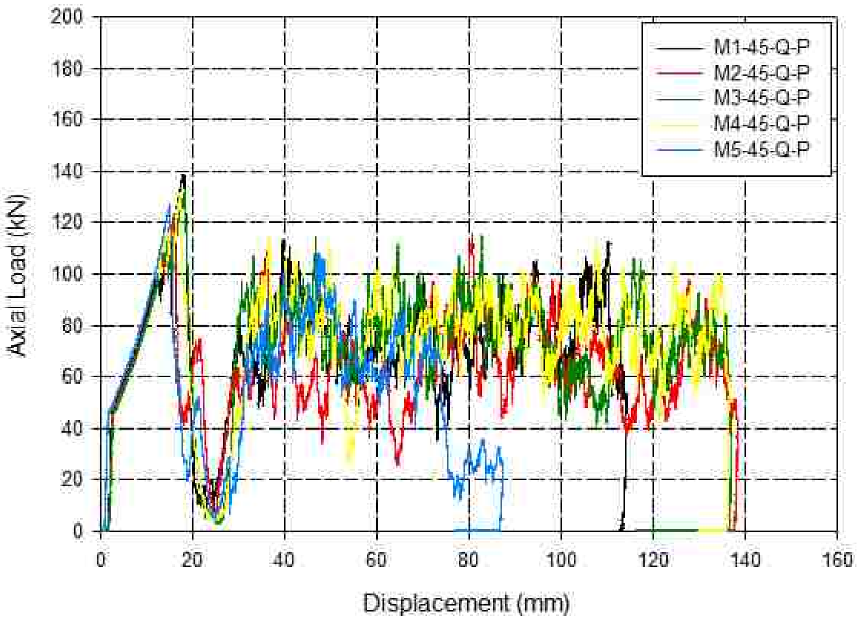

Figure 2.4 Load/displacement responses of AZ31B Mg extrusions 3.175 mm thick and 65 mm outer diameter subjected to quasi-static axial crushing [16].

An ideal mode of deformation of the tube should produce no oscillations in force. A damped response could be achieved if the curve, instead of fluctuating, proceeds horizontally at the level representing the average load. Energy dissipating mechanisms do exist that can produce such a steady response. Three examples that will be discussed in this section are axial inversion, axial splitting, and axial cutting.

Referring to the load/displacement responses for progressive folding of aluminum, presented in Figure 2.2, and axial crushing of magnesium, presented in Figure 2.4, note that for the same extrusion geometry, the average load for aluminum is significantly higher than for magnesium. These figures illustrate that different materials have different energy-absorbing capability. Similarly, one must bear in mind that not all crashes have the same kinetic energy level. Based only on energy requirement and for a given extrusion geometry (diameter, thickness, length), aluminum would be a more suitable material for high energy impacts, whereas magnesium would be a more suitable material for low energy impacts. However, since the energy from a crash cannot be anticipated, one cannot select the best energy absorbing material beforehand. Therefore, an ideal energy absorber should possess two qualities, which are to: (1) damp the load to a constant level over the entire displacement, and (2) be capable of adaptively adjusting this load level such that the energy is dissipated over as much of the total extrusion length as possible.

Axial inversion is a deformation process made possible by axially pushing a hollow, sacrificial tube which fits over a die having a radius of curvature. As the tube is pushed through the die, the tube wall flares outward, as depicted in Figure 2.5 [17]. The load/displacement response is nearly constant, and the average load differs slightly depending on the die’s radius of curvature according to Figure 2.6 [18]. This adjustability in the load with changing die radius suggests that axial inversion could potentially be used as an adaptive energy dissipating mechanism. If one developed a die that could adaptively adjust its radius prior to impact, the average load could be controlled, and thus the SEA could be controlled. However, despite having a smooth response, the SEA is far from that achievable in progressive folding because axial inversion has limited modes of energy dissipation. The dominant modes are friction between the die and extrusion, and curling or bending of the tube wall. Additionally, axial inversion is sensitive to the die’s radius of curvature: a small radius may cause the extrusion to fail by progressive folding, and a large radius would make the extrusion wall more prone to split apart.

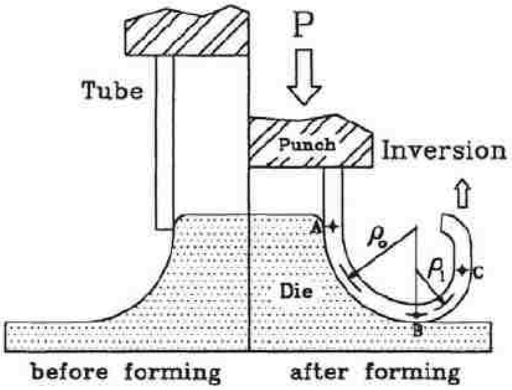

Figure 2.5 Schematic of axial inversion using conical die [17].

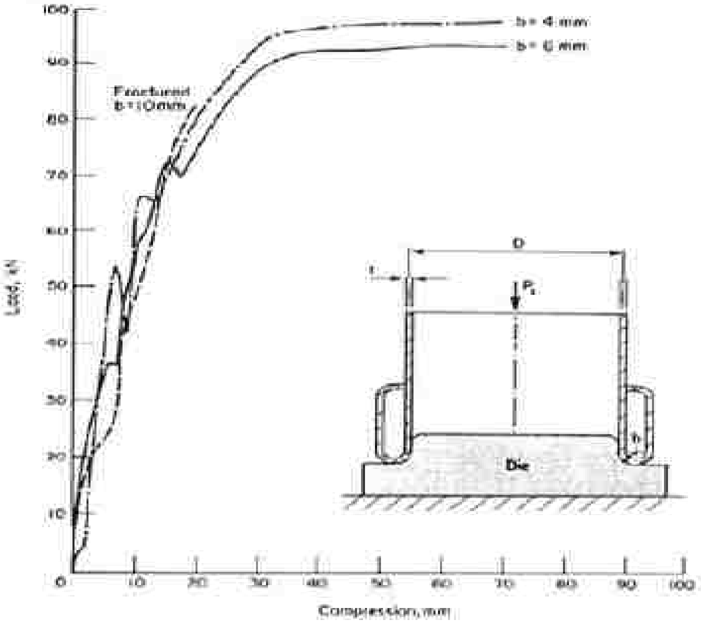

Figure 2.6 Load/displacement response of circular tube under compressive load [18].

Axial splitting is another energy dissipating technique similar to axial inversion in that a sacrificial extrusion is pushed through a die to force the outer wall to flare outward. However, in splitting, the extrusion is forced through a cone rather than a die with a curved radius. If the cone angle is sufficiently large, the wall of the axially pushed extrusion can divide into separate petals and peel the extrusion like a banana. In addition to friction and bending, as seen in axial inversion, near-tip tearing of the walls in axial splitting contributes to the total energy dissipation, making axial splitting a more effective technique than axial inversion. The cone angle also influences the degree of curling of the petals: a wider cone angle induces more curling than a shallow cone angle, therefore increasing the total energy absorption. As depicted in Figure 2.7 [19], wider cone angles produce higher average axial loads, indicating that axial splitting could be made into an active energy dissipating technique. One could design a cone that adaptively adjusts its angle prior to impact. However, given the minute increase in axial force using a cone angle of 75 degrees rather than 45 degrees, splitting appears to have limited potential for adjusting the SEA. Additionally, the initial tear introduces an undesired peak load in the force/deflection response.

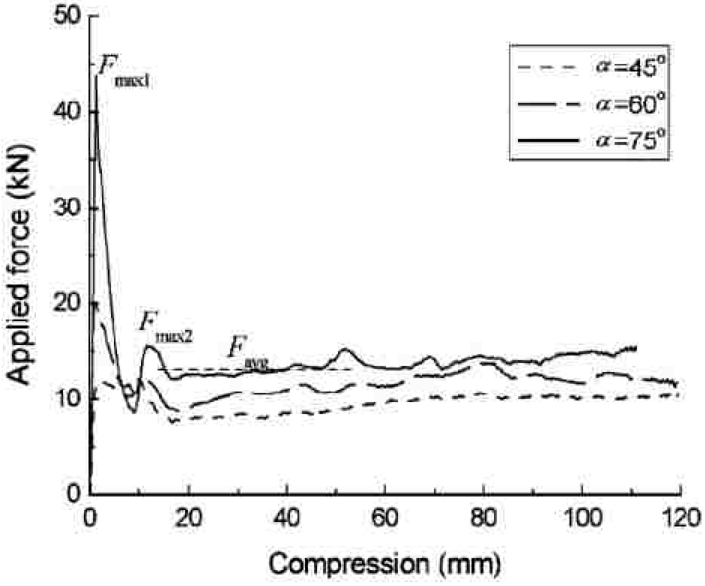

Figure 2.7 Load/displacement responses of circular aluminum tubes splitting under compressive load [19].

The initial peak load in splitting can be mitigated by modifying the extrusion geometry with an intentional stress concentration. Marshal and Nurick [20] provide an in depth literature review of various crush initiator geometries in tubular structures. In one example, as shown in Figure 2.8 [21], a cylindrical indentation is made on either side of the tube which serves to initiate collapse at those locations, stabilize the collapse process, and reduce the initial load. Tubes with beads of different size were subjected to axial compression tests, and shown to significantly reduce the initial peak load as depicted in Figure 2.9 [22].

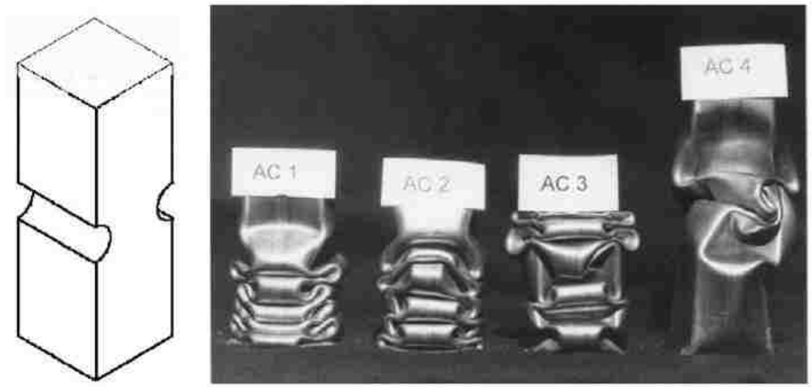

Figure 2.8 Opposing cylindrical indentations (bottom) subjected to axial crushing [21].

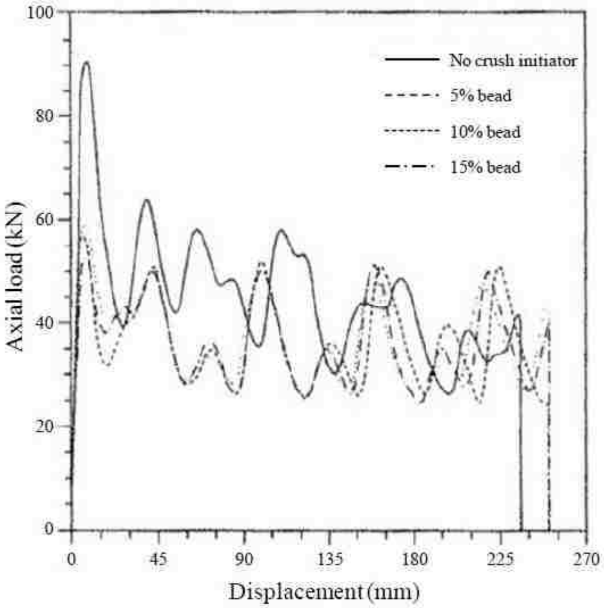

Figure 2.9 Load/displacement response of square tubes with bead initiators of different size vs. no initiator [22].

A novel energy-dissipating system, patented by Altenhof *et al.* [10], comprises a hollow round AA6061-T6 aluminum tube compressed axially against a number of fixed blades on a specialized tool, effectively cutting through the tube and producing "petalled sidewalls" [23], as shown in Figure 2.10. In addition to other energy dissipation modes, axial cutting demonstrates the same modes as seen in axial splitting, but with a reduction in the initial peak load. Under compressive load, the hard AISI 4140 steel cutting tool subjects the extrusion to stress concentrations in the vicinity of the blades. This localized initial deformation eliminates any peak load in the force/displacement response. During

Figure 2.10 Experimental setup of AA6061-T6 extrusion in quasi-static cutting before test (left) and after test (right) using 5 blades.

cutting, the force is sustained at a nearly constant level for the length of the cutting distance, yielding a crush force efficiency (CFE) as high as 96 percent [24]. Numerous experimental and numerical investigations [11,23-32] have demonstrated that the force/displacement response is highly predictable and repeatable.

As shown in Figure 2.11 [25], one can see not only the stable load/deflection response, but the range of average loads achievable when using a different number of cutting blades. Given a 1.5 mm wall thickness and 44.45 mm outer diameter extrusion, a range of approximately 13 kN to 19 kN can be achieved when varying the number of blades from 3 to 5. In addition, the strain-rate insensitivity of AA6061-T6 has demonstrated that regardless of the strain rate, the average cutting force is nearly identical if the same number of blades is used. AA6061-T6 is therefore a practical material of choice for adaptive crash devices: since any crash situation will have an unpredictable loading rate, an ideal energy absorbing material should not only possess high yield strength and high ductility, but also little to no strain hardening such that its flow stress during deformation is not affected by the strain rate.

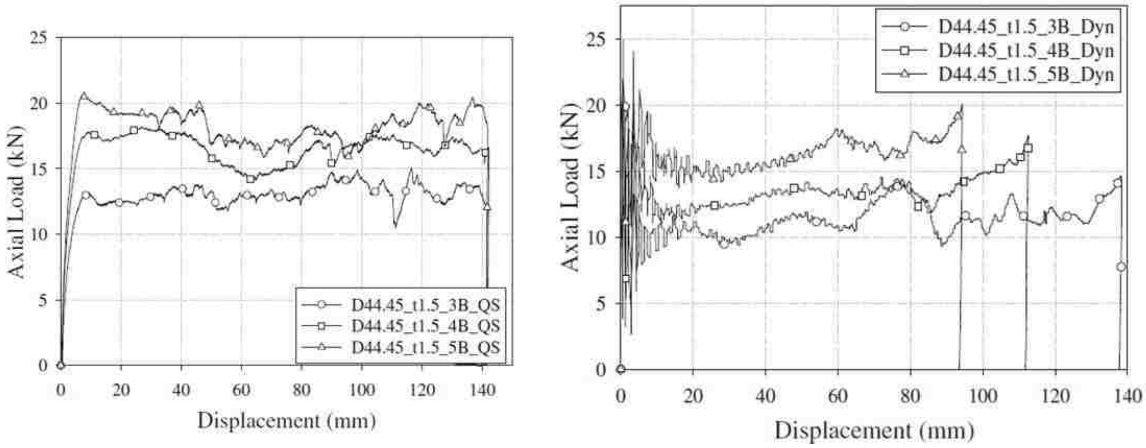

Figure 2.11 Load/displacement responses of quasi-static (left) cutting and dynamic cutting (right) of AA6061-T6 extrusions using 3, 4, and 5 blades [25].

An analytical cutting model developed by Jin and Altenhof [27] predicts the cutting force for AA6061-T6 extrusions to within 10 % error. The closed form solution of the steady state cutting force in axial cutting is written as:

$$F = (n + 4\mu cos\zeta cot\theta) \cdot \left[\frac{\pi}{\sqrt{3}} \frac{\sigma_0 t^2 r_m}{n R_{axial}} + \frac{2}{\sqrt{3}} \sigma_0 T t + \frac{\sigma_0 t^2}{2\sqrt{3}} (B + R_r) \cdot \left(\frac{1}{R_r cos\theta} + \frac{1}{r_0 + r_m} + \frac{1}{r_m + r_i} \right) + \frac{4}{\sqrt{3}} \sigma_0 t B \theta + 0.366 \sigma_0 t R_r cos^2\theta \cdot (1 + 0.55\theta^2) \right] \qquad \text{Eq. 2.1}$$

The complete nomenclature is described in [27], but in general, the force depends on the geometry of the extrusion (i.e. R_r, r_o, r_m, t), material properties (i.e. σ_0, μ), geometry of the blade (i.e. B, T, ϑ), and the number of blades used (n). Worth noting as well is that the steady-state cutting force is independent of the extrusion length. This characteristic is useful for adaptability because it means any arbitrary total length of cut through the extrusion will only affect the energy absorbed and not the average cutting force.

The energy dissipation modes in axial cutting are well described through Eq. 2.1 as it constitutes a summation of the various energy rates (normalized with velocity to obtain a unit of force). Embedded in the first term in brackets is a dependence on the frictional energy. The force would be underestimated by a factor of 3 if friction was not taken into account. Five terms, each representing a different energy rate, are contained within the square brackets in Eq. 2.1: the first term is the petalled sidewall bending mode, which accounts for approximately 35% of the total energy. The second term is the chip formation ahead of the cutter blade, which accounts for approximately 25% of the total energy. The third term is the energy rate of far-field bending also indicated by the stable flap zone in Figure 2.12 [27]. The fourth term is transient zone flap bending, indicated in Figure 2.13 by the region on the extrusion located near the tapered face of the blade. The fifth term is the energy rate by circumferential membrane stretching. The latter three modes account for approximately 12 to 15 % each of the total energy. Clearly, the effectiveness of axial cutting is indicated by the additional energy dissipation modes that are nonexistent in axial splitting or in axial inversion.

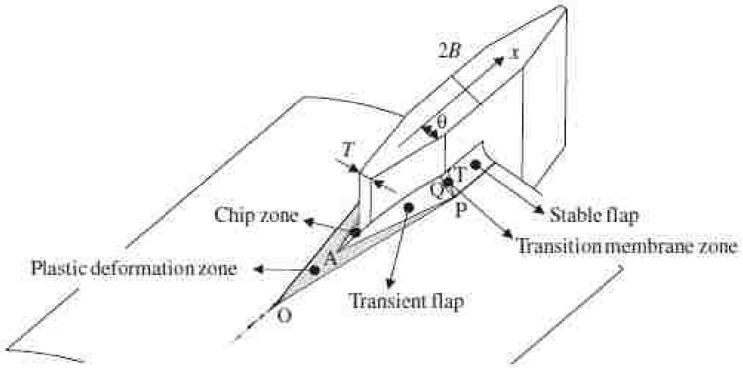

Figure 2.12 Schematic of the deformation modes resulting from the penetration of a single cutter blade through the sidewall of a circular tube [27].

2.2 Active Energy Dissipation

Energy dissipation mechanisms classified as active are a limited area of research and few publications can be found on this topic in the open literature. In addition, active energy dissipation does not refer to the electronic systems designed to prevent a vehicle from frontal or rear collisions, known as crash avoidance systems. These systems have certainly improved the safety of vehicles [33]. However, many crash events occur too suddenly to have any foreseeable warning for a crash avoidance system to detect in time and maneuver the vehicle out of harm’s way. In the event of an unavoidable crash, vehicles must still be designed to absorb the energy effectively. On one hand, a passive energy absorber has no control over the load/deflection response once it is mounted in a vehicle frame or any other structure. On the other hand, an active energy absorber is capable of adjusting the expected load/deflection response either during the process of deformation or prior to deformation.

The predictability of cutting deformation allows one to adjust the load/deflection response during deformation by varying the extrusion geometry. For example, Figure 2.13 [31] shows that a step or even linear profile can be prescribed in the load/deflection response simply by varying the extrusion thickness along the axial direction. If a structure required a higher level of energy dissipation at the later stage of the deformation process, then cutting using an AA6061-T6 extrusion with the geometry of Figure 2.13(a) demonstrates how that can be achieved. Also note that both of the load/deflection responses in Figure 2.13(b) nearly overlap, yet were subjected to different loading rates. Therefore, in one way, this technique of deformation is adaptive because any speed of impact will result in the same profile. However, in another way, this technique is not adaptive because the geometry of the extrusion is predefined, which also predefines the cutting force levels. True adaptability would be to somehow add or remove material in order to adjust the extrusion thickness while axial cutting deformation is occurring simultaneously, but such a concept sounds farfetched.

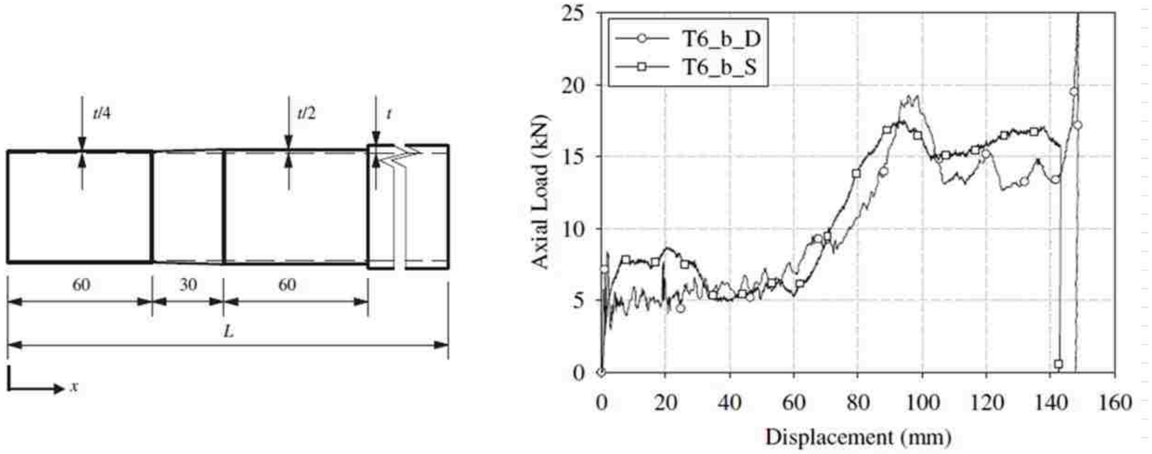

(a) (b)

Figure 2.13 Control of the load/displacement curve by varying thickness of AA6061-T6 extrusion [31].

Bielecki [34] explains that a complete adaptive crashworthiness system must comprise a sensor to detect the collision in advance, a controller to apply the adaptive dissipation strategy, and the actively controlled energy dissipaters. A more detailed explanation to adaptive crashworthiness as a concept is described by Holnicki-Szulc and Knap [35]. The idea is applied to a truss (e.g. the subframe of a train rail car) in which a damper is mounted in line between each member. The energy absorption of the truss would be optimized if the deformation is shared over the entire structure rather than localized in one zone. The authors' suggest that such a deformation could be achieved in theory through adaptive crashworthiness. Their approach is to control the yield strength of each truss member while the structure is plastically deforming simultaneously. The ideal internal pressure in each cylinder is determined by a complex algorithm and adjusted continuously: in principle, zones of the truss subjected to higher loads are made stronger (higher internal pressures), and zones of the truss subjected to lower loads are made weaker (lower internal pressures) such that the overall deformation is more uniformly distributed. From a conceptual point of view, the idea is attractive especially since the load/deflection response of a damper is nearly constant. Unfortunately, one cannot validate the effectiveness of the concept because it has never been studied experimentally. Additionally, using dampers to adjust the yield strength of the structure while it is deforming seems implausible: allowing the truss to deform plastically while the dampers themselves remain intact and functional is hard to believe. Each member would need to be controlled to deform purely in the axial direction for the dampers to function properly. If any member buckles, then surely a damper will also deform or at least leak fluid and fail to work. Moreover, even if pure axial deformation is achieved, a large amount of axial space is required to mount the damper. So, the plastic deformation of the member itself contributes less to the total energy dissipation because less material is available when a damper is present.

Wagstrom et al. [36] designed an adaptive energy absorbing mechanism in a vehicle that has a more practical approach. They developed a vehicle chassis where a portion of the sub-frame could be detached through some deployment mechanism. Although this work was entirely numerical, the concept seems feasible because the mechanical system need not be overly complex. They simulated a frontal offset crash, where the detachable sub-frame is deployed in one case, and not deployed in the other case. The corresponding numerical force/displacement responses are depicted in Figure 2.14 [36]. The release mechanism adaptively adjusts the force/displacement response by reducing the peak deceleration level and extending the deformation over a longer displacement. This work demonstrates a plausible adaptive energy absorbing system, but unfortunately does not produce the constant load/displacement response that is desirable.

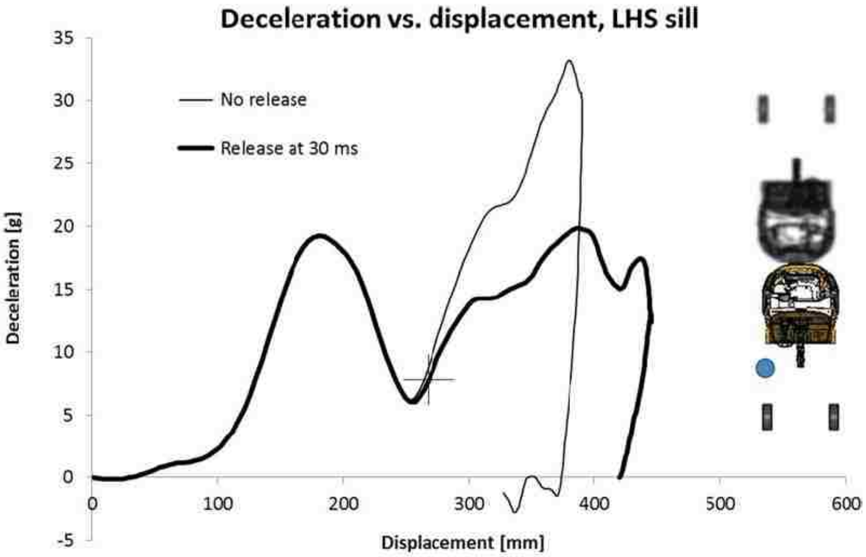

Figure 2.14 Load/displacement response of frontal crash simulation at 35 km/h, 100 mm lateral offset, with and without release [36].

An adaptive energy absorbing device that does exist in practice is the magnetorheological damper (MRD) [37]. An MRD is an adaptive energy absorber because it can actively adjust its damping resistance, which depends on the viscosity of the fluid inside the cylinder. The fluid contains particles of iron which agglomerate when subjected to a magnetic field. Thus, the fluid viscosity, and ultimately the damping resistance, is a function of the strength of the applied magnetic field which controls the density of iron particle clusters. MRD’s are found mainly in engineering applications subjected to vibration: examples include vehicle suspension systems [38], rotating machinery such as washing machines [39], and buildings and bridges for earthquake mitigation [40]. In all of these cases, the load application is periodic, which is not the nature of the load application in crashes. MRD’s used in impact situations are not as common, but they have been investigated. For example, Wereley et al. [41] performed a theoretical analysis of a dropping payload on an MRD, with the purpose of determining the optimal damping resistance based on the payload mass, dropping speed, and available stroke length. The Bingham number (the ratio of the magnetorheological yield force to the passive damping force) is a measure of the magnetic field strength required to achieve the optimal damping resistance, where a Bingham number of zero signifies that no magnetic field is applied. The authors developed a theoretical model that gives the optimal Bingham number in various drop cases that ensures as much of the available stroke length is used and the peak force transmitted to the mass is below a threshold considered a “soft landing”. In a second example, Milecki and Hauke [42] developed a model of the sudden braking process on an industrial assembly line using an MRD. They also built an experimental setup consisting of a wagon mass at the top of an inclined ramp and a shock absorber at the bottom of the ramp. Experimental tests were completed using a passive shock absorber in one case and a custom MRD with control hardware and software in another case. The model of the MRD braking force was validated by the similar force/displacement and force/time responses seen in the experimental tests. The major finding was that the controlled damper eliminated the sudden peaks in the force seen in the uncontrolled damper tests, which were the result of the piston bouncing in the cylinder at the end of the stroke.

2.2 Summary of Literature Review

An ideal load/displacement response with regards to crashworthiness is one that is steady and predictable. Although progressive folding deformation does have a high energy absorption capability and some degree of predictability in the force/displacement response, its high-amplitude oscillations in the force are undesirable. Therefore, progressive folding is not favourable for adaptive crashworthiness. Energy absorbing mechanisms that achieve a desirable, constant load/displacement response are axial inversion, axial splitting, and axial cutting. Inversion was found to be less effective than splitting or cutting since it has the fewest modes of energy dissipation. Splitting has an undesired spike in the load/displacement response during initial tearing. Cutting not only has the largest number of energy dissipation modes of the three mechanisms, but also has no initial peak load in the response. However, these three mechanisms were only ever investigated as passive energy absorbers. Papers that discussed adaptive energy absorption (and also result in a steady load/displacement response) considered a predefined structure or used a system of dampers. Predefined structures may produce the desired profile of the force/displacement response given a set energy level, but cannot allow for adjustability if energy requirements change. Trusses incorporating dampers with adjustable internal pressure to adaptively control each member's yield strength has been studied at the conceptual level, but lacks credibility as a practical solution. MRD's are a practical approach to adaptive energy absorption, but are more suited for vibration isolation or emergency braking. Under the severe energy dissipation requirements of a crash, MRD's would likely deform and be rendered dysfunctional. What would be necessary for an adaptive crash absorber is that its own plastic deformation possesses the force/displacement response and adjustability of an MRD.

Considering the three passive energy absorbing mechanisms, cutting seems to have the most potential for adaptability. Referring back to Figure 2.11, note that the cutting force in each test is a function of the number of blades used: a higher number of blades results in a higher cutting force. Since the total cutting displacement is the same in all tests, then the SEA is controlled by changing the number of blades. Therefore, the SEA could be adjusted without requiring the geometry of the sacrificial extrusion to change. Cutting could be made as an adaptive crash absorber because only the tool would need to adapt, by adjusting the number of blades immediately prior to a crash.

3.0 RESEARCH OBJECTIVES

Currently, the cutting tools developed by Altenhof, Jin, and Majumder [10] have a fixed number of blades. A cutter with a minimum of four blades is required for a stable cutting failure. From experience, a cutter with more than eight blades has been shown to circumferentially stretch so significantly that the extrusion binds with the cutting tool. Therefore, the practical number of blades ranges from four to eight. The scope of this thesis will involve the design of a single cutting tool that can adjust the number of blades from four to eight. The tool design will not be one in which the number blades can be manually configured on a universal hub. Instead, the tool will automatically adjust the blade number immediately prior to an impact event. Therefore, the design will require a sensor to detect the impact event sufficiently ahead of time, a controller to trigger the optimal blade number configuration, and a mechanical deployment system. The tool should be relatively simple to ensure an economical design. Too complex a design raises manufacturing costs and reduces the probability that the electromechanical system deploys reliably, which would render the device impractical. The design must be durable, meaning that it has to remain functional after being subjected to many tests. In practice, the tool only needs to work a single time because the crash would likely destroy the whole device. However, for research purposes, a large number of tests must be performed to assess the performance of the tool under different loading conditions. In practice, the tool may be designed for a particular diameter, but in this research, the tool should accommodate AA6061-T6 extrusions having a range of diameters. The scalability may be important to assess because different diameters may not result in similar performance. This thesis will be limited to the design and numerical modeling of this device. However, the data acquisition hardware and test stand will be integrated into the design so that the device will be ready for experimental testing by the completion of this thesis, which aims to achieve the following goals:

1. Conceptualize several design approaches of a tool having cutter configurations between 4 and 8 blades, before converging on a single best design based on engineering principles.

2. Build a finite element (FE) model of each component and virtually assemble the device.
3. Perform a static stress analysis of the blades to assess whether they can handle the worst load condition.
4. Develop a rigid body model of the mechanical deployment dynamics to assess the response time, vibration, and settling time.
5. Develop models of the bolt preloads and the mechanical deployment dynamics using elastic materials for the entire assembly.
6. Develop numerical models of the cutting process to evaluate the stress on the tool components, the force/displacement response of the extrusion, and petal deformation.
7. Compare the axial cutting force obtained numerically with the analytical steady-state cutting force model developed in [27].
8. Validate the numerical models of the mechanical deployment dynamics by designing a simplified experimental version of the device and measuring critical data about its response time and impact load.
9. Design the electronic system used to control the blade deployment mechanism.
10. Prepare the drawings and select all materials and stock parts to have the device ready for manufacturing.

4.0 DESIGN ITERATIONS OF THE ADAPTIVE CUTTER

This chapter provides the detailed process behind all of the design iterations. Section 4.1 is an overview of the preliminary sketches leading to the first detailed design approach, which possessed elements that would remain throughout nearly all of the design iterations, namely the use of springs, electro-mechanical actuators, and cutter configurations with 4, 6, or 8 blades. Section 4.2 dissects all of the detailed computer aided design (CAD) models considered, including the pros and cons behind each approach.

4.1 Preliminary Design Iteration Phase

The first design approach considered blades that could displace from a concealed position to the active cutting position by sliding linearly over rods. The original sketches of the first cutter design are shown in Figure 4.1. A cross made of cylindrical rods is welded from the axle (the rod along the centerline axis) to the outer rim, forming a web. Four holes through which the four blades could deploy to the activated position are machined in the outer rim. Each custom shaped blade has a cylindrical cavity, which fits over the rod and presses against a linear compression spring. Coils of copper wire, wound around the blade hub, has a current flowing through to produce a magnetomotive force to push the blade against the compression spring and maintain its concealed position. When the current is shut off, the magnetomotive force is removed and the compression spring pushes the blade radially outward to its activated position. Four additional fixed blades (not shown in the drawing) would be integrated on the outside of the ring. Three cutting configurations are theoretically possible: (1) 4 blades (4 fixed blades on outer rim with the 4 spring loaded blades concealed), (2) 6 blades (4 fixed blades and 2 opposing spring loaded blades deployed), and (3) 8 blades (4 fixed blades and the 4 spring loaded blades deployed). The inner wall of the circular AA6061-T6 extrusion would fit over the outer ring with some amount of clearance.

A blade protrusion height of at least 10 mm beyond the outer rim would be needed to accommodate an AA6061-T6 extrusion diameter size of 100 mm (or typically even smaller). An acceptable blade response time would be a few tens of milliseconds,

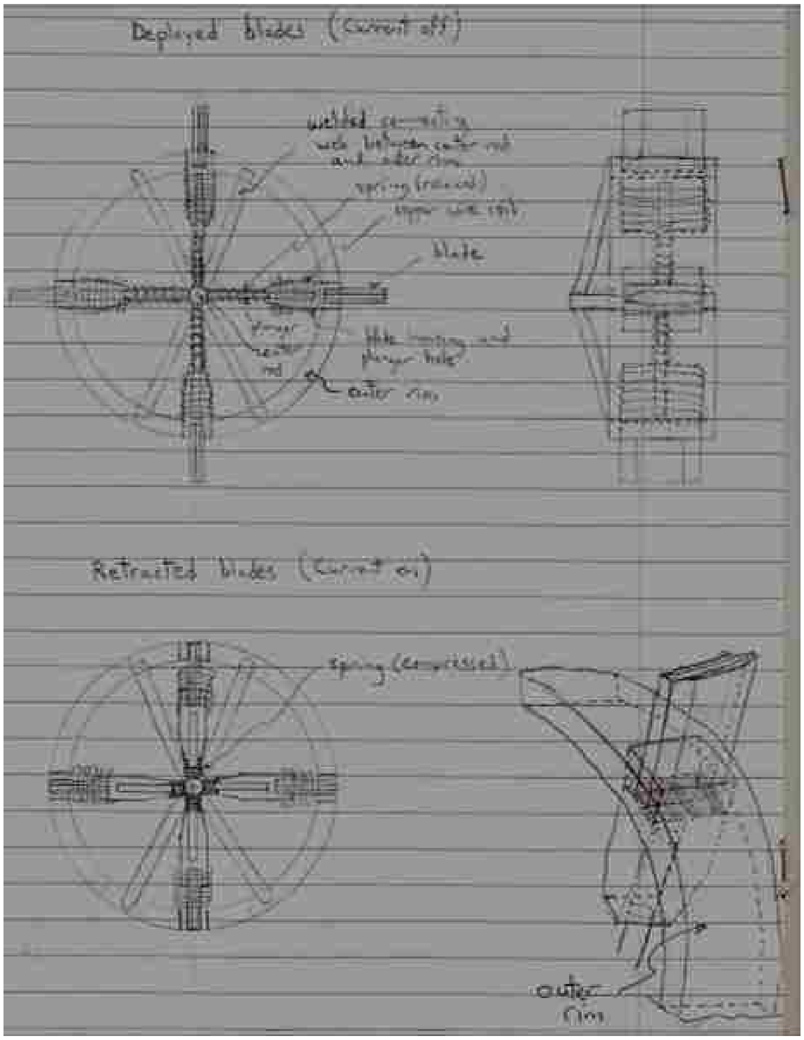

Figure 4.1 Original sketches of the first adaptive cutter design concept.

but achieving this response time requires a spring with very high spring stiffness and long displacement range, and given the geometry of the frame, a spring this small in coil diameter and wire diameter would overstress the wire. This cutter frame is therefore not a practical design and so the copper coil geometry is not even necessary to calculate. A larger spring contained in a cavity rather than constrained over a rod would render the spring design more feasible.

The original sketches of the second design conceived are shown in Figure 4.2. Noting from the front view, an integral cross and rim are formed from a single solid disk of steel by machining four slices out of the front face. Four cavities are machined on the outer periphery to fit the linear compression springs and blades/blade hubs. Four additional fixed blades would be integrated in the outer rim (again not shown in the sketch). Since more room is available to increase the mean diameter of the spring, it can achieve the required stiffness and range of displacement without stressing the wire to failure under static loading. Note the only purpose for the cross shape in the frame is to provide a shaft over which the copper wire can be wound. The magnetomotive force necessary to hold the blades in their concealed positions dictate the required copper wire geometry and current. A simple model of a magnetic circuit can be developed (for one blade) to determine the viability of the copper windings. Given the geometry of the cutter design in Figure 4.2, one will find that approximately 200 amp-turns are required, which

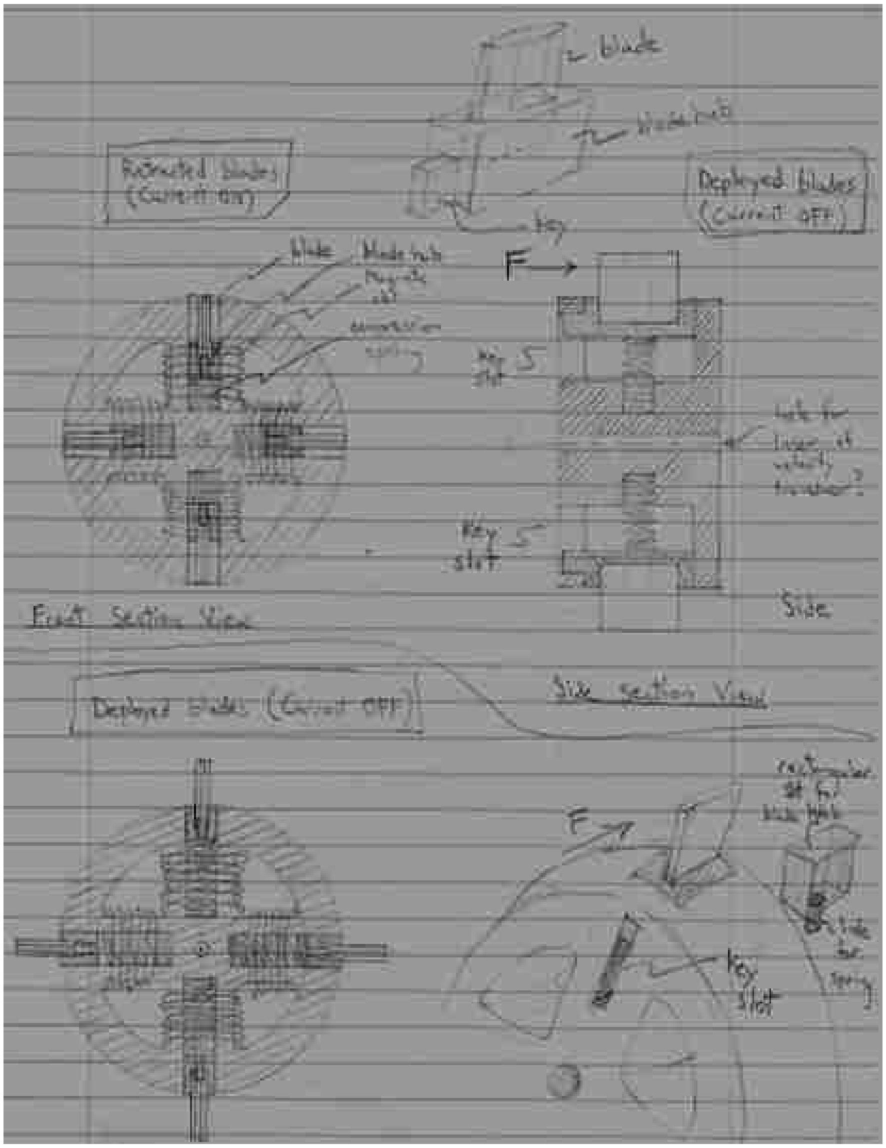

Figure 4.2 Original sketches of the second adaptive cutter design concept.

poses a problem: no practical combination of turns and current level could achieve 200 amp-turns within the confinement of the cutter frame. Due to lack of space, only a few turns of the copper wire would be possible, and consequently, the supplied current would need to be very high. These results indicate that using copper windings to provide the external compressive force against such a stiff spring is not feasible because the required high current is both dangerous and wasteful of electrical energy.

A more efficient approach to the electrical system would be to have one that is always off (rather than always on as is the case in Figure 4.2) and only turn on when the

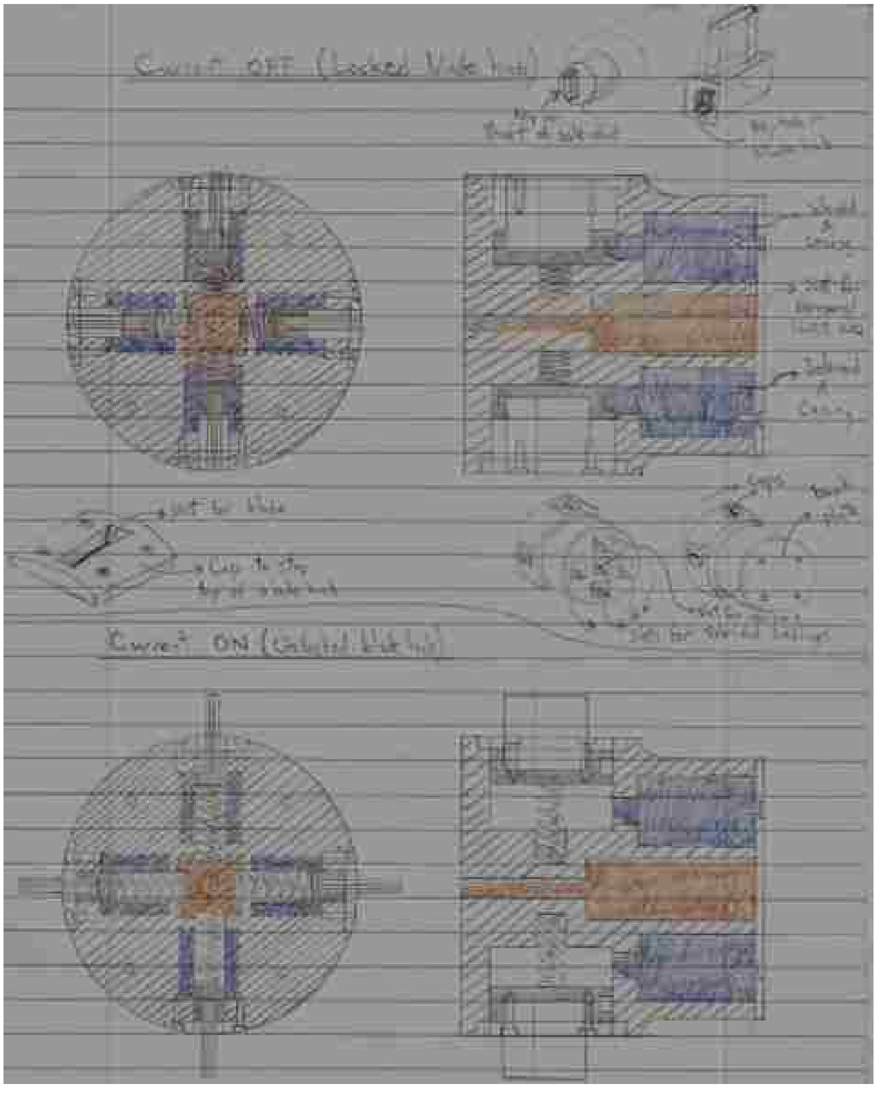

Figure 4.3 Original sketches of the third adaptive cutter design concept.

blade must be deployed. Abiding by this new design philosophy led to the idea of using some sort of mechanical locking system to hold the blade against the compressed spring at all times. Only when the blade must be deployed would the mechanical lock be removed by means of an electronic system.

Linear motion type solenoids are commonly used in practice to latch and unlatch a mechanical device, such as in some automated door locks. Figure 4.3 illustrates the third adaptive cutter design sketches which use pull-type solenoids. The cutter frame is similar in design to that of the second iteration, using the same peripheral cavities, sliding blades, and springs. Four additional fixed blades, not shown in Figure 4.3, would be integrated on the outside of the frame as well. One difference is that no cross shape is machined since no copper windings are used in this design. In addition, a thicker cylindrical steel stock is used in order to have the room to machine pockets in the back of the frame to house 4 small, pull-type solenoids (in blue). Each blade is held in place against a loaded compression spring by means of the solenoid shaft engaging a notch at the back of the blade hub. When the solenoid is activated, the shaft is pulled back and the blade is deployed. As before, one of 3 cutting configurations would be employed: either 4 blades (4 fixed blades), 6 blades (4 fixed blades and 2 deployed blades), or 8 blades (4 fixed blades and 4 deployed blades).

4.2 Detailed Design Iteration Phase

Upon revisiting the preliminary design shown in Figure 4.3, one could devise a custom locking mechanism that requires only one solenoid to deploy either 2 or all 4 of the spring-loaded blades. Such a design would require a kind of latch that, when moved in one direction, only disengages 2 of the blades, but when moved in another direction, disengages all 4 of the blades. When the latch is not moved at all, all 4 blades remain locked and concealed.

Although not commonly found, stock 3-position linear motion solenoids do exist. The shaft of these solenoids can move linearly left or right from a neutral center position depending on which direction the current is flowing. By controlling only the current direction, the solenoid shaft can be positioned accurately in 2 configurations in addition

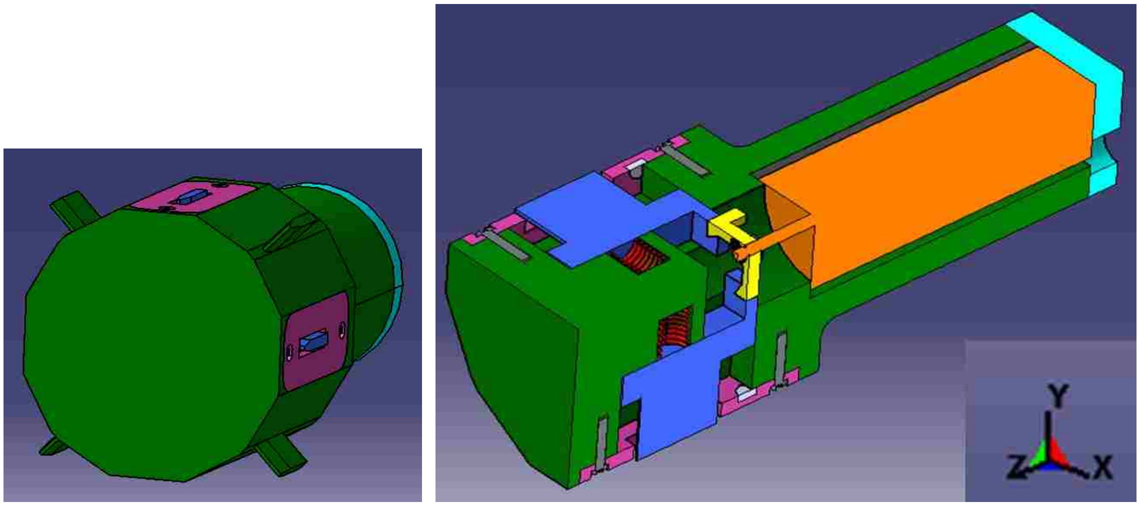

(a) (b)

Figure 4.4 (a) CAD model of the first detailed adaptive cutter design. (b) Section views showing internal mechanics of device in 4-blade configuration.

to the neutral center position. Such a solenoid with a specially devised latch is presented in Figure 4.4, the first detailed geometric adaptive cutter model designed in CATIA V5. The 3-position solenoid (in orange), housed within the frame (in green) is a Geeplus C3PT-12 series. A cross-shaped adaptor (in yellow) is fastened onto the solenoid shaft by means of two retaining rings. The dovetails at the four extremities of the cross-shaped adaptor provide the means for a special locking/unlocking mechanism that allows 3 cutting configurations to be achieved: with the solenoid shaft in its center (or neutral) position, the four sliding blades (in blue) are held in place by the engagement between the dovetail slot in the back of the blades and the dovetail "keys" on the adaptor. When the solenoid shaft translates in the positive *z-axis* a prescribed 5 mm, the two sliding blades along the *y-axis* are disengaged from the dovetail keys, allowing the springs to push the blades outward against the cap (in pink) and exposing them through the periphery of the frame. However, because the two dovetail keys along the *x-axis* are fatter axially, the two corresponding sliding blades along the *x-axis* remain locked, revealing a total of 6 blades. When the solenoid shaft translates along the negative *z-axis* a prescribed 5 mm, the dovetail keys disengage from all 4 sliding blade dovetail slots, revealing the 8-blade configuration. After the 6-blade or 8-blade configuration is set, resetting the blades back in the concealed position is done manually.

A more detailed analysis of this design is not worth pursuing because the main concern is with regard to the dovetail/slot engagement after impact occurs with the AA6061-T6 extrusion. In the 4-blade or 6-blade configuration, where cutting would occur while the dovetail keys are still engaged in the slots, any slight vibration of the sliding blade would likely lead to a fracture at the dovetail joints. Given the main concern regarding the dovetail adaptor, a locking/unlocking mechanism that uses rotary motion rather than translational motion may be more impact-resistant and robust.

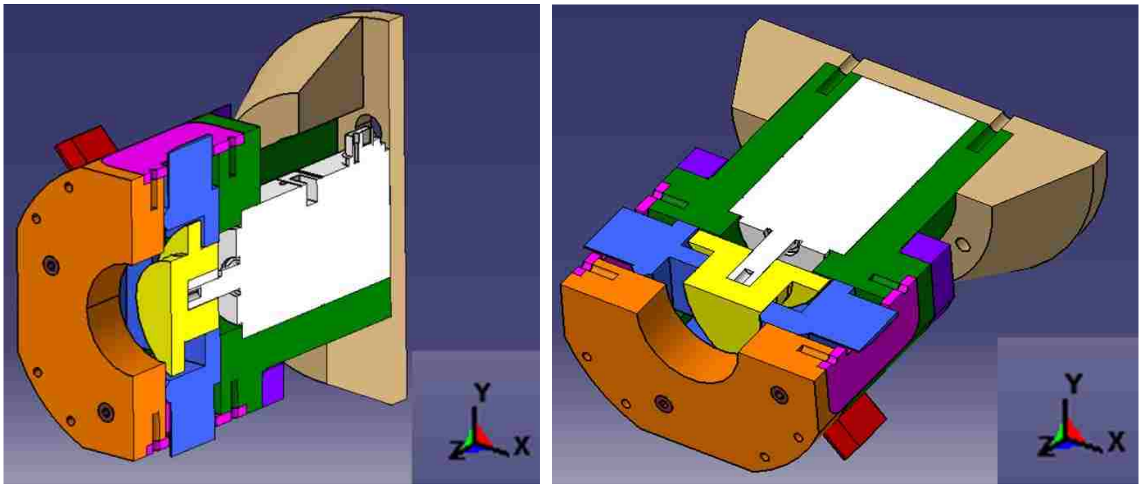

(a) (b)

Figure 4.5 CAD model of the rotary cam adaptive cutter with section views of 4-blade configuration along the (a) *y-axis*. (b) *x-axis*.

Depicted in Figure 4.5, a cutter that uses a rotary cam to push the desired number of blades into the exposed position directly was considered next. Also note the fixed blades (in red) are interchangeable, the frame (in green) manufacturing is reduced in complexity by assembling separate front and back plates, and the cam adaptor (in yellow) and electronic triggering device (i.e. a servomotor) are visibly more solid than the flimsy solenoid shaft and thin dovetail adaptor of the last design.

An opening is machined in the smaller diametric section of the frame (in green) to house an SGMJV series Yaskawa rotary servomotor (in white). A specially shaped adaptor consisting of three cams stacked in series (in yellow) fits over the keyed shaft of this servomotor. The base of the frame is fastened to a conical shaped deflector (in tan) which serves to deflect the petals of the cut AA6061-T6 extrusion.

With the servomotor shaft stationary, the four sliding blades are concealed inside the frame and cutting is done with the four fixed blades. The unique shapes of each sliding blade hub and the rotary cam provide the means to deploy either the 6-blade or 8-blade configuration. Viewed from the front, when the servomotor shaft rotates clockwise 90 degrees, the two blades along the *y-axis* are pushed into the exposed position, but the two blades along the *x-axis* remain concealed because the cam clears the underside of those hubs. Cutting is done with six blades in this case. Viewed from the front, when the servomotor shaft rotates counterclockwise 90 degrees, the cam pushes all four sliding blades into the exposed position to give the 8-blade arrangement.

The design of the cam will enlighten the reader as to why this adaptive cutter was not considered for further analysis. An important metric in cam design is the pressure angle, which is the angle formed at the contact interface between the cam and the follower. If this angle is too steep (greater than 30 degrees [43, 44]), the follower may jam in the slot. Analytical calculations were performed to determine the instantaneous pressure angle of the cam as a function of rotation angle assuming a cycloidal displacement profile. To avoid jamming, one should use as large a total cam rotation as possible with as gradual as possible a change in cam profile. However, designing a cam with a range of rotation greater than 90 degrees in either direction without unintentionally displacing the other sliding blades is figured to be impossible. As a result, the cam in Figure 4.5 is designed with the smallest base circle diameter and lowest eccentricity that can be achieved without jamming. Unfortunately, the result is an oversized cutter frame, requiring AA6061-T6 specimens more than 110 mm in diameter.

Another pitfall is high cost and complexity of using a servomotor, which can be programmed to perform any number of rotation sequences. A servomotor is a poor choice economically for an application that only requires two relatively simple actions or no action at all. The previous cutter design used a solenoid, which was more practical because that device only had 3 possible configurations, exactly the same number as the number of cutter blade configurations.

Realizing the high cost and complexity of the servomotor, and the oversized frame around a rotary cam, the next adaptive cutter design revisited the solenoid and

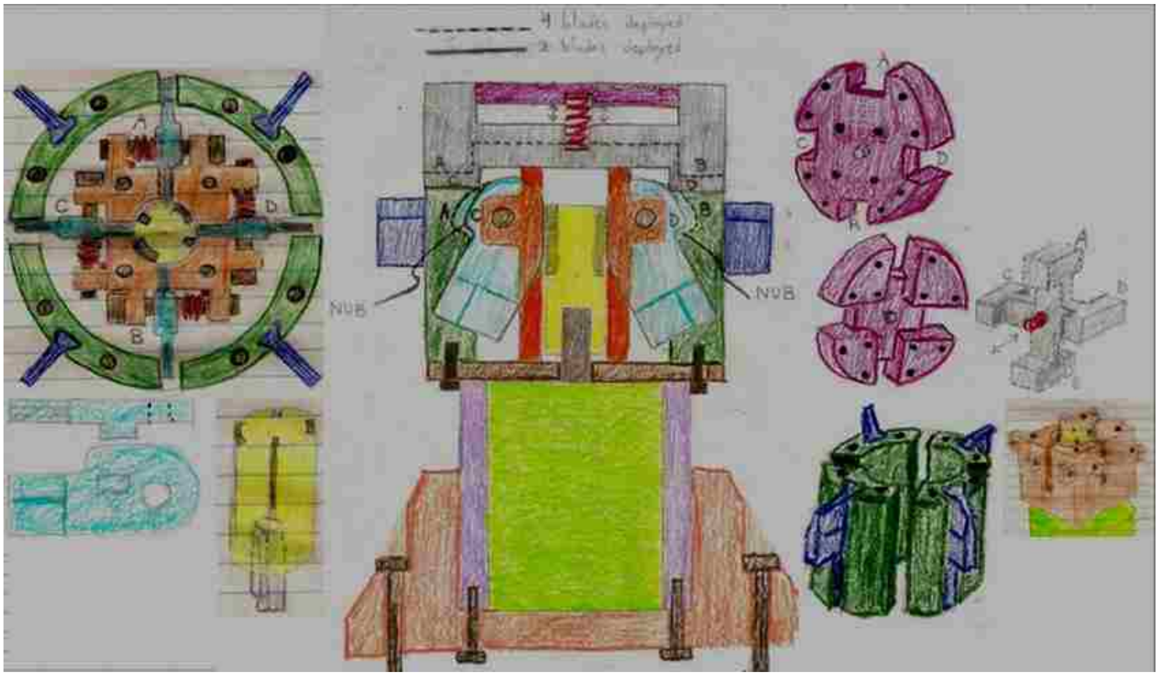

Figure 4.6 Original sketches showing the concept of an adaptive cutter with blades that pivot about bolt shafts like switchblade knives.

spring-loaded blade approach. A bi-stable rotary solenoid was considered (as its shaft is heftier than that of a linear solenoid) to disengage a lock, releasing spring-loaded blades.

The first design using an approach of rotating blades was inspired by Swiss switchblade knife design. Figure 4.6 shows the original sketches of the assembly and the various parts, which have been colored for clarity. This design has not been further drawn in CAD because a simpler, more practical rotary blade approach was conceived before reaching that stage.

Four fixed blades (in dark blue) slide into dovetail slots machined into the main frame (in dark green). Inside the main frame, a smaller frame (in orange) supports four switchblades (in light blue) which freely pivot about bolt shafts. A bi-stable rotary solenoid (in lime green), which has a rotation range of 30 degrees in either direction, is housed at the back of the device. A cylindrical adaptor (in yellow) having four axial notches around the circumference is fit over the solenoid shaft. Each switchblade is preloaded with a torsion spring, but is hindered from swinging upward because it pushes against the surface of the solenoid adaptor. A cross-shaped lock (in silver) is fit through a cross-shaped groove behind the front cover (in deep purple) and loaded with a compression spring (in red). This lock is critical because its function is to prevent the deployed switchblades from swinging back down from their activated positions once the force from cutting (which acts downward) takes place.

Note that the design would be mechanically simpler if the switchblades swung downward because no secondary lock is necessary: once deployed in the fully outward position, the back of the switchblades could press against a surface (such as the main frame), providing the needed supporting force against the cutting force which acts in the opposing direction. However, this approach must be discarded because the switchblades, upon swinging downward, would strike the inner wall of the AA6061-T6 test specimen. Therefore, an upward swinging switchblade is the only possible alternative.

As one can see from Figure 4.6, an upward swinging switchblade design (with 3 cutter configurations) that must support a significant cutting force in the downward direction is quite mechanically complex. Two separate, spring-loaded locks are required to make the system function: the switchblade is disengaged via the first lock (i.e. the yellow solenoid adaptor), and then the upward rotational motion of the switchblade must trigger a second lock (i.e. the silver cross-shaped lock) which falls behind a “nub” to prevent the switchblade from swinging back down. Additionally, given the strict space available in the center of the cutter, the body length (axial length) of the torsion spring cannot be very long. A high stiffness is difficult to achieve in a torsion spring with a short body length because there are few coils, which delays the switchblade response time.

Referring to the left hand image of the device in Figure 4.6 will help the reader understand how the switchblades are deployed. When the solenoid shaft does nothing, cutting is done with 4 blades. When the solenoid shaft rotates 30 degrees clockwise, the notches in the adaptor line up with and deploy only switchblades labeled *C* and *D*, while switchblades labeled *A* and *B* remain locked because they are still pressing against the adaptor. Thus the 6-blade configuration is achieved. Conversely, when the solenoid shaft rotates 30 degrees counterclockwise, the notches in the adaptor line up with all of the switchblades, deploying the 8-blade configuration.

The adaptive cutter would be tremendously simplified if the switchblades rotated about an axis that is parallel, rather than perpendicular as in the design just presented, to the axis of the AA6061-T6 specimen. First, no additional locking mechanism would be needed to keep the blades from rotating back in the opposing direction. Second, the assembly could be made with fewer and simpler to manufacture parts.

Assuming a similar structure to house the bi-stable rotary solenoid as in Figure 4.6, the rest of the design shown in Figure 4.7 consists of few parts: four fixed blades machined out of single blocks of tool steel are fastened to the ring-shaped backing plate (in dark blue). Four identical switchblades pass through shoulder bolts (in dark brown) which are fastened between the backing plate and a front cover. Not only are fewer parts required, but the switchblades can be made “beefier” towards the root of the blade where stresses would be the most critical. Due to lack of space, the switchblades in the last design in Figure 4.6 had to be thin near the bolt to allow room for the torsion spring. Thus, those switchblades would likely have suffered much higher stresses at the blade root and in the vicinity of the bolt. Additionally, the bolt shaft would bear most of

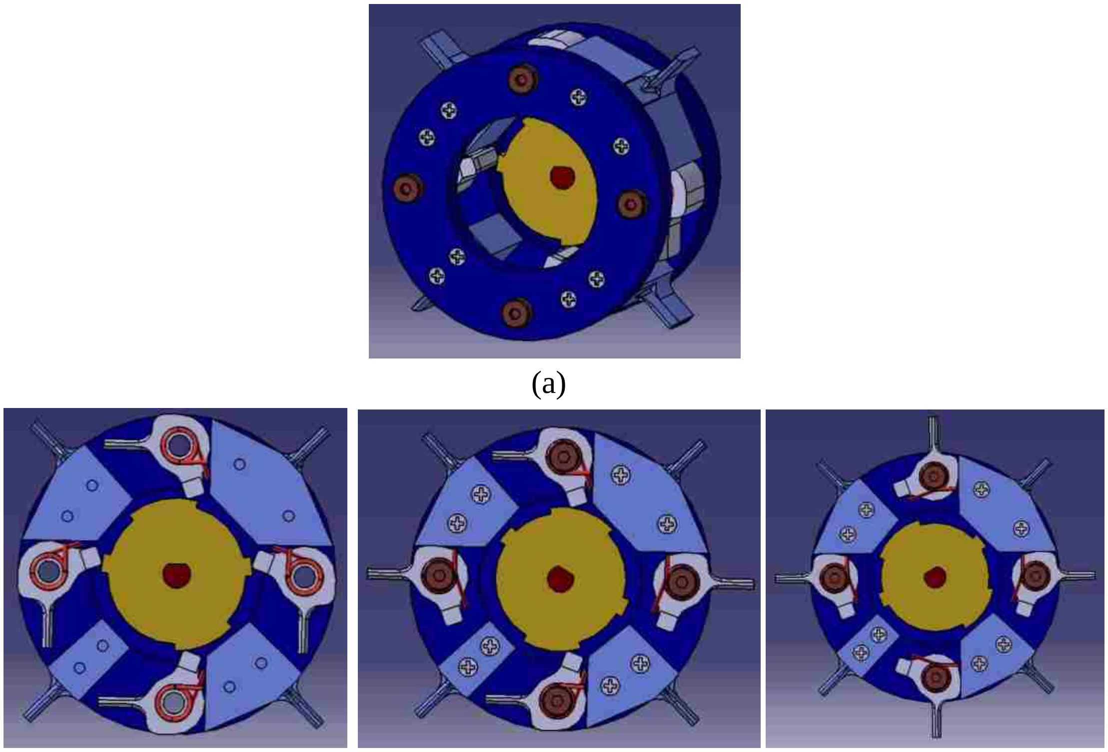
(a)

(b) (c) (d)

Figure 4.7 CAD model of the rotary switchblade adaptive cutter design. Front views with cover plate removed showing adaptor position for (b) 4 blades. (c) 6 blades. (d) 8 blades.

the cutting load (in shear). Conversely, in Figure 4.7, the switchblade consists of more material around the vicinity of the bolt which should mitigate stress concentrations in the bolt area. Further, the orientation of the bolt allows for more room axially to use a torsion spring with longer body length. In other words, the torsion spring could have more coils (for higher stiffness) than the torsion spring chosen for the design of Figure 4.6, resulting in a shorter response time. The stock torsion spring used in the design of Figure 4.7 has a stiffness 2.5 times higher than the torsion spring chosen for the previous cutter design.

The deployment mechanism is similar to that of Figure 4.6, using an adaptor (in yellow) with notches of different sizes around the circumference. In Figure 4.7(b), the adaptor position has all 4 switchblades (in silver) locked, and cutting is done with the four fixed blades (in light blue). As depicted in Figure 4.7(c), to cut with 6 blades, the adaptor rotates clockwise 30 degrees (viewed from the front), where sufficient clearance is provided at the notches to release 2 of the torsionally spring-loaded blades. The other 2 switchblades remain locked as their points of contact with the adaptor do not meet up with a notch. In Figure 4.7(d), to cut with 8 blades, the adaptor rotates 30 degrees counterclockwise (viewed from the front) so that the 4 switchblades line up with a notch and deploy.

To increase the versatility of this device by accommodating a range of AA6061-T6 aluminum specimen diameters, rather than deploying from the inside-out, as in Figure 4.7, the switchblades should be deployed from the outside-in. In that case, all the blades could be made longer and all the components could be larger, further simplifying their manufacturing and reducing their stresses during impact.

Having the switchblade rotate from the outside-in will also require the solenoid to be relocated to the outside of the frame in some way. The first adaptive cutter idea to use a solenoid on the outside of the frame rather than along the longitudinal axis is shown in Figure 4.8. The solenoid (in red) has mounted on its shaft a gear-shaped adaptor (in yellow) which drives a ring gear (in brown) a set angular amount in one direction or the other. Once again, similar to the adaptor of the previous 2 adaptive cutter designs, notches are made at precise locations along the inner wall of the ring. When a notch lines up with a switchblade (which is torsionally spring-loaded) at the region of contact, the

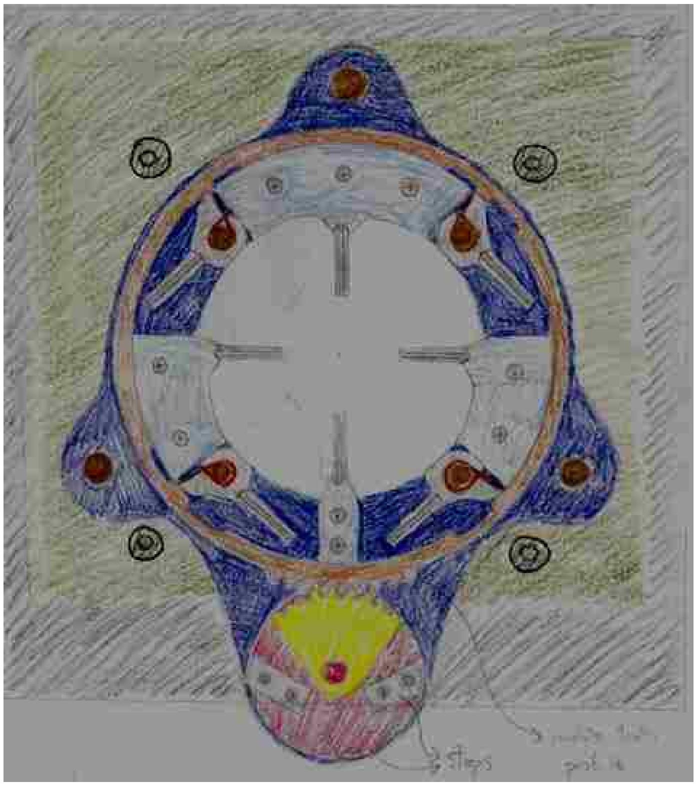

Figure 4.8 Design concept of a switchblade adaptive cutter with blade rotation from the outside-in and a ring/gear lock.

switchblade is allowed to deploy into position. Fastened onto the back cover (in dark blue) are a set of fixed blades as well as two end stops to precisely control the amount of rotation of the solenoid shaft. A brass ring (in brown) slips axially over the fixed blades. A portion of the ring contains involute gear teeth, which engage a set of involute gear teeth on the solenoid adaptor (in yellow). Fastened onto the fixed blades is a front cover (not shown) which serves two important functions: (1) Preventing the brass ring from sliding out axially, and (2) Providing a means to mount the shoulder bolts through which the switchblades and torsion springs can be mounted.

This design retains the simplicity of the design in Figure 4.7, but has larger pieces which will more likely handle the cutting load and be easier to manufacture. The design also accommodates AA6061-T6 extrusion outer diameters ranging from 44.45 mm to 63.5 mm. However, the major concern is the load transfer to the solenoid shaft and casing upon impact. The vibration of the impact between the gear teeth at the ring/adaptor contact interface would transfer a load that is perpendicular to the solenoid shaft, risking permanent damage. Instead, the solenoid should be decoupled from the rest of the system. Somehow, the shaft of the solenoid can only be in direct contact with the locking/ unlocking mechanism before (and not during) the time cutting takes place.

One approach to decouple the solenoid uses a similar assembly to that of Figure 4.8, but incorporates a belt drive system, which would likely transfer very little load to the solenoid shaft under impact. The first belt-drive adaptive cutter design is shown in Figure 4.9. Note that the similar components and assembly suggest that the adaptive cutter is beginning to converge to a final design. The adaptive cutter itself is similar to the design in Figure 4.8, so that portion of the assembly will not be described to avoid repetition. The main difference here is that the locking/unlocking ring (in white) works like a sprocket rather than a gear. The ring, which is made of Teflon to minimize friction and rotary inertia, has three sprockets which pass through holes in a belt. The belt is a composite material comprised of a polyester core with a urethane coating which possesses little stretch and a high coefficient of friction to prevent slippage. The belt is wrapped around a nylon pulley which mounts over the shaft of the BRS5065 bi-stable rotary solenoid. A solenoid substructure (in orange) consisting of standard sized angle plates is fastened to the base plate (in neon green) and hangs over the side of the support column (in black). The casing for a tubular type rotary solenoid, such as the one considered in this and the last few designs, is quite robust. Unlike motors, these solenoids do not have sensitive electronic components such as encoders or brushes that may be damaged due to impact. The interior of the casing only has magnets which may be prone to damage, but would require a significant direct impact to the casing. Nonetheless, ground source vibration to the casing can still be minimized by wrapping it around some damping material. Neoprene pads of ¼ inch thickness are placed on all four sides and bottom of the solenoid casing as a protective shell.

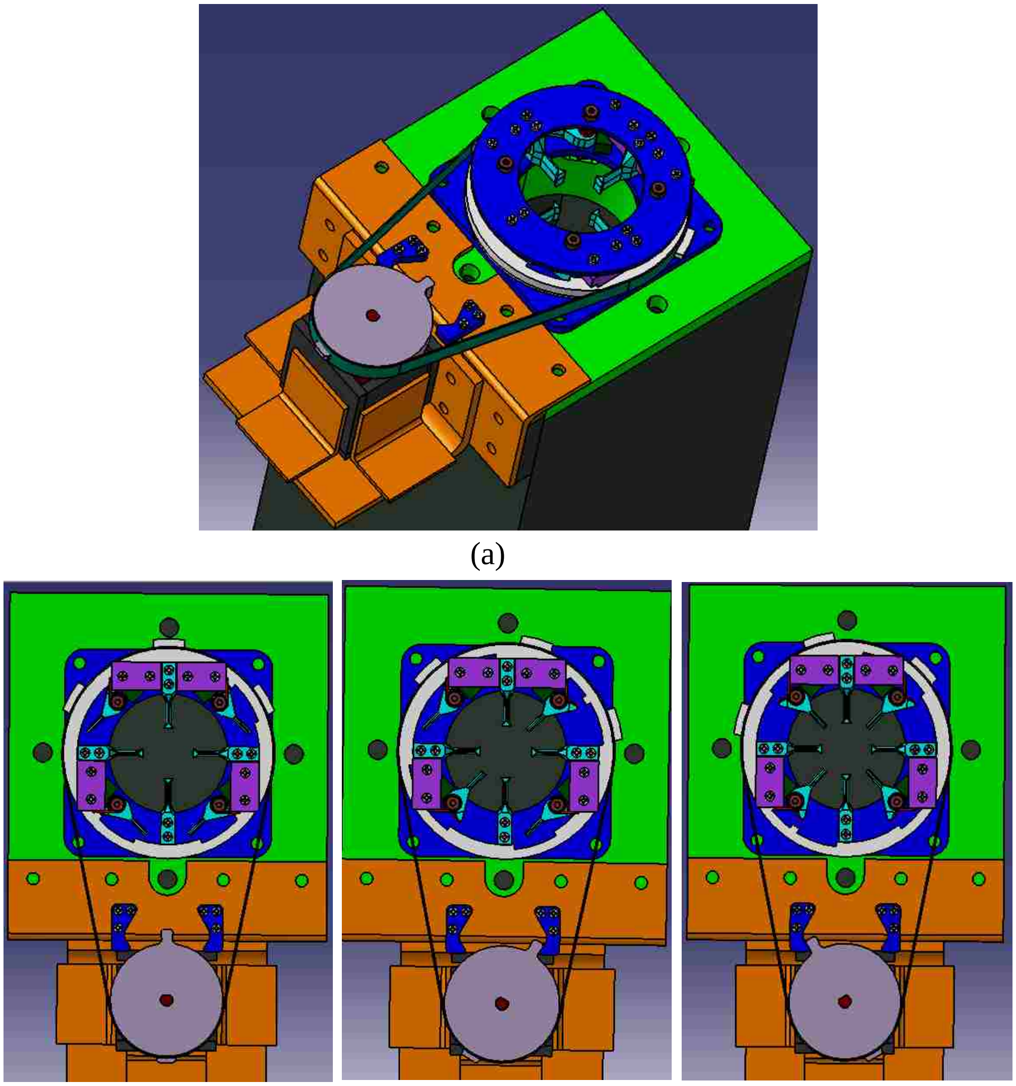

(a)

(b) (c) (d)

Figure 4.9 (a) CAD model of the rotary switchblade cutter design using belt drive. Front views with cover plate removed showing adaptor position for (b) 4 blades. (c) 6 blades. (d) 8 blades.

At this stage, a quasi-static cutting experiment using a fixed cutter developed by [10] with 8 blades was performed to assess whether the amount of petal flaring from a 3.175 mm thick AA6061-T6 specimen could be accommodated without interfering with the structure of the adaptive cutter. Although significant flaring of the AA6061-T6 extrusion was expected using 8 blades, the detailed profile of the extrusion deformation using 8 blades was never documented. A quasi-static cutting test using 4 blades was also performed to document the minimum flaring expected in the adaptive cutter. The lengths and angles of the petals were measured post test so that the deformed specimens could be modeled in CATIA. The CAD models of these cut extrusions along with sample photographs are shown in Figure 4.10. As seen in Figure 4.10(b), the amount of petal flaring using 8 blades was more extreme than expected.

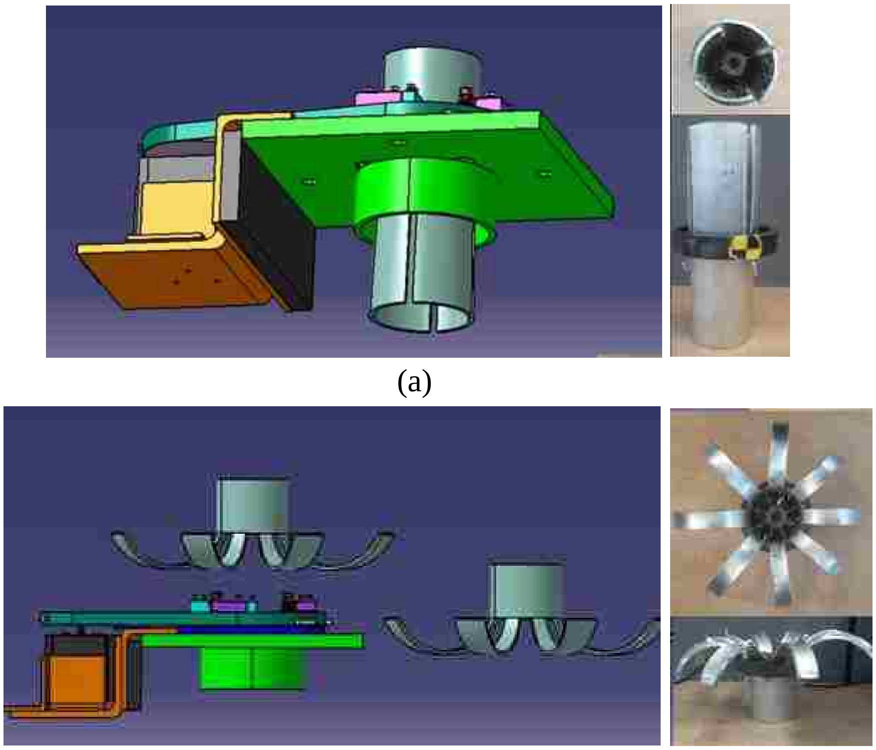
(a)

(b)

Figure 4.10 Comparison between petal flaring of 3.175 mm thick AA6061-T6 extrusions when cutting with (a) 4 blades. (b) 8 blades.

This deformation pattern with 8-blade cutting imposes one of two possible design changes: one option is to include a cylindrical container below the base plate (as shown in Figure 4.10) to constrain the petals from flaring too significantly. The other option is to raise the adaptive cutter on a platform so that the petals may have space to clear the underside of the back cover. The latter option was pursued because with the former option, the petals may scrape the inner wall of the container, possibly resulting in a fluctuating force/deflection response.

Illustrated in Figure 4.11 is the same adaptive cutter design of Figure 4.10 except that the structure is raised on four support legs (in red) and a separate platform (in orange). Given that the petals will not deform perfectly symmetrically, as indicated by the photograph in Figure 4.10(b), completely avoiding contact underneath the device is deemed impossible without detrimentally reducing the height of the blades and thicknesses of the back cover and elevated platform. Instead, the elevated platform and support legs are shaped and positioned in such a way to minimize the possibility of poor contact between the extrusion petals and other parts in the device. The underside of the elevated platform is chamfered to conform to the profile of the AA6061-T6 petals and serves to guide the petals rather than prevent flaring. As seen in Figure 4.11(b), the extrusion petals separate more as they move further outward radially. The four support legs, being located far outward radially and in line with the four fixed blades, have enough clearance between the extrusion petals. The only poor region of petal/device contact is at the solenoid support structure as seen in Figure 4.11(a). Besides the two petals with poor contact, this adaptive cutter design raises another concern. One questions if the solenoid will still be able to rotate after the shaft is preloaded with a tense belt. Even though the torque rating of the rotary solenoid is known, it is a “no-load torque”.

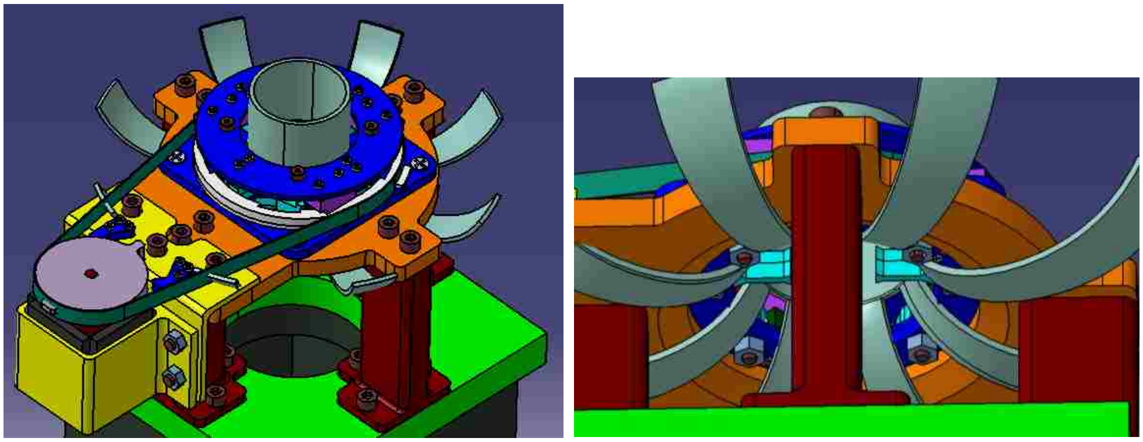
(a) (b)

Figure 4.11 (a) CAD model of the adaptive cutter using a belt drive and an elevated support structure. (b) Underside showing petals flaring with 8 blades.

An alternative would be to use four separate pull type solenoids located at each support leg to trigger each switchblade individually. This approach would have several advantages over the current design: (1) The two petals having poor contact with the device in Figure 4.11 would be avoided. (2) The Teflon ring, belt and pulley would be removed and replaced with individual pins to jam the switchblades locked, simplifying the design. (3) Using four weaker pull type solenoids turns out to be more economical than using a single, more powerful, bi-stable rotary solenoid. While each of the pull-type solenoids costs $48.00 for a total of under $200, one bi-stable solenoid of the power considered in the belt design can cost over $400. (4) Since each solenoid only has to overcome the frictional force of one stiff torsion spring, one can rely on its successful performance with more confidence than the design requiring the bi-stable rotary solenoid to overcome the frictional force of four stiff torsion springs and a tense belt.

An adaptive cutter design using 4 pull-type solenoids is shown in Figure 4.12. Each Teflon pin (in pink) provides the means to jam each switchblade locked while also decoupling each solenoid from each switchblade. The switchblade applies a load against the pin which rests against the corner of the fixed blade. The shaft of the solenoid itself could be used as the locking entity, but the impact from cutting would damage the solenoid. The Teflon pin is also not directly attached to the shaft of the solenoid as it would still not be decoupled from the switchblade. Instead, fastened onto the solenoid shaft is a pick (in dark green), which passes through a small hole on the side of the Teflon pin. An all-around clearance of 0.127 mm between the pick and Teflon pin ensures that any vibration of the switchblade would not have a direct path of solid material to the solenoid shaft. The SOTUL0230051 pull-type solenoids [45] (in maroon) are simply mounted onto angle plates (in yellow) with a hex nut. Neoprene pads (in black) are

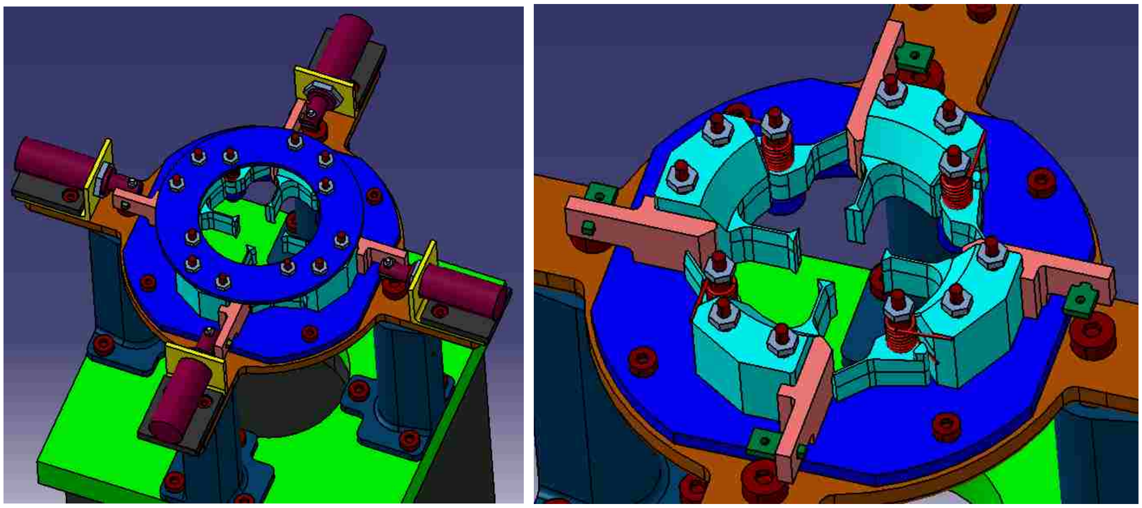
(a) (b)

Figure 4.12 (a) CAD model of the rotary switchblade cutter design using 4 linear pull-type solenoids. (b) Front cover and solenoids removed for clarity.

shimmed tightly below the casing of the solenoid to minimize ground source vibration. Dytran model 1210V2 ring style force sensors have been integrated between each support leg and the elevated platform (in orange) so that the cutting force could be measured.

The adaptive cutter of Figure 4.12 was deemed ready for further engineering analysis. However, after generating numerical models of the cutting deformation, the results of which are presented in Appendix G, the adaptive cutter design was found to be unacceptable. Specifically, the blade spacing in the 6-blade configuration which is not axisymmetric, but only symmetric about 2 axes, resulted in uneven petal flaring, twisting the fixed blades to catastrophic failure. Additionally, the ¼ in diameter of the shoulder bolts passing through the switchblades were also undersized as the stresses during cutting in either the 6-blade or 8-blade configuration led to their plastic failure.

A redesign of the adaptive cutter was required that mitigates these two major problems with the previous design. The assembly of the new adaptive cutter, referred to as the quadrotor, is shown in Figure 4.13. From (a), the same support legs and Dytran 1210V2 ring style load cells are used, except the legs are positioned at the corners of the adaptor plate (brown), locating them further apart. From (b), an elevated platform (orange) of the same ½ in thickness and similar geometry is fastened over the support legs. From (c), the solenoids, angle plates, neoprene pads, and solenoid adaptor are identical to the previous design. From (d), two sets of identical rotary blades, referred to as the 3-bladed cutter (in lilac) and 4-bladed cutter (in teal blue), slip over ½ in diameter shoulder bolts that are fastened between the front and back covers. An Acxess torsion spring model PT078-781-7.000-MW-LH-2.000-N-IN fits over each ½ in bolt shaft. This torsion spring has an angular working range of 156 degrees and a torsional stiffness of 6.562 N·mm/deg. Its 17.5 mm body length fits within the axial space available between the top surface of the blade and bottom surface of the front cover. Fastened onto the back cover are 4 L-shaped blocks that serve as: (1) end stops to position the rotary cutters, (2) fixed surfaces for one arm of each torsion spring, and (3) mounts onto which the front cover is fastened. These blocks also contain a rectangular slot through which the Teflon pins (white) can slide securely. A K&J Magnetics plastic-coated neodymium magnet 12.7 mm^3, depicted in yellow in Figure 4.13(d), is held in place by its own 31.1N

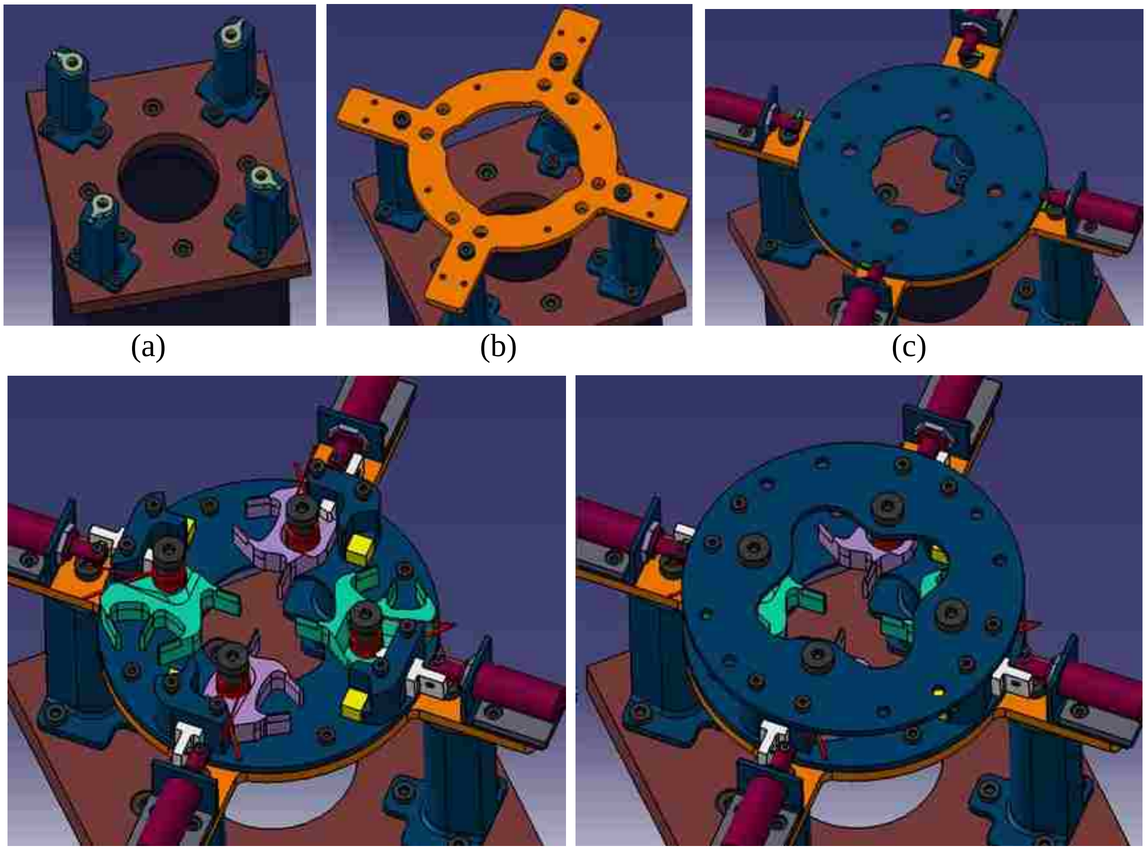
(a) (b) (c)

(d) (e)

Figure 4.13 CAD model assembly of the quadrotor adaptive cutter design. (a) Support legs with Dytran 1210V2 load cells. (b) Elevated platform. (c) Back cover and solenoid substructure. (d) Full assembly with front cover removed. (e) Full assembly with front cover.

magnetic pull in a machined corner of each L-block. The purpose of the magnet is to catch the side face of the blade on impact as the cutter pivots into position. Note the plastic coating on the Neodymium magnet prevents chipping and is designed for repeated impacts. Without the magnet, the blade would bounce off the surface of the L-block and require significantly more time to settle. Finally, from (e), the front cover is fastened onto the top surface of the L-blocks. Four pairs of additional through holes are seen in the front cover and are used to fasten jaw housings that will be described later in this section.

The three blade configurations and method of blade deployment are illustrated in Figure 4.14(a) through (c). Note from the bottom image in Figure 4.14(a), all four cutters

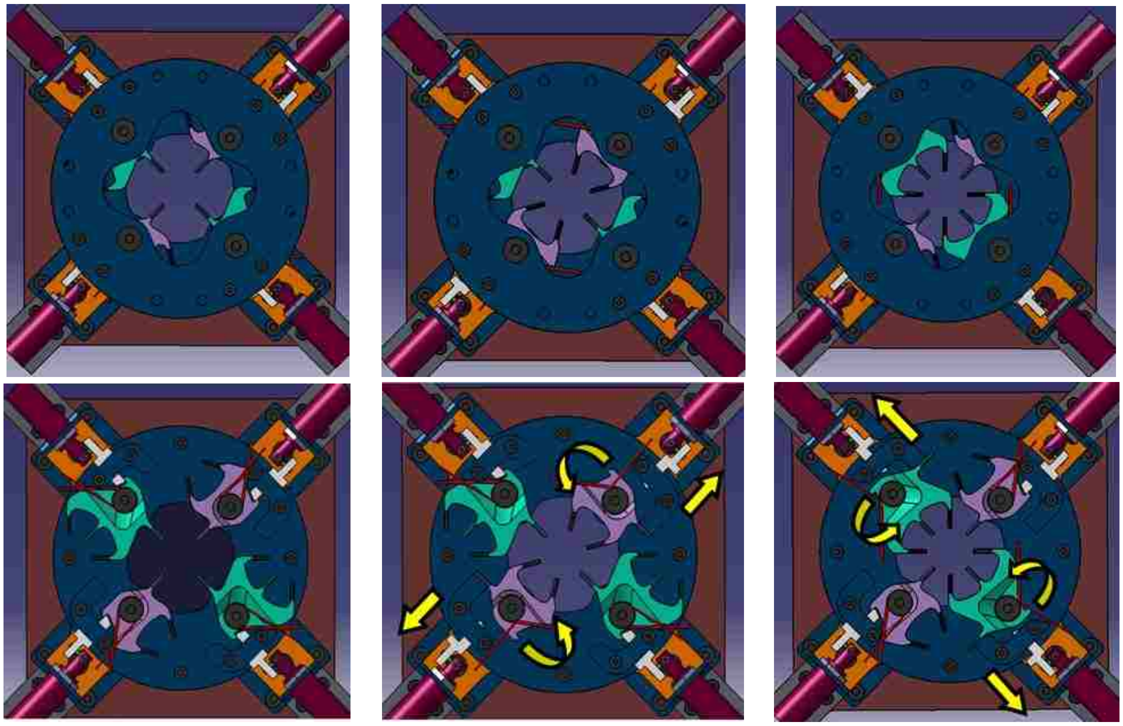
(a) (b) (c)

Figure 4.14 CAD models of the three blade configurations for quadrotor blade adaptive cutter design with front cover shown (top) and front cover removed (bottom): (a) 4 blades. (b) 6 blades. (c) 8 blades.

are preloaded with torsion springs and tend to rotate counterclockwise. Each Teflon pin contacts the side face of an embossed feature on each cutter to prevent it from rotating counterclockwise. Each of the L shaped blocks also has a chamfer that prevents the blade from rotating further clockwise, accurately controlling its position. The geometries of the 3-bladed cutter and 4-bladed cutter are such that the spacing is equal about the circumference in the 6-blade configuration and 8-blade configuration, respectively. In addition, near the bolt hole region of each cutter, material has been removed to form a depression. This hollowed region reduces the cutter mass and rotary inertia, decreasing the response time, and also provides the axial room to fit the torsion spring beneath the front cover. The junction between the taller region and the depression in each cutter lies on a slant to reduce the stress concentration during cutting.

For the 4-blade configuration, none of the solenoids are activated. For the 6-blade configuration, in Figure 4.14(b), the top right and bottom left solenoids are activated, pulling back the Teflon pins and deploying the two 3-bladed cutters. Also, a minimum of

1.4 mm clearance exists between the 3-bladed cutter and 4-bladed cutter as the 3-bladed cutter pivots into position. For the 8-blade configuration, in Figure 4.14(c), while the two 3-bladed cutters remain stationary, the top left and bottom right solenoids are activated, pulling back the Teflon pins and deploying the two 4-bladed cutters.

The previous adaptive cutter had four fixed blades onto which the AA6061-T6 extrusion could be mounted because those blades never changed position. However, in the quadrotor adaptive cutter, any of the four cutters could be pivoting, so the extrusion cannot be mounted directly onto any of these blades. To overcome this problem, the extrusion can be elevated above the blades with a small clearance. A system using four compression spring-loaded jaws, depicted in Figure 4.15, was devised that not only elevates the extrusion, but also self-centers it. From Figure 4.15(a), onto the front cover are fastened four housings, each having a cylindrical hole through which a compression spring and the shaft of a jaw (in brown) can freely slide. Each jaw shaft contains a slit pin (in yellow), which is press fit through a hole on the jaw shaft and slides through a slot machined in the jaw housing. This slit pin constrains the jaw shaft from rotating in the housing and prevents the spring from accidentally pushing the jaw out of its housing when no extrusion is present. The section views in Figures 4.15(b) and (d) show that the smallest diameter (44.45 mm) and largest diameter (63.5 mm) extrusions, respectively, are possible to mount in the four jaw chuck. The compression spring is an Acxess spring model PC028-375-10.000-MW-1.500-C-Z-IN. This spring has the necessary working range to accommodate the smallest to largest extrusion diameters. Also, even when the quadrotor device is subjected to minor vibration, the spring stiffness of 0.46 N/mm results in a normal force sufficient to hold the extrusion steadily: 6.7 N per jaw (26.8 N total) for the 44.45 mm diameter extrusion, and 11.1 N per jaw (44.5 N total) for the 63.5 mm diameter extrusion. To position the extrusion axially with a 1 mm clearance above the cutters, a 0.5 mm radius groove machined on the extrusion’s outer wall, located below the bottom tooth in Figure 4.15(c), serves as an identifying mark. Holding the extrusion only along its sides induces very little stress in the jaw shaft, as presented in Appendix H.

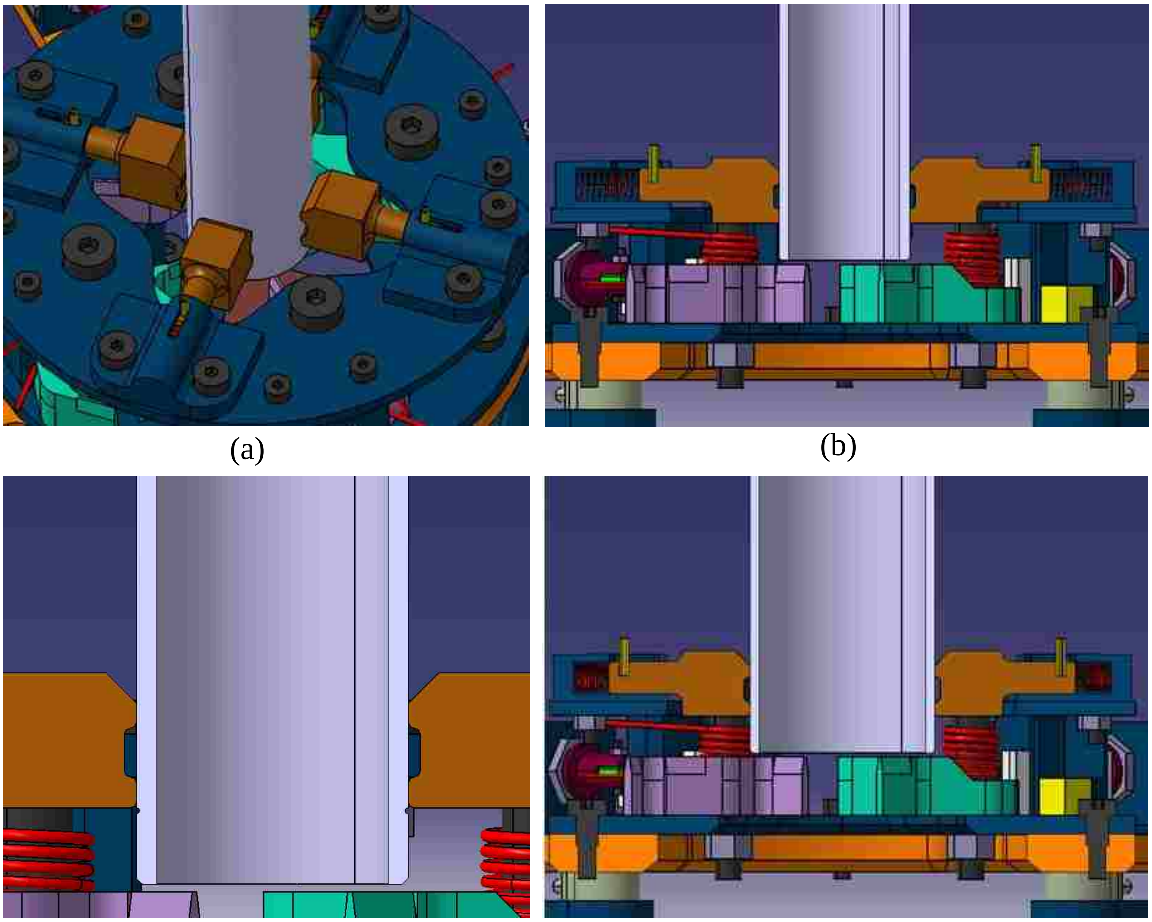

(a) (b)

(c) (d)

Figure 4.15 CAD model of the compression spring loaded 4-jaw chuck. (a) Isometric view. (b) Section view with 44.45 mm diameter extrusion. (c) Small positioning groove on outer diameter of extrusion below bottom jaw teeth. (d) Section view with 63.5 mm diameter extrusion.

5.0 FINITE ELEMENT MODELS OF THE QUADROTOR ADAPTIVE CUTTER

This chapter delves into the details the FE models developed to simulate the functioning of the quadrotor adaptive cutter. The meshes of every single component in the device were constructed manually from 2-dimensional sketches and sweeping techniques in LS-PrePost v4.3. Though no mesh sensitivity studies were performed, best attempts were made to achieve a fine mesh discretization in all numerical models. The FE modeling was developed for simulation in LS-DYNA v971. First, simple static FE models of the 3-bladed cutter and 4-bladed cutter were constructed to preliminarily assess whether their geometries could support the expected cutting loads. Second, the influence of the extrusion impact on the jaw assembly without any cutting was simulated to assess the jaw design. Third, rigid body models of the solenoid activation and deployment of each cutter were constructed to assess both response times and whether vibration was a critical factor. Fourth, all the parts in the models of the rotary cutter motion were changed to elastic materials to better assess response times, stresses, effect of vibration and friction, and ensure contact (especially with materials of different elasticity) was handled properly. Fifth, models of the bolt preloads were constructed for each bolted connection separately to achieve the desired tensile preloads. Sixth, “pre-cutting” models of the entire cutting device in each configuration (4 blades, 6 blades, and 8 blades) were constructed to ensure the device was preloading all the bolts and deploying the rotary cutters as expected before cutting. Last, cutting simulations were constructed for the three configurations to determine whether the device could handle the stresses and if the force/deflection responses were acceptable. The device durability based on the stresses in cutting is discussed in Chapter 6.0.

5.1 Bolted Connections in the Quadrotor Adaptive Cutter

This section discusses the modeling techniques used to achieve the proper preloading at the bolted connections in the quadrotor adaptive cutting device. In one approach, a discrete linear spring with an initial offset was used to achieve clamping, while also invoking damping to reduce the vibratory response. Although in some cases this technique was satisfactory, in connections where bolt shafts passed through three plates rather than two, the preloads were highly fluctuating nonetheless. For that reason, another bolt modeling technique was tried that uses a gradual application of externally applied axial forces to achieve clamping. This latter modeling approach was found to be more suitable for the pre-cutting and cutting simulations of the quadrotor adaptive cutter.

5.1.1 Clamping Using a Discrete Spring and Invoked Damping

The bolts and nuts are modeled using solid, hexahedral elements with single point integration and elastic materials. However, as seen in Figure 5.1, the nodes on the top face of the bolt head are shared with a disk made of rigid shell elements (in red). Along the periphery of the nut hole (or plate hole if no nut is used), the nodes are shared with a ring made of rigid shell elements (in green). An extra node is defined at the center of the rigid ring and associated with that part using *CONSTRAINED_EXTRA_NODES_ NODE. A discrete linear spring element is attached between the central node of the disk and the extra node at the center of the ring. In Figure 5.1(a), the spring is initially in a tensile state and provides zero clamping force. In Figure 5.1(b), at the first time step, the spring tension is released, which forces the head of the bolt to move down, clamping the plates sandwiched between the rigid disk and ring shells. Note the reason for using a rigid disk is to distribute the load on the underside of the bolt head. If the spring was attached to the central node on the elastic bolt head, the load would not distribute effectively and

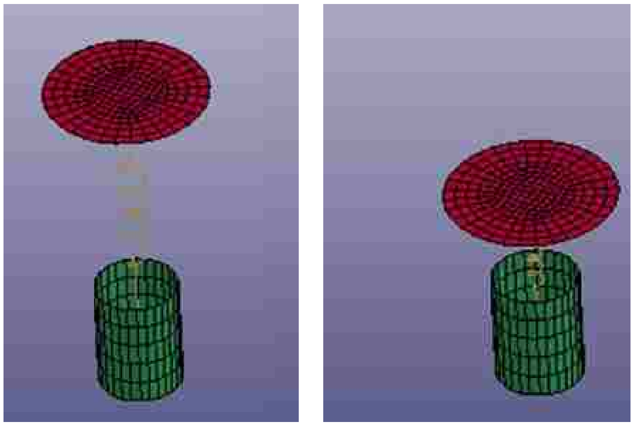
(a) (b)

Figure 5.1 Rigid shell disk, discrete linear spring, and rigid shell ring for instantaneous bolt clamping. (a) Spring in tension at time=0. (b) Spring released after time=0 generating a clamping force on plates (deformation is exaggerated in image for clarity).

the elements would tend to hourglass near the spring attachment point. Also, the rigid ring is needed because the extra node in *CONSTRAINED_EXTRA_NODES_NODE cannot be associated with an elastic part.

Determining the required displacement (or offset) of the spring for every bolted connection is an iterative process. The step-by-step procedure is similar to one developed by Reid [46] and is as follows:

1- The required tensile preload, F, for each bolt is calculated analytically based on the tightening torque, T (provided in the manufacturer's data sheet for each shoulder bolt), the torque coefficient, K, for the specific thread size, and the thread diameter, d. This relationship is

$$F = \frac{T}{K \cdot d} \qquad [47]$$

2- The stiffness of the spring in the LS-DYNA model needs to be defined. It is manually calculated as $k = AE/L$, where

A: Cross sectional area of shoulder bolt diameter
E: Modulus of elasticity of bolt material (steel)
L: Length of shoulder bolt below head

3- The spring offset is guessed in the LS-DYNA model. The offset is defined as a positive value in *ELEMENT_DISCRETE which initializes the spring in tension. At the start of the simulation, the spring is released instantaneously, clamping the bolt head and nut (or plate) together.

4- The bolt model is simulated.

5- The axial force is checked at the bottom face of the bolt head. If the tensile load is within 10% of the calculated tensile preload in step 1, the offset specified in step 3 is accepted. If the tensile load is outside of this accepted error, a different offset value is specified.

6- Steps 3 to 5 are repeated until the specified offset results in a tensile load that is within acceptable tolerance to the calculated preload.

Releasing the spring tension instantaneously induces a high frequency vibratory response, causing the axial force in the bolt to oscillate. To reduce the spring vibration further, damping to the spring was invoked using *DAMPING_PART_STIFFNESS with the maximum recommended Rayleigh damping coefficient of 0.25. This bolt modeling technique worked effectively for shorter bolts passing through only two plates. Also, the law of energy conservation was verified with an energy balance. However, in bolted connections having three layers of material clamped together, the axial preload remained highly oscillatory even with invoked damping. The bolt modeling technique presented in the next section achieves both the requirements of achieving a stable axial preload as well as satisfying energy conservation.

5.1.2 Clamping Using Externally Applied Axial Forces

The solution to achieving a stable preload while also not violating the law of energy conservation is a simple change to the model presented in Section 5.1.1: the spring is altogether removed and replaced with a pair of equal and opposite axial forces acting to compress the bolt head and nut together. The concept is shown in Figure 5.2(a) and (b). In (a), at time=0, the rigid disk shell and ring shell are subject to no load. In (b), at the first time step, an axial force is applied at the center of the disk, and an equal and opposite axial force is applied at the extra node in the middle of the ring. Dynamic effects associated with instantaneous loading are avoided by ramping the axial forces over a time span of 1 ms and holding them constant for the remainder of the simulation. Additionally, the bolt model is simpler: it contains fewer parts; the spring energy, which is not physically present in the real bolt, is not computed; and no spring offset needs to be assumed to achieve the desired preload. Instead, the desired axial force is equal to or very close to the analytically calculated preload. In some cases, due to initial gaps between parts, the bolt preload may be slightly different than the defined axial forces, but determining a suitable axial load is easier than determining a suitable spring offset. Ultimately, the modeling technique presented in this section was applied for all bolted connections in the quadrotor adaptive cutter for the pre-cutting and cutting simulations.

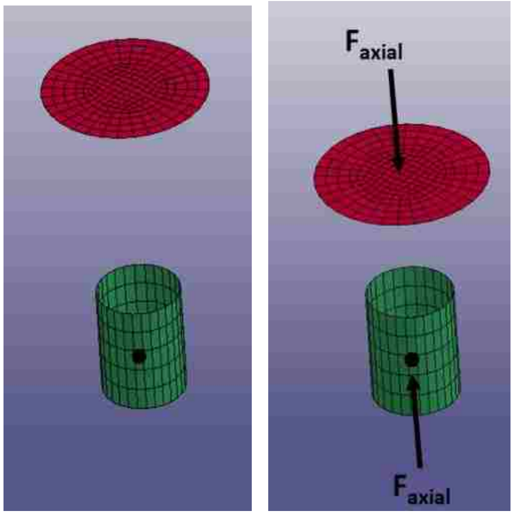

(a) (b)

Figure 5.2 Rigid shell disk, rigid shell ring, and external axial loads for gradual bolt clamping. (a) No load applied at time=0. (b) Equal and opposite axial forces applied gradually and held constant after 1 ms until end of simulation (deformation is exaggerated in image for clarity).

5.2 Model of the Torsion Spring

This section outlines a model developed for the torsion spring used to drive the 3-bladed cutter and 4-bladed cutter using elastic materials. Note that a torsion spring element can only be attached to a rigid part because the node at which the spring is connected must have rotary inertia. In elastic materials, the elements have rotary inertia, but individual nodes do not. Conversely, a linear spring element does not necessarily have to be attached to a rigid part because individual nodes in elastic materials have translational inertia.

A modeling approach believed to correctly represent the motion of the torsional spring for the elastic 3-bladed cutter is depicted in 5.3 (a) and (b). From (a), based on the wire geometry of the actual torsion spring, the last coil and arm, referred to as the loop, is meshed with solid hexahedral elements using single point integration and 3 elements through the thickness. The material of the loop is defined as *MAT_RIGID and assigned an elastic modulus and density of 200 GPa and 8000 kg/m^3, respectively. From (b), a discrete torsion spring element is attached between the rigid shell disk located on the bolt

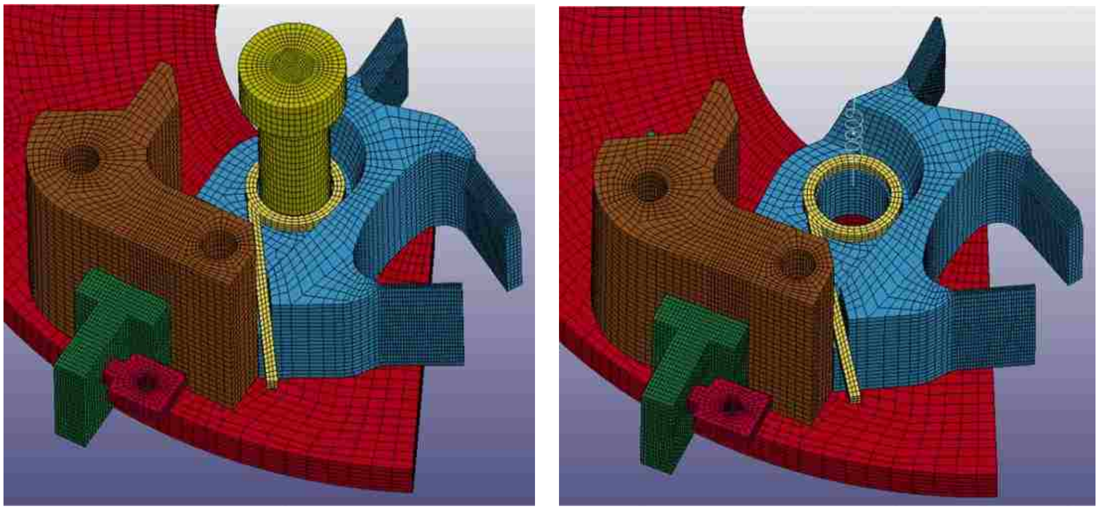
(a) (b)

Figure 5.3 Mesh of elastic 3-bladed cutter with a rigid loop representing last coil of torsion spring. (a) Parts used in the model. (b) Bolt hidden to show the torsion spring element along axis of hole.

head and an extra node defined along the axis of the bolt near the same plane as the loop. The extra node is associated with the loop part using *CONSTRAINED_EXTRA_NODES_NODE. Since the torsion spring element is already aligned with the bolt axis, the orientation option in *ELEMENT_DISCRETE is left blank. The angular offset required to preload the spring is specified as 2.53 radians (145 degrees). Ultimately, the preloaded discrete torsion spring element causes the arm of the rigid loop entity to apply a push force against the 3-bladed cutter, which is actually a good representation of how the real torsion spring will physically work.

The same modeling approach just outlined here for the torsion spring on the elastic 3-bladed cutter is also applied to the elastic 4-bladed cutter. To avoid repetition, the torsion spring model for the 4-bladed cutter is not shown.

5.3 Pre-Cutting Simulations of the Quadrotor Adaptive Cutter

In this section, the FE models for the three configurations of the quadrotor adaptive cutter, prior to cutting, are described.

A half model of the quadrotor adaptive cutter, excluding the extrusion, is shown in Figure 5.4. All the parts shown are modeled using solid, hexahedral elements with

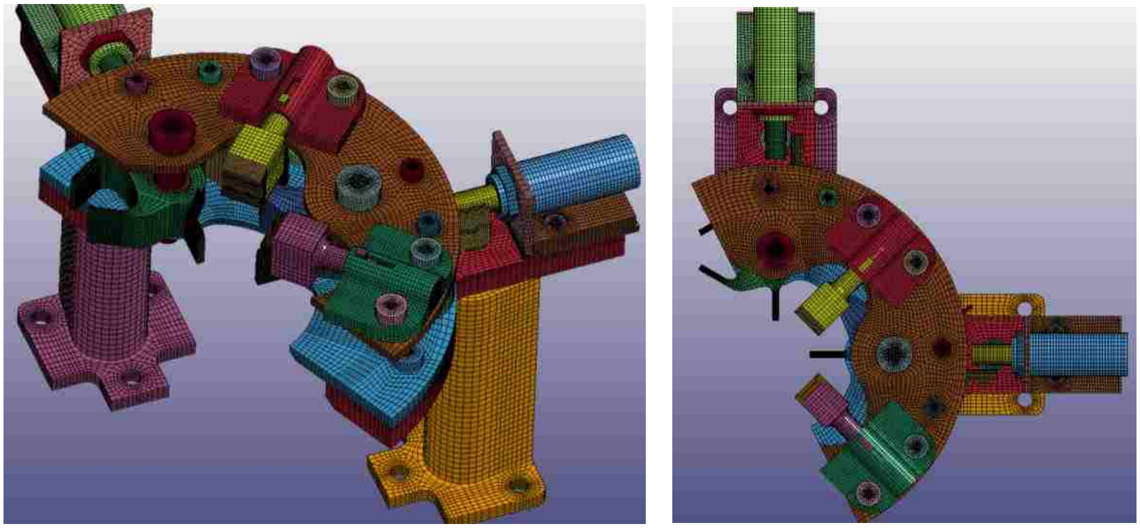

(a) (b)

Figure 5.4 Half model of quadrotor adaptive cutter for the 3 configurations in the pre-cutting simulations. (a) Isometric view from above. (b) Top view.

single point integration and at least four elements through the thickness in any component. *MAT_ELASTIC with the density and elastic modulus of steel (i.e. 8000 kg/m^3 and 200 GPa, respectively) are specified for the majority of the parts. The pin material is defined with *MAT_ELASTIC using the density and elastic modulus of Teflon (i.e. 2160 kg/m^3 and 1.6 GPa, respectively) and a Poisson ratio of 0.46. The neoprene pad material is defined using *MAT_MOONEY-RIVLIN_RUBBER with a density of 1.2 kg/m^3 and Poisson ratio of 0.49. The coefficients A and B in this keyword are specified as 552 and 138, which were taken from an example on the LS-DYNA support website [48] and properly converted to the base units used in this model (kg, mm, s). Hourglass control was applied to the steel components by setting IHQ=6, QM=1 in *HOURGLASS. The Teflon pin and neoprene pad were challenging to model without experiencing extreme hourglassing as they contact the much stiffer material steel. However, contact is well modeled by setting IHQ=5 and QM = 0.1 (default value) in a separate *HOURGLASS card for the Teflon pin and neoprene pad. Contact between all of the parts is modeled using *CONTACT_SURFACE_TO_SURFACE and individual pairs of segment sets (i.e. a total of 286 segment sets). The static and dynamic friction coefficients for steel on steel contact are 0.55 and 0.50, respectively. The coefficient of friction at the cutter/bolt interface and cutter/back cover interface is 0.16, replicating lubricated contact. The contact between the 3-bladed cutter and magnet, and the 4-bladed cutter and magnet, for the 6-blade configuration and the 8-blade configuration, respectively, is obliged to stick upon impact using *CONTACT_AUTOMATIC_ SURFACE_TO_SURFACE_TIEBREAK and setting OPTION=1. For Teflon on steel, the static and dynamic friction coefficients are 0.18 and 0.16, respectively. Any contact with the neoprene pad is assigned static and dynamic coefficients of friction of 0.70 each. All contact algorithms were assigned a decay coefficient of 10^6 and viscous damping coefficient of 25%. To prevent any accidental axial rotation of the solenoid casing, an axial rotation constraint is set in *BOUNDARY_SPC_SET with reference to a local coordinate system placed on the axis of the solenoid casing. That local coordinate system is created using *DEFINE_COORDINATE_NODES, which references existing nodes to define the three local axes. Rather than modeling the clamping force between the hex nut, angle plate and solenoid casing, *CONTACT_SURFACE_TO_SURFACE_TIED was specified between the hex nut hole periphery and solenoid casing. The periphery of the holes at the bottom of the support legs are fully constrained as all parts below the support legs are considered far enough away from the regions of concern. Also note that each steel pick, which in reality is fastened to the end of the solenoid shaft, is simply "glued" inside the slot of the shaft using *CONTACT_SURFACE_TO_SURFACE_ TIED. Since the bolt and the hole through the solenoid shaft are not critical zones in the adaptive cutting device, meshing these features would have been unnecessarily tedious.

The model of the jaw assembly is described in Appendix G, so the interested reader may refer to that section. The only difference in the pre-cutting models is that the jaw does not have a slit pin because as mentioned in Appendix G, it was unable to maintain contact with the jaw shaft. Instead, a key is meshed directly on the jaw shaft to ensure that the preloaded linear spring will not push the jaw out of its housing. Additionally, the models for the bolts and torsion springs were described in sections 5.1 and 5.2, respectively, and so are not repeated for brevity.

The limits of the boundaries of symmetry are the same for the three blade configurations, depicted in Figure 5.4(b). First, the boundaries of symmetry are not those of reflective symmetry like a mirror. They are actually boundaries of rotational symmetry, similar to that seen in a fan hub with repeated blades. In order for LS-DYNA to interpret the nodal displacements, velocities, and accelerations of each node in the device as rotationally symmetric, not reflectively symmetric, *BOUNDARY_CYCLIC is specified using the node set at either boundary. Both node sets must be located on parts that span continuously from one boundary to the other. For that reason, both node sets strictly contain the front cover, back cover, and elevated platform, as only these three components have continuous material spanning from one boundary to the other. The 3-bladed cutter and jaw housing are not cut along the boundaries, but partially overlap the boundaries, because *BOUNDARY_CYCLIC does not apply to parts that are repeated intermittently. Also note the planes selected do not slice through any bolts so that they could be clamped properly in the model. Second, due to the different geometry and radial position of the 3-bladed cutter and 4-bladed cutter, the three configurations of the quadrotor must use a half model rather than a quarter model. The mesh for this half model contains a total of 1,027,092 nodes forming 871,525 elements.

Referring to Figure 5.4(b), the three pre-cutting models consist of the following inputs:

1. For the 4-blade configuration, the shoulder bolts clamp the parts in the device. The simulation end time is 1.5 ms to allow enough time for the bolt preloads to settle.
2. For the 6-blade configuration, the simulation end time is 30 ms. In this case, the shoulder bolts clamp the parts in the device, and then after 1.5 ms has elapsed, the top solenoid shaft is prescribed an upward displacement using BOUNDARY_PRESCRIBED_MOTION_NODE referring to a node on the back face and in the center of the solenoid shaft. The load curve specified for the solenoid shaft motion is 6 mm in 4 ms, known from the solenoid manufacturer’s specifications. The pick on the shaft pulls out the Teflon pin, releasing the 3-bladed cutter, which is preloaded with a torsion spring.
3. For the 8-blade configuration, the shoulder bolts clamp the parts in the device, and then after 1.5 ms has elapsed, the right solenoid shaft is prescribed a displacement to the right following the same technique as described for the 6-blade configuration, except that the simulation end time is 42 ms.

5.3.1 Pre-Cutting in the 4-Blade Configuration

The effective stresses and energy balance of the system for the quadrotor adaptive cutter in the 4-blade configuration prior to cutting are shown in Figure 5.5. Globally, the highest stress due to bolt preloading is in the front cover near one of the ¼ in bolts through the L-block being 163 MPa. One local red zone of 246 MPa is highly localized at the sharp edge beneath each M8 bolt head near the fillet radius of the jaw housing. Since the bolt heads will have some form of fillet radius, a contact stress this high is not

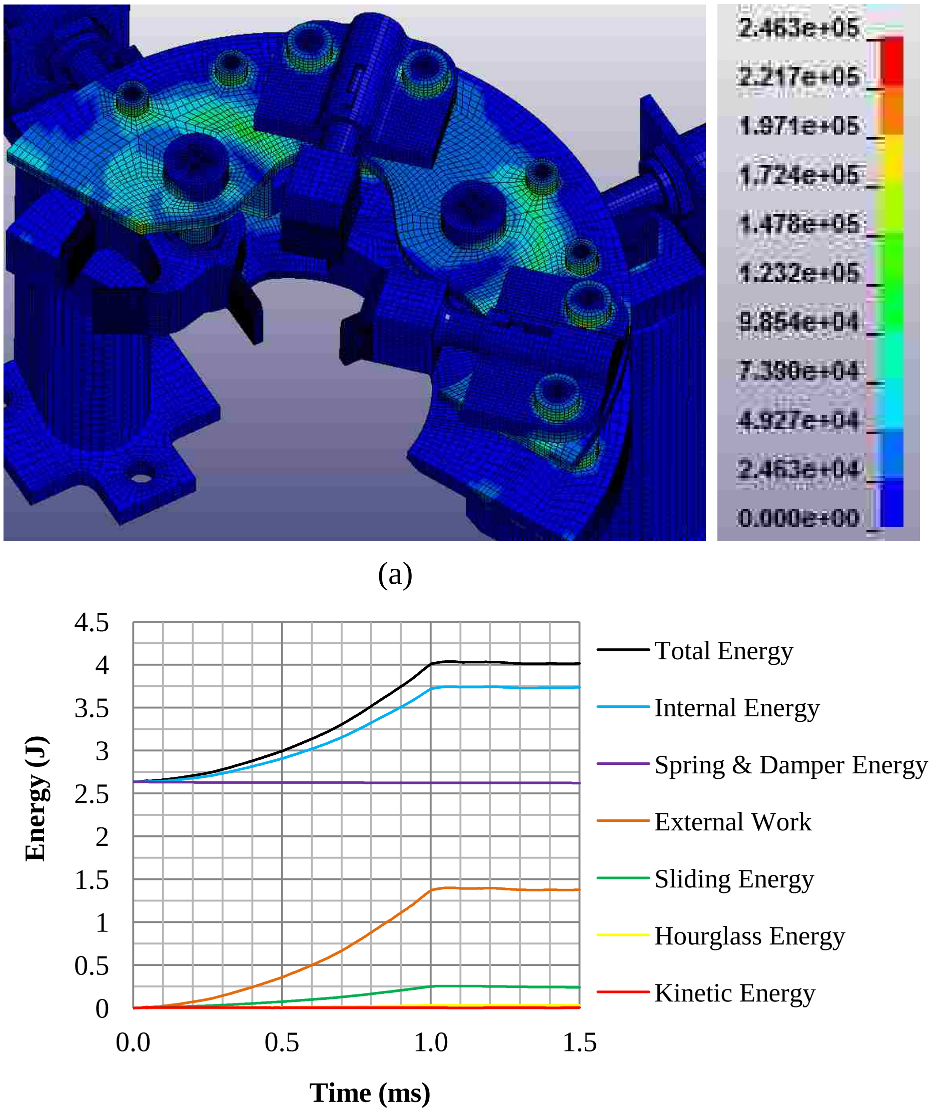

(a)

(b)

Figure 5.5 Pre-cutting model of quadrotor in 4-blade configuration (a) von Mises stresses (kPa). (b) System energies.

expected. One important check is to verify from the plot of system energies, shown in Figure 5.5(b), whether the total energy of the system is equal to the external work applied to the system at all times. Note that LS-DYNA does not compute the work done to initially preload a discrete spring element. Instead, the spring energy at time=0 should be considered as the work done to initially preload all the springs. Therefore, the model does indeed satisfy the physical law of energy conservation: the total energy is in balance with the sum of the external work and the spring energy at time=0. As indicated by the external work line, the axial forces for each bolt are applied gradually over 1 ms and held constant afterwards. The internal energy derives from elastic deformation of material under the bolt preloads. The spring energy derives from the two preloaded linear springs in the jaw housings as well as the two torsionally preloaded springs at each cutter. The spring energy is constant, as expected, since both cutters are locked and both jaws are held in place via the key/slot contact. Sliding energy derives from the axial movement between the bolts and plate holes during the clamping stage. Since the applied axial load is steady by 1 ms, the sliding energy also remains constant after 1 ms. Kinetic and hourglass energies are negligible.

Figures 5.6 through 5.11 are provided to show the effective stresses due to preloading of the bolts and the axial preloads at each bolted connection.

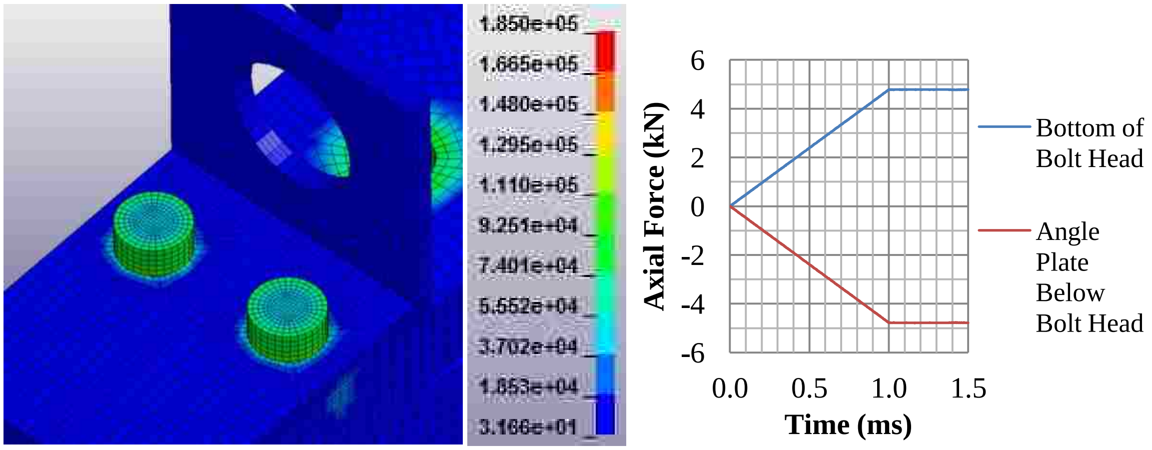

(a) (b)

Figure 5.6 M6 bolts through angle plate. (a) von Mises stresses (kPa). (b) Numerical axial preload at bolt head contact interface.

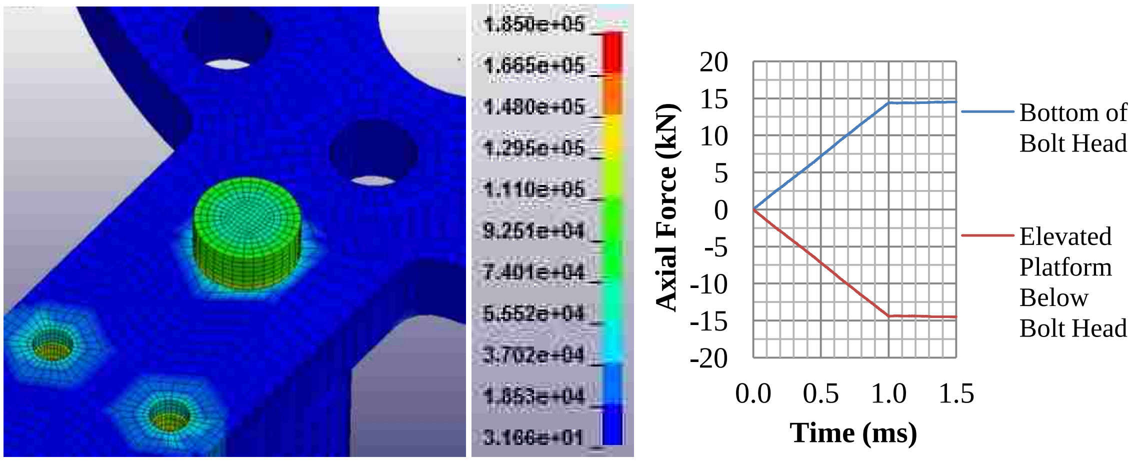

(a) (b)

Figure 5.7 M10 bolt through elevated platform. (a) von Mises stresses (kPa). (b) Numerical axial preload at bolt head contact interface.

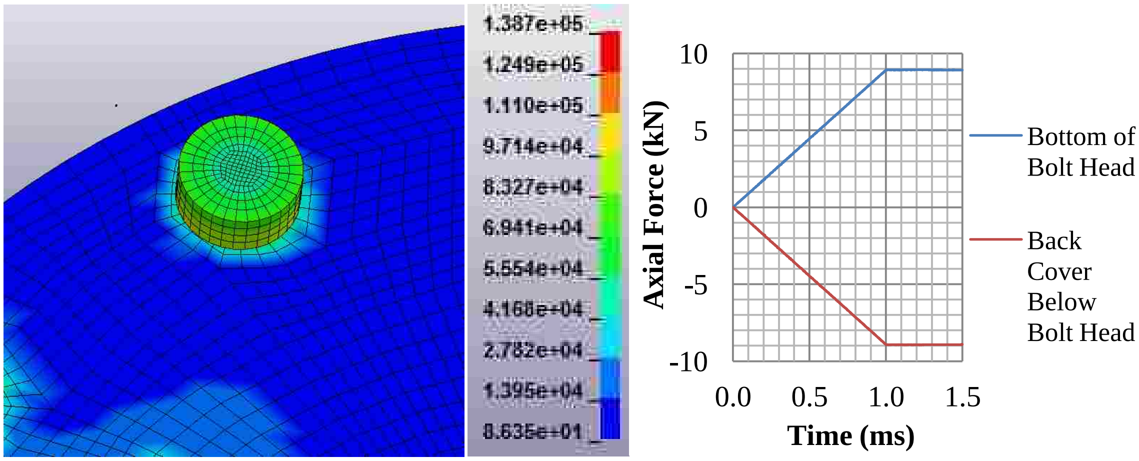

(a) (b)

Figure 5.8 M8 bolt through back cover. (a) von Mises stresses (kPa). (b) Numerical axial preload at bolt head contact interface.

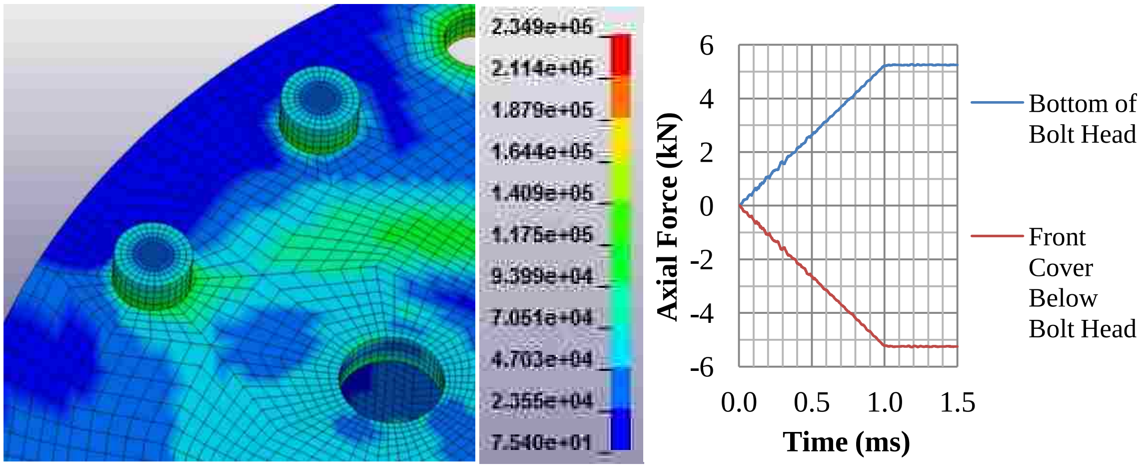

(a) (b)

Figure 5.9 ¼ in bolts through L-block. (a) von Mises stresses (kPa). (b) Numerical axial preload at bolt head contact interface.

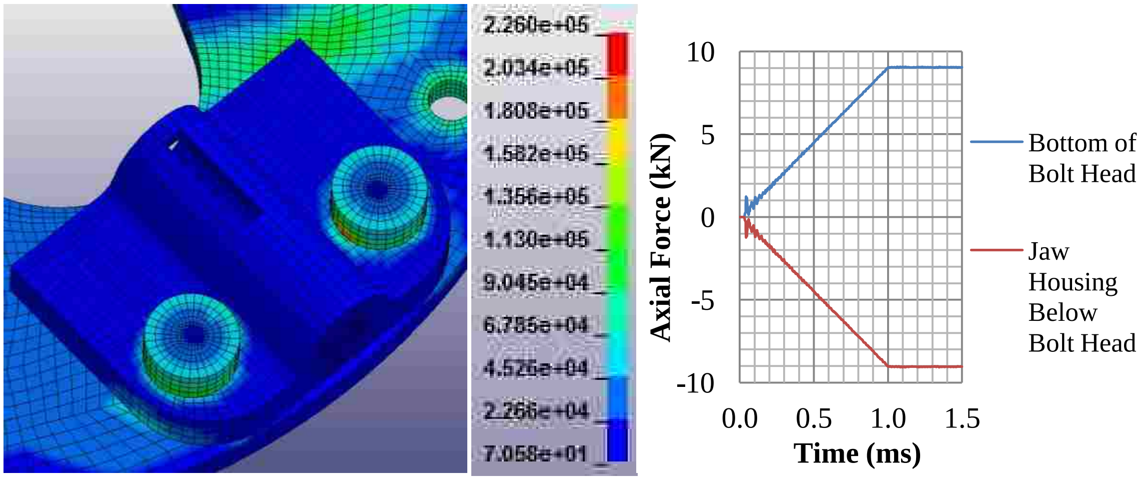

(a) (b)

Figure 5.10 M8 bolts through jaw housing. (a) von Mises stresses (kPa). (b) Numerical axial preload at bolt head contact interface.

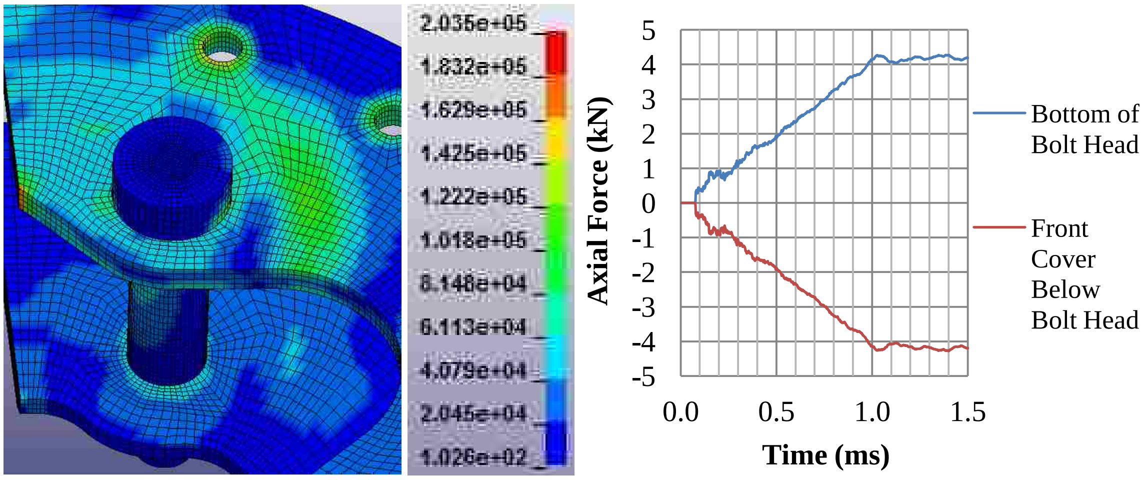

(a) (b)

Figure 5.11 ½ in bolts through cutter. (a) von Mises stresses (kPa). (b) Numerical axial preload at bolt head contact interface.

In all cases, the pre-stress distributions should not result in plastic deformation during clamping, meaning that none of the bolts have been over tightened. Additionally, the axial preload after 1 ms in each case (when the full load is applied) is near constant, which is desired so as not to influence the stresses during the later cutting stage. Strictly under bolt preloading, the critical stress zone in the whole device is 163 MPa, located in the front cover near the ¼ in hole indicated in yellow in Figure 5.11. This area is subjected to the compressive stress from the preload of the ¼ in bolt as well as bending stress due to preloading of the ½ in bolt. As seen in Figure 5.11, the clamping force of the ½ in bolt subjects the front cover to cantilever bending. Actually, if the ½ in bolt is clamped to the manufacturer’s recommended tensile preload, the stresses in the front cover would be in the 1000 MPa range, which would require the front cover be made of a tool steel. To reduce the stress from preloading, the clamping force in the ½ in bolt is intentionally prescribed lower than recommended by the manufacturer. As a result, the axial force at the bolt head/front cover contact interface in Figure 5.11(b) fluctuates slightly more than seen in all the other bolted connections. However, this oscillating load is minute since the stress defined by the green fringe in the front cover oscillates between 120 MPa and 130 MPa, which is an amplitude of only ±5 MPa. The range of oscillating stresses due to preloading the ½ in bolt are deemed acceptable, and increasing the preload to achieve a smoother plateau in axial load would overstress the front cover.

Additionally, note the purpose of the ½ in bolt is not to clamp the front and back covers together, but simply to provide an axis of rotation for the rotary cutter.

A comparison between the numerical axial preload and analytically calculated preload for each bolted connection is provided in Table 5.1. Apart from the ½ in bolt, the numerical preload is within the tolerable range of 10% error from the analytically calculated value. Numerically, the axial preload is expected not to equal exactly as prescribed in the load curve because the bolts and plates in the numerical model are separated by small gaps to prevent initial penetrations. Moreover, the axial preload of any bolt under consideration will be influenced by the clamping action of other bolts in the same vicinity because they also contribute to some amount of plate deflection. Finally, recall that the prescribed axial preload for the ½ in bolt was intentionally made lower than the analytically calculated value, which explains why the error in that case is substantial.

Table 5.1 Analytical and numerical parameters for each bolted connection of the quadrotor adaptive cutter.

Bolted connection	**Tightening torque, *T***	**Torque coeff., *K***	**Diam. of thread, *d***	**Analytic preload = *T*/(*K*·*d*)**	**Numerical preload**	**Error**
	(kN·mm)	**(-)**	**(mm)**	**(kN)**	**(kN)**	**(%)**
M6 bolts through angle plate	5.42	0.22	5	4.93	4.78	3.0
M10 bolts through elevated platform	28	0.22	8	15.91	14.5	8.9
M8 bolts through back cover	12	0.22	6	9.1	8.92	2.0
1/4 in bolts through L-block	5.65	0.22	4.83	5.32	5.25	1.3
M8 bolts through jaw housings	12	0.22	6	9.1	9.04	0.7
1/2 in bolts through cutter	53.1	0.21	9.53	26.5	4.2	84.2

5.3.2 Pre-Cutting in the 6-Blade Configuration

The effective stresses in the quadrotor during pre-cutting are mostly influenced by the bolt preloads. In the 6-blade configuration, other than the 3-bladed cutter during impact with the magnet, all other parts have practically the same effective stresses as in

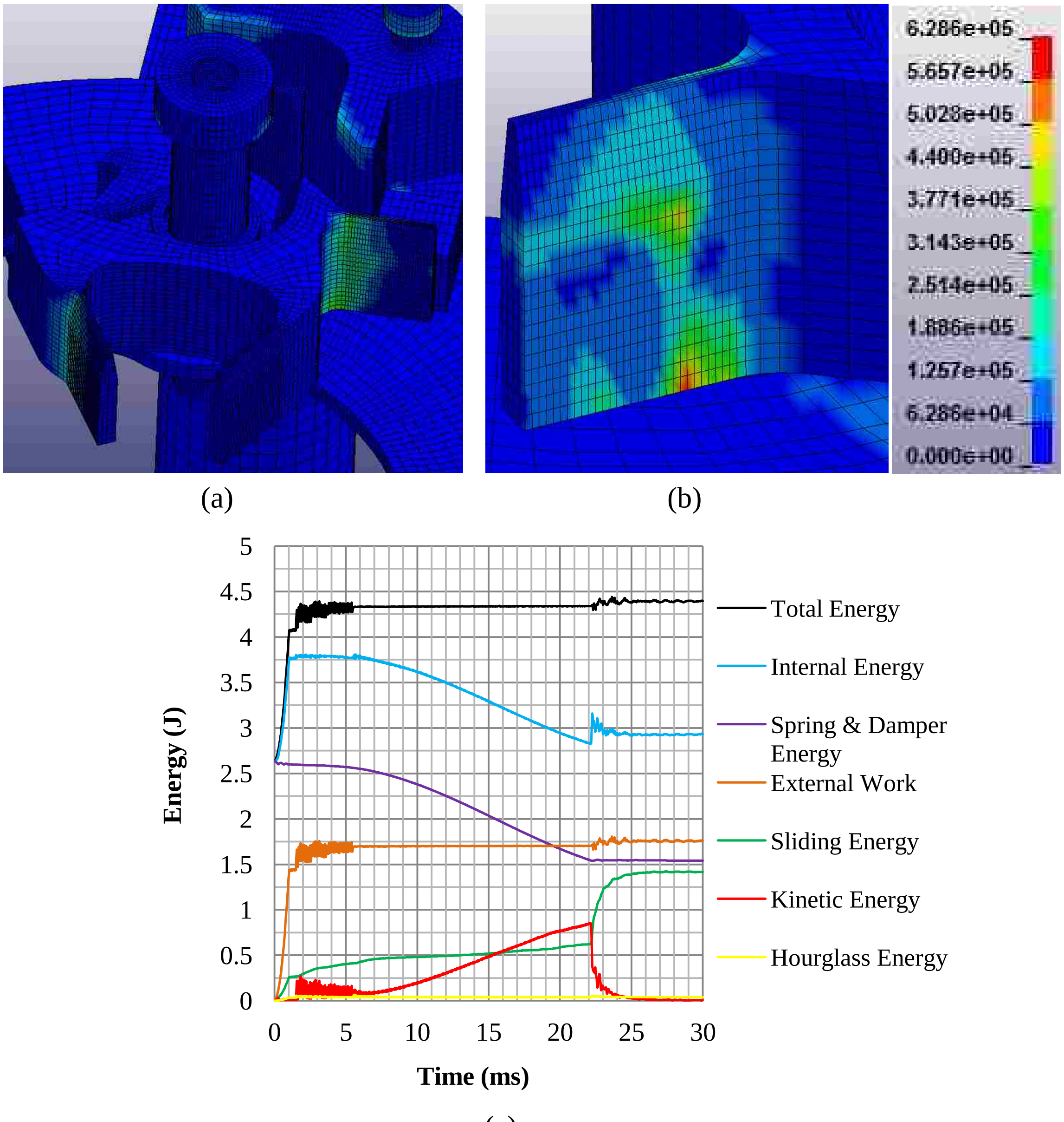

(a) (b)

(c)

Figure 5.12 Pre-cutting model of quadrotor in the 6-blade configuration. (a) 3-bladed cutter von Mises stresses (kPa). (b) Blade face contacting magnet von Mises stresses (kPa). (c) System energies.

the 4-blade configuration. The maximum effective stress in the 3-bladed cutter occurs at the initial impact with the magnet, and is shown in Figures 5.12(a) and (b). The critical area is the side of the impacting blade near the root, showing a peak stress of 314 MPa at 22.5 ms, which drops to 223 MPa and 156 MPa by the 23 ms and 23.5 ms marks, respectively. These stress magnitudes are not concerning since many tool steels have far higher yield strengths in tension (i.e. some over 2000 MPa). A few localized stress regions in Figure 5.12(b) in red and yellow of 625 MPa and 500 MPa, respectively, are overestimated because of sharp edge to sharp corner contact between the taper of the blade and the chamfer of the L-block. These edges would have radii, albeit small ones, which would reduce the contact stresses there. In addition, these zones are principally compressive, and tool steels have higher yield strengths in compression than in tension.

The system energies in Figure 5.12(c) are balanced as expected, indicating the model does not violate any physical laws. The relaxing of the torsion spring that drives the 3-bladed cutter is represented by the decreasing spring energy which only remains constant after the time of impact at 22.5 ms. The elastic deformation during bolt preloading is shown by the internal energy in the first 1 ms. After 1 ms, the elastic deformation of material is negligible as the internal energy response parallels the spring energy until the time of impact. The jump in internal energy at the time of impact of 22.5 ms indicates the brief high stress induced in the 3-bladed cutter. The kinetic energy drops at the moment of impact, and then vibrates slightly. Although the cutter sticks on impact, the free blades sway back and forth like a tuning fork for a brief 5 ms before the blades are fully settled at 28 ms. Note this slight swaying is also evident by the 188 MPa stress in light blue at the root of one of the free blades. As expected, positive, steadily increasing sliding energy is seen until 22.5 ms at which time a sudden jump in sliding energy occurs due to the product of large frictional resistance and minute vibration. After bolt preloading is stabilized by 1.5 ms, the transient phase in the next 4 ms in the kinetic energy and external work is explained by the dynamics of the rapid displacement of the solenoid shaft from rest. During this 4 ms period, a rapid back-and-forth contact between the pick on the solenoid shaft and the hole in the Teflon pin occurs: as one face of the pick initially pushes against one face of the hole in the Teflon pin, its inertia causes the opposing face of the pin hole to come into contact with the opposing face of the pick. The latter contact slows down the Teflon pin, and so the pick once again hits the side of the hole that was in contact initially. The cycle repeats a few times until the shaft has displaced its complete 6 mm.

As seen in Figure 5.13, the force at impact between the 3-bladed cutter and the magnet is sensitive to the material model of the magnet. In reality, the magnet material is also coated with a layer of hard plastic, which has been ignored in the model to avoid the further complexities in meshing, polymeric material definitions, and contact. In both Figures 5.13(a) and (b), the modulus of elasticity and density for steel (i.e. 200 GPa and 8000 kg/m^3, respectively) were defined for the magnet, however in (a), the magnet is rigid, and in (b), the magnet is elastic. The difference in peak load from 8 kN to 3 kN is significant to point out because that means one should expect the experimental impact loads, discussed in Chapter 7.0, to lie somewhere between these extremes. Since the magnet cannot in reality be rigid, the measured peak impact is likely not above 8 kN.

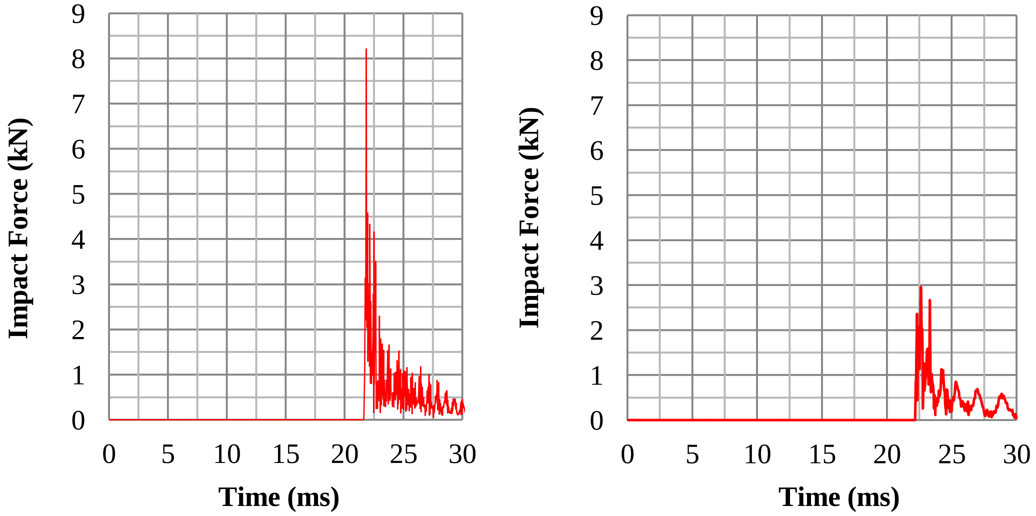

(a) (b)

Figure 5.13 Impact force between magnet and 3-bladed cutter of quadrotor (a) Result with a rigid magnet. (b) Result with an elastic magnet.

5.3.3 Pre-Cutting in the 8-Blade Configuration

Similar to the 6-blade configuration, in the 8-blade configuration, other than the 4-bladed cutter during impact with the magnet, all other parts have practically the same effective stresses as in the 4-blade configuration. The maximum effective stress in the

4-bladed cutter occurs at the initial impact with the magnet, and is shown in Figures 5.14(a) and (b). The critical area, namely the side of the impacting blade near the root, has a peak stress of 321 MPa. These stresses which occur at a time of 31 ms drop to negligible levels by 33 ms. Note the stress ranges for the 4-bladed cutter are again not of concern compared to the yield strength of tool steels available. A few localized stress

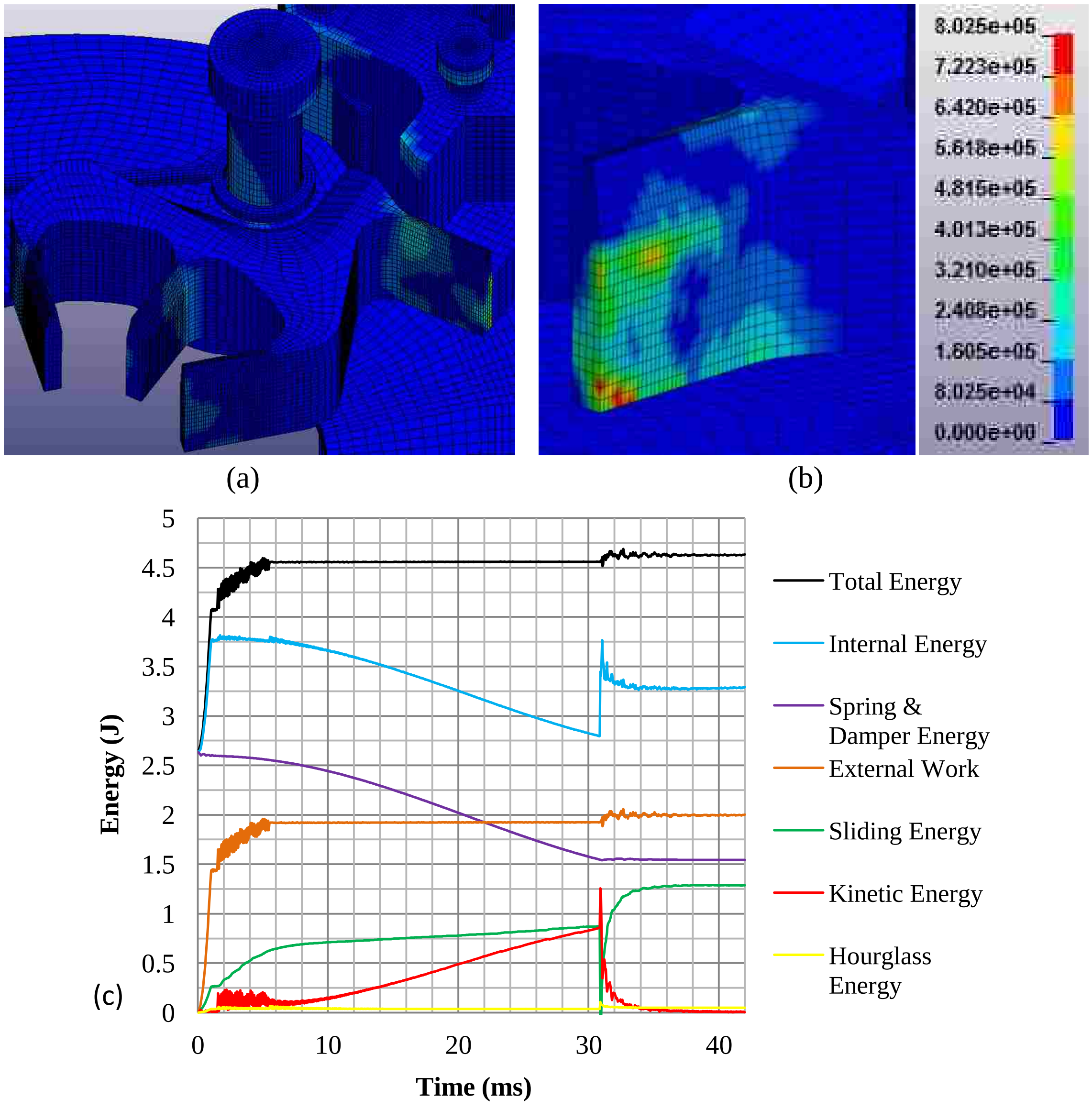

(a) (b)

(c)

Figure 5.14 Pre-cutting model of quadrotor in the 8-blade configuration. (a) 4-bladed cutter von Mises stresses (kPa). (b) Blade face contacting magnet von Mises stresses (kPa). (c) System energies.

regions in Figure 5.14(b) in red and yellow of 800 MPa and 640 MPa, are overestimated because of sharp edge to sharp corner contact between the tapered edge of the blade and the chamfer of the L-block, and the tip of the blade and the edges of the magnet. As stated before, all these edges would have some form of radii, which would reduce the contact stresses.

The system energies in Figure 5.14(c) are balanced as expected. Each energy form follows a similar trend as seen in Figure 5.12(c) for the 3-bladed cutter in the previous section, and so will not be explained to avoid repetition. The critical difference is the slower response time of 31 ms for the 4-bladed cutter, noted by the sudden drop in kinetic energy. A slower response time is anticipated since the mass and rotary inertia for the 4-bladed cutter are higher than the 3-bladed cutter by factors of 2 and 3, respectively. Additionally, not captured on the energy/time plot, is the brief 5 ms swaying of the free blades after impact, until they are fully settled by 36 ms. The 160 MPa fringe stresses at the roots of the free blades also indicate this minor vibration.

As seen in Figure 5.15, the peak force at impact from the 4-bladed cutter on the magnet ranges between 4 kN and 8.7 kN, depending on the material model selected for the magnet. Later, in Chapter 7.0, the experimentally measured peak impact force will be shown to fall in between this range.

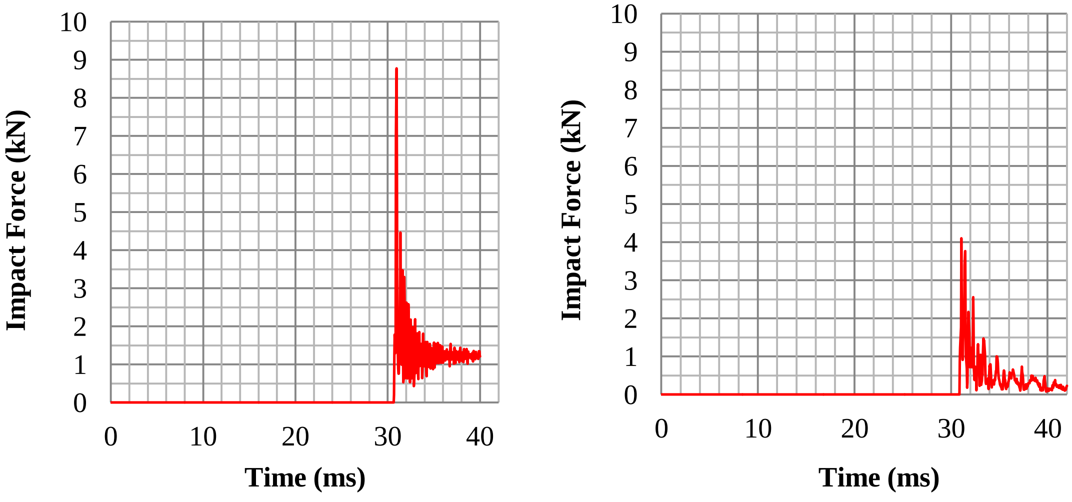

(a) (b)

Figure 5.15 Impact force between magnet and 4-bladed cutter of quadrotor (a) Result with a rigid magnet. (b) Result with an elastic magnet.

5.4 Axial Cutting Simulations of the Quadrotor Adaptive Cutter

For a large deformation process, such as axial cutting, the massive mesh distortion of Lagrangian type elements may lead to significant numerical error. An alternative element formulation more suitable for significant deformation is the Arbitrary Lagrangian Eulerian (ALE). Note that the material coordinates and mesh coordinates for the Lagrangian element formulation are one and the same. However, in the Eulerian element formulation, the material coordinates and mesh coordinates are dissociated, such that the material moves through the mesh. In the ALE element formulation, the Lagrangian and Eulerian element formulations are used together as follows:

1. At the first time step, the material and mesh deformation is evaluated using the Lagrangian element formulation.
2. Prior to the next time step, the mesh coordinates are remapped to their original positions in a process referred to as advection, while the material coordinates are not remapped. In other words, the mesh returns to an undistorted state while the material assumes its next deformed state.
3. Material is transported to the remapped mesh using the Eulerian element formulation.
4. At the next time step, deformation of the material and mesh is evaluated using the Lagrangian element formulation.
5. Steps 2 through 4 are repeated until the end time of the simulation is reached.

In order to remap the material coordinates in step 2, an airmesh must surround the original location of the extrusion material. Additionally, the airmesh must be large enough to accommodate the transported extrusion material as its petals flare outward. According to [11], material transport using the Eulerian element formulation is shown to predict the axial cutting process with the important energy dissipation mechanisms very well. Also, no crack propagation was observed in SEM micrographs of the cut petalled sidewalls of AA6061-T6 extrusions, indicating acceptable use of the Eulerian element formulation [11] and no need to include a damage model.

For each configuration, only the AA6061-T6 aluminum extrusion with the smallest diameter (44.45 mm) and thickest wall (3.175 mm) is considered because this specimen size results in the largest cutting force with the longest cantilever arm on the blades, resulting in the highest stresses in the device. The blade deployment stage has been omitted from the cutting simulations for the 6-blade and the 8-blade arrangement to save tremendously on CPU cost. The justification for skipping this step in the cutting simulations is that the resulting stresses on the 3-bladed cutter and 4-bladed cutter as they impact their corresponding magnets are significantly lower than the stresses during cutting. Therefore, the pre-cutting stage will not affect the durability of the device.

Simulations of the dynamic cutting tests were completed using LS-DYNA v971 on a personal computer having the following specifications: the processor was an Intel Xeon E5-2687W operating at 3.1 GHz with 32 virtual cores and having 64 GB of random access memory. The end time in all three cases was 8 ms, and with no mass scaling invoked, the total run times were 79 hours, 149 hours, and 120 hours for the 4-blade configuration, 6-blade configuration, and 8-blade configuration, respectively.

The models for the 3 cutting configurations are shown in Figure 5.16(a) to (c). The model of the quadrotor itself is identical to that outlined in section 5.3 and shown in Figure 5.4. The new, additional components in Figure 5.16 are the models of the airmesh (purple) and extrusion (olive green). The airmesh and extrusion are made of solid, hexahedral elements, with single point integration. Depicted in all the right side images, the extrusion comprises a single row of elements, whose bottom nodes are merged with the nodes on the top face of the airmesh. The extrusion in the vicinity of the cutting blades has 12 elements through the thickness, having aspect ratios between 1 and 3, to accurately capture the cutting deformation in those regions. The smallest element dimension in the extrusion or airmesh is 0.20 mm. Further away from the cutting zone on either side of each cutting blade, transition elements are used to reduce the number of elements through the thickness to 4. The radial and axial dimensions of the airmesh were chosen such that the deformed extrusion would be completely contained within the walls of the airmesh. In *SECTION_SOLID, both the extrusion and airmesh are assigned ELFORM = 12, which is single point integration with material and void. *INITIAL_

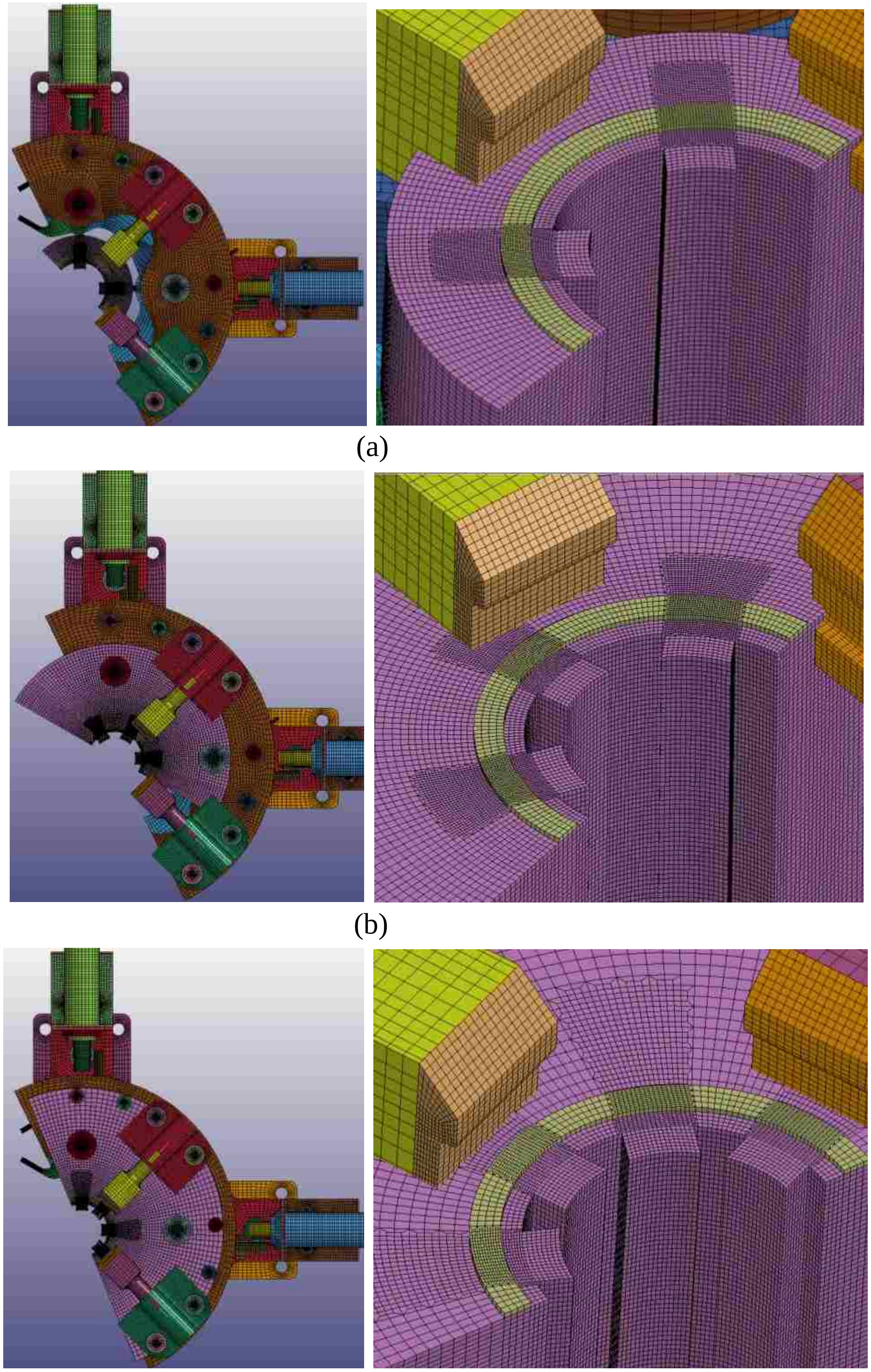

(a)

(b)

(c)

Figure 5.16 Cutting models of quadrotor for the 3 configurations. Top views (left) and up close views of airmesh (right). (a) 4 blades. (b) 6 blades. (c) 8 blades.

VOID_PART for the airmesh defines it as empty space through which the extrusion material is transported. A pressure inflow is assigned to the extrusion at the nodal interface with the airmesh by setting AET=4 in *SECTION_SOLID for the extrusion. The incoming velocity of the extrusion material is specified in *BOUNDARY_ PRESCRIBED_MOTION using the node set at the extrusion/airmesh interface and a load curve of 7 m/s for all time. An end time of 8 ms was chosen as the steady state cutting force was reached by this time.

The extrusion and airmesh use a *MAT_ELASTIC_PLASTIC_HYDRO material model with the mechanical properties of AA6061-T6 aluminum (i.e. density of 2700 kg/m^3, shear modulus of 32.88 GPa, yield stress of 271.6 MPa). A piecewise linear curve for the yield stress versus the effective plastic strain is defined with 16 discrete points determined experimentally; the same values specified in [11] were used. This material model computes the shear strains, but not the normal strains. To account for the normal strains, a pressure versus volume relationship is applied to the extrusion and airmesh using an *EOS_LINEAR_POLYNOMIAL equation of state. The inputs specified in this keyword are C1 = 75.63 GPa, E0 = 0, and V0 = 1, which are the same values defined in [11].

Note from Figure 5.16 that in all configurations, the boundaries of the extrusion and airmesh do not line up with the boundaries of the adaptive cutting device for an important reason: the boundaries of rotational symmetry in the adaptive cutter cannot be applied to the extrusion and airmesh because *BOUNDARY_CYCLIC only accounts for rotational symmetry in nodal positions, velocities, and accelerations, ignoring rotational symmetry in mass and energy transport. Given that prior to each succeeding time step, the extrusion material is transported using the Eulerian element formulation, symmetry in mass and energy transport must be considered. Therefore, instead of rotational symmetry, reflective symmetry is applied to the extrusion and airmesh. So for the 4-blade configuration, referring to the left image of Figure 5.16(a), one plane of reflective symmetry lies at 45 degrees clockwise with respect to the right cutting blade, and the second plane of reflective symmetry lies at 45 degrees counterclockwise with respect to the top cutting blade. Reflective symmetry is applied by creating two local coordinate systems, one located on each plane of the airmesh, using *DEFINE_COORDINATE_

NODES, and constraining motion of the nodes in these two planes in all directions except parallel to their respective planes using *BOUNDARY_SPC_SET. The same technique is applied for the 6-blade and 8-blade configurations in Figures 5.16(b) and (c), respectively.

Contact between the extrusion material and cutter blades (including the other parts in the quadrotor device) is modeled using *CONSTRAINED_LAGRANGE_IN_SOLID. A master part set is defined for the extrusion and airmesh, and a slave part set is defined for the 3-bladed cutter, 4-bladed cutter, jaw teeth, back cover, and elevated platform. The remaining inputs on each card of this keyword are set as NQUAD = -3, CTYPE = 4, DIREC = 2, MCOUP = 0, PFAC = 0.2, FRIC = 0.1, and INTFORC = 1, with all other inputs left as default values, which is identical to the specifications in [11]. *DATABASE_FSI applied to the slave part set outputs the contact forces from the extrusion material acting on the cutters and the other components in the slave part set.

Finally, the contact between the jaw teeth and the extrusion is intentionally avoided, as noted by the gap between these two entities in all the right side images of Figure 5.16. With only half of the extrusion modeled, if the force of each jaw is applied on the sides of the extrusion, it will tilt from the axial direction because no jaw exists on the opposing side to balance the holding force. To prevent tilting of the extrusion, contact is avoided as the key on each jaw shaft presses against the slot in the jaw housing, preventing the jaw from protruding any further inward radially. The stresses in the jaw assembly during contact with the extrusion sides have been investigated in Appendix H and were found to be negligible. The jaw assembly is only included in the cutting model to see how the force on the blades during cutting will transfer through the rest of the quadrotor device.

The extrusion deformations for the 3 cutting configurations are depicted in Figures 5.17(a) to (c). As expected, the petals of the extrusion in (a) flare only slightly and symmetrically at either boundary of the airmesh. No contact is made between the extrusion and any other parts in the device than the blades. In (b), the petals also deform symmetrically but flare to a higher degree than the 4-blade configuration. Although the petals curl towards the back cover, the outer wall of the extrusion has approximately

4 mm of clearance below the rim defining the back cover's central hole. Slight circumferential stretching of the extrusion during cutting causes rubbing contact between the jaw teeth and the extrusion outer wall. However, apart from the jaw teeth and the cutter blades, no other contact is made with the extrusion, which has a positive effect on the cutting force/time response. With 8 blades, in (c), the extrusion deformation is again symmetric, but flares even more than for the 6-blade configuration. The flaring is

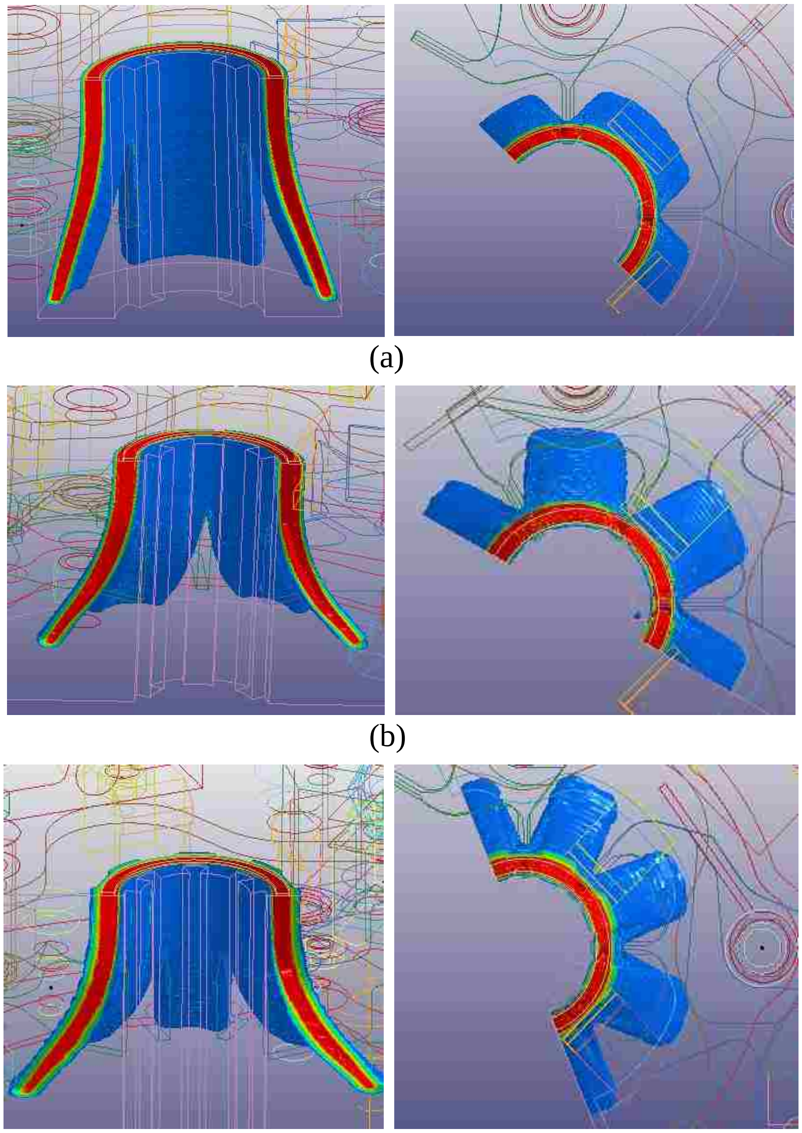

(a)

(b)

(c)

Figure 5.17 Deformation of extrusion during cutting for the 3 configurations of quadrotor. Front views (left) and top views (right). (a) 4 blades. (b) 6 blades. (c) 8 blades.

significant enough that the petals eventually make contact with the rim of the central hole in the back cover. This rubbing influences the cutting force/time response, but not detrimentally. If the petals flared to the extent of contacting the top face of the back cover, the petals would likely break off under continued axial loading and negatively influence the force/time response.

The forces from the extrusion acting on the blades for the 3 configurations are shown in Figure 5.18(a) to (c). One must first acknowledge that the initial goal of designing an adaptive cutting device that is capable of adjusting the force level is demonstrated here (at least virtually). On the left side graph in (a), most of the cutting force is in the axial direction (*z-axis*), achieving a near constant level of 21 kN by 7 ms. The near constant cutting force of 21 kN for two blades, or 42 kN for 4 blades, is consistent with experimental measurements in [11] and the prediction from the analytical model in Eq. 2.1 for the same extrusion thickness and diameter. The *x* and *y* forces, which are practically zero, derive from the outward radial rubbing contact between the extrusion and blade side faces. To compare with the fluid-structure interaction output file, the axial forces measured at the load cell/elevated platform contact interface are shown on the right side graphs in Figure 5.18. Note from (a) that the axial force reading of 29 kN by 7 ms must be subtracted by 15 kN which is the axial preload of the bolt passing through the load cell. Therefore, the axial force measurement is approximately 14 kN. Since each load cell is positioned far outward radially from the cutter blades, the axial force reading for all configurations is expected to be lower than if the load cells were located directly below the blades. However, given the geometry of the device, measuring the load at a closer radial position is not possible because the extrusion petals in the 6-blade and 8-blade cutting configuration would interfere damagingly with the support legs. On the left graph in (b), again most of the cutting force is in the axial direction (*z-axis*), which rises rapidly from 0 to 27.5 kN between 3 and 4 ms. However, the load gradually increases to 34 kN by the end time of 8 ms. The constant rubbing contact between the circumferentially stretching extrusion outer wall and the jaw teeth appears to ramp the cutting force. Although the force response is smooth between 4 and 8 ms, it is not as steady as seen for the 4-blade configuration, in which the extrusion made no contact with the device at any other location but the cutting zone. The *x* and *y* forces, which are not

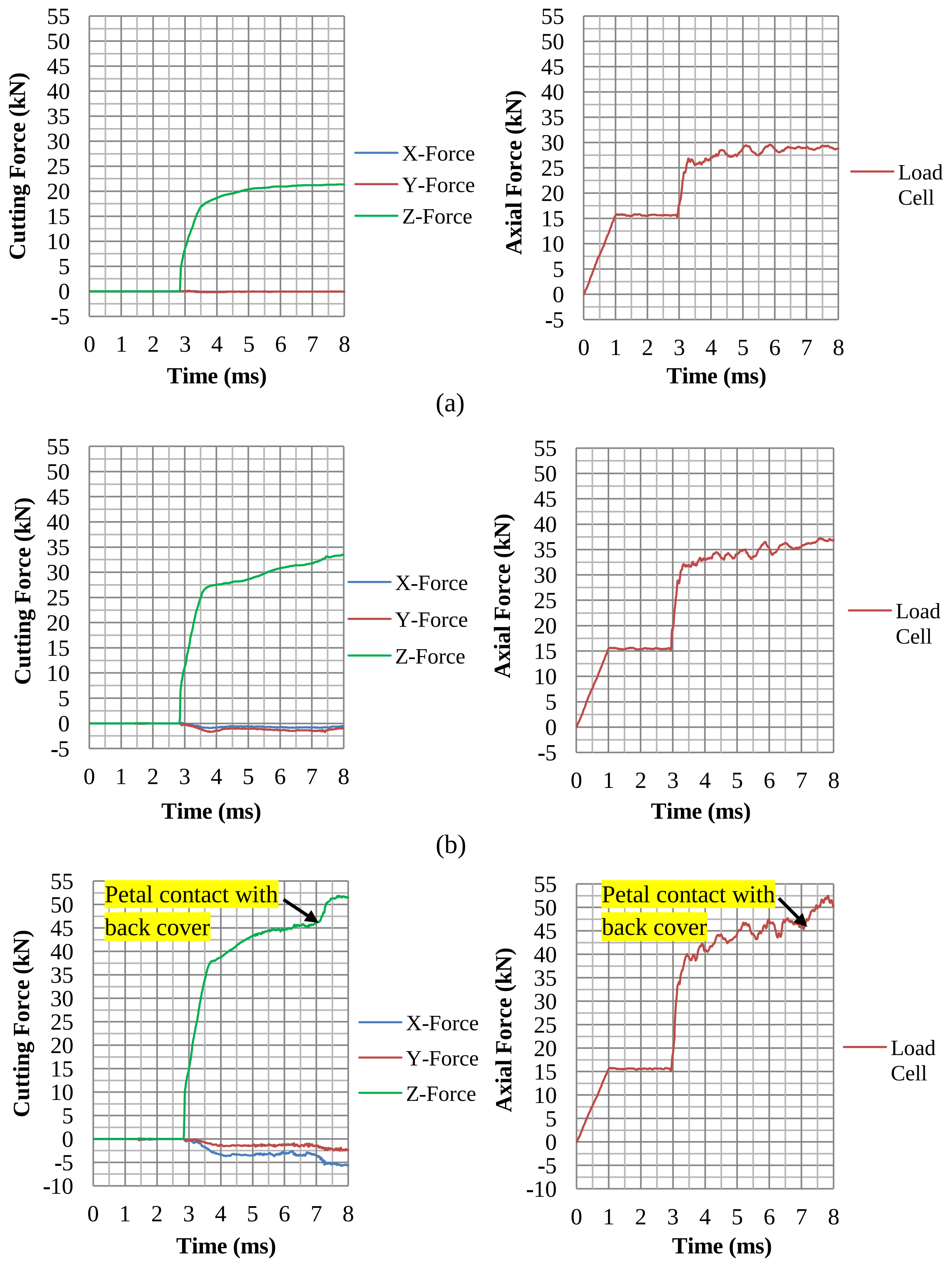

(a)

(b)

(c)

Figure 5.18 Cutting force/time response for the 3 configurations of quadrotor at blades (left) and at load cell (right). (a) 4 blades. (b) 6 blades. (c) 8 blades.

practically zero in the 6-blade configuration, derive from the outward radial rubbing contact between the extrusion and blade side faces as well as contact between the extrusion outer wall and the jaw teeth. From (c) most of the cutting force is in the axial direction (*z-axis*), which reaches a steady value of 45 kN between 5 and 7 ms, but steps up to a steady 51 kN between 7 and 8 ms as a result of contact between the extrusion outer wall and the back cover. The *x* and *y* forces, which are more substantial compared to the other configurations, derive from the outward radial rubbing contact between the extrusion and blade side faces as well as contact between the extrusion outer wall and the back cover. These non axial force components also increase stepwise at 7 ms, the same time the petal/back cover contact initiates.

Given the extreme degree of petal flaring for 8 blades, avoiding any contact between the extrusion and the cutter device is deemed impossible without further reducing the thickness of the blades and back cover, which would result in stresses too high to be managed by any currently available tool steels. Alternatively, including some form of tube that can constrain the extrusion from flaring too greatly may be worth investigating in the future. The idea was considered in Chapter 4 in Figure 4.10, but instead the design approach using an elevated platform was pursued because a more desirable force/displacement response was believed could be achieved this way. An apparatus developed by the German Aerospace Center (DLR) used to perform experimental cutting tests showed no flaring of the extrusion when cutting with either 4, 5, or 6 blades, yet the force/displacement responses were steady in all cases. If the same result could be achieved using a petal “container” in the quadrotor device, then its parts could be made thicker, requiring less durable (and less expensive) steels, and the concerning chance that petals flare over rather than under the back cover would be eliminated. Also, the load cells could be placed directly under the back cover and closer to the 3-bladed cutters and 4-bladed cutters to obtain more accurate measurements.

The effective stresses in the quadrotor for the worst loading condition, namely cutting in the 8-blade configuration, are illustrated in Figure 5.19. Globally, highest stresses are in the two cutters and the back cover which is under severe contact stress especially near the rim of the central hole. In (a), the heavy pressing contact between the 4-bladed cutter into the sharp edge of the central hole rimming the back cover results in a

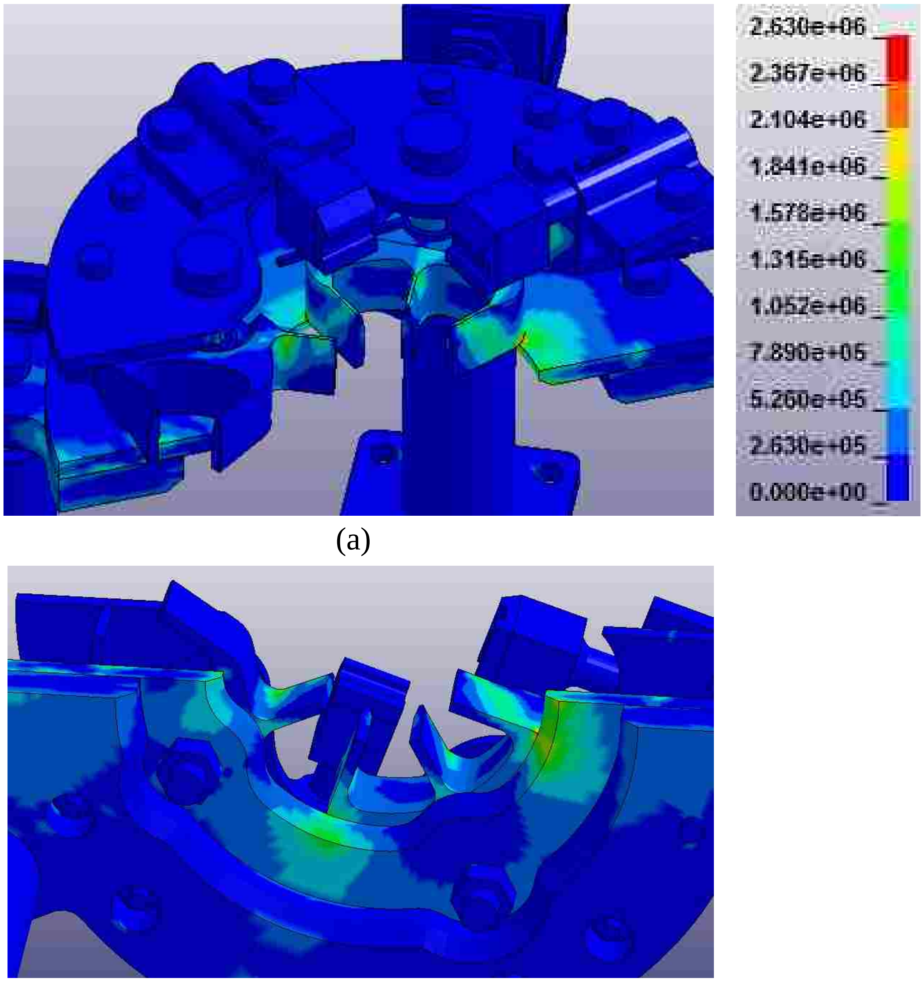

(a)

(b)

Figure 5.19 von Mises stresses (kPa) in quadrotor during cutting in 8-blade configuration. (a) View from above. (b) View from below.

localized stress, indicated by the red fringe. In reality, this edge will have a small radius, which reduces the stress concentration. Additionally, the results from nCode DesignLife 12.1 in Chapter 6.0 will reveal that this contact zone is the area that will most likely fail first in the back cover. However, the critical zone in the 4-bladed cutter is actually in the blade taper region, where tensile stresses are more prevalent.

From Figure 5.20(a), the critical region in the 3-bladed cutter is at the root of the taper being approximately 1763 MPa. The secondary critical region in the 3-bladed cutter is near the bolt hole on the side that presses into the shaft. Under the cutting load, both cutters are pulled radially inward, subjecting the bolt shafts to a large shear component. The corresponding ½ in bolt in (b) has a peak stress of 360 MPa at the contact region.

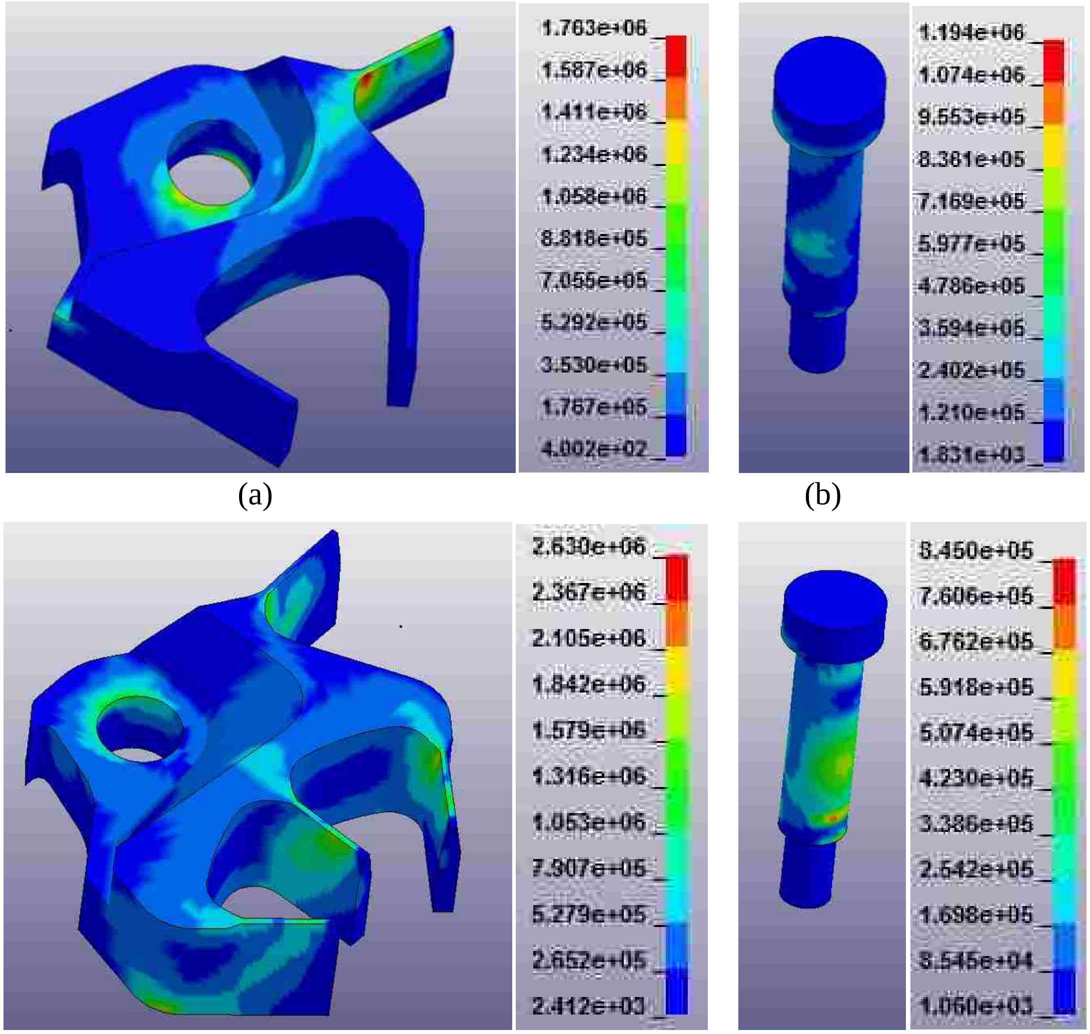

(a) (b)

(c) (d)

Figure 5.20 von Mises stresses (kPa) in cutters and ½ in bolts of quadrotor during 8 blade cutting (a) 3-bladed cutter. (b) ½ in bolt through 3-bladed cutter. (c) 4-bladed cutter. (d) ½ in bolt through 4-bladed cutter.

From Figures 5.20(c) and (d), however, the peak stresses in the 4-bladed cutter and corresponding ½ in bolt being 1842 MPa and 597 MPa, respectively, are more severe than for the 3-bladed cutter. This result makes sense because 3/4 of the cutting force depicted in 5.18(c) is supported by the 4-bladed cutter. Nonetheless, the stresses are effectively distributed throughout the 4-bladed cutter, as they are for the 3-bladed cutter, rather than heavily focused at the blade roots and near the hole. The 597 MPa stress on the bolt may seem high compared to the rated yield strength of 800 MPa, but the results from nCode DesignLife in Chapter 6.0 will reveal that these ½ in bolts will endure an infinite fatigue life. Another region of interest in (c) is the blade contacting the magnet. Although not as high as the three loaded blades on the 4-bladed cutter, the stress on the blade touching the magnet is higher than expected. That blade is loaded on its side face near the root because the cutting force has an outward radial component as the extrusion petals flare outward.

Table 5.2 Critical von Mises stresses in each component of quadrotor adaptive cutter.

		4 Blades	**6 Blades**	**8 Blades**	
		(Cutting)	**(Cutting)**	**(Cutting)**	
No.	**Component**	**Max Stress (MPa)**	**Max Stress (MPa)**	**Max Stress (MPa)**	**Critical Stress (MPa)**
1	Support Leg	289	496	643	643
2	Elevated Platform	259	461	700	700
3	Angle Plate	105	145	221	221
4	Neoprene Pad	156 kPa	284 kPa	376 kPa	376 kPa
5	Solenoid Casing	49	78	105	105
6	Solenoid Shaft	82	34	37	82
7	Mounting Hex Nut	74	159	142	159
8	Solenoid Adaptor	46	59	232	232
9	Teflon Pin	8	8	9	9
10	Back Cover	435	761	1800	1800
11	Front Cover	187	210	274	274
12	3-Bladed Cutter	1150	1634	1763	1763
13	4-Bladed Cutter	1270	1144	1842	1842
14	Long L-Block	274	1000	572	1000
15	Short L-Block	293	506	505	506
16	Jaw	49	68	105	105
17	Jaw Housing	112	112	135	135
18	M8x10 Sh Bolt	121	206	381	381
19	M6 Hex Nut	229	236	263	263
20	1/4 in Sh Bolt	207	226	348	348
21	#10 Hex Nut	271	280	280	280
22	1/2 in Sh Bolt	251	615	597	615
23	3/8 in Hex nut	163	236	286	286
24	M10x35 Sh Bolt	340	454	664	664
25	M6x6 Sh Bolt	146	162	231	231

Green cells indicate less than 50 % of yield strength of highest grade tool steels
Yellow cells indicate 75% to 85% of yield strength of highest grade tool steels

The effective stress contours in the remaining components of the quadrotor adaptive cutter have not been presented for brevity and because the stresses are not outstanding. Instead, the peak effective stresses in all the parts are summarized for the three cutting configurations in Table 5.2. As expected, the 8-bade cutting configuration is generally the worst case for all of the parts. Only the long L-block has significantly higher stress in the 6-blade cutting configuration. This result makes sense since the long L-block is closest to the 3-bladed cutter, and two of its blades rather than just one are loaded in the 6-blade cutting configuration. For the 8-blade cutting configuration, the stresses of most concern are in the 3-bladed cutter, 4-bladed cutter, and back cover. However, high grade tool steels exist that have yield strengths in the low 2000 MPa range. As for the other components, the stresses are much lower and should be handled by appropriately selected steel grades. The next chapter will show the results of a durability analysis for each of these components. The results will indicate infinite life in many parts, or at least tens of thousands of life cycles to failure in the high stress components since these peak stresses are localized and of short duration. Finally, although the neoprene pad and Teflon pin could not be evaluated for durability, their peak stresses are approximately 10 % and 50 % of their yield strengths, respectively, and so should not be near plastic failure.

6.0 DURABILITY ANALYSIS OF THE QUADROTOR ADAPTIVE CUTTER

The stresses in each component of the quadrotor, shown in Table 5.2, suggest that the device could withstand the worst loading case. However, the quadrotor adaptive cutter will be subjected to multiple impact tests throughout its lifetime in a research environment. Therefore, the grade of steel selected for each part in the device should be based on a durability analysis.

Parts subjected to fatigue can fail over time by the initiation of a microscopic crack in the material, which further opens after each cycle until catastrophic dynamic crack propagation. The life cycle of a part subjected to fatigue loading can be based on the stress amplitude or on the strain amplitude at the crack tip. The stress-life approach considers the crack tip to open under purely elastic stress, and can reliably predict the number of cycles to failure if they are over 10,000 [49] (i.e. high cycle fatigue or HCF) and the stresses are not highly concentrated at a notch [50]. A typical stress-life curve for 1045 steel is shown in Figure 6.1(a) [51], where the range between 10,000 and 10^6 is based on the Basquin elastic equation, which is linear on a logarithmic scale and is based purely on elastic stress at the crack tip. The constant line beyond 10^6 cycles, known as the endurance limit, indicates that for repeated crack tip stress of 45 ksi or less, 1045 steel would never fail. In some cases though, if the repeated stress is close to the material's

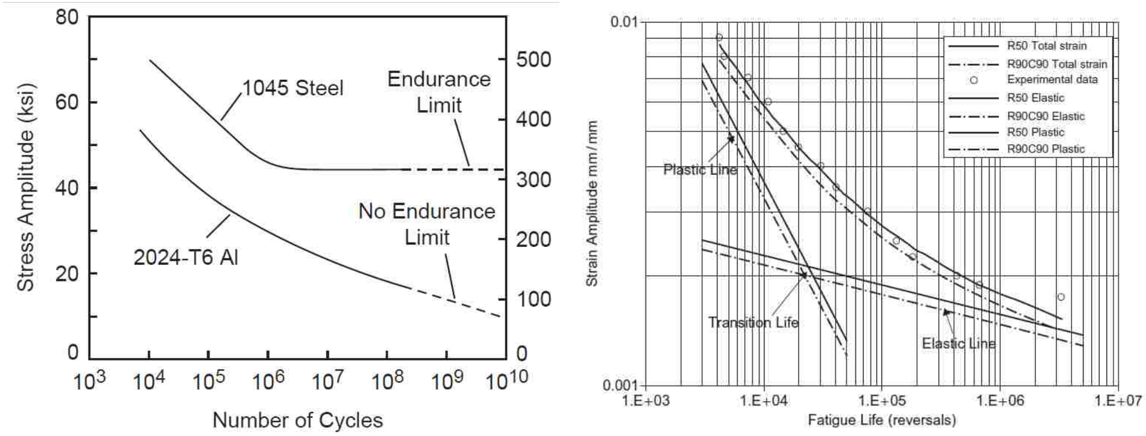

(a) (b)

Figure 6.1 Sample curves showing fatigue life of steels based on (a) Amplitude Stress vs. Cycles to Failure [51]. (b) Amplitude Strain vs. Cycles to Failure [52].

yield strength, suggesting life cycles below 10,000 (i.e. low cycle fatigue or LCF), or the repeated stresses are highly localized at a notch, the number of cycles to failure predicted in the stress-life approach is unreliable. In these cases, the failure at the crack tip is controlled by the strain amplitude rather than the stress amplitude. The strain-life approach considers not only elastic strain, but the localized plastic strain at the crack tip which controls the crack growth in the early stages. An example of a strain-life curve is shown in Figure 6.1(b) [52], defined by the Coffin-Manson equation for the plastic line, and the Basquin equation for the elastic line. The mathematics of the stress-life approach, having only the elastic component, is much easier than the strain-life approach. The mathematics of the strain-life approach, having plastic and elastic stresses to be dealt with separately, is more complicated because the calculation procedure is iterative, and therefore a numerical solver is required. Given that the quadrotor adaptive cutter has concentrated stresses in some of the components, namely the two cutters and the back cover, the strain-life approach will need to be used for these parts at least. Also, the high critical stresses will likely be close to the yield strength of the selected steel, warranting use of a strain-life solver.

6.1 Selected Materials and Fatigue Life of Quadrotor Adaptive Cutter

The durability of each part in the quadrotor adaptive cutter was performed using the commercial software nCode DesignLife 12.1 by HBM. The user friendly software tool reads the binary output file from the FE model and predicts the cycles to failure for each element in the part based on the selected material, selected fatigue solver, and selected loading condition.

For most of the parts, the worst loading condition based on Table 5.2 was the cutting simulation using 8 blades. Two exceptions are the long L-block and the short L-block, which had higher stresses in the 6-blade cutting condition. Each part was investigated individually in nCode by applying these steps:

1. A material is selected (i.e. a steel grade) and assigned to the part.
2. The fatigue solver is chosen. For the 3-bladed cutter, 4-bladed cutter, back cover, and long-L-block, the strain-life solver is selected with a Morrow

correction factor, which is found to give reliable results for steels in the LCF regime [53]. For all other parts, the stress-life solver is chosen because the critical stresses are not localized and are far below the yield strength of the selected material, resulting in a life of 100,000 cycles or more.

3. A “time step” load type (transient analysis) is selected so that the solver considers the stress at each element of the part at every time step of the FE simulation.
4. nCode is run and the life contours are reviewed. If the number of cycles to failure is too low (< 10,000 cycles), a steel with a higher yield and ultimate strength is selected and nCode is run again. For the larger parts in the device, if the number of cycles to failure is exceedingly high (10^6 or more), then a lower grade, more economical steel is selected and nCode is run again.

The life contours of the main components in the quadrotor adaptive cutter are presented in Figures 6.2 through 6.10.

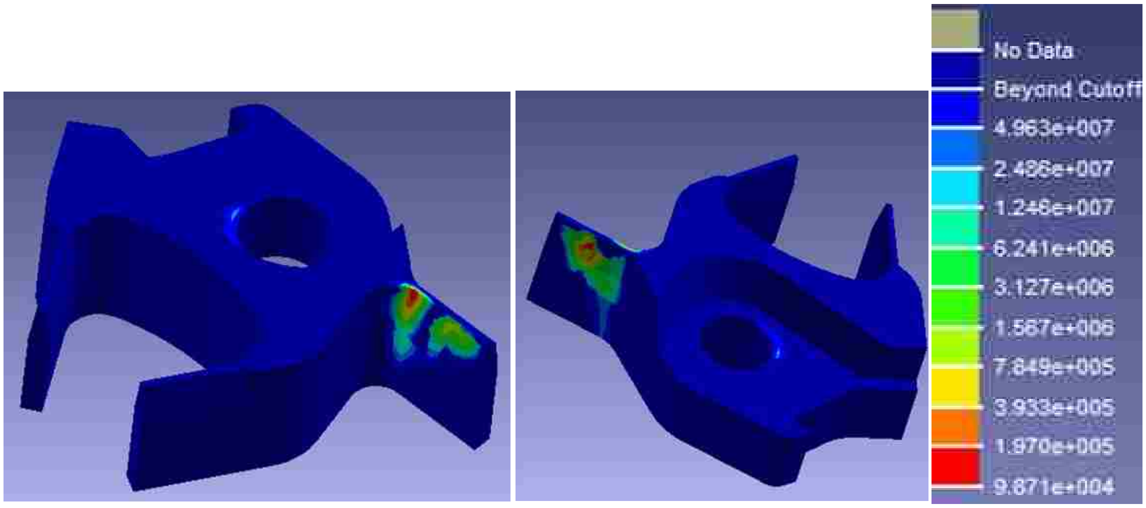

Figure 6.2 Life contours (cycles to failure) in 3-bladed cutter for 8-blade cutting condition based on Strain-Life solver from nCode DesignLife 12.1.

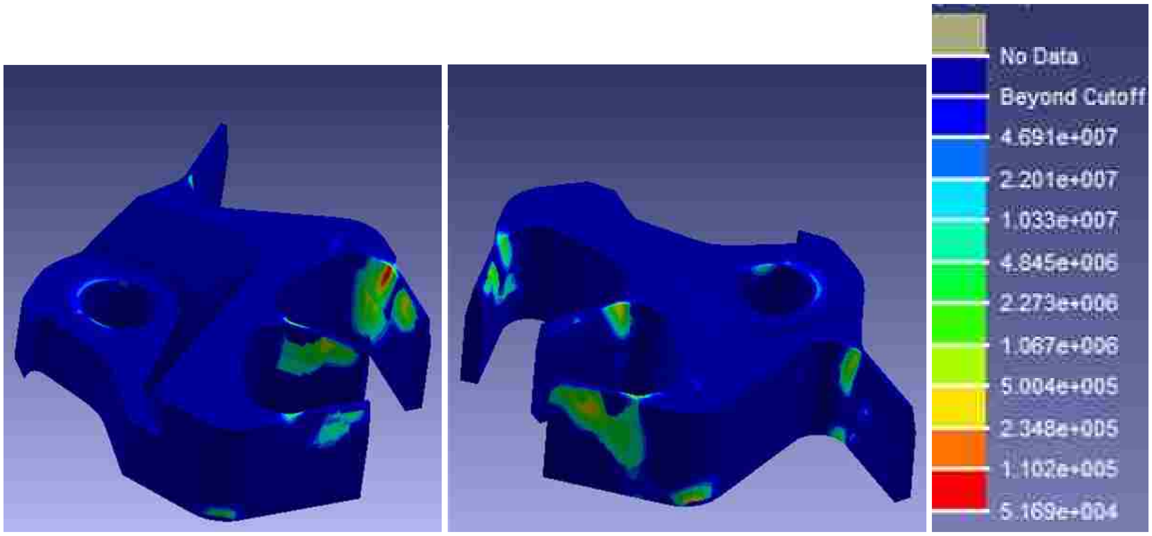

Figure 6.3 Life contours (cycles to failure) in 4-bladed cutter for 8-blade cutting condition based on Strain-Life solver from nCode DesignLife 12.1.

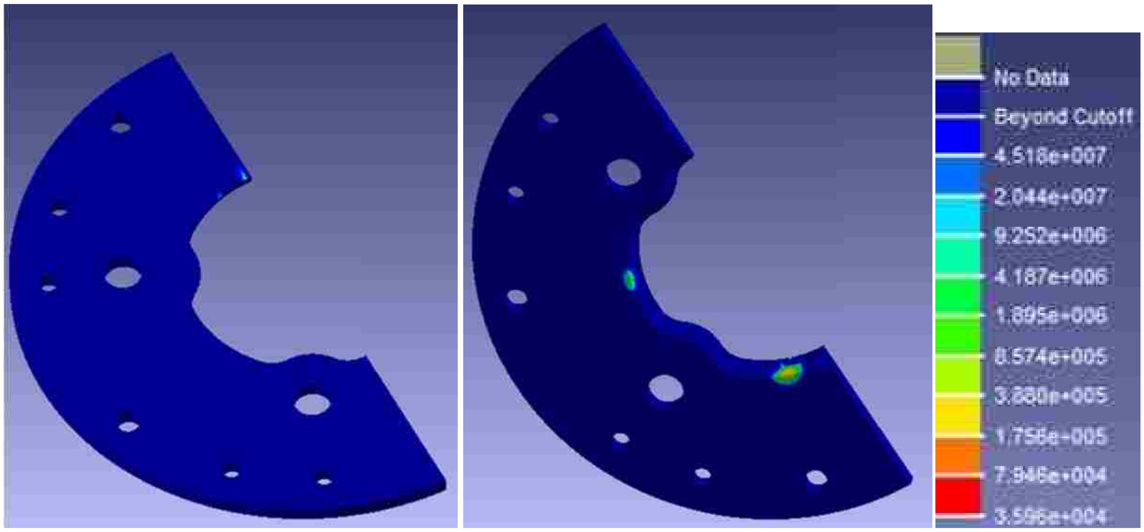

Figure 6.4 Life contours (cycles to failure) in back cover for 8-blade cutting condition based on Strain-Life solver from nCode DesignLife 12.1.

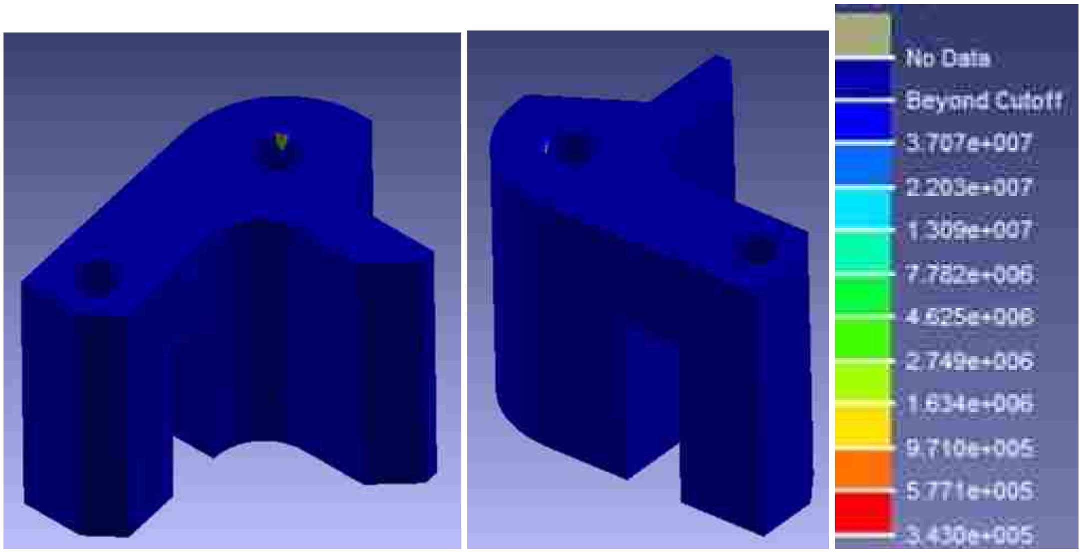

Figure 6.5 Life contours (cycles to failure) in long L-block for 6-blade cutting condition based on Strain-Life solver from nCode DesignLife 12.1.

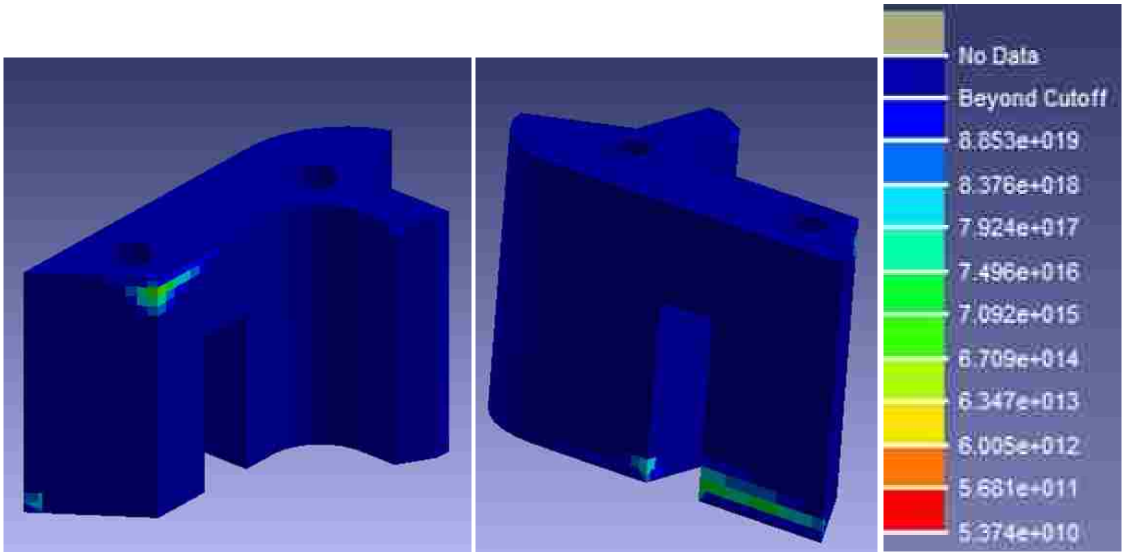

Figure 6.6 Life contours (cycles to failure) in short L-block for 6-blade cutting condition based on Stress-Life solver from nCode DesignLife 12.1.

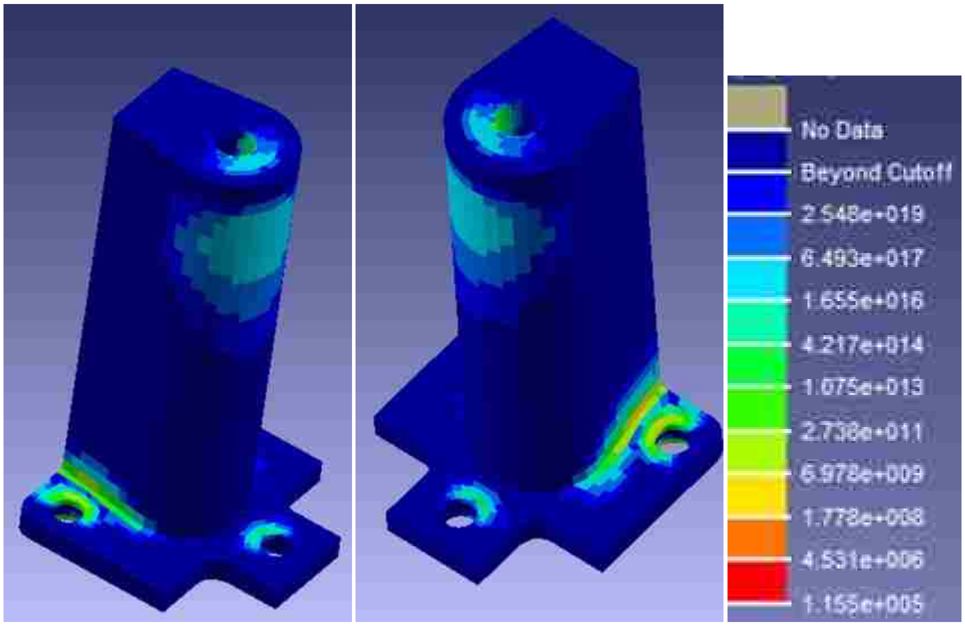

Figure 6.7 Life contours (cycles to failure) in support leg for 8-blade cutting condition based on Stress-Life solver from nCode DesignLife 12.1.

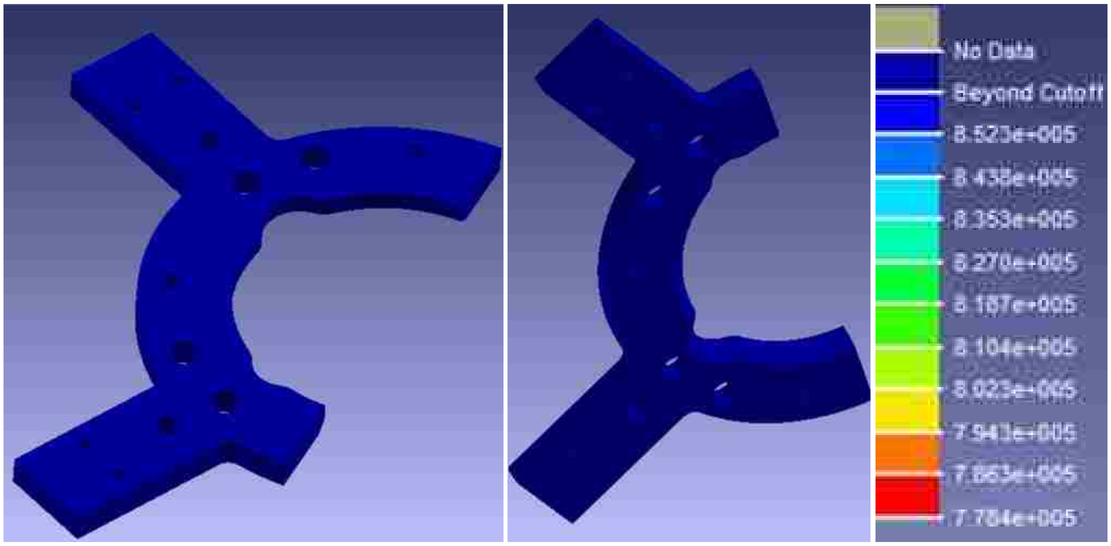

Figure 6.8 Life contours (cycles to failure) in elevated platform for 8-blade cutting condition based on Stress-Life solver from nCode DesignLife 12.1.

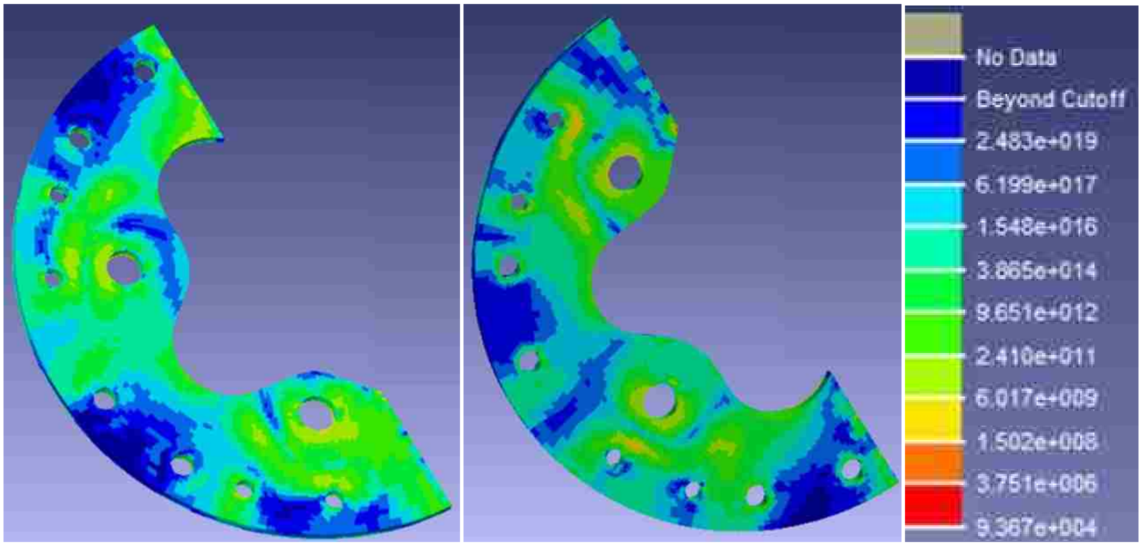

Figure 6.9 Life contours (cycles to failure) in front cover for 8-blade cutting condition based on Stress-Life solver from nCode DesignLife 12.1.

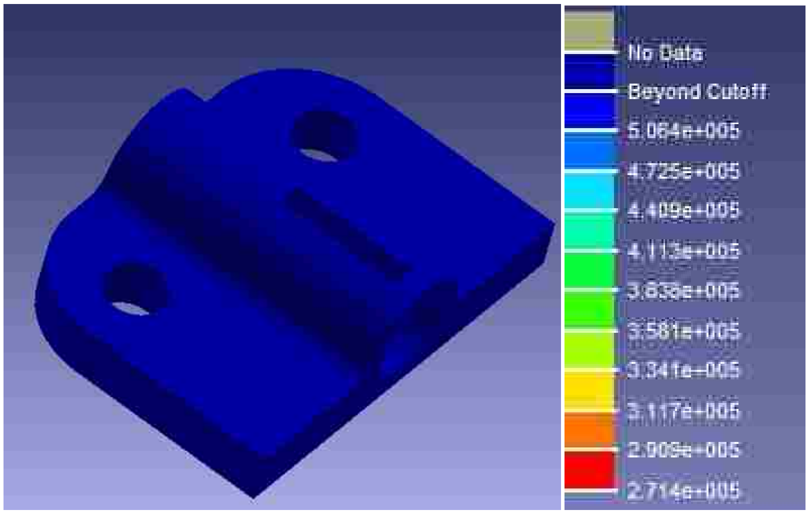

Figure 6.10 Life contours (cycles to failure) in jaw housing for 8-blade cutting condition based on Stress-Life solver from nCode DesignLife 12.1.

Note that the strongest tool steel available in the nCode material library was selected for the 3-bladed cutter and 4-bladed cutter in Figures 6.2 and 6.3, respectively. Using the strain-life solver, the number of cycles to failure is indicated in limited regions, namely the blade roots on the tapered side and around the hole. As a check on the strain-life solver's reliability, the stress-life solver was also tried for the two cutters. However, the cutoff number of cycles to failure is several orders of magnitude higher for the stress-life solver than the strain life solver. Consequently, the regions of failure detected by the stress-life solver were not as distinct as for the strain-life solver. For example, in Figure 6.3, the strain-life solver indicates a clearly defined region in red (51,000 cycles) at the root of the blade on the 4-bladed cutter, but the stress-life solver had indicated this same area in red (5,800 cycles) and orange (300,000 cycles). Therefore, the significant range of life computed within such a localized area by the stress-life solver confirmed that it is not as reliable as the strain-life solver at predicting the life at regions of high stress concentration.

For the 3-bladed cutter and 4-bladed cutter, the critical regions are at the same blade roots near the taper as indicated in the stress contours in Figure 5.20. Note that the region on the 4-bladed cutter that contacts the edge of the back cover is not the most critical zone, as expected, being shown in yellow (230,000 cycles) rather than in red (51,000 cycles) like the blade root.

The back cover in Figure 6.4 is also made of a high grade tool steel, but is not the same one as that for the two cutters even though the critical stress is roughly the same magnitude. Since both cutters have sliding contact with the back cover, if the back cover was made of the same tool steel as the cutters, the surfaces at the sliding interface would wear by galling over time.

The localized peak stress at the ¼ in hole in the long L-block in Figure 6.5 warranted use of the strain-life solver because the stress-life solver resulted in an inconsistent number of cycles to failure choosing the same material and load type. The stress-life solver was computing an inconsistent slope to the elastic line because the crack tip growth at the ¼ in hole was likely not only elastic. The early stage is better represented by the plastic strain line of the strain-life solver. Conversely, the strain-life solver computed an identical life contour in the long L-block in multiple runs choosing the same material and load type.

The same 4140 steel as the long L-block was specified for the short L-block in Figure 6.6 to save on cost. Ordering two separate 1.5 in thick plates of steel, one of 4140 and the other of lower grade, would be more costly than ordering a single 1.5 in thick 4140 steel plate that is double in width. Additionally, due to minimum order sizes and the small size of the L-blocks, a lot of material would be wasted in using different steels for each L-block.

The materials for the support leg, elevated platform, and back cover, in Figures 6.7, 6.8, and 6.9, respectively, were selected based on the possibility that the quadrotor adaptive cutter would be tested quasi-statically before conducting any impact tests. If tested quasi-statically, these three parts would be subject to high stress for a significant period of time (i.e. a few minutes rather than a few milliseconds). During impact testing, in which the load lasts only a few milliseconds, the support leg could survive 52,000 cycles with a low carbon steel, the elevated platform could survive 43,000 cycles with a high carbon steel, and the front cover could survive 50,000 cycles with a low carbon steel. However, if tested quasi-statically, the life of these three parts would be much shorter because the time step loading is much longer than a few milliseconds. Therefore, grades of steel with higher strength were chosen, resulting in the life cycles of 110,000, 700,000, and 93,000 for the support leg, elevated platform, and front cover, respectively.

The location of failure in the jaw housing, from Figure 6.10, is focused at the outside edge of the hole through which the jaw shaft slides. The zones from red to light blue are virtually invisible because they are contained within a few elements; the image resolution in nCode's fringe output is not sharp enough. Although the stress is localized, the stress-life approach was still used because the stress is much lower than the yield strength of the material selected (low carbon steel), resulting in a life of 270,000 cycles.

All the remaining components have infinite life and the selected materials have been summarized in Table 6.1. The solenoid casing is subjected to higher critical stress than the solenoid shaft, and since both are assumed to be made of the same grade of steel, only the durability of the casing was checked. Even assuming the lowest strength steel in nCode's library, the solenoid casing has an infinite life. The M10x35 and ½ in diameter bolts are the highest stressed of all the bolts in the quadrotor as seen from Table 5.2. These two bolts have an infinite life assuming the lowest shoulder bolt yield strength of 800 MPa. Since the stresses in the other bolts are much lower, they were not checked because an infinite life would be expected using the same material.

Table 6.1 Selected materials for each steel component of quadrotor adaptive cutter.

No.	Component *	Selected Material	Yield Str. (MPa)	Ultimate Str. (MPa)	Cycles to Failure
1	Back cover	SAE Steel Grade 1050M Rc54	2100	2360	36,000
2	4-Bladed Cutter	SAE Steel Grade 9254 Al_Rc58	2270	2950	51,000
3	3-Bladed Cutter	SAE Steel Grade 9254 Al_Rc58	2270	2950	98,000
4	Front Cover	Carbon Steel SAE1035_169_CON	410	550	93,000
5	Support leg	SAE Steel Grade 1090M Rc 29	751	1251	115,000
6	Jaw Housing	Struct. grade carbon steel S235J0	235	360	270,000
7	Long L-Block	SAE Steel Grade 4140 Rc31	929	1043	343,000
8	Elev. Platform	Quench and tempered steel 41Cr4	800	1000	700,000
9	Short L-Block	SAE Steel Grade 4140 Rc31	929	1043	Infinite
10	Jaw	Stainless steel X2CrTiNb18	230	430	Infinite
11	Angle Plate	Struct. grade carbon steel S355J0	355	510	Infinite
12	Solenoid Casing	Struct. grade carbon steel S185	185	310	Infinite
13	Solenoid Shaft	Struct. grade carbon steel S185	185	310	Infinite
14	Solenoid Pick	Struct. grade carbon steel S355J0	355	510	Infinite
15	Mount Hex Nut	Quench and tempered steel 41Cr4	800	1000	Infinite
16	M8x10 Sh Bolt	Quench and tempered steel 41Cr4	800	1000	Infinite
17	M6 Hex Nut	Quench and tempered steel 41Cr4	800	1000	Infinite
18	1/4 in Sh Bolt	Quench and tempered steel 41Cr4	800	1000	Infinite
19	#10 Hex Nut	Quench and tempered steel 41Cr4	800	1000	Infinite
20	½ in Sh Bolt	Quench and tempered steel 41Cr4	800	1000	Infinite
21	3/8 in Hex Nut	Quench and tempered steel 41Cr4	800	1000	Infinite
22	M10x35 Sh Bolt	Quench and tempered steel 41Cr4	800	1000	Infinite
23	M6x6 Sh Bolt	Quench and tempered steel 41Cr4	800	1000	Infinite

*Teflon pin and neoprene pad not shown in list

6.2 Material Sensitivity on Fatigue Life of 4-Bladed Cutter

In a research setting, the device will need to survive thousands of impacts in its lifetime in order to obtain data from repeated tests without frequently replacing components. In practice, such a device may be mounted in a vehicle or a train rail car,

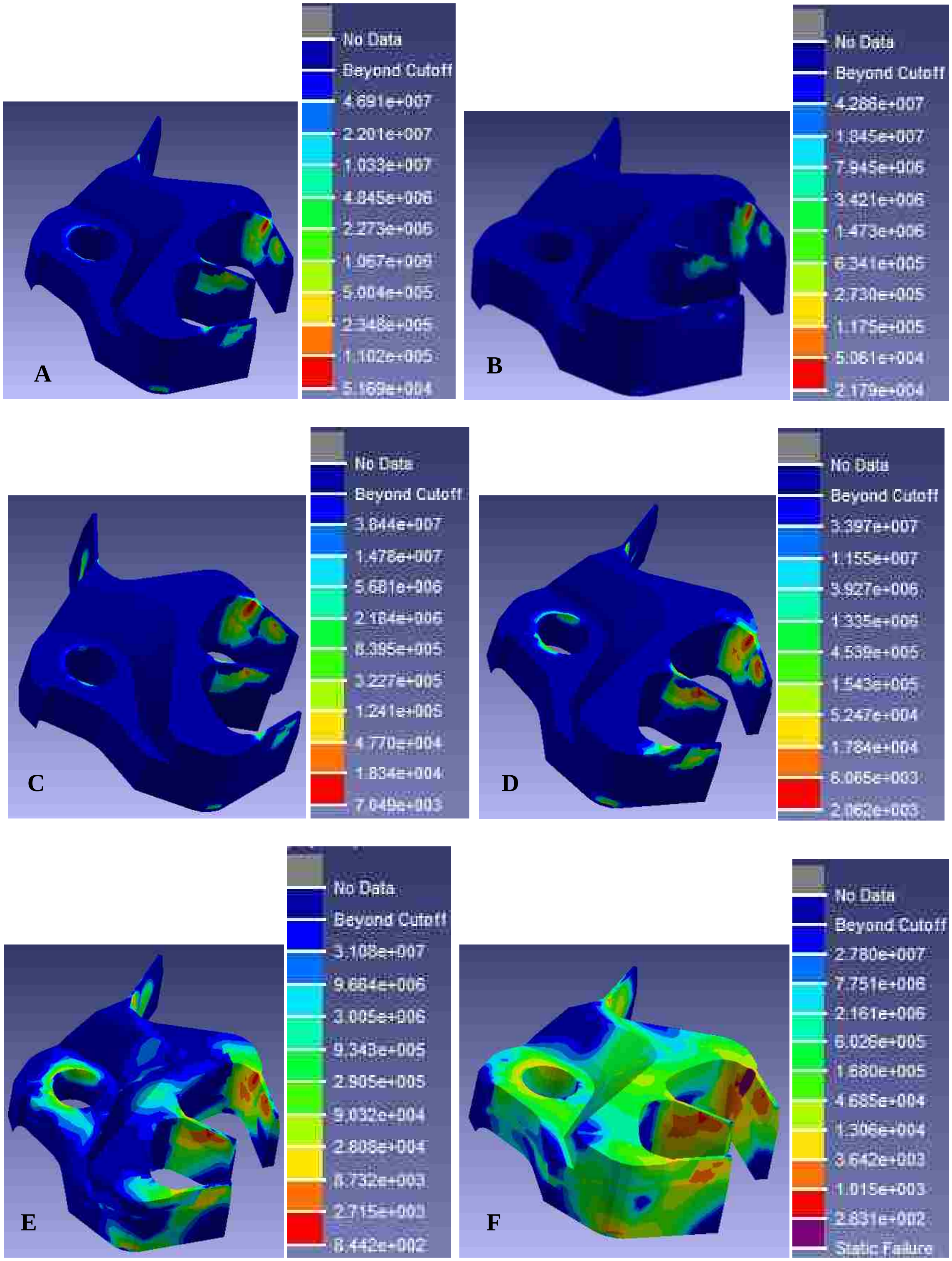

Figure 6.11 Life contours (cycles to failure) in 4-bladed cutter for 6 different grades of steel A, B, C, D, E, and F subjected to cutting in the 8-blade configuration. Strain-Life solver from nCode Designlife 12.1 used.

Table 6.2 Life predictions for different steel grades A, B, C, D, E, and F assigned to 4-bladed cutter.

Letter	**Selected Material**	**Yield Str. (Mpa)**	**Ultimate Str. (Mpa)**	**Cycles to Failure**
A	SAE Steel Grade 9254 Al RC58	2270	2950	51,000
B	SAE Steel Grade 4620 RC 59	1317	2227	22,000
C	SAE Steel grade 4130 Al RC 46	1285	1483	7,050
D	SAE Steel grade 4140 RC 31	929	1043	2,000
E	SAE Steel Grade 1090 RC 33	678	1147	840
F	Carbon Steel SAE 1080 NORM	227	415	Static Failure

and would only need to survive a single crash. The high cost of tool steels would render the quadrotor device rather unappealing. However, cheaper, lower grades of steel could be used for the various parts in the device if it need not survive thousands of times. The sensitivity of fatigue life with selected steel grade was studied for the 4-bladed cutter as it is one of the most critically loaded parts in the quadrotor. Figure 6.11 shows the progressive change in the life cycle contours as well as number of cycles to failure for different steels A through F. Generally, as indicated in Table 6.2, the number of cycles to failure decreases with decreasing yield and ultimate strength. Note that steels B through F have yield strengths below the maximum stress of 1842 MPa in the 4-bladed cutter, as previously presented in Table 5.2, yet the strain-life solver in nCode does not indicate static failure until using steel F. Since the high stresses in the cutter are localized and last for a short duration, macroscopic plastic failure does not occur at the first impact. The growing regions of possible failure are noticeable from steels D to E to F, where steel F would fail at the first impact (region in purple). The 840 cycles to failure demonstrated by steel E should not be assumed face value, but this result indicates that it should survive at least one impact. Therefore, steel E, having a yield strength of 678 MPa and ultimate strength of 1147 MPa would be a more economical choice in a practical application than steel A (yield strength 2270 MPa, ultimate strength 2950 MPa) which was selected for the purpose of research.

7.0 EXPERIMENTAL TESTING FOR NUMERICAL MODEL VALIDATION

This chapter presents an apparatus designed to replicate the blade deployment without constructing the complete quadrotor adaptive cutting device. The purpose of constructing a simplified device is to validate the numerical models developed in Chapters 5.3.2 and 5.3.3. The questions that could be answered without having the complete quadrotor are:

1. For the 3-bladed cutter and 4-bladed cutter, does the modeling technique for the torsion spring in Chapter 5.2 result in consistent angular displacement versus time responses as those measured experimentally?
2. Are the impact loads for the 3-bladed cutter and 4-bladed cutter similar to those predicted by the numerical model?
3. Does the neodymium magnet allow the 3-bladed cutter and 4-bladed cutter to stick on impact?

A CAD model of the apparatus is shown in Figure 7.1. Figure 7.1(a) shows the setup for the 3-bladed cutter and Figure 7.1(b) shows the assembly for the 4-bladed cutter. The same parts for the 3-bladed cutter assembly were reused in the 4-bladed cutter assembly, except for a different cutter, sliding pin, and L-block. The base plate was a 12.7 mm thick aluminum gauge cut to a 457.2 mm x 457.2 mm square. A 1050V6 Dytran load cell with integrated electronic piezoelectric (IEPE) technology was fastened to the L-block. This load cell has ranges of 22.2 kN in compression and 2.2 kN in tension. A custom impact cap made of a mild steel is fastened to the load cell. A K&J Magnetics plastic-coated 12.7 mm^3 neodymium magnet with 31.1 N pull force was held in place on the impact cap using its magnetic force. The same torsion spring model PT078-781-7.000-MW-LH-2.000-N-IN used in the quadrotor was used in this simplified apparatus. Note the geometries of the 3-bladed cutter and 4-bladed cutter were modified slightly to simplify manufacturing: the taper on the blade tips was removed because no cutting was involved in this experiment, and the outlines of the depressions were vertical instead of slanted. The masses and inertia tensors of both cutters were negligibly affected by

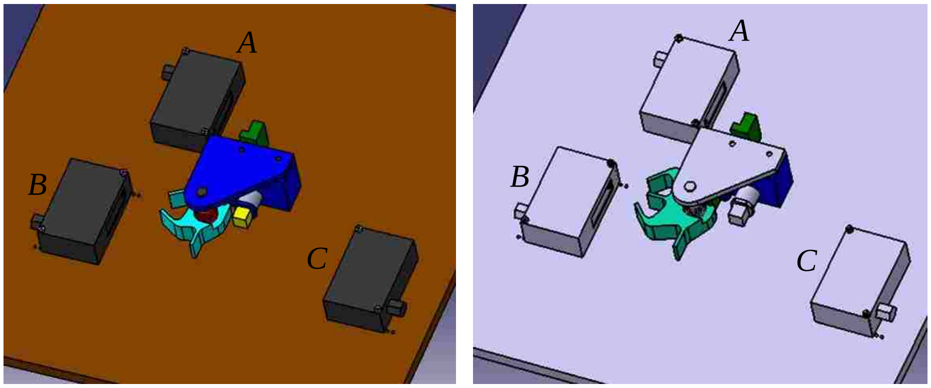

(a) (b)

Figure 7.1 CAD model of the cutter deployment apparatus. (a) 3-bladed cutter assembly. (b) 4-bladed cutter assembly. Parts shown in grey are reused.

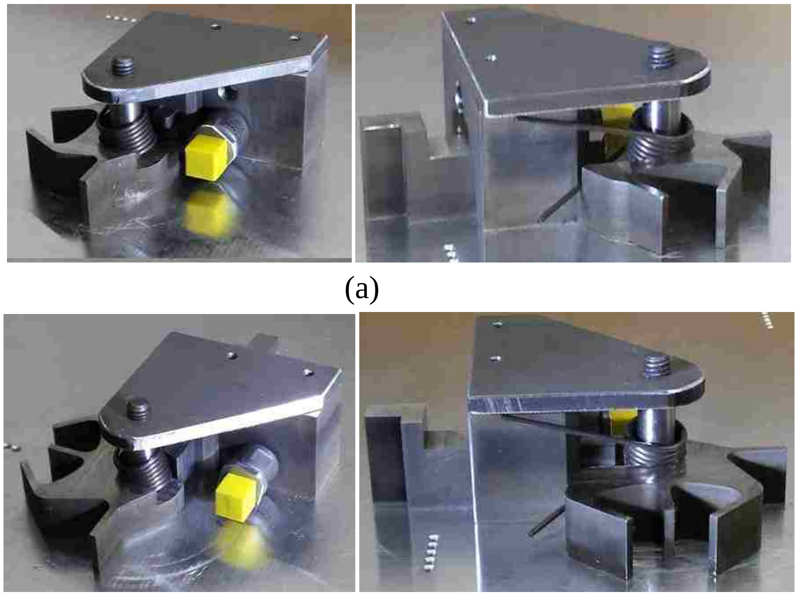

(a)

(b)

Figure 7.2 Photographs of cutter deployment apparatus. (a) 3-bladed cutter assembly. (b) 4-bladed cutter assembly.

applying these changes. The cutters, L-blocks, and sliding pins were made of a P20 steel. The top cover plate was made of a mild steel. The depressions in both cutters were machined on a computer numeric controlled (CNC) machine and their outer profiles were cut on a wire electric discharge machine (EDM). The profiles of the L-blocks, sliding pins, and front cover were also cut on a wire EDM. The ½ in shoulder bolt shaft, the bottom faces of each cutter, the slots and sliding pins were coated with oil lubricant. Also fastened to the base plate, were three non-contact Acuity AR700 laser displacement transducers: referring to Figure 7.1, the one labeled *A* had a range of 12.7 mm; the one labeled *B* had a range of 25.4 mm; and the one labeled *C* had a range of 101.6 mm. As the pin which locks the cutter in place was pulled out manually, the torsion spring drove the cutter to rotate about the ½ in bolt and hit the neodymium magnet. A Photron SA4 high speed camera, located above the apparatus, recorded the motion of the cutter. The camera settings were a frame rate of 3000 frames/sec, shutter speed of 1/10,000 sec, and image resolution of 1024 x 1024 pixels^2. Up-close photographs of the preloaded cutter assemblies with the 3-bladed cutter and 4-bladed cutter are shown in Figures 7.2(a) and (b). A far-field view of the entire experimental setup is provided in Appendix F.

The data measured from the load cell and laser displacement transducers was sent via the NI9233 and NI9215 modules, respectively, located in a compatible National Instruments Compact DAQ case, and stored as a text file in a LabVIEW enabled laptop. The NI9233 and NI9215 modules have capacities of 50 kHz per channel and 100 kHz per channel, respectively. The high speed camera was connected to the Compact DAQ and laptop via the NI9401 module. A custom LabVIEW program controlled when the high speed camera started recording, based on the change in voltage of laser displacement transducer *A*. As the pin is manually pulled out of its slot, an embossed lip on the pin crosses the path of the laser from laser displacement transducer *A* at the same instant the pin and the cutter are disengaged. The change in displacement measured by laser displacement transducer *A* induces a voltage change, which is the condition for LabVIEW to acquire data and output a TTL signal from the NI9401 module to the high speed camera, thus starting to record video. The time that the cutter comes into contact with the magnet is indicated not only by the high speed video, but also by the displacement data from laser displacement transducer *C*. As the side of the blade approaches the magnet, the 3 mm wide tip of the blade crosses the path line of the laser from laser displacement transducer *C*, inducing a sudden decrease in the measured displacement. For the 3-bladed cutter assembly, the sampling frequency and total number of recorded samples were 50 kHz and 1500, respectively, resulting in a total recording time of 30 ms. For the 4-bladed cutter assembly, the sampling frequency and total number of recorded samples were 50 kHz and 3000, respectively, resulting in a total recording time of 60 ms.

7.1 Experimental Results for the 3-bladed Cutter

This section presents the experimental findings from 85 tests conducted with the blade deployment apparatus using the 3-bladed cutter. As mentioned in section 7.0, the distance from the 12.7 mm laser displacement transducer (laser *A* in Figure 7.1(a)) to the side face of the sliding pin is recorded the instant the stepped feature on the pin crosses the path of the laser, which is the same time the pin has fully disengaged the 3-bladed cutter. Figures 7.3(a) and (b) show a small sample of these tests as well as the envelope in which the pin's displacement for 85 tests is contained, respectively. Note that at the beginning of the timeline, some tests are delayed approximately by 0.5 ms, which occurs because the laser crosses the edge of the step feature on the pin before its flat surface. Because of the small clearance between the pin and the slot, the pin pullout direction may sometimes not be perfectly perpendicular to the laser. However, this slight time delay did not propagate to the other 2 laser displacement transducers, so did not significantly influence the cutter's response time. In other words, a time shift to the right for the 12.7 mm laser displacement transducer did not necessarily result in a time shift to the right for the other 2 laser displacement transducers. A dimple in the displacement curve is seen at

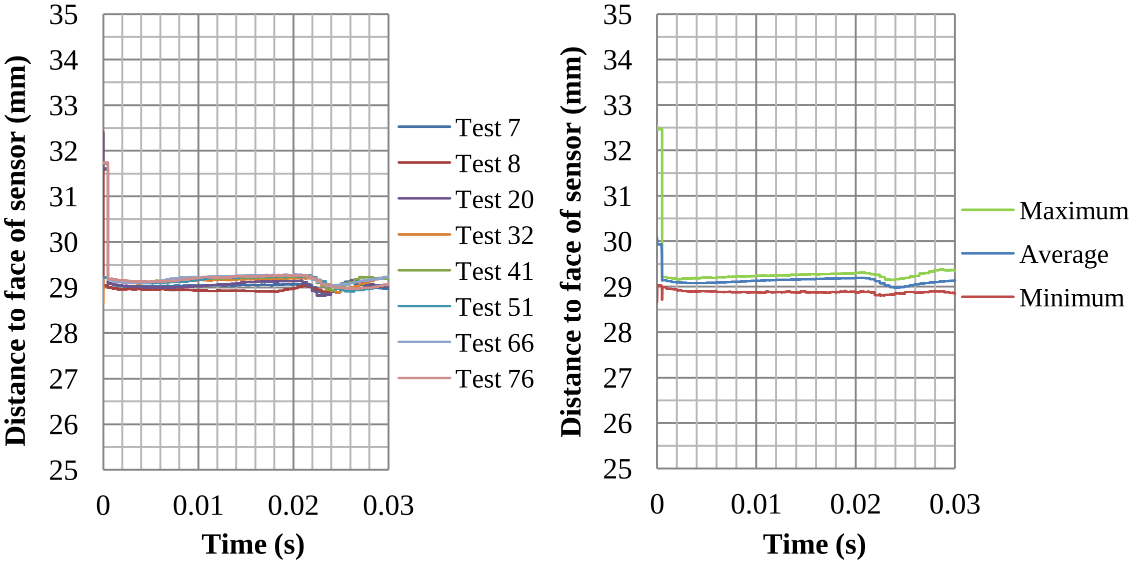

(a) (b)

Figure 7.3 Distance from face of 12.7 mm laser displacement transducer to side face of pin for 3-bladed cutter assembly. (a) 8 sample tests. (b) Envelope for 85 tests.

approximately 22 ms, indicating the time the cutter has struck the load cell, which shakes the L-block and pin slightly. Since a clearance of 0.05 mm exists between the pin and the slot, some variance on the displacement of the pin is expected. The error between the curve defining the minimum of the displacement envelope and the curve representing the accepted average of the displacement envelope is defined as

$$Cumulative\ Error\ =\ \frac{1}{t_{end}-t_{start}}\int_{t_{start}}^{t_{end}}\left|\frac{displacement_{avg}-displacement_{min}}{displacement_{avg}}\right|dt \qquad \text{Eq. 7.1}$$

Where t_{end} and t_{start} are the times at the end and start respectively of the interval in consideration. Similarly, the error between the curve defining the maximum of the displacement envelope and the curve representing the average of the displacement envelope is

$$Cumulative\ Error\ =\ \frac{1}{t_{end}-t_{start}}\int_{t_{start}}^{t_{end}}\left|\frac{displacement_{avg}-displacement_{max}}{displacement_{avg}}\right|dt \qquad \text{Eq. 7.2}$$

Given the large number of experimental data points (1500) collected in the time interval of 0.03 seconds, numerical integration by the rectangular rule was sufficient to evaluate the cumulative errors. The cumulative errors for the minimum and maximum displacement of the pin were computed to be 0.84% and 0.58%, respectively.

The same sample of 8 tests recorded by the 25.4 mm laser displacement transducer (laser *B* in Figure 7.1(a)) is shown in Figure 7.4(a). The mid-span between the two blades that are 60 degrees apart is indicated at time = 0. Upon rotation of the cutter, the circular profile between these 2 blades is captured until the discontinuity at 5 ms, indicating when the blade crosses the path of the laser. The outer profile of the cutter continues to be measured until approximately 18 ms, when the laser touches the ½ in bolt and the displacement transducer is outside its useable range. A selected representative average displacement/time response from a total of 70 tests, including the envelope defined by minimum and maximum responses containing all the tests are depicted in Figure 7.4(b). Although a total of 85 tests were conducted, the 25.4 mm laser displacement transducer data was affected by light saturation in 15 of these tests. Specifically, at the 18 ms mark, the displacement would rise suddenly. Though this region of time is not of interest for the 25.4 mm laser displacement transducer data,

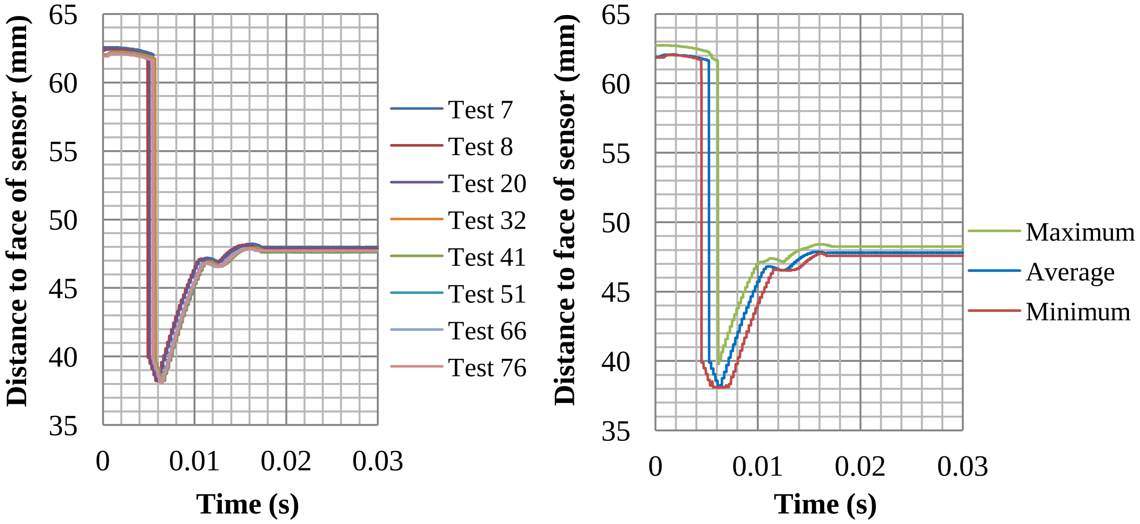

(a) (b)

Figure 7.4 Distance from face of 25.4 mm laser displacement transducer to 3-bladed cutter. (a) 8 sample tests. (b) Envelope for 70 tests with one test selected as a representative average.

including the tests with this nonphysical discontinuity would have resulted in a misleading cumulative error computation. So based on 70 tests and a time interval of 30 ms, the cumulative error for the minimum curve and maximum curve are calculated to be 2.10% and 2.8%, respectively. This tight window indicates a highly repeatable response for the 3-bladed cutter throughout its entire rotation.

The same sample of 8 tests recorded by the 101.6 mm laser displacement transducer (laser *C* in Figure 7.1(a)) is shown in Figure 7.5(a). During the first 14 ms, the displacement is constant because the laser is only in contact with the shaft of the ½ in bolt. However, the 3-bladed cutter is rotating during this time. Only at the 14 ms mark does the taller 20 mm height of the 3-bladed cutter cross the laser's path. The radius at the blade root is captured between 14 ms and 20 ms, at which time the tip of the blade comes into view causing a second discontinuity in the displacement/time response. The total response time of the 3-bladed cutter is well represented by the drop at approximately 20 ms as the cutter did stick to the neodymium magnet on impact. A total of 73 tests were considered in defining the minimum and maximum envelope shown in Figure 7.5(b). Among 85 tests, 12 tests were discarded when computing the cumulative error because

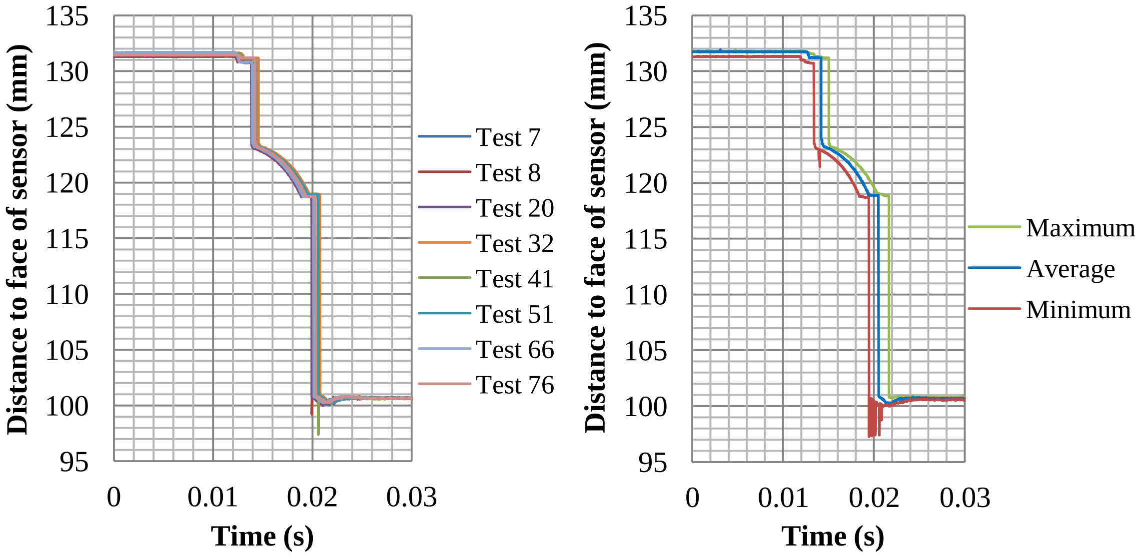

(a) (b)

Figure 7.5 Distance from face of 101.6 mm laser displacement transducer to 3-bladed cutter. (a) 8 sample tests. (b) Envelope for 73 tests with one test selected as a representative average.

these showed a sudden drop and rise between 14 ms and 15 ms, which is not physically possible. In these 12 tests, the 101.6 mm laser displacement transducer was saturated by the reflecting light at the edge of the geometric feature as it came into view at the 14 ms mark. The cumulative errors defined by Eq. 7.1 and Eq. 7.2 based on 73 tests were computed to be 1.2 % and 2.1 %.

The consistency in the response time based on the 73 tests in the 101.6 mm laser displacement transducer data was computed using a 99% confidence interval, defined as

$$\bar{t} - Z_{\frac{\alpha}{2}}\frac{\sigma}{\sqrt{n}} \leq Response\ Time \leq \bar{t} + Z_{\frac{\alpha}{2}}\frac{\sigma}{\sqrt{n}} \qquad \text{Eq. 7.3}$$

Where $\bar{t}$ is the sample mean (20.39 ms), σ is the sample standard deviation (0.37 ms), n is the sample size (73), and $Z_{\alpha/2}$ is the Z score for 99% of a normally distributed population (2.58). Given these parameters, with 99% confidence, the average response time of a large sample size is expected to be within the following interval:

$$20.28\ ms \leq Response\ Time \leq 20.50\ ms$$

The load at impact for the same sample of 8 tests is shown in Figure 7.6. Recall the numerical impact force in the LS-DYNA pre-cutting simulation for the 3-bladed cutter, in Figure 5.13, was sensitive to the material model chosen for the magnet. Though the mechanical properties of steel were defined for the magnet, whether it was rigid or elastic highly influenced the impact load. A rigid material model resulted in a peak load of 8 kN, whereas an elastic material model resulted in a peak load of 3 kN. Experimentally, the peak load at least falls somewhere in between being approximately 4.1 kN. Therefore, the stresses expected on the blade at impact in the deployment stage should be far from plastic yielding, especially when the much stronger SAE 9254 Al RC58 steel is used in the real cutter design.

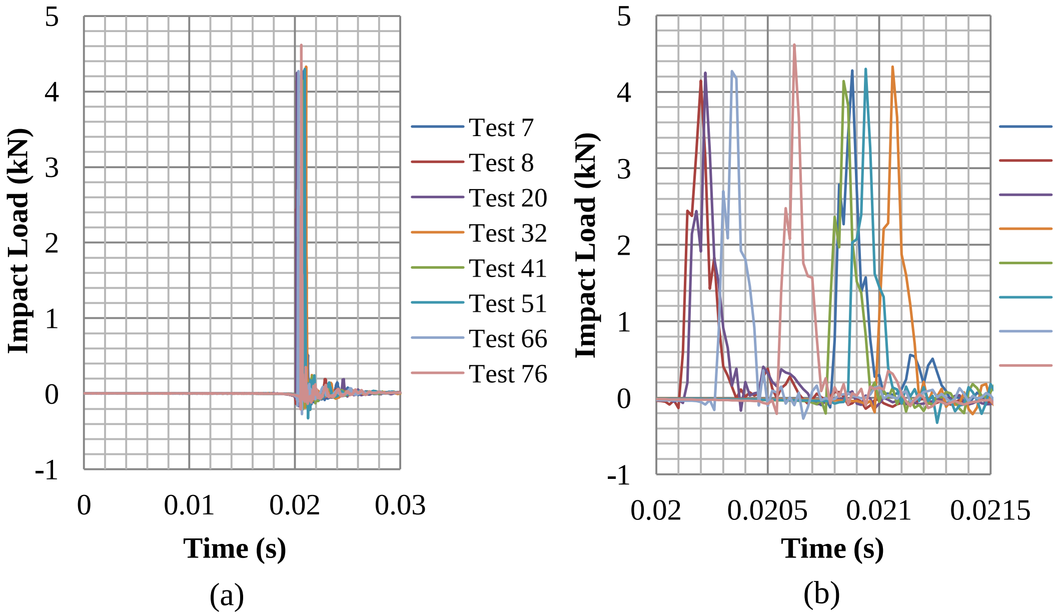

Figure 7.6 Impact load from 3-bladed cutter on load cell. (a) 8 sample tests. (b) Same 8 sample tests zoomed-in between 20 ms and 21.5 ms.

The load at impact was found to be sensitive to the face chosen on the magnet. Before each test, the magnet was removed to ensure the impact cap was securely tightened. However, in early tests, the magnet was placed back on the impact cap without taking careful note of the face chosen. Since the plastic coating thickness on the cube shaped magnet is not highly uniform on each face, a side with thinner coating would result in a higher impact load. To ensure more reliable load measurements, a side of the magnet with a thinner plastic coat thickness was noted by the 15th test, and used consistently thereafter. Another factor not accounted for in the LS-DYNA model is the effect of the magnetic field on the approaching blade. Rather than modeling the magnetic field, contact between the blade and magnet was assumed to stick on impact. However, the magnetic field may have accelerated the blade near the end of the cutter's rotation, resulting in a higher impact velocity and higher impact load. The plastic coating and magnetic field were possibly competing factors on the load magnitude since the former tended to decrease the load and the latter tended to increase the load. One final parameter that contributes to the variance in the load measurements is the impact velocity. The impact velocity will vary between each test as the sharp edges of the harder P20 steel blades scored the softer aluminum plate, creating a new surface profile after each test. Although the adaptive cutting device will have a high grade tool steel back cover, which should prevent any gouging, scratching could be minimized by adding a small fillet radius along the perimeter on the bottom of the cutter.

The consistency in the load profiles indicated in Figure 7.6(b) was assessed for 68 tests by calculating the cumulative error for each succeeding test. From Eq. 7.1, the accepted average load/time response was assumed to be the first test (starting when the same magnet face was used) because the surface of the aluminum plate was close to its as-manufactured state. The score marks on the surface had only accumulated with more tests, damaging the surface further. Before evaluating the cumulative error, each load/time response was offset in time to when the load first reached a value of 0.01 V (0.2224 kN) to fairly compare each load/time profile, ignoring the time when impact occurred. The cumulative error in the load/time response for each succeeding test compared with the first test is plotted in Figure 7.7. Note that the error does not increase continuously, but fluctuates quite steadily with each passing test. This result is a good indication that the device performance is not degrading over time despite the increasing area of scratches on the plate. The average error of 266 % is rather high, but bear in mind it is not the error of a single data point, but that of a load profile over some span of time. An error of this magnitude should be expected given that the load is sensitive to the magnet coating, exactly where the magnet is placed on the load cell cap, and the impact velocity, which changes with the changing plate surface condition.

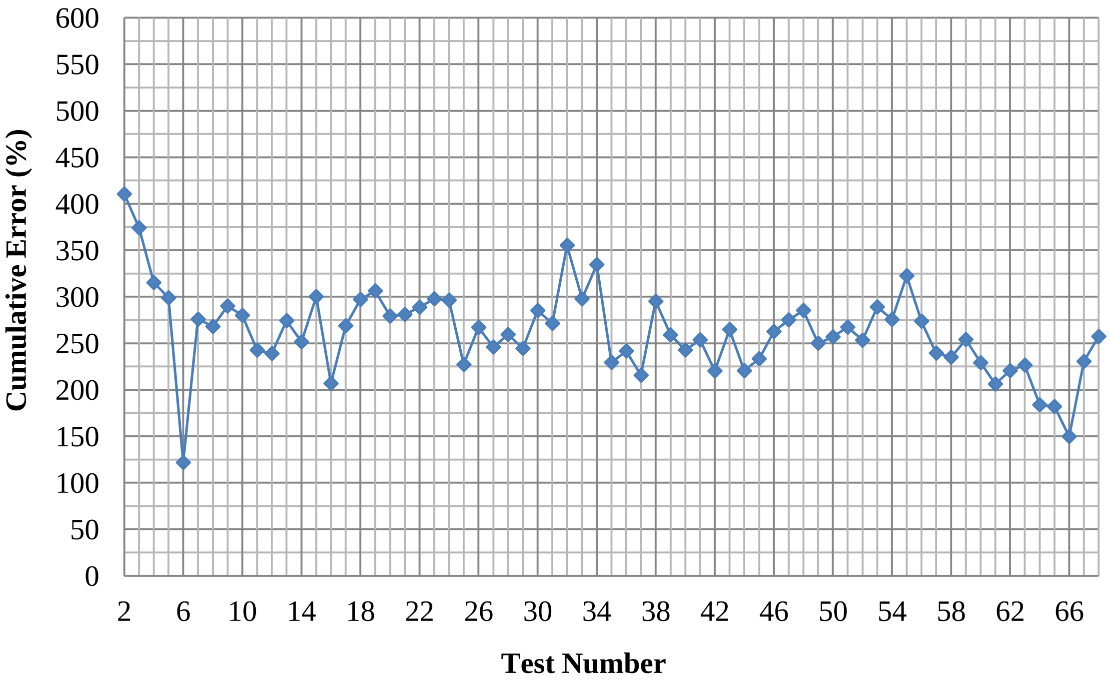

Figure 7.7 Cumulative error in the load/time response using Test # 1 as the accepted average for the 3-bladed cutter.

A 99% confidence interval was also evaluated for the peak load based on 69 tests. With a mean load of 4.34 kN and a standard deviation of 0.17 kN, the average peak load of a large sample size would fall within the following interval:

$$4.29\ kN\ \leq\ Average\ Peak\ Load\ \leq 4.39\ kN$$

At every fifth test, the video of the blade deployment recorded with the high speed camera was saved for image tracking analysis. ProAnalyst, a digital image tracking software, was used to measure and track the angle of the 3-bladed cutter throughout its rotation, as depicted in Figure 7.8. The bright reflecting light on the aluminum plate and steel cutter caused the software to lose track of geometric features such as the blade tip. To combat this effect, a strip of black hockey tape approximately the same width and length of the blade was adhered over the top surface of the blade to absorb the light. A circular dot was then drawn in white marker over the black tape. The contrasting colour enabled ProAnalyst to effectively track the region on the blade defined by the box labeled “1*” throughout its rotation. Another patch of black hockey tape approximately 12 mm^2

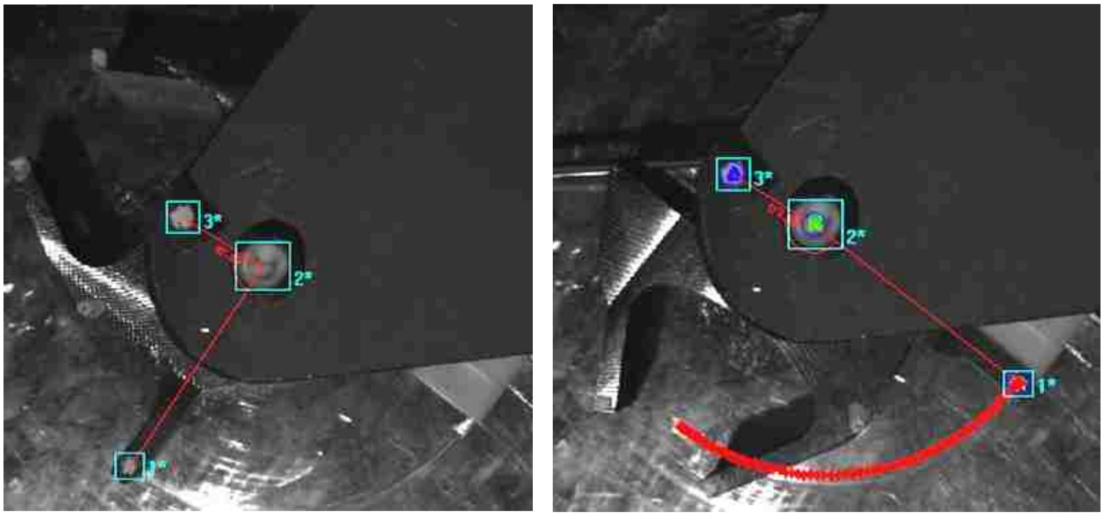

(a) (b)

Figure 7.8 Top view of 3-bladed cutter assembly with selected regions for image tracking. (a) Start time of deployment. (b) End time of deployment.

was adhered to the front cover and a white dot drawn, indicated by the box labeled “3*”. The bolt tip was also coloured white as seen in the box labeled “2*”. Given that box 1 is a point on the rotating entity, box 2 is the axis of rotation, and box 3 is a fixed point of reference, the angle formed by the line connecting these three regions could be measured and tracked automatically.

Whether the 3-bladed cutter bounced upon impact with the magnet could be seen in the high speed video. Not only did the 3-bladed cutter not bounce, it consistently stuck at impact after 85 tests. The slightest lifting of the blade away from the magnet or lifting of the magnet away from the impact cap had not even occurred before settling down. Additionally, the magnet would be more difficult to dislocate in the actual adaptive cutting device because the magnet will be placed in a corner of thick material. The magnet’s hold force on the L-block should also be approximately 70 % greater than on the load cell impact cap because a metal thickness of at least 10 mm is required to achieve the magnet’s full holding potential. The thickness of the impact cap for the experimental apparatus on the other hand is only 3 mm.

A total of 16 videos were analyzed for tracking of the 3-bladed cutter’s angle as a function of time. With the initial angular position offset to zero degrees, the angle/time responses are as depicted in Figure 7.9(a). In theory, the total rotational angle should be

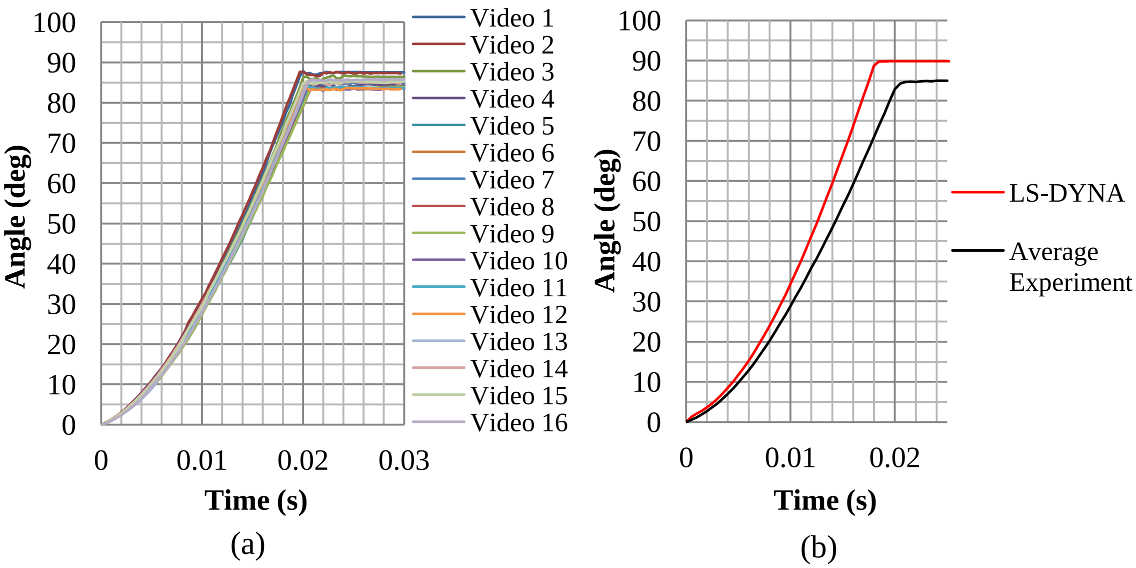

Figure 7.9 Angular position of the 3-bladed cutter vs. time. (a) ProAnalyst tracking data. (b) Average experimental response and numerical simulation.

90 degrees. However, experimentally the total angle is slightly less at approximately 85 degrees. Seen in the high speed footage, the whole front cover shifts very slightly as the rotary inertia of the cutter pulls the bolt in shear. This shift explains why the full range of angular motion measured experimentally is closer to 85 degrees than to 90 degrees. Note this experimental setup has a front cover cantilevered over a single support block, but the real adaptive cutter has a stiffer front cover being supported by 4 L-blocks, as previously shown in Figure 4.13(e), so should not flex out of place during either cutter's rotation. The FE pre-cutting models of the complete adaptive cutter in Chapter 5.3 also indicated no shifting of the front cover. Moreover, the shoulder of the bolts passes through all of the parts in the real adaptive cutter. However, in this experiment, the bolts are threaded in the front cover, and so do not maintain axial position as accurately as a completely shouldered connection.

The average angle/time response for the 3-bladed cutter from the 16 videos analyzed is overlaid with the angle/time response in the LS-DYNA pre-cutting simulation of the 6-blade configuration in Figure 7.9(b). Experimentally, recall the high speed camera only starts recording when the pin has fully disengaged the cutter. Therefore, to compare fairly, the LS-DYNA angle/time response shown has been offset 4 ms backward in time because the solenoid requires 4 ms to fully disengage the Teflon pin from the cutter. The experimental angle becomes shallower than the angle from the model as time progresses. This result is expected because friction between the cutter and base plate becomes more significant as the cutter's velocity continuously increases. Also, after each test, the surface profile of the base plate changes having formed new peaks and worn in new valleys. So the friction coefficient, or the surface roughness, is not a constant parameter as it is in the LS-DYNA simulation. Nonetheless, the growing area of score marks on the plate with increasing number of tests did not delay the response time of the 3-bladed cutter or prevent it from sticking to the magnet on impact. To illustrate, as seen in Figure 7.10, the cumulative error of each succeeding experimental angle/time responses were compared with the first experimental angle/time response assumed to be the accepted average response. As was the case for the load/time response, the error in the angle/time response for each succeeding video compared to the first video fluctuates steadily, meaning the cutter's response throughout its entire rotation (not only its response time) does not degrade as more tests are performed. Also, despite the changing plate surface quality, the average error of 5.8 % is significantly lower than the average error in the load/time response.

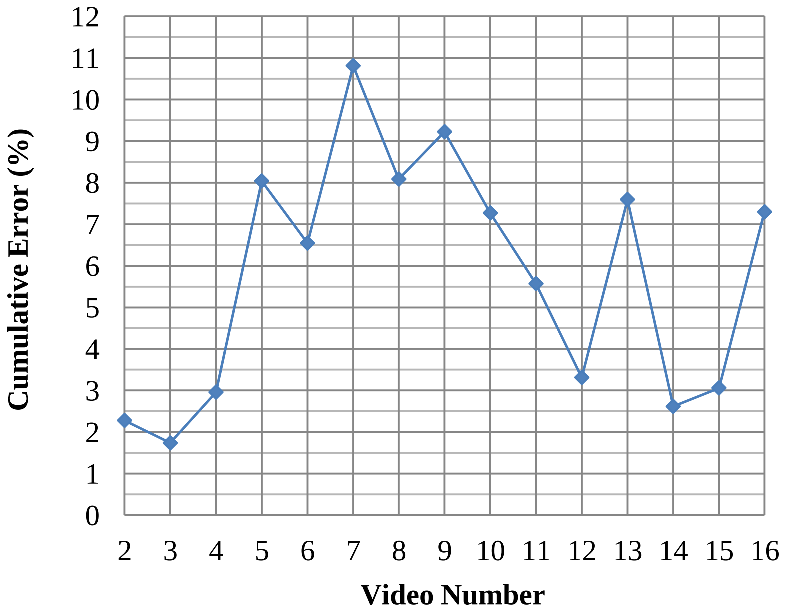

Figure 7.10 Cumulative error in the angle/time response using Video # 1 as the accepted average for the 3-bladed cutter.

To quantify the error between the angle/time responses of the LS-DYNA simulation and the average experimental, a parameter proposed by Oberkampf and Trucano [54] termed the validation metric was computed. Assuming zero experimental error, the validation metric *V* is defined as

$$V = 1 - \frac{1}{t_{end}-t_{start}} \int_{t_{start}}^{t_{end}} tanh\left(\left|\frac{Num_{Result}(t)-Exp_{Result}(t)}{Exp_{Result}}\right|\right) dt \qquad \text{Eq. 7.4}$$

Where a value of 1 would indicate perfect matching responses between the experimental measurements and numerical prediction. Based on the time interval of 25 ms, the validation metric is computed to be 0.779, which is fair especially since experimentally, the softer material of the base plate allowed the cutter to gouge the surface, slowing down the cutter slightly. The right hand term in Eq. 7.4 is a similar definition to Eq. 7.1 for the cumulative error. Using Eq.7.1 results in a cumulative error of 24.4 %, but the right hand term in Eq.7.4 is equal to 22 %. Note the *tanh* function prevents a negative value for *V*.

7.2 Preface to the Experimental Results for the 4-bladed Cutter

The repeated sliding of the 3-bladed cutter over the aluminum base plate had produced score lines over its surface. As depicted in Figure 7.11(a), the highest concentration of score marks is along the arc covered by the blade that contacted the magnet. Because the performance of the 3-bladed cutter was shown to be consistent throughout the tests, the surface condition of the plate was initially assumed to have little effect on the performance of the 4-bladed cutter. However, early tests with the 4-bladed cutter using the badly scored surface of the plate from the 3-bladed cutter tests resulted in significant bouncing on impact. Although the time of the initial hit between the 4-bladed cutter and magnet seemed consistent (approximately 35 ms), the settling time was not, ranging anywhere between 65 ms and 90 ms. Eliminating or minimizing the bounce effect was therefore crucial in order to predict the settling time and ensure the total response time was reasonable. Even if the settling time could be more consistent, it should preferably be below 80 ms so that an impacting entity moving at 12 m/s can be detected from 1.5 m or less before triggering the cutters. Otherwise, the impacting entity would have to be detected from farther away, rendering the adaptive cutter less practical. The plate surface was gouged most significantly by the main blade on the 3-bladed cutter after its nearly 100 tests. The surface was run-in accommodating the geometry of the

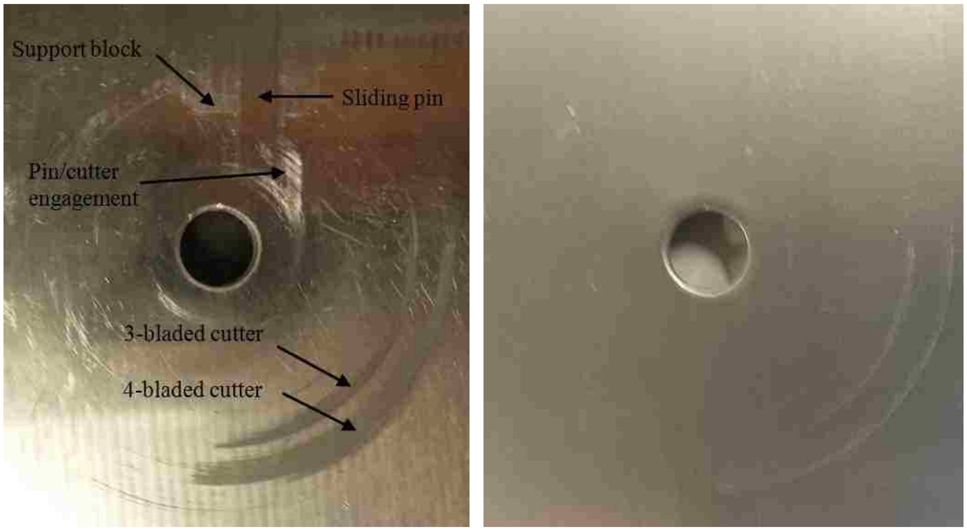

(a) (b)

Figure 7.11 Surface condition of aluminum plate. (a) After approximately 100 tests with 3-bladed cutter and 100 tests with 4-bladed cutter. (b) After manual sanding and polishing.

3-bladed cutter, but after switching over to the assembly for the 4-bladed cutter, the surface was neither polished or run-in to accommodate the geometry of the 4-bladed cutter. From the high speed video, it appeared that the 4-bladed cutter rotation had slight jerking motion rather than smooth motion like for the 3-bladed cutter. The motion appeared to stick then slip by the intermittent gouging of the blade into the plate. These sudden angular accelerations may be the reason for the bounce effect in the 4-bladed cutter, but this idea is speculative.

Sanding and polishing the surface of the aluminum plate was determined to be the critical factor in significantly reducing the bounce and obtaining consistent data for the 4-bladed cutter. The blade only slightly lifted off of the magnet at impact, resulting in much shorter and predictable setting times. Sanding was performed by hand at the scored area on the aluminum plate using 4 progressively finer grits of wet sandpaper followed by a manual polishing: benchmark waterproof sandpaper having grits of 400, 600, 1500, and 2000 were used to sand the scored area of the plate. Starting with 400, the paper was wetted with tap water and sanding was performed in a back-and-forth motion in a single direction for 15 minutes. Sanding at each successive step was performed with the next highest number sandpaper grit and water in a back-and-forth motion for 15 minutes, but in a direction perpendicular to the previous step. After the 2000 grit sandpaper step was complete, a dab of Brasso metal polish was applied to a dry cloth and rubbed over the aluminum plate for 10 minutes. The texture and coloration of the polished plate is seen in Figure 7.11(b).

A stronger neodymium magnet of 102.3 N pull force (rather than the 31.1 N pull force of the magnet used for the 3-bladed cutter) was an additional element that needed to be incorporated in the device to reduce the bounce. This neodymium magnet is the same dimension (12.7 mm^3) and is coated with nickel-copper-nickel, which although does not dampen the impact load as effectively as plastic, is nonetheless impact resistant.

To check whether the 102.3 N pull magnet was strong enough for the 4-bladed cutter, the ratio of magnetic pull force to rotational kinetic energy for each cutter at the time of impact was computed. The angular velocities at impact for the 3-bladed cutter and 4-bladed cutter were determined by curve fitting and differentiating the angle versus time ProAnalyst tracking data, presented later in Section 7.4. The velocity at impact for the 3-bladed cutter was 16 rev/sec and that for the 4-bladed cutter was 11 rev/sec. The mass moment of inertias of each cutter about the bolt axis were retrieved from the CAD model, and were 8.1×10^{-5} kg-m^2 and 2.614×10^{-4} kg-m^2 for the 3-bladed cutter and 4-bladed cutter, respectively. Thus, the rotational kinetic energy of the 3-bladed cutter was 0.41 J and the rotational kinetic energy of the 4-bladed cutter was 0.62 J. So the ratio of pull force to rotational kinetic energy was 76 for the 3-bladed cutter, and 165 for the 4-bladed cutter. This more than double in ratio of 165 was assumed to mean that the 102.3 N pull magnet would be strong enough to catch the 4-bladed cutter on impact given that the 31.1 N magnet was strong enough to catch the 3-bladed cutter on impact 85 consecutive times. However, that assumption was false since bouncing of the 4-bladed cutter still occurred.

To prevent the magnet from dislodging from the load cell upon impact, the magnet was duct taped to the load cell: 2 strips of duct tape, each approximately 12 mm wide and 100 mm long, were adhered together by overlapping one over the other in a cross-shape and adhering the intersecting area to the face of the neodymium magnet that would be hit by the cutter blade. With the magnet placed on the impact cap by virtue of its magnetic pull, the overhanging strips of tape forming the cross were adhered firmly against the load cell and support-block. Taping down the magnet was also beneficial by obtaining consistent load data. Without tape, tests in which the magnet dislodged had underestimated the impact load.

Note that material of at least 10 mm is required to achieve the magnet's full holding force potential. Since the impact cap is only 3 mm thick, the magnet will only hold onto the cap with 30 % of its maximum hold force. In the real adaptive cutter, the magnet will be jammed in a corner of thick material, so should have approximately 70 % stronger hold force than it does on the load cell impact cap. Therefore, duct tape should not be necessary in the actual cutter device.

7.3 Experimental Results for the 4-bladed Cutter

This section presents the experimental findings from 85 tests conducted with the blade deployment apparatus using the 4-bladed cutter and a freshly sanded and polished base plate. The displacement/time profile from the sliding pin measured by the 12.7 mm laser displacement transducer in Figure 7.12(a) shows a similar trend as for the tests using the 3-bladed cutter assembly. Specifically, some of the tests have a drop in

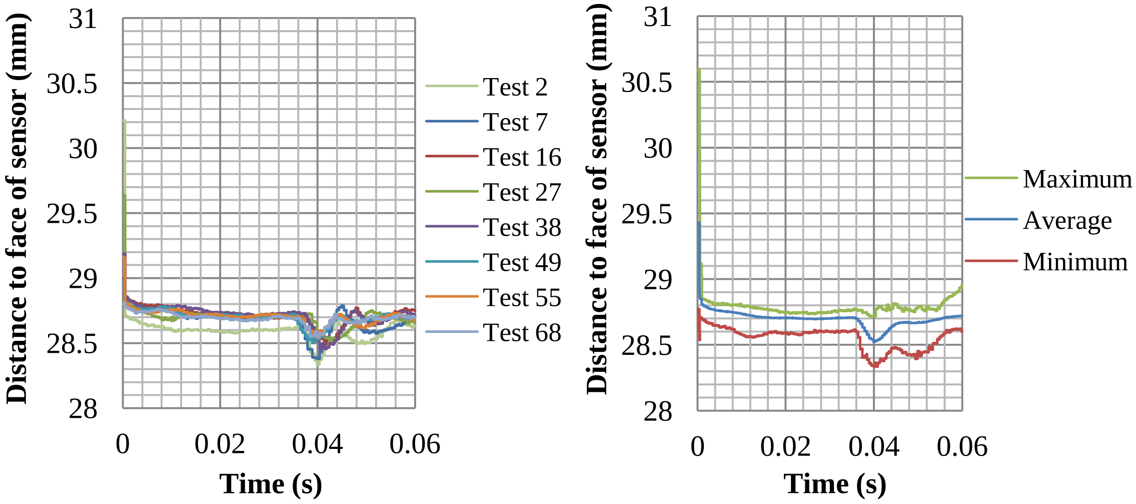

(a) (b)

Figure 7.12 Distance from face of 12.7 mm laser displacement transducer to side face of pin for 4-bladed cutter assembly. (a) 8 sample tests. (b) Envelope for 70 tests.

displacement at the 0.5 ms time of measurement, which is caused by the laser contacting the edge of the stepped feature on the pin before the flat surface. This drop would occur if the pin is pulled out at any slight angle that is not perpendicular to the laser's path, which can happen since the pin is pulled out manually and a 0.05 mm clearance exists between the pin and its slot. This time delay is insignificant though as the displacement/time profile for the 101.6 mm laser displacement transducer was not necessarily delayed by the same amount. The dimple in the response at 40 ms reflects how the 4-bladed cutter impacting the magnet shakes the block and pin to a greater extent than the 3-bladed cutter had. A total of 70 tests were considered in presenting the displacement/time envelope in Figure 7.12(b). Actually, 85 tests were conducted, but 15 of these tests used a stainless steel washer between the cutter and base plate to elevate the cutter above the surface. Although the response time and impact load were negligibly affected using the washer, the laser from the 101.6 mm laser displacement transducer detected the side of the cutter instead of the ½ in bolt during the first 20 ms of rotation. The cumulative error calculation for the 101.6 mm laser displacement transducer would have been misleadingly poor if the tests using the washer were included. For that reason, all the laser displacement transducer computations were based on the 70 tests using the sanded and polished plate and no washer. From Eq. 7.1, the cumulative error for the 12.7 mm laser displacement transducer between the minimum line of the envelope and the average line is 0.52 %. From Eq. 7.2, the cumulative error for the 12.7 mm laser displacement transducer between the maximum line of the envelope and the average line is 0.34 %. Both errors are very small, but higher for the minimum line because after the time of impact, the pin generally shifted closer to the 12.7 mm laser displacement transducer.

The data from the 25.4 mm laser displacement transducer was out of range for most of the rotation of the 4-bladed cutter. Since a limited portion of the 4-bladed cutter's profile was measured by this transducer, the data was not plotted. The span of this transducer only just fit within the distance between the blade root and blade tip on the 3-bladed cutter. Though the data from the 25.4 mm transducer was a useful backup measurement for the 3-bladed cutter, it is not a critical measurement for either cutter anyway.

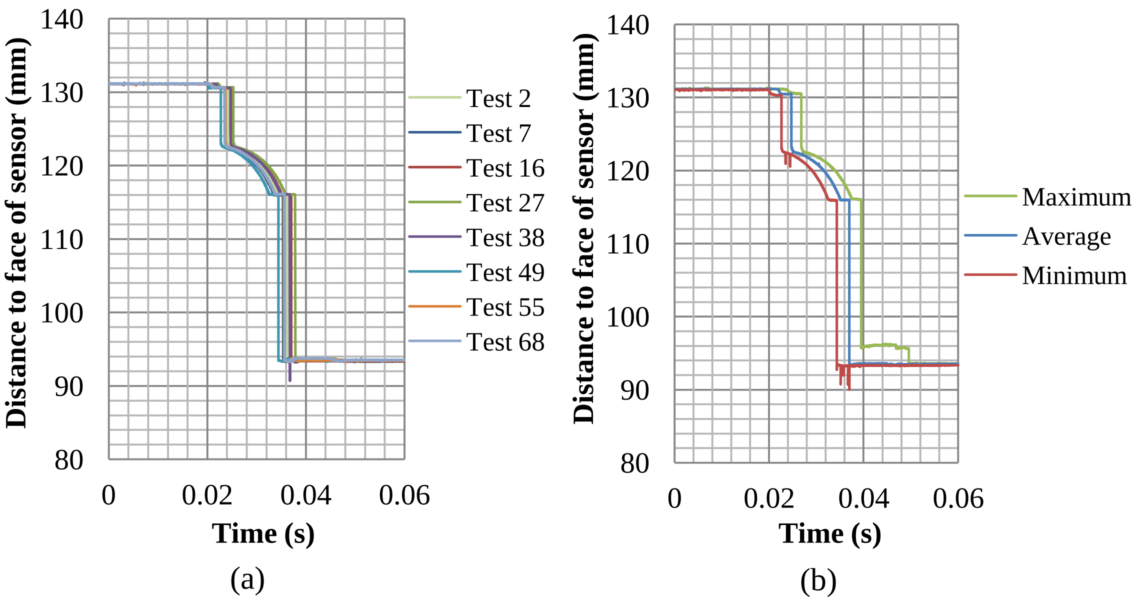

Figure 7.13 Distance from face of 101.6 mm laser displacement transducer to 4-bladed cutter. (a) 8 sample tests. (b) Envelope for 70 tests with one test selected as a representative average.

On the other hand, obtaining useful data from the 101.6 mm laser displacement transducer is necessary to be able to assess the consistency of the displacement/time response for the 4-bladed cutter. A sample of 8 tests and the envelope containing all of the tests are provided in Figures 7.13(a) and (b). The displacement/time profile is similar to that for the 3-bladed cutter, but only further delayed in time. The laser is detecting only the bolt shaft for the first 24 ms even though the 4-bladed cutter is rotating during this period. The first sudden drop is associated with the taller 12 mm region of the cutter crossing the laser's path. The curved profile between 24 ms and 35 ms corresponds to the radius at the blade root. The final drop indicates the time when the blade tip has come into view of the laser, which is also the time the blade initially contacts the magnet. Not indicated in Figure 7.13 is the fact that the cutter bounced off the magnet at the first hit, misaligning the cutter by a maximum of 5 degrees before hitting the magnet a second time and sticking. The misalignment was too small to be detected by the 101.6 mm laser displacement transducer as the corner of the blade tip was still in view of the laser. If the bounce was more significant, as it was in early tests without the polished base plate, the displacement profile would show a sudden rise back up to the 115 mm mark and drop again. With such a minute bounce though, the second hit is only indicated by the high speed video and the load measurement.

The window of 70 tests in Figure 7.13(b) is nearly as tight as it was for the 3-bladed cutter because the cumulative errors for the minimum line and maximum line compared with the representative average line are 1.05 % and 2.4 %, respectively. The accuracy of the time the 4-bladed cutter first hits the magnet was also computed using a 99 % confidence interval. Using Eq. 7.3, based on a sample of 70 tests, a sample mean initial hit time of 36.14 ms, and standard deviation of 1.13 ms, the average time the cutter first strikes the magnet will be within the following interval:

$$35.79\, ms \ \leq \ Time\ of\ First\ Hit \ \leq 36.49\, ms$$

This narrow interval indicates that the 4-bladed cutter will first strike the magnet at a predictable time. Note the interval is not quite as narrow as it was for the 3-bladed cutter. A higher frictional resistance in the 4-bladed cutter assembly specifically related to chip formation of the base plate compared to the 3-bladed cutter assembly is believed to contribute to this wider time interval. The greater chip formation in the 4-bladed cutter is evidenced photographically by the larger area of score marks in Figure 7.11(a). Though the pre-cutting simulations include frictional energy losses, this chip formation contributes an internal energy that is not included in the pre-cutting simulations, and is difficult to quantify in the analytical energy balance discussed in Section 7.4. However, the high speed video of the 4-bladed cutter does show that tests which lined up closer to the green line in Figure 7.13(b) had visibly larger flecks of aluminum debris being scraped off.

The load at impact for the same sample of 8 tests is shown in Figure 7.14(a). Recall the numerical impact force in the LS-DYNA pre-cutting simulation for the 4-bladed cutter, in Figure 5.15, was sensitive to the material model chosen for the magnet. Though the mechanical properties of steel were defined for the magnet, whether it was rigid or elastic highly influenced the impact load. A rigid material model resulted in a peak load of 9 kN, whereas an elastic material model resulted in a peak load of 4 kN. Experimentally, the peak load at least falls somewhere in between being approximately 4.5 kN. Therefore, the stresses expected on the blade at impact in the deployment stage

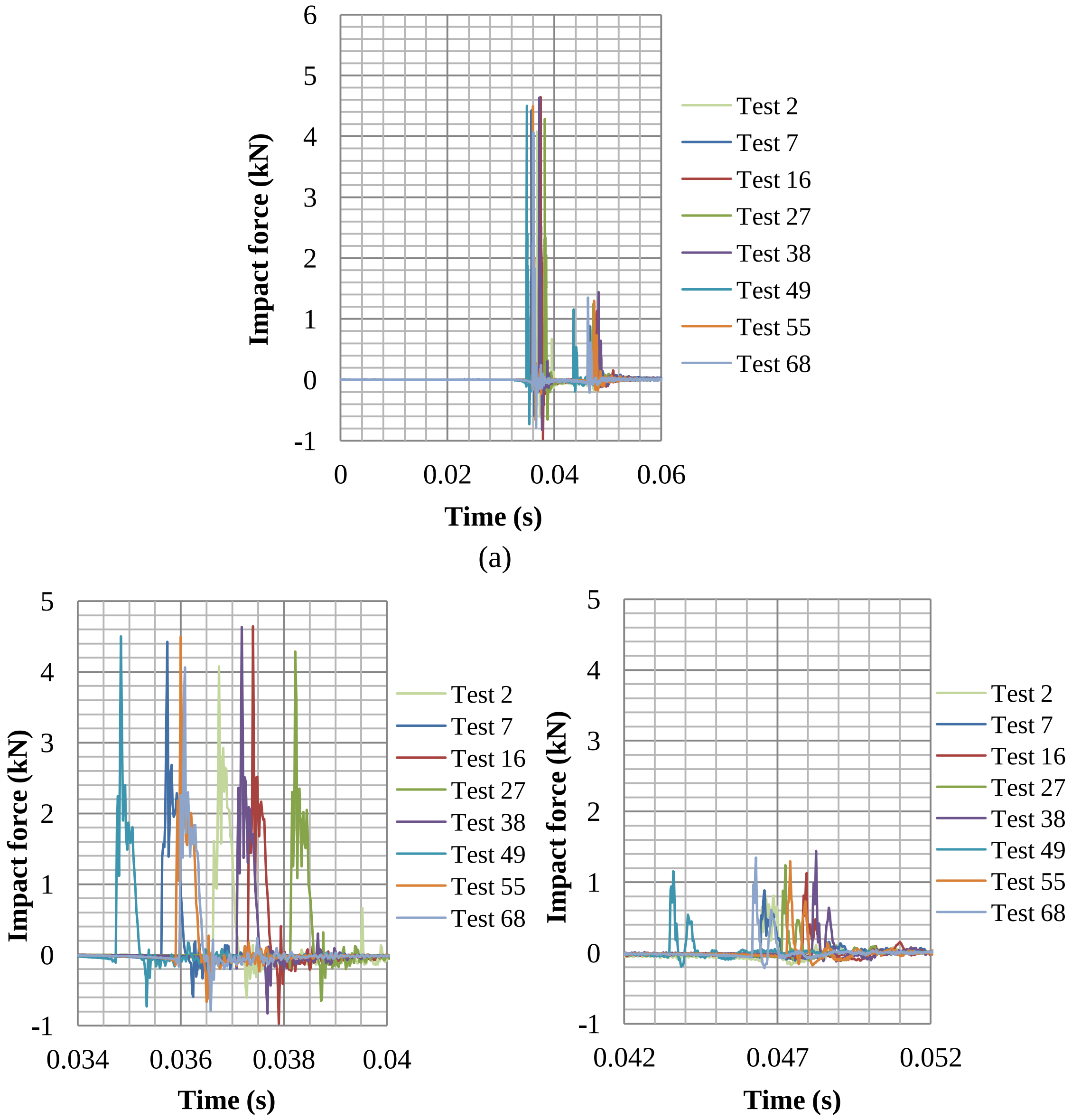

(a)

(b)

(c)

Figure 7.14 Impact load from 4-bladed cutter on load cell. (a) 8 sample tests. (b) Same 8 sample tests zoomed-in to first peak load. (c) Same 8 sample tests zoomed-in to second peak load.

should be far from plastic yielding, especially when the much stronger SAE 9254 Al RC58 steel is used in the real cutter design. The lack of a perfect sticking for the 4-bladed cutter experimentally does not reflect the LS-DYNA simulation. However, two key characteristics of the experiment will not be repeated in the actual adaptive cutter device. First, the back cover is a hard steel which should not result in the scoring effect seen experimentally with the aluminum plate. Second, the magnet should have a threefold increase in holding force being cornered in the 14 mm thick section of the L-block than on the 3 mm thick impact cap. The 4-bladed cutter under these conditions may actually stick on impact. In any case, to adjust the cutter deployment simulation with the slight bounce effect would be complicated because the magnetic field would need to be modeled. Including an electromagnetic solver is an added complexity not worth the effort since the validation metric on the angle/time response for the 4-bladed cutter (shown later) is still acceptable based on the conditions of the current experiment. The angle/time response is only expected to improve with the actual components and materials.

The LS-DYNA simulation however did correctly predict that the peak load would be slightly higher for the 4-bladed cutter than the 3-bladed cutter. In addition to its larger mass moment of inertia, the 4-bladed cutter comes into contact with a magnet that has a threefold stronger pull force (102.3 N instead of 31.1 N) and is coated with a metal (nickel-copper-nickel) instead of plastic. The combination of these factors was likely going to result in a higher impact load.

A 99% confidence interval was calculated for the maximum impact load for 85 tests. With a sample mean of 4.46 kN, standard deviation of 0.31 kN, the maximum load lies within the following interval:

$$4.36\ kN\ \leq\ Maximum\ load\ \leq 4.56\ kN$$

Referring to Figure 7.14(b), note that after the first impact, the force briefly becomes negative by as much as -1 kN, indicating the sensor is measuring a tensile load. As the 4-bladed cutter bounced off at the first impact, the blade tended to pull the magnet away from the load cell cap. This negative (tensile) load was not nearly as pronounced for the 3-bladed cutter as it stuck on impact with no bounce.

Not only the maximum load magnitudes, but also the shape of the load/time profiles for the first and second peaks in Figures 7.14(b) and (c), respectively, appear consistent. To quantify this consistency, the cumulative error was calculated for each succeeding test. From Eq. 7.1, the accepted average load/time response was assumed to be the first test because the surface of the aluminum plate was close to its freshly polished state. The score marks on the surface had only accumulated with more tests, damaging the surface further. Before evaluating the cumulative error, each load/time response was

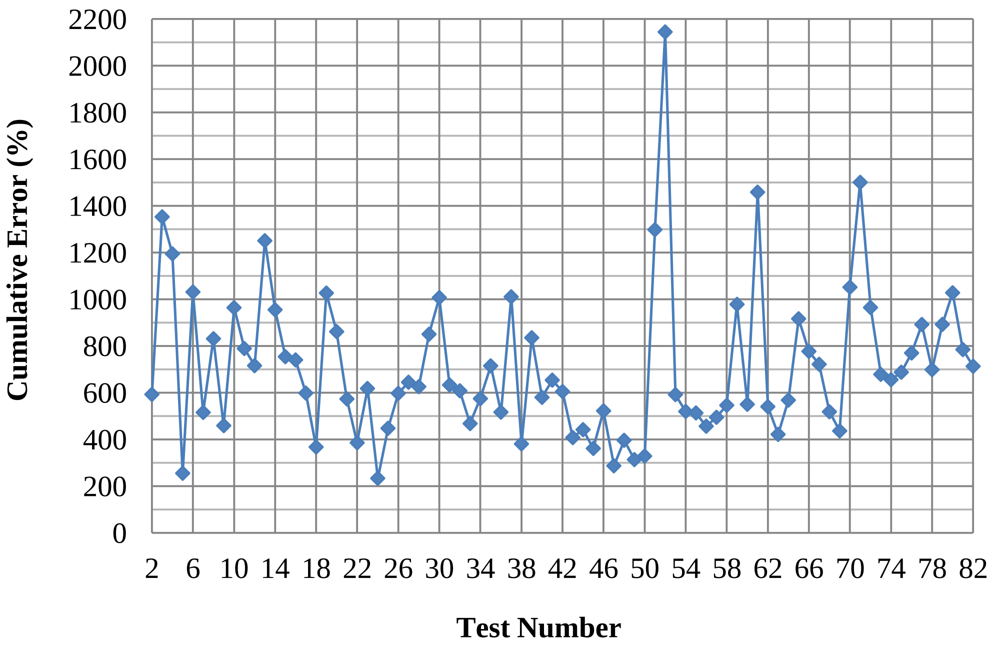

Figure 7.15 Cumulative error in the load/time response using Test # 1 as the accepted average for the 4-bladed cutter.

offset in time to when the load first reached a value of 0.01 V (0.2224 kN) to fairly compare each load/time profile, ignoring the time when the first impact occurred. The cumulative error in the load/time response for each succeeding test compared with the first test is plotted in Figure 7.15. Note that the error does not increase continuously, but fluctuates quite steadily with each passing test. This result is a good indication that the device performance is not degrading over time despite the increasing area of scratches on the plate. The average error of 716% is quite high, but this error in load is integrated over a span of time, not an instantaneous quantity. Moreover, unlike for the 3-bladed cutter, the cumulative error for the 4-bladed cutter takes into account the load profile for two peaks, not just a single one. Since the timing of the second peak varies, the cumulative error will be larger for tests where the second peak does not align well in time with the second peak of test # 1. However, the cumulative error was computed in this way to ensure that the timing of the second peak was not getting progressively slower with each passing test.

The settling time determined from a frame by frame analysis of the high speed video was found to line up well with the time of the second peak in the load data. So, the time of the second peak in the load data was used in computing a 99% confidence interval for the settling time. Again based on 85 tests, with a sample average of 46.27 ms, a sample standard deviation of 1.49 ms, the average settling time falls within the following interval:

$$45.81\,ms \le Settling\ time \le 46.73\,ms$$

The 99% confidence interval for the settling time is nearly as narrow as the confidence interval for the time of the initial hit, indicating that the 4-bladed cutter response is repeatable, despite not sticking to the magnet at the first hit.

At every fifth test, the video of the cutter deployment recorded with the high speed camera was saved for image tracking analysis using ProAnalyst. Identical to the 3-bladed cutter procedure, black hockey tape and dots of white marker were used providing an effective contrast for ProAnalyst to automatically track the motion of the blade. Seen in Figure 7.16, a strip of black hockey tape was adhered to the top edge of the blade that would contact the magnet and then marked with a white dot. Marking the bolt bottom face in white identified the cutter's axis of rotation. A patch of black hockey tape was also adhered to the front cover and marked with a white dot to provide the third point needed to perform an angle measurement. All the dots were tracked without travelling off target at any time, as noted by the smooth arc in Figure 7.16(b). Recall from Section 7.2

(a) (b)

Figure 7.16 Top view of 4-bladed cutter assembly with selected regions for image tracking. (a) Start time of deployment. (b) End time of deployment.

that to prevent from dislodging upon impact, the stronger magnet of 102.3 N pull force used in the tests with the 4-bladed cutter had to be duct taped to the load cell, which can be seen in these photographs as well.

As mentioned a few times in this section, the 4-bladed cutter does not stick, but lifts slightly off the magnet after the first impact. At approximately every fifth test, the angular displacement of the cutter was analyzed. The bounce effect is captured as a small valley in the angle/time response as depicted in Figure 7.17, but the maximum misalignment from the 90 degree position is only 5 degrees in the worst cases. The settling time as a result is not significantly higher than the time of the initial hit, as was indicated by their respective confidence intervals. Also, with such a small degree of bounce, the cutter did not regain enough kinetic energy to bounce again on the second hit, but stuck on impact.

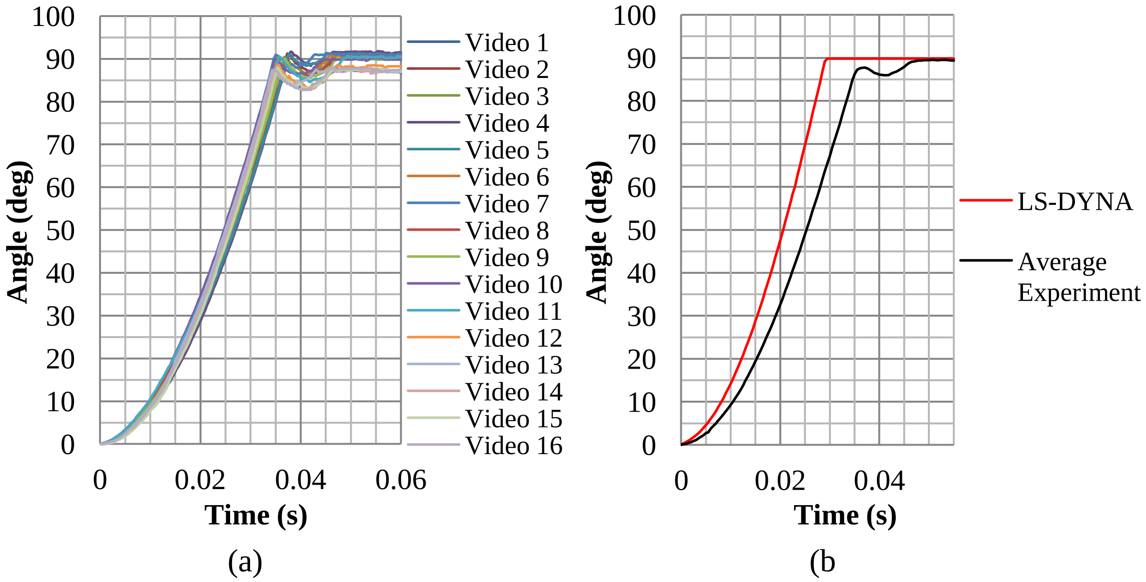

Figure 7.17 Angular position of the 4-bladed cutter vs. time. (a) ProAnalyst tracking data. (b) Average experimental response and numerical simulation.

To ensure that the angle/time response was not degrading with each passing test, the angle/time profile for each video was compared with that of the first video in a cumulative error calculation. Since the first video was the nearest to its freshly polished state, it was considered to be the accepted average response. Similar to the 3-bladed cutter, the cumulative error of the angle/time response for the 4-bladed cutter in

Figure 7.18 fluctuates steadily with an average of 7.2 %, indicating no trend in progressive degradation.

Experimentally, recall the high speed camera only starts recording when the pin has fully disengaged the cutter. Therefore, to compare fairly, the LS-DYNA angle/time response shown in Figure 7.17(b) has been offset 4 ms backward in time because the solenoid requires 4 ms to fully disengage the Teflon pin from the cutter. The angle/time response predicted numerically for the 4-bladed cutter has a lower validation metric of 0.70 than the model for the 3-bladed cutter, which was 0.78. In other terms, the cumulative error from Eq. 7.4 is 30 %, and the cumulative error using Eq. 7.1 is 35.4 %. Note from Figure 7.17(b) that the model already diverges from the average experimental early on in the rotation. Numerically, the cutter rotates faster than it does experimentally right from the moment the sliding pin has been disengaged. Conversely, the model for the 3-bladed cutter in Figure 7.9(b) matches closely with the experimental for the first 20 degrees of rotation before progressively slowing down. One qualitative reason for this difference is the level of plastic deformation of the plate indicated by the area of gouging marks by each cutter in Figure 7.11(a). The lower validation metric of 0.70 for the

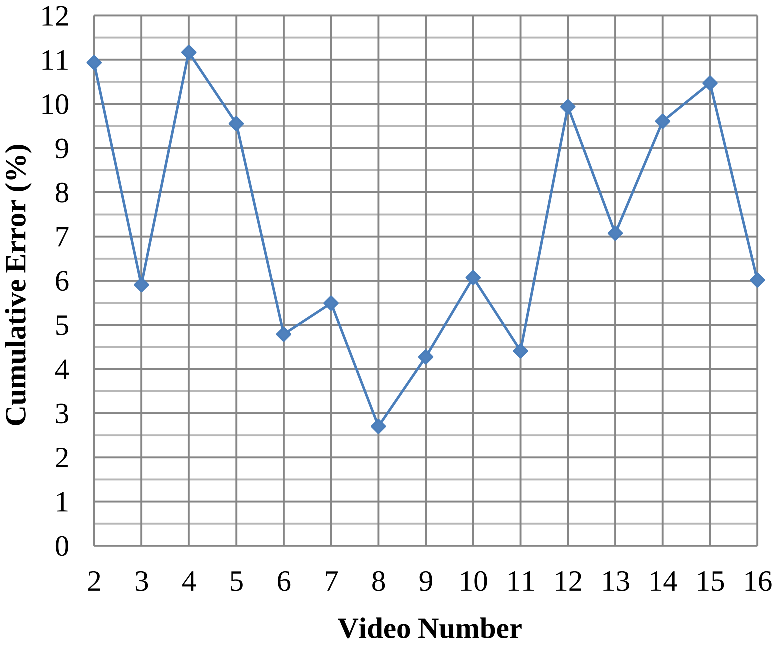

Figure 7.18 Cumulative error in the angle/time response using Video # 1 as the accepted average for the 4-bladed cutter.

4-bladed cutter is attributed to the higher frictional energy loss particular to chip formation and slight bounce not accounted for in the model. If this experimental setup was modified using the actual back cover steel material (not aluminum), and the magnet lodged in a thick corner of metal to increase its holding force, the 4-bladed cutter would likely not scratch the back cover and also possibly stick on impact, thus better agreeing with the LS-DYNA pre-cutting simulation. The energy loss associated with this experiment is quantified in Section 7.4 to demonstrate its negative effect on the angle/time predictions for both cutters.

7.4 Experimental Kinematics, Dynamics, and Energy Losses For the 3-Bladed Cutter and 4-Bladed Cutter

Kinematic and dynamic parameters for each cutter were determined from known measureable quantities to find out whether these parameters have any correlation with each cutter's angle/time validation metrics. First, using the average angle/time response for each cutter, a 3rd order curve fitting technique was used to have the angle as a function of time of the form

$$Angle\ (t) = a_3 t^3 + a_2 t^2 + a_1 t + a_0 \qquad \text{Eq. 7.5}$$

Where the 4 unknown constant coefficients a_i are solved simultaneously in 4 linear equations. The first and second derivatives of this polynomial are taken and describe the angular velocity and angular acceleration as a function of time, respectively. Although ProAnalyst could plot the angular velocity and angular acceleration directly from the angular tracking measurements, taking numerical derivatives of the angle/time measurements between each frame usually results in jagged profiles of the velocity and acceleration, which are poorly represented. Smoother angular velocity and angular acceleration profiles are achieved by first curve fitting the angle/time data and differentiating accordingly.

The curve fits for both cutters appear to be modeled with an appropriate cubic polynomial as noted by the near overlap of the curve fit with the experimental data in Figures 7.19(a) and (c). The R^2 values of the curve fit angle/time responses compared with the experimental angle/time responses are 0.99993 for the 3-bladed cutter and 0.99995 for the 4-bladed cutter. Figure 7.19(b) indicates for the 3-bladed cutter that

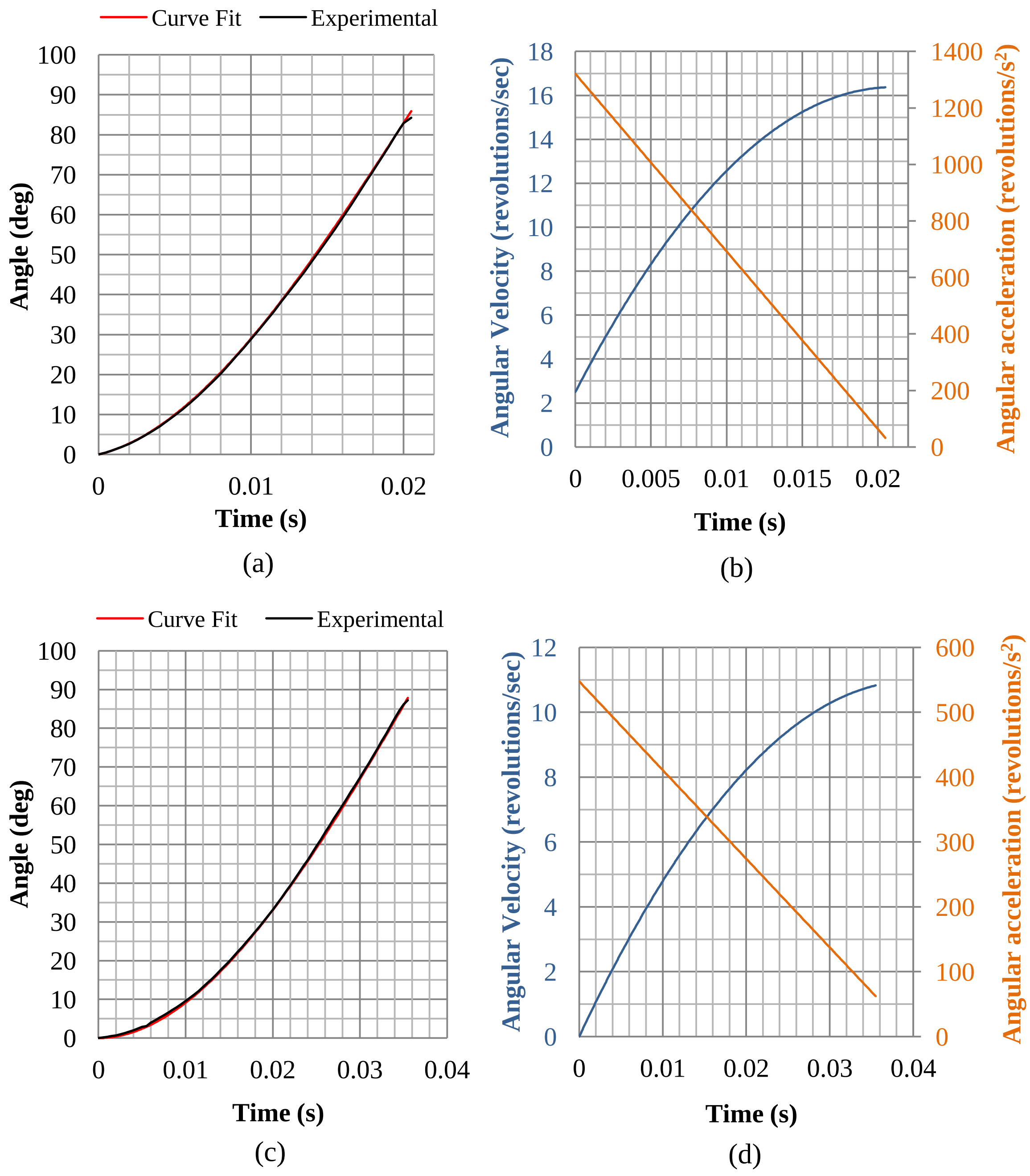

(a) (b)

(c) (d)

Figure 7.19 Cubic spline curve fit of angle/time response and its derivatives for the 3-bladed cutter (a and b) and the 4-bladed cutter (c and d).

though the cutter is accelerating throughout its rotation, it approaches a terminal velocity by the time it strikes the magnet. The 4-bladed cutter on the other hand does not taper off in angular velocity as the angular acceleration does not approach zero by the time it contacts the magnet. This leftover acceleration of 60 rev/sec^2 in (d) may contribute to the fact that the 4-bladed cutter does not stick to the magnet upon the first impact. Note as well that the 3-bladed cutter begins with a much more significant amount of acceleration than the 4-bladed cutter, but that acceleration dies down rapidly in time. The driving force slowing down the 3-bladed cutter more effectively than the 4-bladed cutter is not really understood. A speculation is that since the rotational kinetic energy of the 3-bladed cutter is lower than for the 4-bladed cutter, and both cutters slide on the same surface, a smaller rotation angle is required to dissipate the 3-bladed cutter's kinetic energy in the form of frictional sliding.

Based on the angular velocity and acceleration responses, one can compute the instantaneous rotational kinetic energy defined as

$$KE_{rot\ i} = \frac{1}{2}\, I_{bolt\ axis}\omega_i^2 \qquad \text{Eq. 7.6}$$

and the instantaneous inertia torque of the cutter defined as

$$T_{cutter\ i} = I_{bolt\ axis}\alpha_i \qquad \text{Eq. 7.7}$$

where $I_{bolt\ axis}$ is the mass moment of inertia of the cutter about an axis passing through the ½ in bolt, ω_i is the angular velocity at the instant of time i, and α_i is the angular velocity at the instant of time i. The mass moment of inertia about the bolt axis was measured in CATIA V5 by assigning the cutter its material (steel) and specifying the reference axis. These values are 8.01 x 10^{-5} kg·m^2 and 2.614 x 10^{-4} kg·m^2 for the 3-bladed cutter and 4-bladed cutter, respectively.

From Figure 7.20(a), beyond 5 degrees, the rotational kinetic energy of the 4-bladed cutter is increasingly larger than that of the 3-bladed cutter. By the end of rotation, the kinetic energy of the 4-bladed cutter is nearly 50 % larger. This substantial difference in rotational kinetic energy would agree with the higher degree of gouging in the plate from the 4-bladed cutter. The inertia torque provides a similar conclusion as throughout the entire range of rotation, the 4-bladed cutter has a higher inertia torque than the 3-bladed cutter. The difference between the inertia torques of both cutters also appears constant with increasing angular displacement.

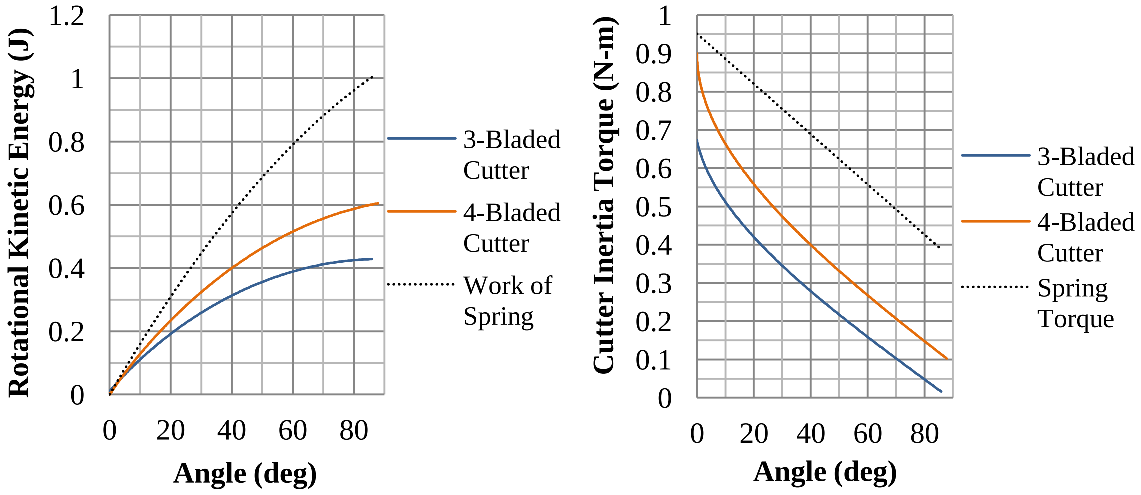

(a) (b)

Figure 7.20 Energy and torque vs. angular displacement for both cutters. (a) Rotational kinetic energy. (b) Inertia torque.

The higher extent of gouging in the plate for the 4-bladed cutter compared to the 3-bladed cutter, as previously depicted in Figure 7.11(a), was attempted to be quantified using analytical approaches: one approach is a torque balance, and the other is an energy balance. The instantaneous frictional torque at every angular position between the plate and cutter could be computed based on a one dimensional free body diagram resulting in the following equation:

$$T_{frict\ i=}\ k_t\left(\theta_{preload}-\theta_i\right)-\ I_{bolt\ axis}\alpha_i \qquad \text{Eq. 7.8}$$

Where k_t is the torsion spring stiffness known from the manufacturer's data specifications to be 0.376 N-m/rad, $\vartheta_{preload}$ is the angle of the torsion spring at the beginning of the cutter rotation (145 deg or 2.503 rad), ϑ_i is the angle of rotation at index i, and the other terms were described earlier in this section.

This analytical equation is likely invalid since the area of contact is not uniform, but localized in some areas with the sharp corners of the cutter, resulting in plastic deformation of the plate. Ignoring other possible forces that may be present in the aluminum chip or debris formation, the frictional torque calculation is misrepresented by assuming it is equal to the instantaneous spring torque subtracted by the instantaneous cutter inertia torque. Since both cutters are driven by the same torsion spring with the same preload, the cutter with the higher inertia torque will have a lower frictional torque.

So according to this computation, the frictional torque is higher for the 3-bladed cutter than the 4-bladed cutter. This result seems contradicting because the validation metric for the angle/time response was lower for the 4-bladed cutter than the 3-bladed cutter, and the level of plastic deformation on the plate is more severe for the 4-bladed cutter. However, an internal energy component associated with chip formation is ignored in the LS-DYNA model that is occurring in this experimental setup. The rotational kinetic energy and inertia torque, both of which are higher for the 4-bladed cutter than for the 3-bladed cutter, would suggest that chip formation present in this experiment is more prone with the 4-bladed cutter.

Energy loss at each state in the cutter's rotation could be lumped into a term in the following energy balance:

$$T_1 + V_1 = T_i + V_i + E_{Loss\ i}$$

Where T_1 and V_1 are the initial kinetic and potential energies of the system, respectively, and T_i and V_i are the kinetic and potential energies at each index in the cutter's rotation. Since the cutter begins from rest, the initial velocity is zero and so T_1 is zero. Thus,

$$E_{loss\ i} = V_1 - V_i - T_i$$

Expanding the terms, the energy loss would be

$$E_{loss\ i} = \frac{1}{2}k_t\left(\theta_{preload}\right)^2 - \frac{1}{2}k_t\left(\theta_{preload} - \theta_i\right)^2 - \frac{1}{2}I_{bolt-axis}\omega_i^2 \quad \text{Eq. 7.9}$$

The problem with this equation is that it too is misleading. Since both cutters are driven by the same torsion spring and preload, noted by the dotted line in Figure 7.20(a), the cutter with the smaller rotational kinetic energy will have higher "energy loss". Again, the 3-bladed cutter would have the higher loss for the entire angular range. However, neither the solution from Eq. 7.8 or Eq. 7.9 explains why the angle/time response from the LS-DYNA model for the 4-bladed cutter has a lower validation metric than for the 3-bladed cutter. Since friction is included in the numerical simulations anyway, the cutter with the higher "energy loss" does not necessarily indicate the cutter with an angle/time response that will deviate the most from the numerical prediction. This energy loss would have to be broken down further into specific forms of loss. One speculates that a portion of the energy loss could be surface to surface friction (mild wear) and another portion to chip formation (severe wear). Although each form of loss is difficult to quantify, based on the photographic evidence in Figure 7.11(a), the energy of chip formation is believed to be more significant for the 4-bladed cutter. Therefore, although the total energy loss for the 4-bladed cutter is smaller, a larger portion of that loss could be chip formation whereas for the 3-bladed cutter, a larger portion could be surface to surface friction.

Furthermore, there may be other kinetic energy sources such as axial vibration, and the motion of the spring that add linear kinetic energy terms, which would make the energy loss of Eq. 7.9 incorrect. Viewing the cutter from the top, the camera lens is in a poor orientation to detect axial vibration, but perhaps at a much higher frame rate, and viewed from a side view instead, the cutter may be seen to have axial vibration as it rotates. Even with a perfectly flat plate surface, the cutters in the LS-DYNA models do indicate a small amount of this axial vibration. For either cutter, the axial velocity only reaches a peak of 75 mm/s and even considering the 4-bladed cutter’s mass of 0.37 kg, the linear kinetic energy does not contribute much to the total kinetic energy. Experimentally on the other hand, the vibration on a rough surface could be more violent because the surface is not perfectly flat and may contribute a non negligible amount to the kinetic energy.

Though the spring does not have much mass, it has some play around the bolt shaft so that it can both rotate and move linearly off-axis. According to the pre-cutting models in LS-DYNA, the kinetic energy of the rigid loop (representing the last coil of the spring) has more than 10% of the 3-bladed cutter's kinetic energy. If the mass and velocity of all 8 coils of the spring are considered, this energy could be more significant. For the 4-bladed cutter, the kinetic energy of the rigid loop and arm is about 5% of the 4-bladed cutter's kinetic energy.

Ultimately, both cutters have respectable validation metrics for the angle/time response being 0.78 and 0.70 for the 3-bladed cutter and 4-bladed cutter, respectively. The deviation from the LS-DYNA model is most strongly associated with the high level of friction between the P20 steel and the aluminum plate experimentally. Numerically, contact between two hard steel surfaces with lubrication was assumed, where no scratching of surfaces would be expected. The lower validation metric for the 4-bladed cutter is speculated to be due to the deeper gouging into the plate, particularly from the sharp corners of the blade, lagging the cutter’s angular speed. The 3-bladed cutter also gouged the plate, but to a lesser extent, and so is speculated to be the reason the angular speed matched more closely with its numerical prediction. Energy loss was quantified in Eq. 7.9, and indicated by the area between the spring work and rotational kinetic energy for each cutter in Figure 7.20(a). A contradicting result was found that the 4-bladed cutter had a lower energy loss than the 3-bladed cutter. However, this energy loss would have to be divided into more specific terms, namely mild and severe wear. The friction of chip formation would constitute a larger portion for the 4-bladed cutter and be expected to hinder its angular speed more than the average surface-to-surface friction with the plate.

Tests should be done using the actual back cover material (hard steel) and a thick support block for the magnet in order to have a stronger hold than on the thin 3 mm impact cap. The response time can be better assessed with the actual materials and components of the adaptive cutting device. The cutters are expected to perform no worse, only better than they did in this experimental setup.

8.0 TEST PLAN FOR FUTURE CUTTING EXPERIMENTS

This chapter explains how the test plan is developed for dynamic axial cutting using the quadrotor adaptive cutter, which will be conducted in the future, but not as part of this thesis. The two key details necessary to develop the test plan are:

1. The range of impact speeds used for each blade number configuration.
2. An appropriate AA6061-T6 extrusion thickness to obtain sufficient axial cutting deformation in each blade number configuration.

The carriage on the low energy droptower, designed by Dr. W. Altenhof, and available in the Structures lab at the University of Windsor, has a maximum velocity of 4.5 m/s without the assistance of the pneumatic mechanism. Therefore, if this droptower is used, the upper bound velocity for the 8-blade cutting configuration will be 4.5 m/s. To determine the optimal velocity ranges for the 3 cutter configurations, the steps outlined next must be followed.

The carriage's kinetic energy at impact and the internal energy from axial cutting must be in balance, as shown in Eq. 8.1:

$$0.5 m_c v^2 = F_c l \qquad \text{Eq. 8.1}$$

m_c: Mass of the crosshead (59.1 kg)
v: Velocity of crosshead at impact
F_c: Cutting force
l: Length of cut

This equation is rearranged to solve for the length of cut as

$$l = \frac{0.5 m_c v^2}{F_c} \qquad \text{Eq. 8.2}$$

The cutting force is calculated from the analytical model presented in Eq. 2.1. For convenience, it is repeated here:

$$F_c = (n + 4\mu cos\zeta cot\theta) \cdot \left[\frac{\pi}{\sqrt{3}} \frac{\sigma_0 t^2 r_m}{n R_{axial}} + \frac{2}{\sqrt{3}} \sigma_0 T t + \frac{\sigma_0 t^2}{2\sqrt{3}} (B + R_r) \cdot \left(\frac{1}{R_r cos\theta} + \frac{1}{r_0 + r_m} + \frac{1}{r_m + r_i} \right) \frac{4}{\sqrt{3}} \sigma_0 t B \theta + 0.366 \sigma_0 t R_r cos^2\theta \cdot (1 + 0.55\theta^2) \right] \qquad \text{Eq. 2.1}$$

The analytical cutting model highly underestimates the cutting force when using more than 5 blades ($n > 5$). A more realistic estimate of the cutting force with 6 blades is to use the computed value of F_c with 4 blades and multiply by a factor of 1.35.

$$F_{c(6\ blades)} = 1.35 * \ F_{c\ (4\ blades)} \qquad \text{Eq. 8.3}$$

A more realistic estimate of the cutting force with 8 blades is to use the computed value of F_c with 4 blades and multiply by a factor of 1.70.

$$F_{c(8\ blades)} = 1.70 * \ F_{c\ (4\ blades)} \qquad \text{Eq. 8.4}$$

The only unknown information in Eq. 2.1 is the thickness and outer diameter of the extrusion. Since the cutting force is not sensitive to the outer diameter, it is assumed to be 44.45 mm, the smallest diameter to be tested using the device. However, the cutting force is highly sensitive to the extrusion thickness, and must be selected. Selecting an appropriate thickness is critical because too thick an extrusion will result in very little axial deformation for the higher blade number configurations. The typical extrusion length is 180 mm, but the axial length of cut will not be close to this value unless the specimen is much too thin. Instead, a shorter baseline axial distance should be used (for example: 55 mm) to determine the range of velocities and be able to fairly compare the 3 cutting configurations. In order to select the extrusion thickness and appropriate velocity ranges for each configuration, the calculated length of cut l in Eq. 8.2 must be the same for the upper bound velocities in each configuration, explained next.

Assuming a thickness of 0.75 mm, the cutting force with 4 blades in Eq. 2.1 is 6.65 kN. So, the cutting force with 8 blades in Eq. 8.4 is 11.30 kN. For 8 blades, the length of cut at the upper bound velocity of 4.5 m/s is equal to 53 mm. Therefore, the upper bound velocity for the 6-blade configuration, which is also equal to the lower bound velocity for the 8-blade configuration, must result in a length of cut that is approximately 53 mm. In addition, the upper bound velocity for the 4-blade configuration, which is also equal to the lower bound velocity for the 6-blade configuration, must result in a length of cut that is approximately 53 mm.

Table 8.1 Appropriate values of extrusion thickness and velocities (in green) for each blade number configuration.

Common to All 3 Configurations				
Symbol	**Description**	**Value**	**Unit**	**Comments**
m_c	Mass of crosshead of low energy droptower	59.10	kg	Known value
t	Thickness of extrusion	0.75	mm	Selected value
4-Blade Configuration				
Symbol	**Description**	**Value**	**Unit**	**Comments**
$v_{up(4)}$	Upper bound of impact velocity	3.40	m/s	Selected value
$KE_{up(4)}$	Upper bound of kinetic energy of crosshead before impact	341.60	J	Computed from $0.5 \cdot m_c \cdot v_{up(4)}^2$
$F_{c(4)}$	Cutting force	6.65	kN	Computed from Eq. 2.1
$l_{up(4)}$	Upper bound length of cut	51.40	mm	Computed from Eq. 8.2
6-Blade Configuration				
Symbol	**Description**	**Value**	**Unit**	**Comments**
$v_{low(6)}$	Lower bound of impact velocity	3.40	m/s	Equals upper bound velocity for 4 blade
$v_{up(6)}$	Upper bound of impact velocity	4.00	m/s	Selected value
$KE_{low(6)}$	Lower bound of kinetic energy of crosshead before impact	341.60	J	Computed from $0.5 \cdot m_c \cdot v_{low(6)}^2$
$KE_{up(6)}$	Upper bound of kinetic energy of crosshead before impact	472.80	J	Computed from $0.5 \cdot m_c \cdot v_{up(6)}^2$
$F_{c(6)}$	Cutting force	8.97	kN	Computed from Eq. 8.3
$l_{low(6)}$	Lower bound length of cut	38.07	mm	Computed from Eq. 8.2 using $KE_{low(6)}$
$l_{up(6)}$	Upper bound length of cut	52.70	mm	Computed from Eq. 8.2 using $KE_{up(6)}$
8-Blade Configuration				
Symbol	**Description**	**Value**	**Unit**	**Comments**
$v_{low(8)}$	Lower bound of impact velocity	4.00	m/s	Equals upper bound velocity for 6 blade
$v_{up(8)}$	Upper bound of impact velocity	4.50	m/s	Max velocity of low energy droptower
$KE_{low(8)}$	Lower bound of kinetic energy of crosshead before impact	472.80	J	Computed from $0.5 \cdot m_c \cdot v_{low(8)}^2$
$KE_{up(8)}$	Upper bound of kinetic energy of crosshead before impact	598.39	J	Computed from $0.5 \cdot m_c \cdot v_{up(8)}^2$
$F_{c(8)}$	Cutting force	11.30	kN	Computed from Eq. 8.4
$l_{low(8)}$	Lower bound length of cut	41.85	mm	Computed from Eq. 8.2 using $KE_{low(8)}$
$l_{up(8)}$	Upper bound length of cut	52.96	mm	Computed from Eq. 8.2 using $KE_{up(8)}$

Table 8.1 summarizes the calculation steps followed to determine the extrusion thickness and velocity ranges. The only parameters selected are indicated by the green

cells, namely the extrusion thickness, the upper bound velocity for the 4-blade configuration, and the upper bound velocity for the 6-blade configuration. Note the lower bound velocity for the 6-blade configuration is equal to the selected upper bound velocity for the 4-blade configuration. Also, the lower bound velocity for the 8-blade configuration is equal to the selected upper bound velocity for the 6-blade configuration. Choosing an extrusion thickness of 0.75 mm and an upper bound velocity of 3.4 m/s for the 4-blade configuration gives a cut length of 51.4 mm. With this same extrusion thickness, choosing an upper bound velocity of 4 m/s for the 6-blade configuration gives a cut length of 52.7 mm.

Based on the crosshead mass of 59.1 kg, an AA6061-T6 extrusion thickness of 0.75 mm, and approximately 50 to 55 mm of axial cut length, the range of velocities for each blade configuration are as shown in Table 8.2. The column titled "trigger distance" indicates the minimum distance the dropping impact plate must be from the top of the extrusion if the cutter configuration is to be deployed in time. For the case of 4 blades, no solenoid is activated, so a trigger distance is not applicable. To compute the distances for 6 blades and 8 blades, the following formulas are applied:

Table 8.2 Range of impact velocities and distance the dropping impact plate must be from top of extrusion to activate configuration in time. Velocities based on 0.75 mm AA6061-T6 extrusion thickness, 59.1 kg crosshead, and approximately 53 mm axial length of cut.

Range of Velocities (m/s)	Optimal Configuration	Trigger Distance (m)
$0.0 < v <= 3.4$	4 Blades	N/A
$3.4 < v <= 4.0$	6 Blades	0.13
$4.0 < v <= 4.5$	8 Blades	0.32

$$Trigger\ distance\ (6\ blades) = v_{up(6)} \cdot t_{3-bl\ cutter} \cdot SF \qquad \text{Eq. 8.5}$$

$$Trigger\ distance\ (8\ blades) = v_{up(8)} \cdot t_{4-bl\ cutter} \cdot SF \qquad \text{Eq. 8.6}$$

where $v_{up(6)}$ is the upper bound velocity in the 6-blade configuration (4 m/s), $t_{3\text{-}bl\ cutter}$ is the experimental response time of the 3-bladed cutter (20.5 ms), $v_{up(8)}$ is the upper bound velocity in the 8-blade configuration (4.5 m/s), $t_{4\text{-}bl\ cutter}$ is the experimental response time of the 4-bladed cutter (47 ms), and *SF* is a chosen safety factor (1.5). The safety factor could be increased if desired because the velocity of the crosshead will not change significantly over the short distance of 32 cm.

Table 8.3 is provided to illustrate the benefit of having 3 cutter configurations. Assuming the extrusion to be 55 mm in length, note that if the 4-blade configuration is used for velocities above 3.4 m/s, the axial length of cut would exceed the total extrusion length. Therefore, 6 blades or 8 blades must be used for velocities above 3.4 m/s. However, above 4 m/s, the 6-blade configuration will result in an axial length of cut exceeding the total extrusion length. In addition, the energy dissipation is more effective using 6 blades for speeds between 3.4 m/s and 4 m/s. The reason is that if the 8-blade configuration is selected instead of the 6-blade configuration for impact speeds below 4 m/s, the length of cut is shorter and the cutting force is higher: At 3.4 m/s for example, the length of cut is shorter by 8 mm, and the cutting force is higher by 2.3 kN.

Table 8.3 Axial length of cut for each blade configuration and impact velocity. Velocities based on 0.75 mm AA6061-T6 extrusion thickness, 59.1 kg crosshead, and approximately 53 mm axial length of cut.

Configuration	**Impact Velocity (m/s)**			**Cutting Force (kN)**
	3.4	4	4.5	
	Axial cutting displacement (mm)			
4 blades	51.4	🟥 71.14	🟥 90.04	6.65
6 blades	38.07	52.7	🟥 66.69	8.97
8 blades	🟨 30.23	41.85	52.96	11.3

Red cells indicate extrusion is cut through entirely if it is 55 mm long
Yellow cell indicates ineffective energy dissipation because it is the product of a higher cut force and shorter axial deformation

Since the droptower has a limited energy capability, the benefit of the 3 configurations is not clearly obvious from Table 8.3. Based on those results, the adaptive cutter may just as well have the configuration of 4 blades or 8 blades. However, if the carriage had a larger mass, say 200 kg, and a maximum possible velocity of 13 m/s, then the energy capability would be substantially higher. A thicker AA6061-T6 extrusion could be tested and a depth of cut longer than 53 mm could be used as a baseline to compare the 3 cutting configurations. Applying the same calculation steps summarized in Table 8.1, but substituting the crosshead mass to be 200 kg, the AA6061-T6 extrusion thickness to be 3.175 mm, and aiming for a 180 mm depth of cut, the new range of velocities would be as shown in Table 8.4. For these thicker extrusions, the 6-blade configuration is beneficial over a larger range of velocities (1.5 m/s) than for the thinner extrusions in Table 8.2 (0.6 m/s). In terms of length of cut, the benefits of the 3 blade configurations are better illustrated from Table 8.5. The 4-blade configuration cannot be used above 9.2 m/s as the extrusion will be cut entirely through. If the 8-blade configuration is selected instead of the 6-blade configuration at speeds below 10.7 m/s, length of cut is shorter and the cutting force is higher: at 9.2 m/s for example, the length of cut is shorter by 28 mm and the cutting force is higher by 16.5 kN. Therefore, for the case of thicker AA6061-T6 extrusions and higher energy capability, 3 possible cutting configurations (4, 6, or 8 blades) is clearly beneficial, whereas thinner AA6061-T6 extrusions subject to low energy impacts do not show a major advantage to having the 6-blade configuration.

Table 8.4 Range of impact velocities and distance the dropping impact plate must be from top of extrusion to activate configuration in time. Velocities based on 3.175 mm AA6061-T6 extrusion thickness, 200 kg crosshead, and approximately 180 mm axial length of cut.

Range of Velocities (m/s)	**Optimal Configuration**	**Trigger Distance (m)**
0.0 < v <= 9.2	4 Blades	N/A
9.2 < v <= 10.7	6 Blades	0.34
10.7 < v <= 12.0	8 Blades	0.85

Table 8.5 Axial length of cut for each blade configuration and impact velocity. Velocities based on 3.175 mm AA6061-T6 extrusion thickness, 200 kg crosshead, and approximately 180 mm axial length of cut.

Configuration	**Impact Velocity (m/s)**			**Cutting Force (kN)**
	9.2	10.7	12	
	Axial cutting displacement (mm)			
4 blades	179.83	243.25	305.94	47.07
6 blades	133.21	180.18	226.63	63.54
8 blades	105.78	143.09	179.97	80.01

Red cells indicate extrusion is cut through entirely if it is 180 mm long

Yellow cell indicates ineffective energy dissipation because it is the product of a higher cut force and shorter axial deformation

9.0 SUMMARY AND CONCLUSIONS

This thesis presented the design and analysis of a cutting device that adaptively adjusts the number of blades in three possible configurations (4, 6, or 8 blades) to axially cut AA6061-T6 aluminum extrusions as a way to dissipate kinetic energy of varying magnitudes effectively. Several design approaches were explored for the mechanics of the blade concealment and deployment. A device with blades that rotate about an axis parallel to the extrusion's longitudinal axis was deemed the best approach because the deployment mechanism was the simplest of all considered. Additionally, the blade volumes can be larger and thus more resistant, space is available for the torsion spring to have more coils making it stiffer and resulting in a faster response time, and the device can be made with fewer and simpler parts. To electronically trigger the blades immediately prior to impact, the use of 4 common pull type solenoids to pull out 4 locking pins (one for each cutter) is more economical and reliable than a complex locking/unlocking mechanism with a single, more expensive solenoid that translates or rotates in three different possible positions. The design, referred to as the quadrotor adaptive cutter, has a relatively simple construction, considering that it must not only deploy one of three possible equally spaced configurations very quickly, but must withstand a severe impact load, accommodate load cells for experimental measurement, and best avoid contact with the extrusion petals as they flare significantly when cutting with 6 or 8 blades. Virtual simulations of the quadrotor demonstrated a good overall performance: given the expected impact speeds, the response times for both cutter geometries were acceptably short. Specifically, the cutters need only be deployed when the dropping crosshead reaches a distance from the extrusion short enough to not accelerate/decelerate suddenly within that remaining distance. Also, all the parts in the quadrotor prior to cutting have negligible stresses, while during cutting still have the durability to survive a few ten thousand cycles at least. Based on the findings of this thesis, the quadrotor is worth constructing to perform dynamic axial cutting experiments.

The key conclusions from the numerical modeling aspect of this thesis are as follows:

1. The blade spacing must be equal about the circumference of the device (not only symmetric about two axes), to avoid blade twisting under the cutting load.
2. A neodymium magnet is necessary to prevent the cutter from bouncing off of the end stop of the L-block, thus reducing the total response time.
3. The stresses on the parts during cutting are highest in the 8-blade configuration, and most severely affect the 3-bladed cutter, 4-bladed cutter, ½ in bolts, and back cover. The highest stresses in the device are at the blade roots of the two 4-bladed cutters as each support 3/8 of the cutting force when using the 8-blade configuration.
4. The part with the shortest fatigue life is the back cover being 36,000 cycles, followed by the 4-bladed cutter being 51,000 cycles, and the 3-bladed cutter being 98,000 cycles. All other parts have 100,000 cycles to failure or more, and in some cases, infinite lives.

The key conclusions from the experimental results of the blade deployment apparatus are as follows:

1. The 3-bladed cutter consistently stuck on the first impact with the plastic-coated neodymium magnet having the 31.1 N pull force, resulting in an angle/time response with a validation metric of 0.78 between the numerical model and the average experimental.
2. The 4-bladed cutter bounced slightly on impact with the nickel-copper-nickel coated neodymium magnet having the 102.3 N pull force, resulting in an angle/time response with a validation metric of 0.70 between the numerical model and the average experimental.
3. The surface condition of the base plate representing the back cover is critical to the performance of the device. Sanding and polishing of the plate was necessary to minimize bouncing in the 4-bladed cutter. However, the actual adaptive cutter should not experience the gouging effect seen experimentally

as the back cover will be made of SAE steel grade 1050M 54 HRC, a material much harder than aluminum.

4. The response times of the 3-bladed cutter and 4-bladed cutter were 20.5 ms and 47 ms, respectively, both having narrow 99% confidence intervals. With a safety factor of 1.5, the solenoids would need to be activated when the dropping crosshead on the low energy droptower is at least 32 cm away from the top of the extrusion.
5. For both cutters, the peak impact loads were found to lie within narrow 99% confidence intervals: 4.29 kN to 4.39 kN for the 3-bladed cutter, and 4.36 kN to 4.56 kN for the 4-bladed cutter. These measured loads are far from magnitudes that would result in plastic deformation of the blade upon contact with the magnet, especially when using SAE steel grade 9254 Al Rc58 for the cutters.

10.0 RECOMMENDATIONS FOR FUTURE WORK

The following recommendations are possible areas of future research opportunities to further develop with regards to adaptive cutting:

1. The simplified blade deployment apparatus could incorporate the linear solenoid to determine whether it is strong enough to pull out the sliding pin. A pin made of Teflon instead of steel would be needed because the friction would be too high for the solenoid to overcome.
2. A fixed cutter developed in [10] having either 6 blades or 8 blades, could be mounted on a specially designed tube and stand that will prevent the extrusion petals from flaring in an axial cutting test. The numerical models for the 8-blade configuration in Appendix G indicated the force/time response would continuously increase if flaring was hindered, but that may not be the case in reality. If cutting is still possible without having the cutting tool and extrusion bind together, and the experimental force/displacement response is acceptable, a similar tube could be incorporated into the quadrotor device to avoid petal flaring. With this modification, the petals would not interfere with the underside of the device, and the support legs on the quadrotor adaptive cutter could also be removed.
3. The quadrotor adaptive cutter can be manufactured, assembled, and tested experimentally.
4. The locations where to mount the laser displacement transducers to obtain the real-time displacement of the droptower crosshead for dynamic axial cutting tests using the quadrotor device must be determined.
5. The LabVIEW program that will acquire the load and crosshead displacement data, control the solenoids using the electronic hardware from Appendix C, and trigger a high speed camera to start and stop recording a dynamic adaptive cutting test must be written.
6. Digital image correlation (DIC) to measure the strain in the cutting device during a dynamic axial cutting test could be included.

7. The shape of the blades could be tapered radially upward, which could aid in self-centering the extrusion in off-axis impacts.
8. A new adaptive cutter design that makes it possible to have a central hub like the fixed cutters in [10] to increase the bending resistance of the blades could be considered. Revisiting the design of Figure 4.12, two opposing fixed blades could be made into a single piece having a central hub. For the remaining 6 blades, rather than having 4 switchblades and 2 other fixed blades, a set of moving blades could slide radially inward and join the central hub.
9. Another design consideration may be to use a coil of copper wire around the bolt shaft and rely on electromotive force to drive the 3-bladed cutter and 4-bladed cutter in the quadrotor device. The design would do away with torsion springs, solenoids, and locking pins. LS-DYNA has an electromagnetic solver [55, 56, 57] and has the capability of coupling electromagnetism with structural mechanics [58, 59, 60, 61]. If such a design using current control is possible, the blade response times could be much faster, being practical for higher velocity impacts such as blast loads.
10. A spring-loaded latch could be devised to prevent the 4-bladed cutter in the quadrotor from bouncing off of the magnet. However, this approach is not recommended for a few reasons:
    a. The reaction time of the spring-loaded latch has to be remarkably fast. The instant the cutter has passed over the latch and hits the magnet, the latch must spring back out to lock the blade from bouncing. It is possible that the latch's reaction time will be too slow such that the cutter will bounce off the magnet surface and end up surpassing the latch before it has time to spring into position.
    b. The logical place to put a latch is through the back cover such that the bottom edge of the cutter as it rotates will trip the latch down. The spring would then push the latch back up to lock the cutter. But drilling holes in that area of the back cover for this latch should be avoided because that is near the area of the critical stress zone on the back cover. Another place for the latch could be below the front cover such that the top edge of the blade will push the latch

upward and the spring will push it back down once the cutter has surpassed the latch. However, the top half of the blade is tapered (not straight like the bottom half of the blade) and so the latch could move back up when the cutter moves in either direction, which prevents the cutter from locking.

   c. Sanding and polishing the plate demonstrated that the bounce effect for the 4-bladed cutter was minimal and the settling time is not detrimentally affected. For the range of impact speeds to be tested with the adaptive cutting device, the settling time of the 4-bladed cutter is acceptable. The impact plate will not have to be detected too far in advance as to be impractical.

11. Instead, if desired, to significantly improve the response time of either cutter, a direct-drive system should be employed rather than relying on the motion of the preloaded torsion spring. An alternative cutter design was partially developed in Appendix E. The belt-drive system in the adaptive cutter design of Figure 4.9 was revisited and combined with elements of the quadrotor adaptive cutter design. By using a servomotor to drive a belt/sprocket/gear system, the cutters can rotate directly as the servomotor rotates, resulting in a response time on the order of a few milliseconds rather than tens of milliseconds. The angular velocity profile of the servomotor can be programmed precisely to allow the cutters to turn the prescribed 90 degrees and decelerate near the end of rotation to prevent a vibratory response at the final position. The use of a belt also decouples the servomotor from the adaptive cutter and thus protects it from direct loads in a dynamic cutting test.

REFERENCES

1. "The Economic Burden of Injury in Canada", SMARTRISK, Toronto, ON, 2009.
2. "Global Status Report on Road Safety 2015", World Health Organization, Geneva, Switzerland, 2015.
3. "2014 Motor Vehicle Accidents: Overview", National Highway Traffic Safety Administration, Washington DC, PA, 2016.
4. "Canadian Motor Travel Collision Statistics 2014", Transport Canada, Catalogue No: T45-3E-PDF, ISBN: 1701-6223, 2016.
5. E. Kramarow, L.H. Chen, H. Hedegaard, and M. Warner, "Deaths From Unintentional Injury Among Adults Aged 65 and Over: United States, 2000-2013", National Center for Health Statistics Data Brief, No. 199, 2015.
6. J.A. Stevens, P.S. Corso, E.A. Finkelstein, and T.R. Miller, "The costs of fatal and nonfatal falls among older adults", *Injury Prevention*, Vol. 12, pp. 290-295, 2006.
7. "IHSA Member Injury Performance for 2014", 2014 Infrastructure Health and Safety Association Annual Report, 2014.
8. H. Fischer, "A Guide to U.S. Military Casualty Statistics: Operation Freedom's Sentinel, Operation Inherent Resolve, Operation New Dawn, Operation Iraqi Freedom, and Operation Enduring Freedom", Congressional Research Service, RS22452, 2015.
9. R. Audysho, "Aluminum foam core density and geometry influences on the deformation mechanisms and energy absorption capacity of foam filled braided tubular structures in axial and transverse loading", M. S. thesis, Department of Mechanical, Automotive, and Materials Engineering, University of Windsor, Windsor, ON, 2014.
10. W. Altenhof, S. Y. Jin, and A. Majumder, "Kinetic energy dissipation system for dissipating kinetic shock energy", U. S. Patent 8347775B2, Jan. 8, 2013.
11. Jin, S.Y., "Novel cutting deformation modes on axially loaded circular AA6061-T6 extrusions for superior crashworthiness performance", Ph. D. dissertation,

Department of Mechanical, Automotive, and Materials Engineering, University of Windsor, Windsor, ON, 2012.

12. W. Abramowicz and N. Jones, “Dynamic axial crushing of circular tubes”, *International Journal of Impact Engineering*, Vol. 2, no. 3, pp. 263-281, 1984.

13. W. Abramowicz and N. Jones, “Dynamic axial crushing of square tubes”, *International Journal of Impact Engineering*, Vol. 2, No. 2, pp. 179-208, 1984.

14. D. Karagiozova and M. Alves, “Transition from progressive buckling to global bending of circular shells under axial impact – Part I: Experimental and numerical observations”, *International Journal of Solids and Structures*, Vol. 41, No. 5-6, pp. 1565-1580, 2004.

15. M. Easton, A. Beer, M. Barnett, C. Davies, G. Dunlop, Y. Durandet, S. Blacket, T. Hilditch, and P. Beggs, “Magnesium Alloy Applications in Automotive Structures”, *Journal of the Minerals, Metals, and Materials Society*, Vol. 60, No. 11, pp. 57-62, 2008.

16. P. Shery, W. Altenhof, R. Smith, E. Beeh, P. Strassburger, and T. Gruenheid, "Experimental observations on the mechanical response of AZ31B magnesium and AA6061-T6 aluminum extrusions subjected to compression and cutting modes of deformation," *SAE Technical Paper* 2017-01-0377, 2017.

17. D.K. Leu, “The curling characteristics of static inside-out inversion of metal tubes”, *International Journal of Machine Tools & Manufacture*, Vol. 40, No. 1, pp. 65-80, 2000.

18. S. R. Reid, “Plastic deformation mechanisms in axially compressed metal tubes used as impact energy absorbers”, *International Journal of Mechanical Sciences*, Vol. 35, No. 12, pp. 1035-1052, 1993.

19. X. Huang, G. Lu, and T.X. Yu, “On the axial splitting and curling of circular metal tubes”, *International Journal of Mechanical Sciences*, Vol. 44, No. 11, pp. 2369-2391, 2002.

20. S.C.K. Yuen and G.N. Nurick, "The energy-absorbing characteristics of tubular structures with geometric and material modifications: An overview", *Applied Mechanics Reviews*, Vol. 61, No. 2, 2008.

21. N. Marshall and G.N. Nurick, "The Effect of Induced Imperfections on the Formation of the First Lobe of Symmetric Progressive Buckling of Thin-Walled Square Tubes", in *Structures Under Shock and Impact*, N. Jones, D.G. Talaslidis, C.A. Brebbia, and G.D. Manolis, Ed., United Kingdom: WIT Press, 1998, pp. 155–168.

22. C.A. Krauss and D.H. Laananen, "A parametric study of crush initiators for a thin-walled tube", *International Journal of Vehicle Design*, Vol. 15, No. 3/4/5, pp. 385-401, 1994.

23. Q. Cheng and W. Altenhof, "Load/displacement and energy absorption performances of AA6061-T6 tubes under a cutting deformation mode", *International Journal of Crashworthiness*, Vol. 10, No. 6, pp. 621-633, 2005.

24. S.Y. Jin, W. Altenhof, and T. Kapoor, "An experimental investigation into the cutting deformation mode of AA6061-T6 round extrusions", *Thin Walled Structures*, Vol. 44, pp. 773-786, 2006.

25. S.Y. Jin and W. Altenhof, "Experimental observations of AA6061-T6 round extrusions under a cutting deformation mode with a deflector", *International Journal of Crashworthiness*, Vol. 13, No. 2, pp. 127-138, 2008.

26. A. Majumder, W. Altenhof, V. Vijayan, and S.Y. Jin, "Quasi-static axial cutting of AA6061-T4 and T6 round extrusions", Proceedings of the Institution of Mechanical Engineers, Part L: Journal of Materials Design and Applications, Vol. 229, pp. 389-397, 2008.

27. S.Y. Jin and W. Altenhof, "An analytical model on the steady-state deformation of circular tubes under an axial cutting deformation mode", *International Journal of Solids and Structures*, Vol. 48, pp. 269-279, 2011.

28. Q. Cheng, and W. Altenhof, "Load/displacement and energy absorption performances of AA6061-T6 tubes under a cutting deformation mode", *International Journal of Crashworthiness*, Vol. 10, No. 6, pp. 621-633, 2005.

29. S.Y. Jin, A. Majumder, W. Altenhof, and D. Green, "Axial cutting of AA6061-T6 circular extrusions under impact using single and dual cutter configurations", *International Journal of Impact Engineering*, Vol 37, pp. 735-753, 2010.

30. S.Y. Jin, W. Altenhof, and Z. Li, "A parametric study on extrusion geometry and blade quantity during axial cutting deformation of circular AA6061-T6 extrusions under impact and quasi-static loading", *International Journal of Impact Engineering*, Vol. 49, pp. 165-178, 2012.

31. S.Y. Jin and W. Altenhof, "Control of load/displacement responses of AA6061 and T4 circular extrusions under axial compressive loads", *International Journal of Impact Engineering*, Vol. 38, pp. 1-12, 2011.

32. S.Y. Jin, and W. Altenhof, "Comparison of the load/displacement and energy absorption performance of round and square AA6061-T6 extrusions under a cutting deformation mode", *International Journal of Crashworthiness*, Vol. 12, No. 3, pp. 265-278, 2007.

33. "Crash avoidance systems rated", *The Globe and Mail*, Page D2, October 3, 2013.

34. T. Bielecki, J. Holnicki-Szulc, and L. Jezequel, "Adaptive car buffer—the concept, design tools and perspectives", in *IEEE/ASME International Conference on Advanced Intelligent Mechatronics Proceedings*, Como, Italy, 2001, pp. 326-330.

35. J. Holnicki-Szulc and L. Knap, "Adaptive crashworthiness concept", *International Journal of Impact Engineering*, Vol. 30, pp. 639-663, 2004.

36. L. Wågström, A. Kling, S. Berge, H. Norin, and H. Fagerlind, "Adaptive structure concept for reduced crash pulse severity in frontal collisions", *International Journal of Crashworthiness*, Vol. 18, No. 6, pp. 597-605, 2013.

37. S. Sugiyama, T. Sakurai, and S. Morishita, "Vibration control of a structure using magneto-rheological grease damper", *Frontiers of Mechanical Engineering*, Vol. 8, No. 3, pp. 261-267, 2013.

38. J. N. Potter, S. A. Neild, and D. J. Wagg, “Quasi-active suspension design using magnetorheological dampers”, *Journal of Sound and Vibration*, Vol. 330, pp. 2201-2219, 2011.

39. C. Spelta, F. Previdi, S. M. Savaresi, G. Fraternale, and N. Gaudiano, “Control of magnetorheological dampers for vibration reduction in a washing machine”, *Mechatronics*, Vol. 19, pp. 410-421, 2009.

40. C. M. D. Wilson and M. M. Abdullah, “Structural vibration reduction using self-tuning fuzzy control of magnetorheological dampers”, *Bulletin of Earthquake Engineering*, Vol. 8, pp. 1037-1054, 2010.

41. N. M. Wereley, Y. T. Choi, and H. J. Singh, “Adaptive energy absorbers for drop-induced shock mitigation”, *Journal of Intelligent Material Systems and Structures*, Vol. 22, pp. 515-519, 2011.

42. A. Milecki and M. Hauke, “Application of magnetorheological fluid in industrial shock absorbers”, *Mechanical Systems and Signal Processing*, Vol. 28, pp. 528-541, 2012.

43. G. H. Martin, *Kinematics and Dynamics of Machines*, 2nd ed., Long Grove, IL, Waveland Press, Inc., 1982.

44. *Cam design: a manual for engineers designers and draftsmen*, Commercial Cam Division, Emmerson Electric Company, Wheeling, IL, USA, 1961.

45. “ElectroMechanicsOnline.com”, 2017, [Online], Available: http://www.electromechanicsonline.com/product.asp?pid=811, [Accessed: June 21, 2017].

46. J. D. Reid and N. R. Hiser, “Detailed modeling of bolted connections with slippage”, *Finite Elements in Analysis and Design*, Vol. 41, pp. 547-562, 2005.

47. R. L. Norton, *Machine Design: An Integrated Approach*, 4th ed., Upper Saddle River, NJ, Pearson Education, Inc., 2011.

48. “LS-DYNA Examples: Contact Rubber”, 2017, [Online], Available: http://www.dynaexamples.com/introduction/intro-by-a.-tabiei/contact/contact-rubber/contact-rubber/?searchterm=rubber, [Accessed: June 21, 2017].

49. M. Gedeon, *Material Brush Performance Alloys Technical Tidbits: Issue No. 67: Stress Life vs. Strain Life*, Mayfield Heights, OH: Materion Brush Inc., 2014.

50. G. Glinka, Class Lecture, Topic: "The Local Stress-Strain Fatigue Method (ε-n)", Department of Mechanical and Mechatronics Engineering, University of Waterloo, Waterloo, ON, Canada, 2010.

51. "Fatigue", in *Elements of Metallurgy and Engineering Alloys*, F.C. Campbell, Ed., Materials Park, OH: ASM International, 2008, Ch. 14, pp. 243-264.

52. Y. L. Lee and M. E. Barkey, "Strain-Based Uniaxial Fatigue Analysis", in *Metal Fatigue Analysis Handbook: Practical problem- solving techniques for computer-aided engineering*, Y. L. Lee, M. E. Barkey, and H. T. Kang, Ed., Butterworth-Heinemann, 2012, Ch. 6, pp. 215-252.

53. *DesignLife Worked Examples*, HBM-nCode, Southfield, MI, U.S.A., 2016.

54. W.L. Oberkampf and T.G. Trucano, "Verification and validation in computational fluid dynamics", *Progress in Aerospace Sciences*, Vol. 38, No. 3, pp. 209-272, 2002.

55. P. L'Eplattenier, "Recent Developments and Roadmap Part 4: Electromagnetics", in *12th International LS-DYNA User's Conference*, Detroit, MI, USA, 2012, pp. 1-16.

56. P. L'Eplattenier and I. Çaldichoury, "Update on the Electromagnetiam Module in LS-DYNA", in *12th International LS-DYNA User's Conference*, Detroit, MI, USA, 2012, pp. 1-10.

57. I. Çaldichoury and P. L'Eplattenier, "Validation Process of the Electromagnetism (EM) Solver in LS-DYNA v980: The TEAM Problems", in *12th International LS-DYNA User's Conference*, Detroit, MI, USA, 2012, pp. 1-14.

58. P. L'Eplattenier, I. Çaldichoury, and J. Shang, "Investigation of the Effects of the Coil Design on Electromagnetic Forming of a Thin-Walled Tubular Aluminum Material", in *12th International LS-DYNA User's Conference*, Detroit, MI, USA, 2012, pp. 1-14.

59. W. Lawson and J. Johnson, "A Simple Weak-Field Coupling Benchmark Test of the Electromagnetic-Thermal-Structural Solution Capabilities of LS-DYNA Using

Parallel Current Wires”, in *13th International LS-DYNA User’s Conference*, Detroit, MI, USA, 2013, pp. 1-20.

60. P. L’Eplattenier, J. Anton, and I. Çaldichoury, “Coupling of the EM Solver with Mechanical and Thermal Shell Elements”, in *13th International LS-DYNA User’s Conference*, Detroit, MI, USA, 2013, pp. 1-10.

61. I. Çaldichoury and P. L’Eplattenier, “Simulation of a Railgun: A contribution to the Electromagnetism module in LS-DYNA v980”, in *12th International LS-DYNA User’s Conference*, Detroit, MI, USA, 2012, pp. 1-12.

APPENDIX A: ASSEMBLY DRAWING AND BILL OF MATERIALS FOR QUADROTOR ADAPTIVE CUTTER

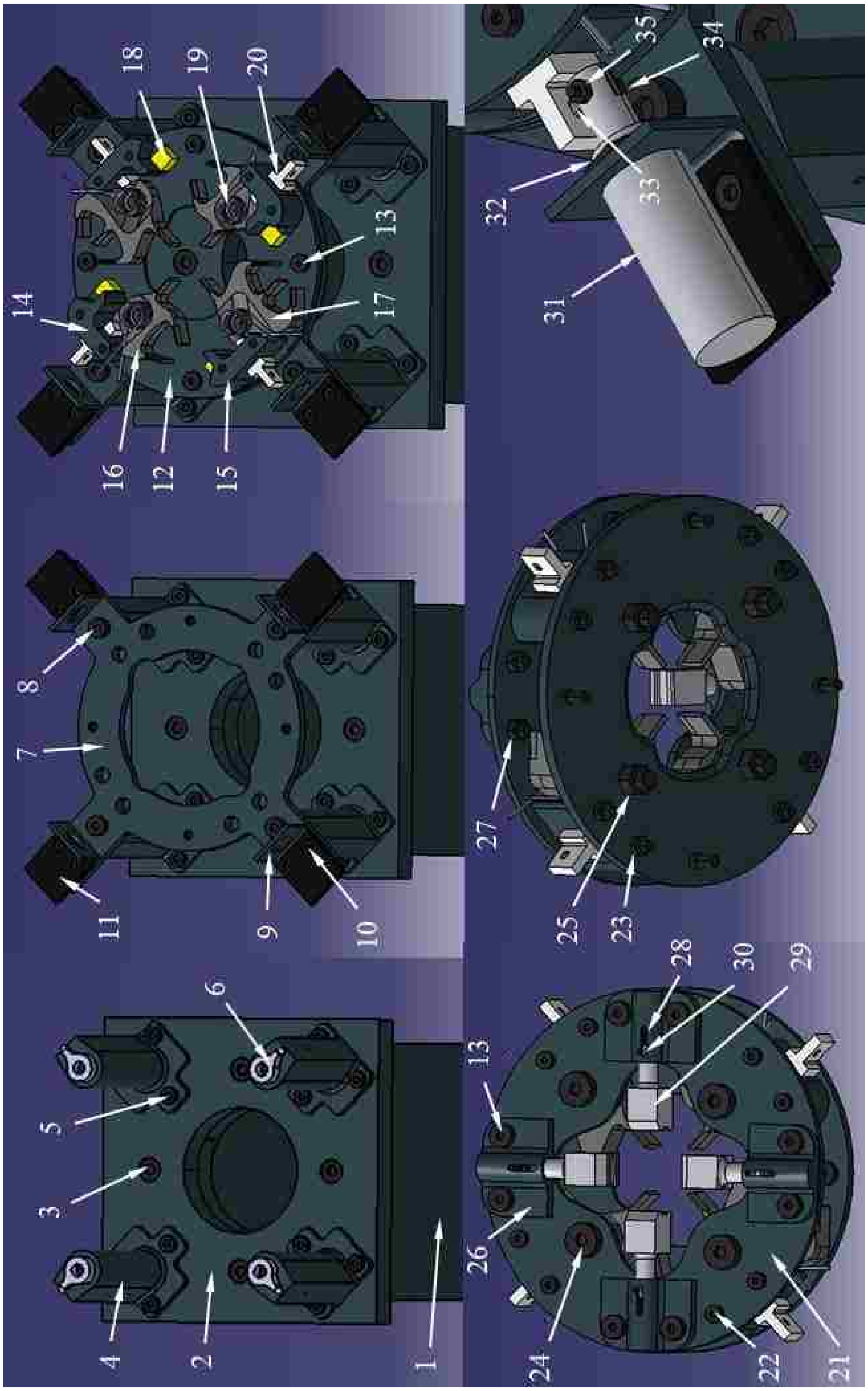

Figure A1: Assembly of Quadrotor Adaptive Cutter.

Table A1: Bill of Materials for Quadrotor Adaptive Cutter.

Part No.	Part Name	Material	Qty	Drawing No.	Manufactured / Purchased Yet?
1	8 in x 8 in column	Steel	1	-	YES
2	Bottom adaptor plate	Mild Steel	1	1	NO
3	M12 diam x 40 mm length socket head cap screw	Hardened Steel	4	-	NO
4	Support leg	SAE Steel Grade 1090M Rc 29	4	2	NO
5	M8 diam x 12 mm length shoulder bolt	Hardened Steel	12	-	NO
6	1210V2 Dytran load cell	-	4	-	YES
7	Elevated platform	Quench and tempered steel 41Cr4	1	3	NO
8	M10 diam x 35 length shoulder bolt	Hardened Steel	4	-	NO
9	Angle plate mount	Structural grade carbon steel S355J0	4	4	NO
10	M6 diam x 6 mm length shoulder bolt	Hardened Steel	8	-	NO
11	Neoprene pad (0.25 in thick)	Neoprene rubber	4	5	NO
12	Back Cover	SAE Steel Grade 1050M Rc54	1	8	NO
13	M8 diam x 10 mm length shoulder bolt	Hardened Steel	12	-	NO
14	Long L-block	SAE Steel Grade 4140 Rc31	2	9	NO
15	Short L-block	SAE Steel Grade 4140 Rc31	2	10	NO
16	3-Bladed cutter	SAE Steel Grade 9254 Al_Rc58	2	14	NO
17	4-Bladed cutter	SAE Steel Grade 9254 Al_Rc58	2	15	NO

Table A1: Bill of Materials for Quadrotor Adaptive Cutter (Continued).

Part No.	Part Name	Material	Qty	Drawing No.	Manufactured / Purchased Yet?
18	Indigo Instruments neodymium block magnet (0.5 in^3, 23 lb pull force)	Neodymium (nickel-copper-nickel coated)	4	-	YES
19	Acxess Spring PT078-781-7.000-MW-LH-2.000-N-IN torsion spring	Music Wire	4	-	YES
20	Teflon pin	Teflon plate	4	7	NO
21	Front Cover	Carbon Steel SAE1035_169_CON	1	13	NO
22	0.25 in diam x 1.75 in length shoulder bolt	Hardened Steel	8	-	NO
23	#10-24 hex nut	Hardened Steel	8	-	NO
24	0.5 in diam x 1.75 in length shoulder bolt	Hardened Steel	4	-	NO
25	0.375 in hex nut	Hardened Steel	4	-	NO
26	Jaw housing	Structural grade carbon steel S235J0	4	11	NO
27	M6 hex nut	Hardened Steel	8	-	NO
28	Acxess Spring PC028-375-10.000-MW-1.500-C-Z-IN compression spring	Music Wire	4	-	NO
29	Jaw	Stainless steel X2CrTiNb18	4	12	NO
30	Slit pin (or spring pin) 1/8 in nominal diameter	Hardened Steel	4	-	NO
31	Linear pull type solenoid SOTUL0230051 (48 V, 10 % duty cycle)	-	4	-	YES
32	Solenoid mounting hex nut	Hardened Steel	4	-	YES
33	Solenoid adaptor (pick)	Structural grade carbon steel S355J0	4	6	NO
34	M3 diam x 16 mm length machine bolt	Hardened Steel	4	-	NO
35	M3 hex nut	Hardened Steel	4	-	NO

APPENDIX B: ENGINEERING PART DRAWINGS FOR QUADROTOR ADAPTIVE CUTTER

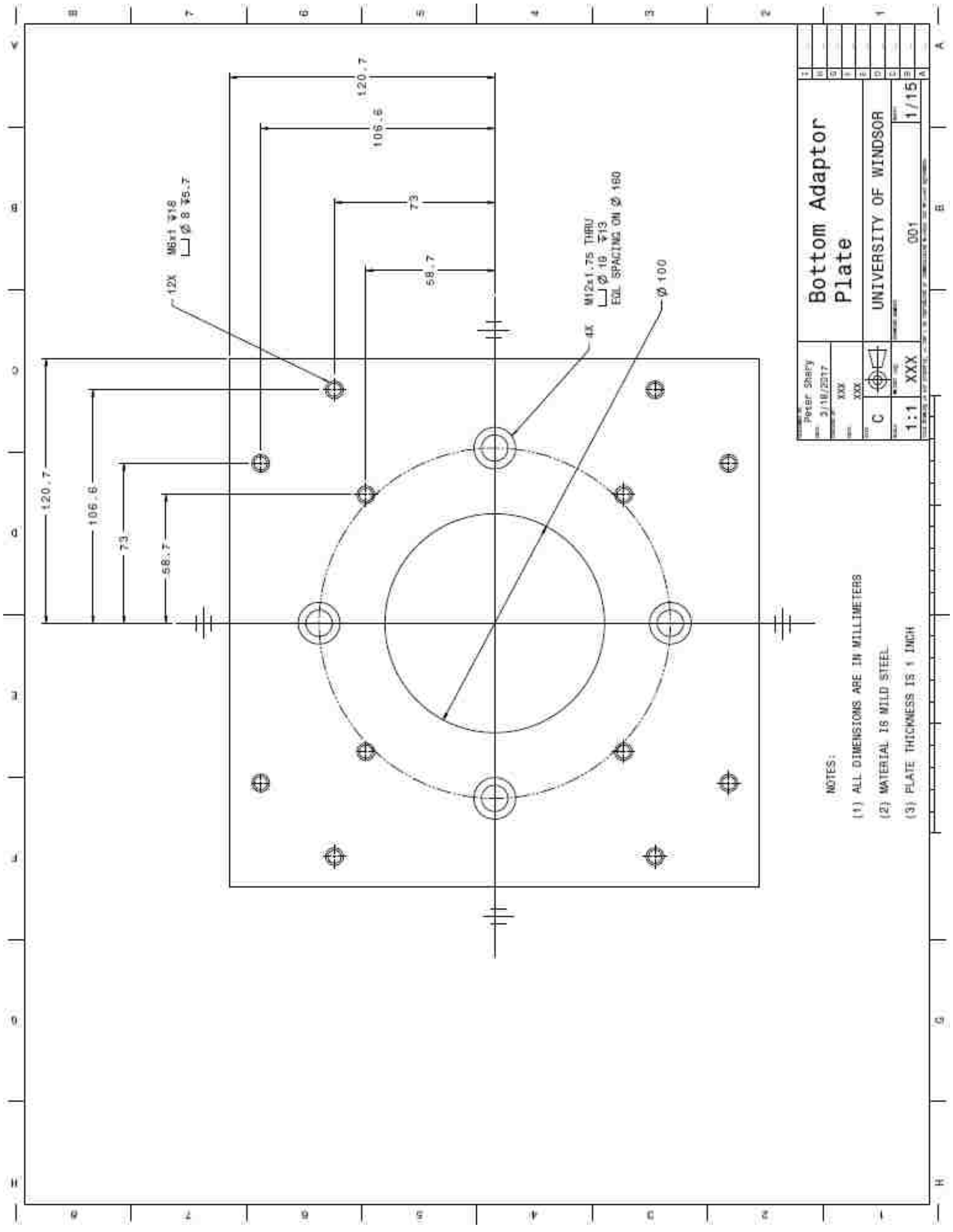

Figure B1: Bottom Adaptor Plate.

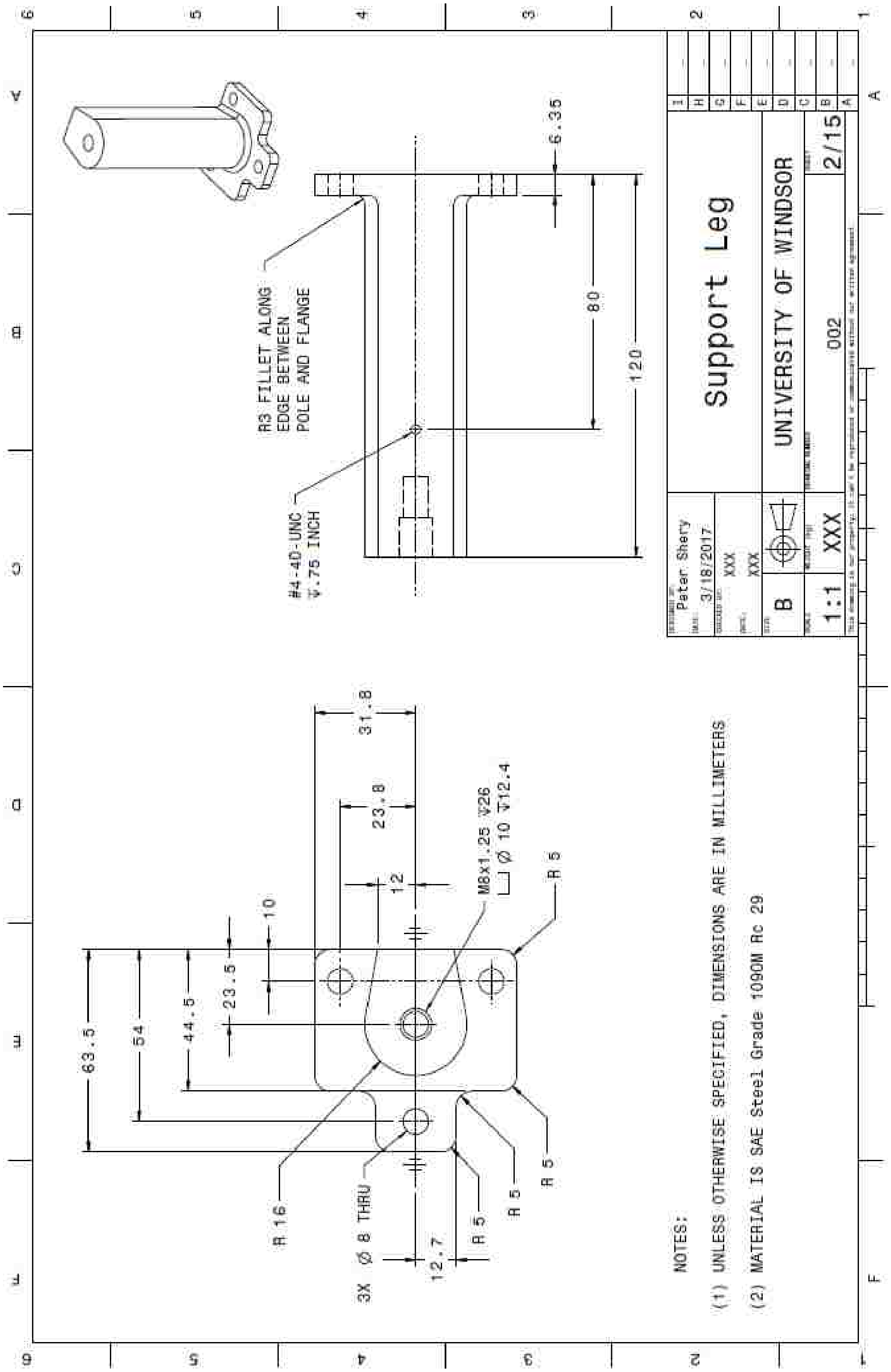

Figure B2: Support Leg.

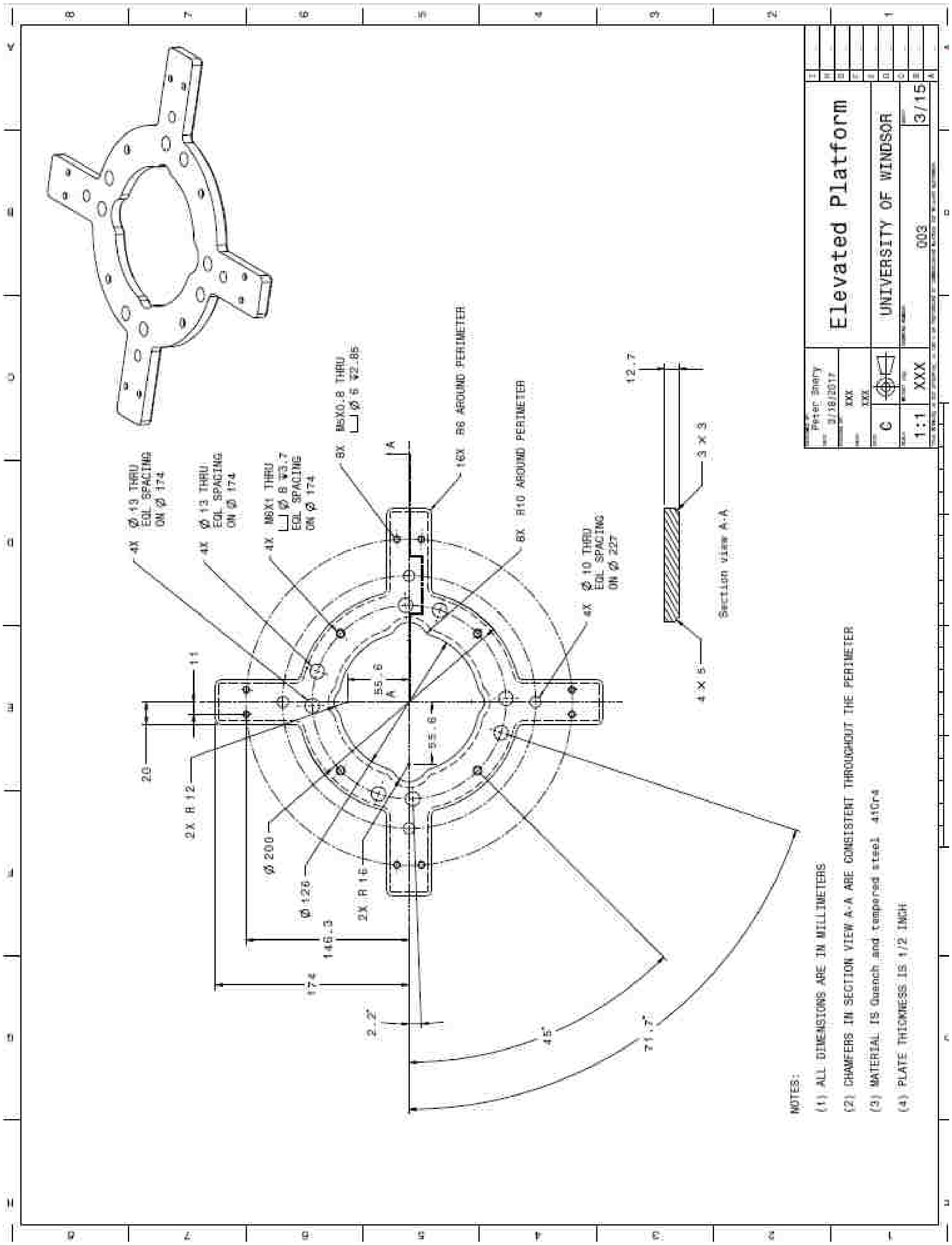

Figure B3: Elevated Platform.

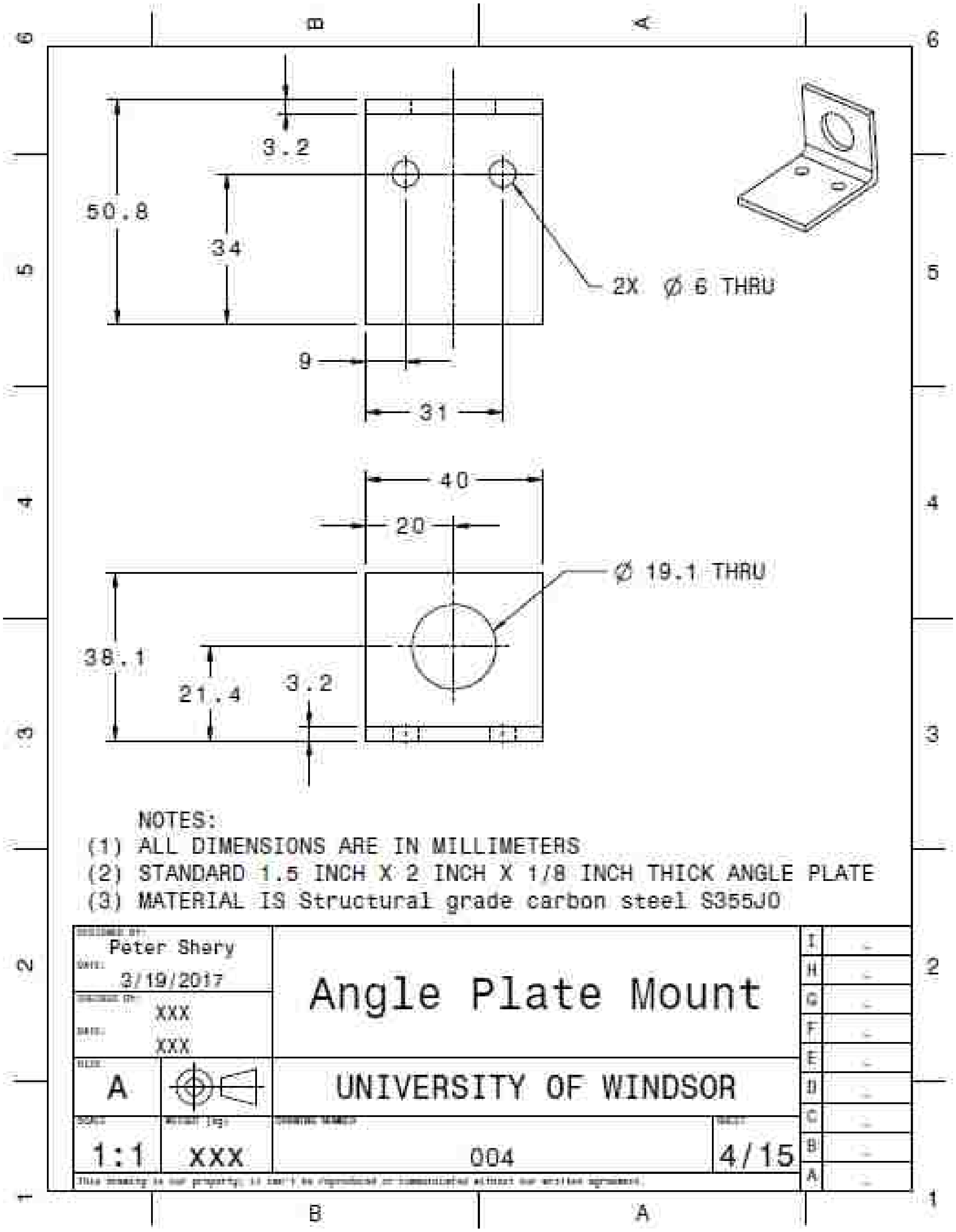

NOTES:
(1) ALL DIMENSIONS ARE IN MILLIMETERS
(2) STANDARD 1.5 INCH X 2 INCH X 1/8 INCH THICK ANGLE PLATE
(3) MATERIAL IS Structural grade carbon steel S355J0

Peter Shary
3/19/2017
XXX
XXX

Angle Plate Mount

A

UNIVERSITY OF WINDSOR

1:1
XXX
004
4/15

Figure B4: Angle Plate Mount.

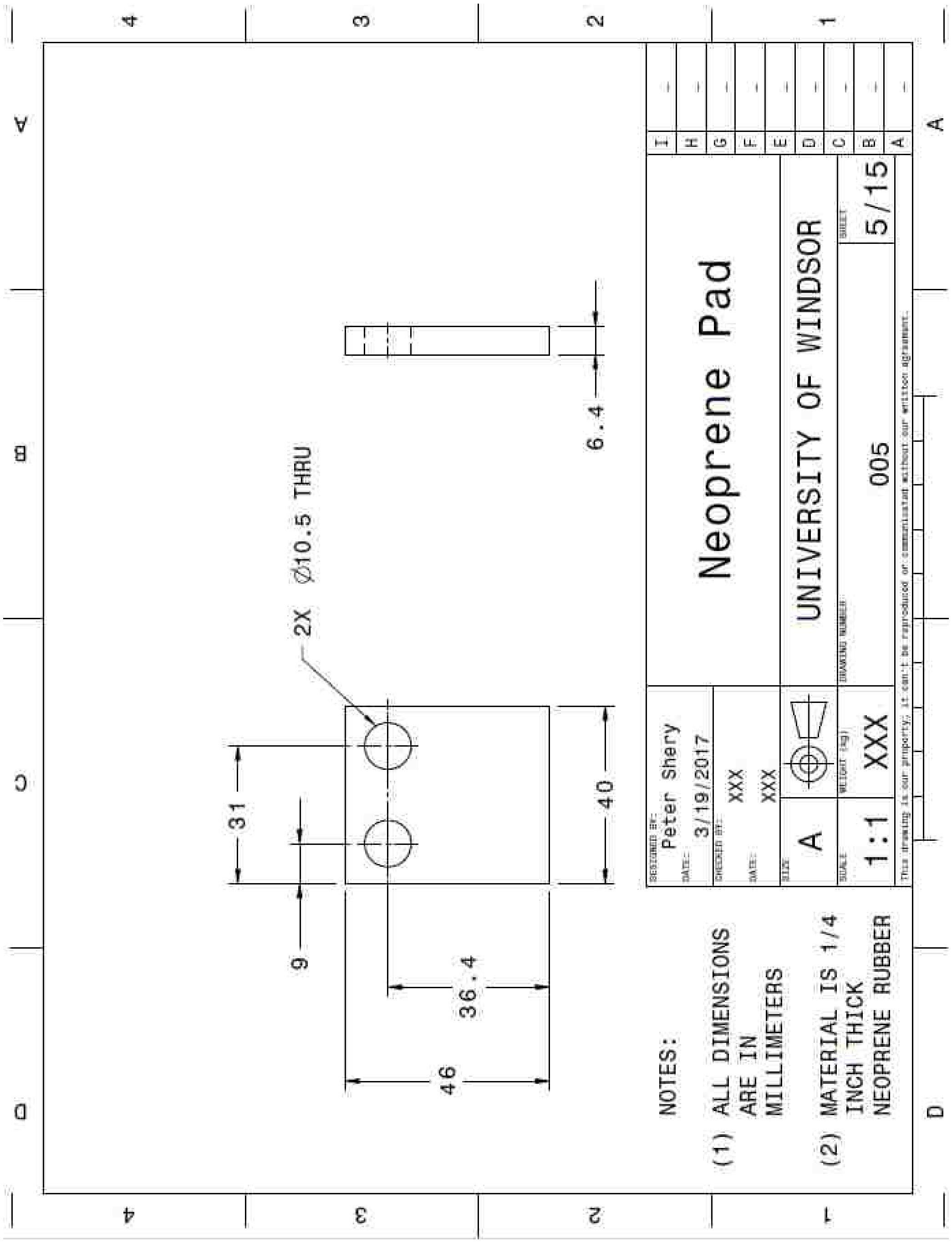

Figure B5: Neoprene Pad.

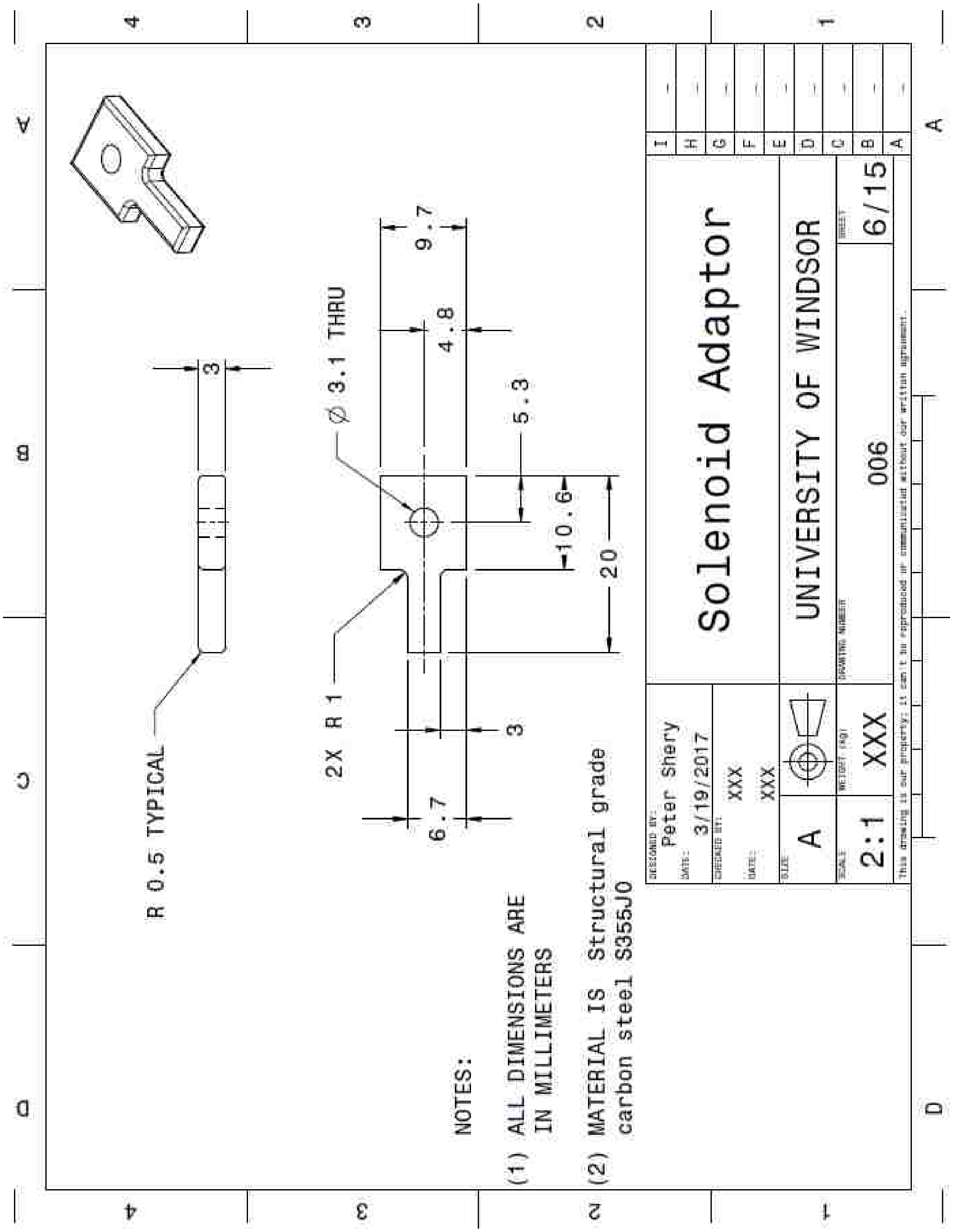

Figure B6: Solenoid Adaptor (Pick).

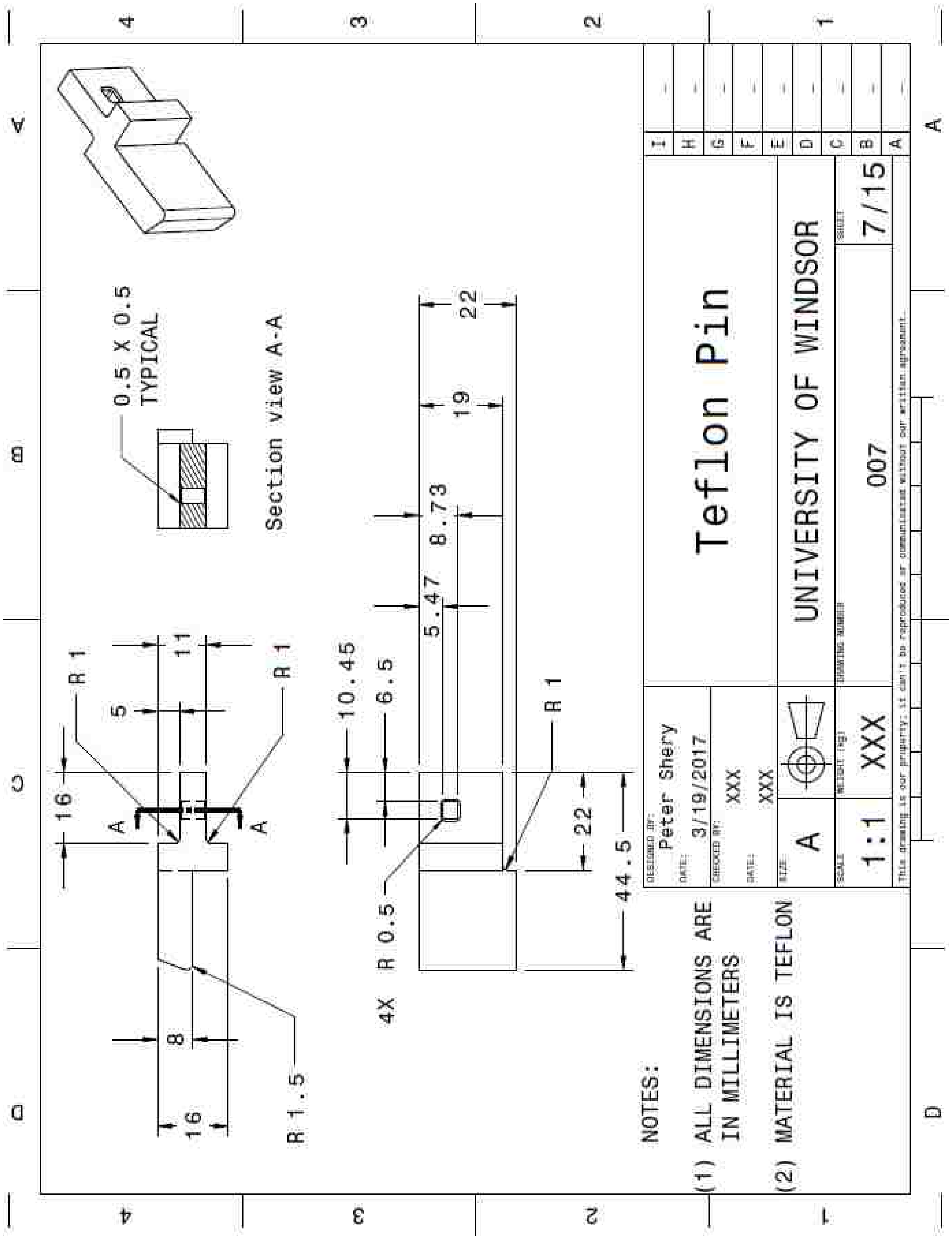

Figure B7: Teflon Pin.

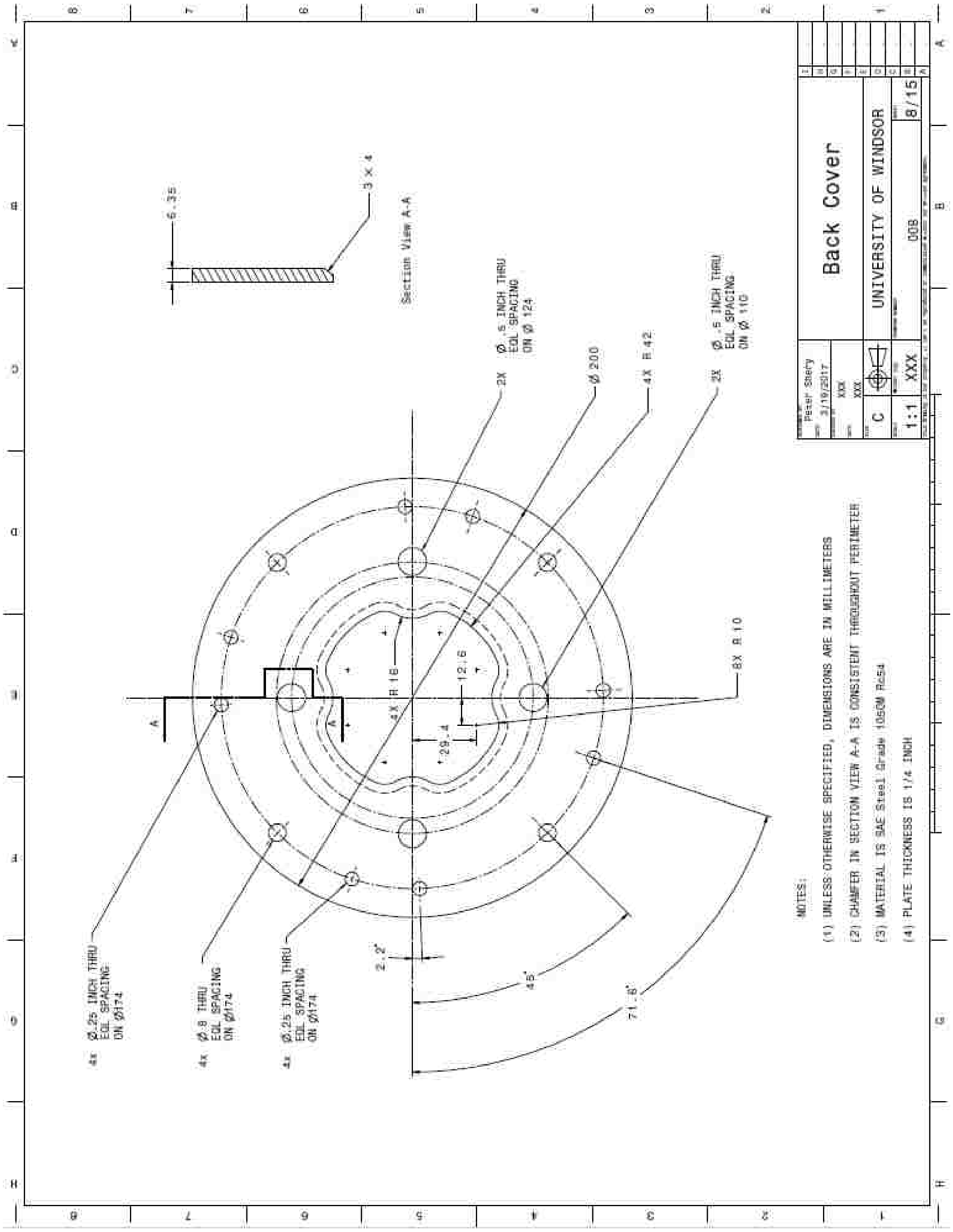

Figure B8: Back Cover.

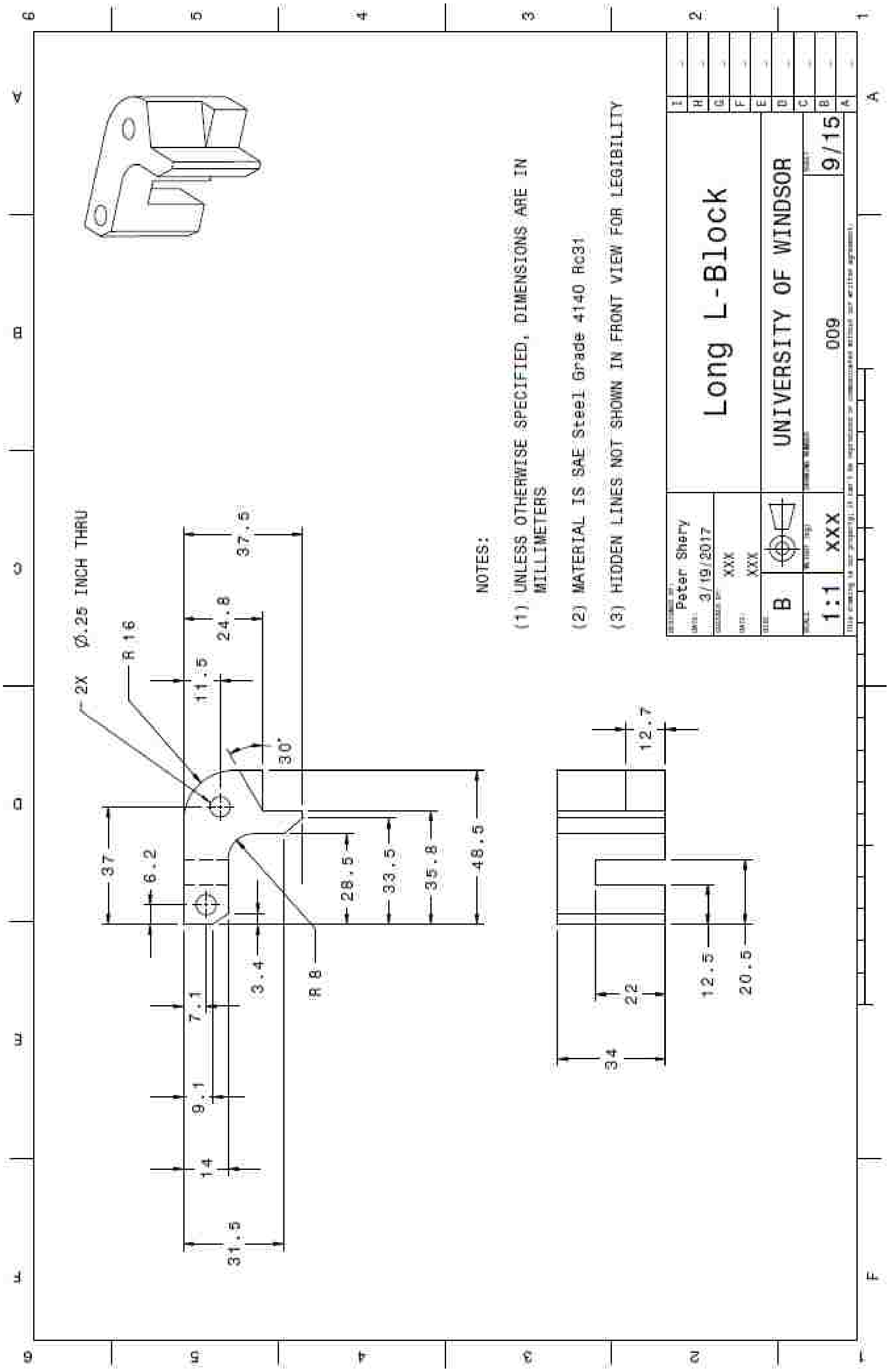

Figure B9: Long L-Block.

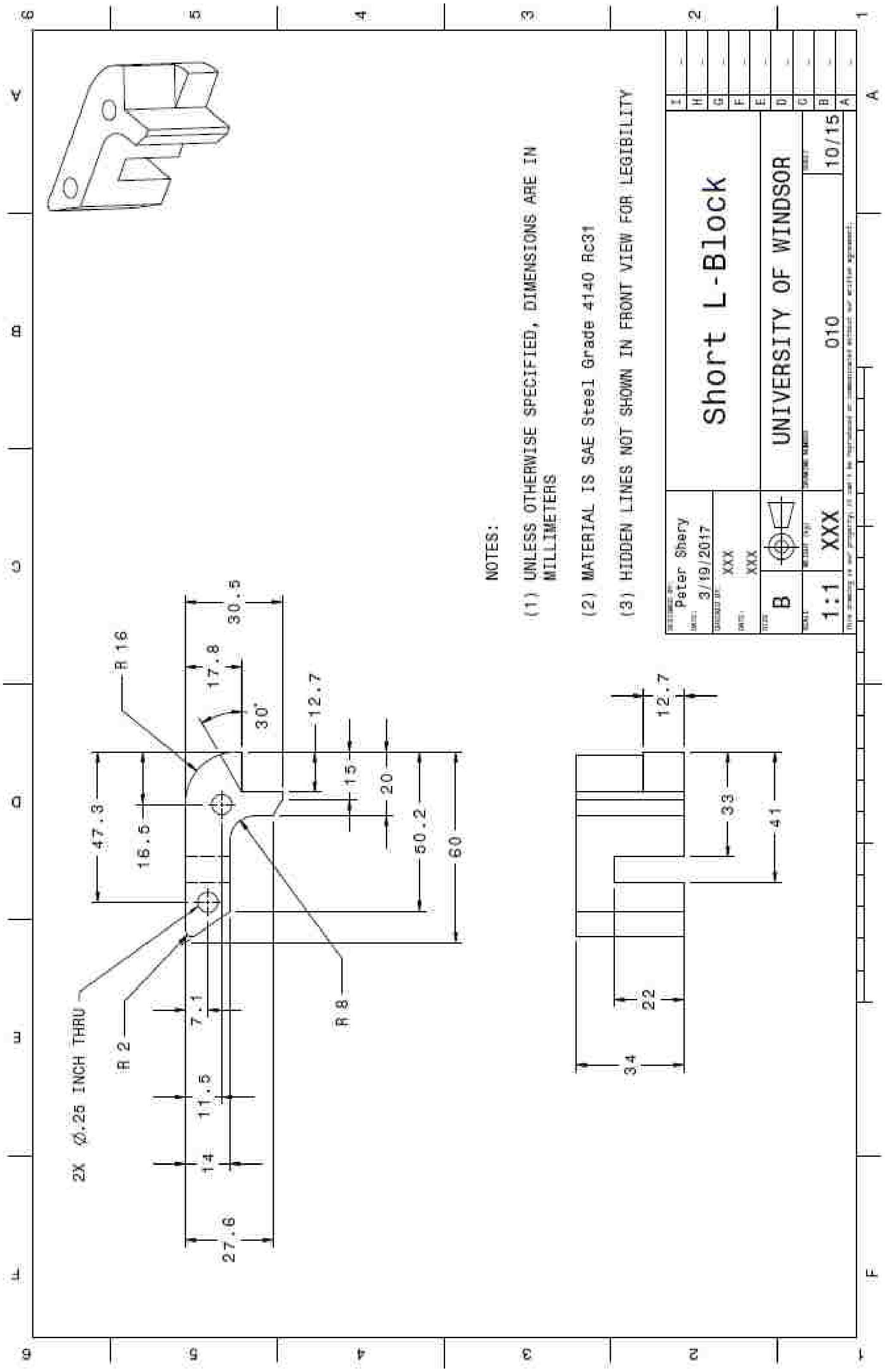

Figure B10: Short L-Block.

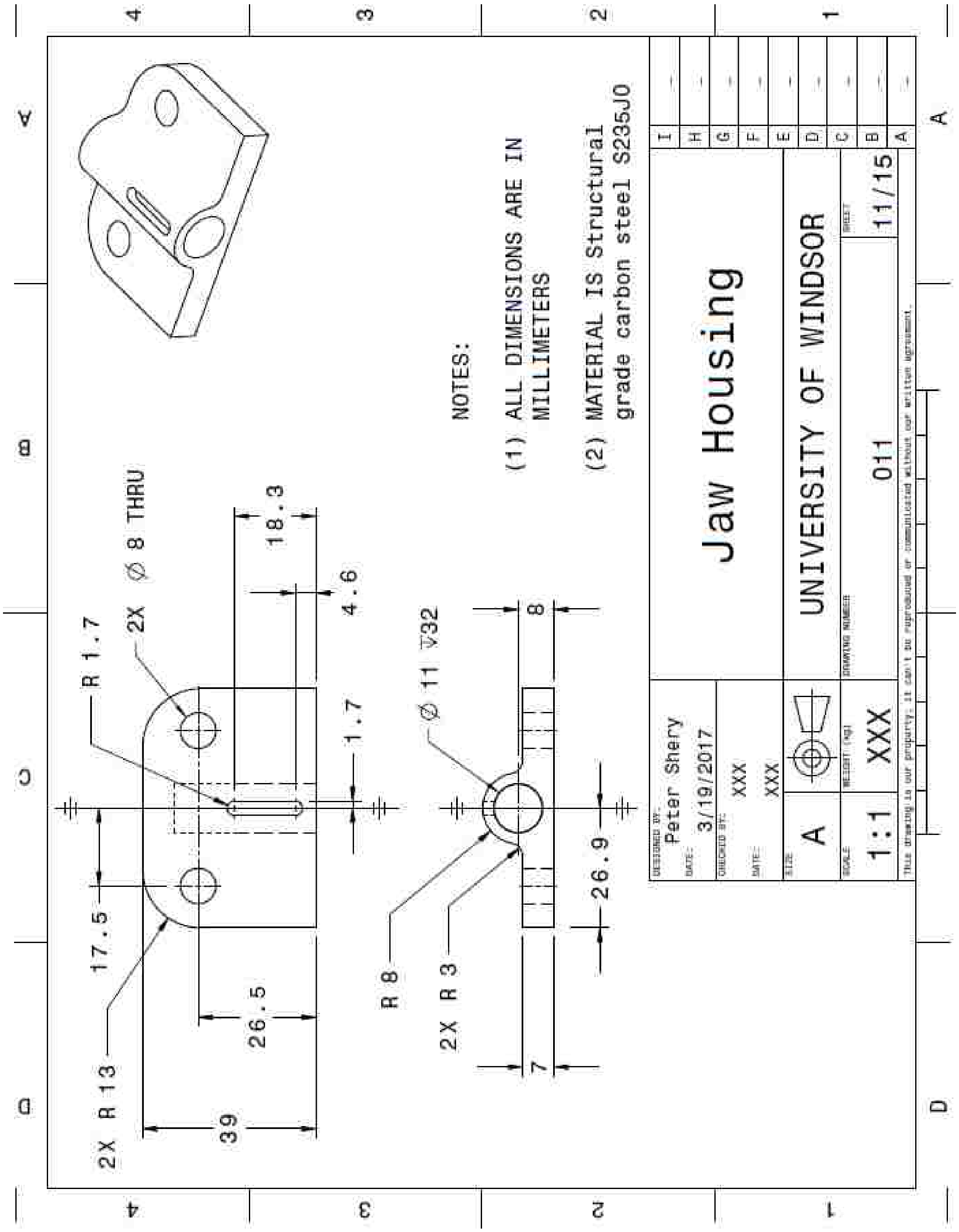

Figure B11: Jaw Housing.

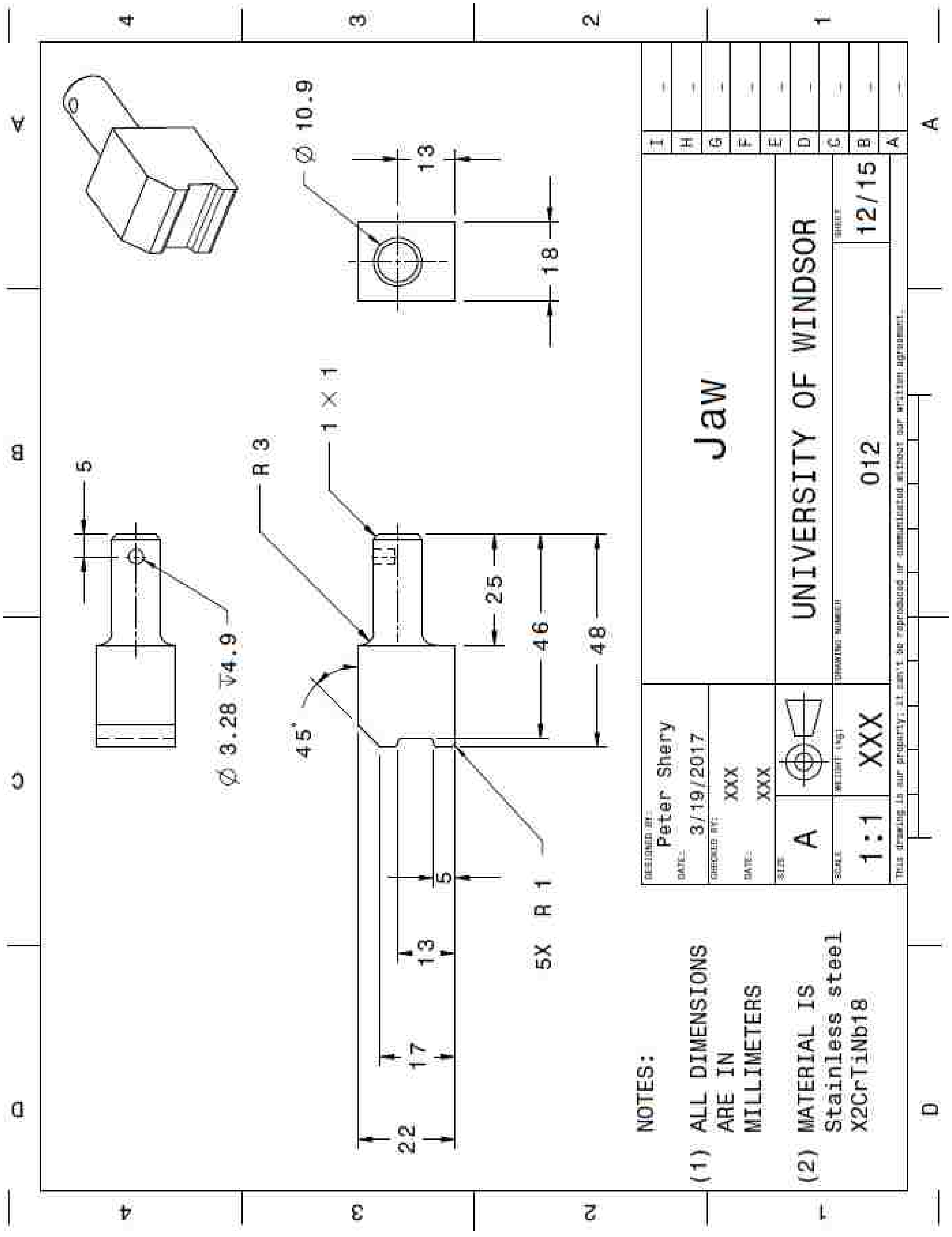

Figure B12: Jaw.

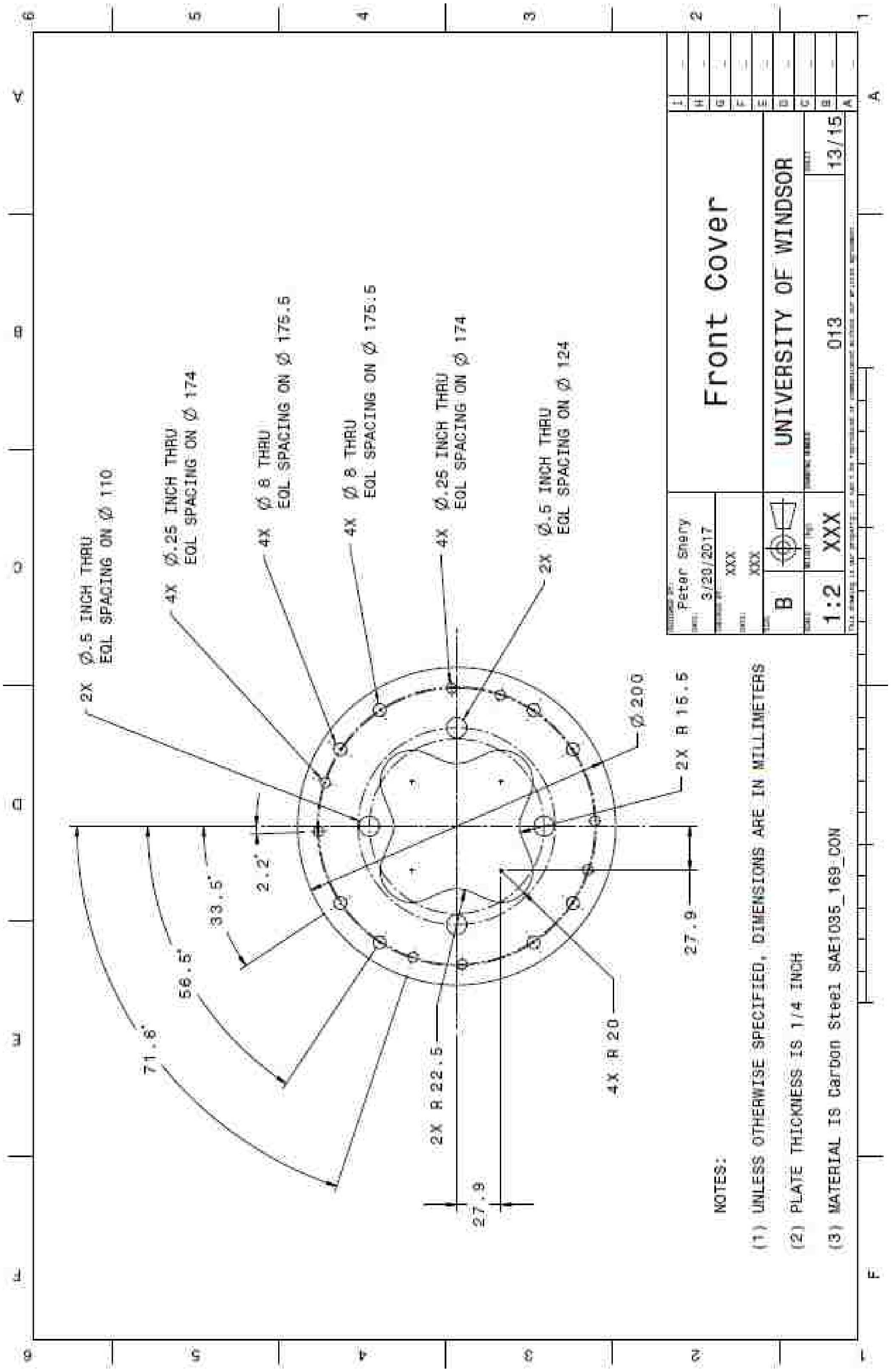

Figure B13: Front Cover.

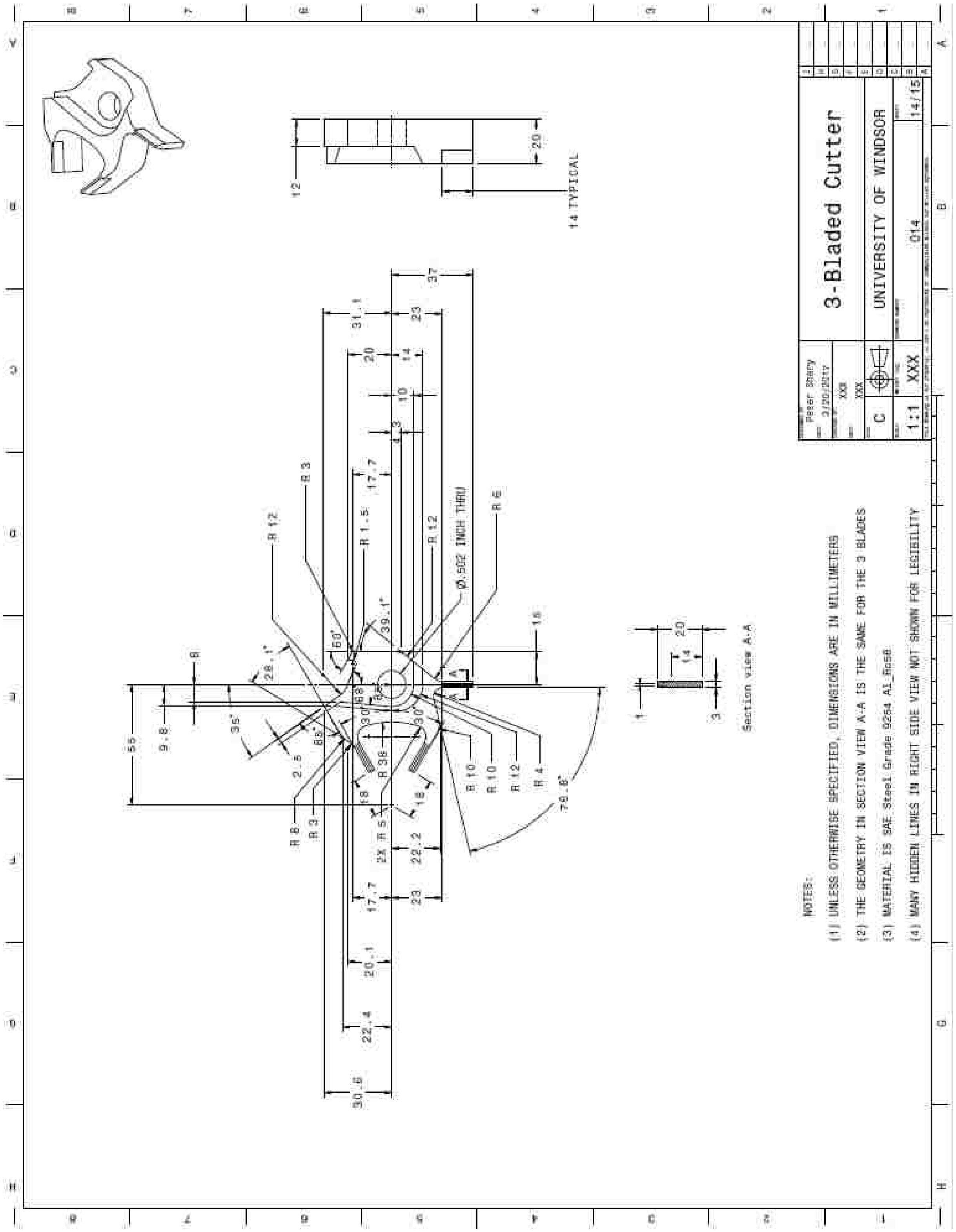

Figure B14: 3-Bladed Cutter.

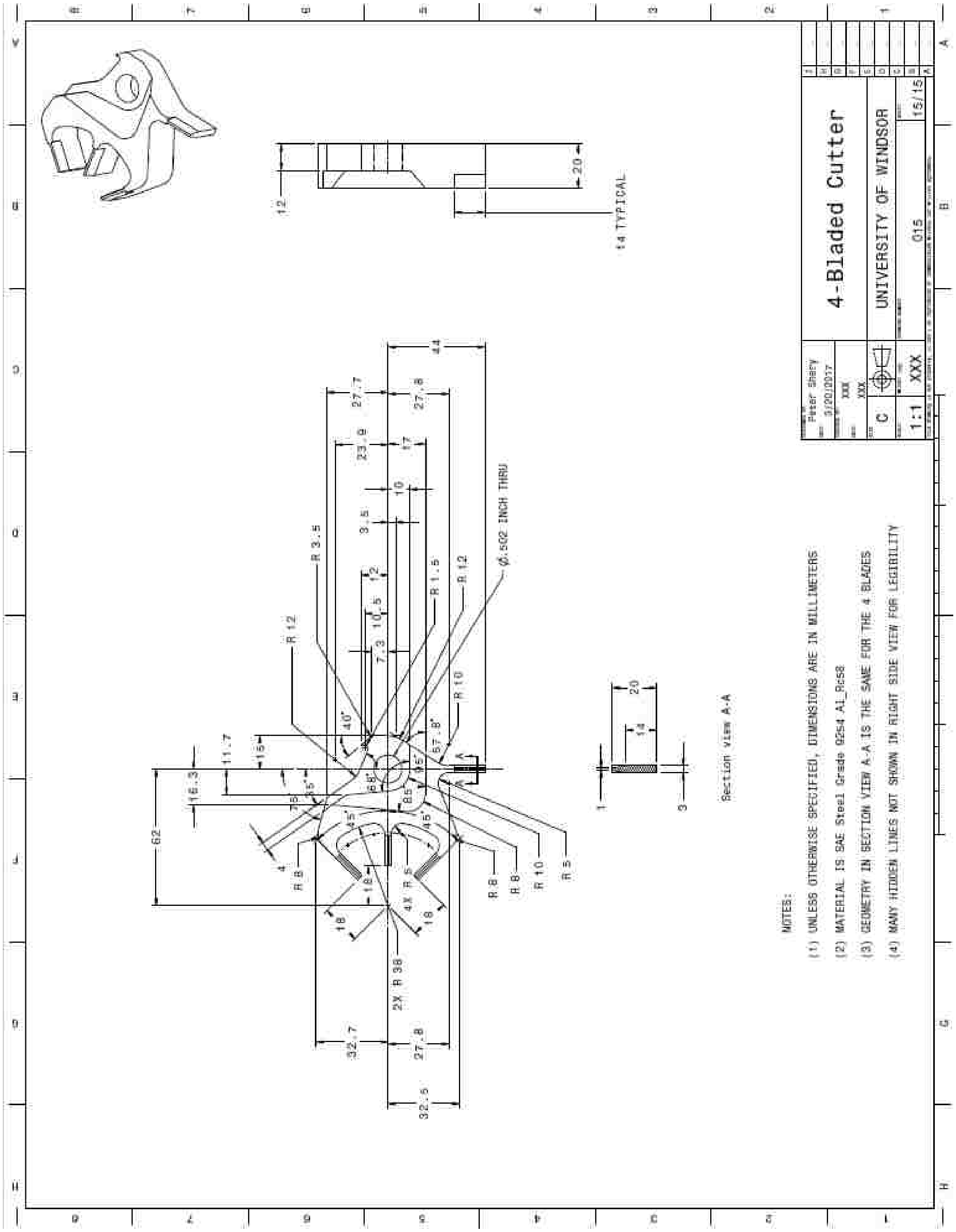

Figure B15: 4-Bladed Cutter.

APPENDIX C: SOLENOID CONTROL SYSTEM AND ELECTRONIC HARDWARE FOR QUDROTOR ADAPTIVE CUTTER

This appendix briefly outlines the electrical system and hardware required to control the solenoids. Note that the solenoids are not simply connected to a power supply with the current on continuously. The solenoids for this application only require a current supply for a brief period of time to deploy the cutters. So, for the vast majority of the time, the solenoids are connected to an open circuit. A relay closes the circuit temporarily allowing current to pass to the desired set of solenoids before opening the circuit afterwards.

Dynamic cutting tests would be performed by dropping a crosshead from a droptower impact testing machine, available in the Structures lab at the University of Windsor. In order to trigger the solenoids at the appropriate time, a data acquisition system is needed that incorporates sensors to measure information about the incoming velocity of the descending crosshead, logic to determine the desired number of solenoids (for the desired blade configuration) at the appropriate time, and a controller to trigger those particular solenoids. Laser displacement transducers are the sensors that measure the displacement of the descending carriage. The displacement information is continuously fed to a laptop that has a custom LabVIEW program, which is the logic and controller of the system. From the displacement data, the LabVIEW program computes the velocity of the impacting plate in real time. Once the crosshead is at a critical distance away from the blades, the LabVIEW program is configured to do one of three possible actions: (1) Inform the output module to send no signal if the velocity is below the threshold for the 4-blade configuration. (2) Inform the output module to send a signal from one channel if the velocity is within the range for the 6-blade configuration. (3) Inform the output module to send a signal from a second channel on the output module if the velocity is above the threshold for the 8-blade configuration.

The velocity ranges for each blade configuration and the critical distance the impact plate must be from the blades when the output signal is sent is determined by equating the droptower carriage's kinetic energy to the AA6061-T6 extrusion's

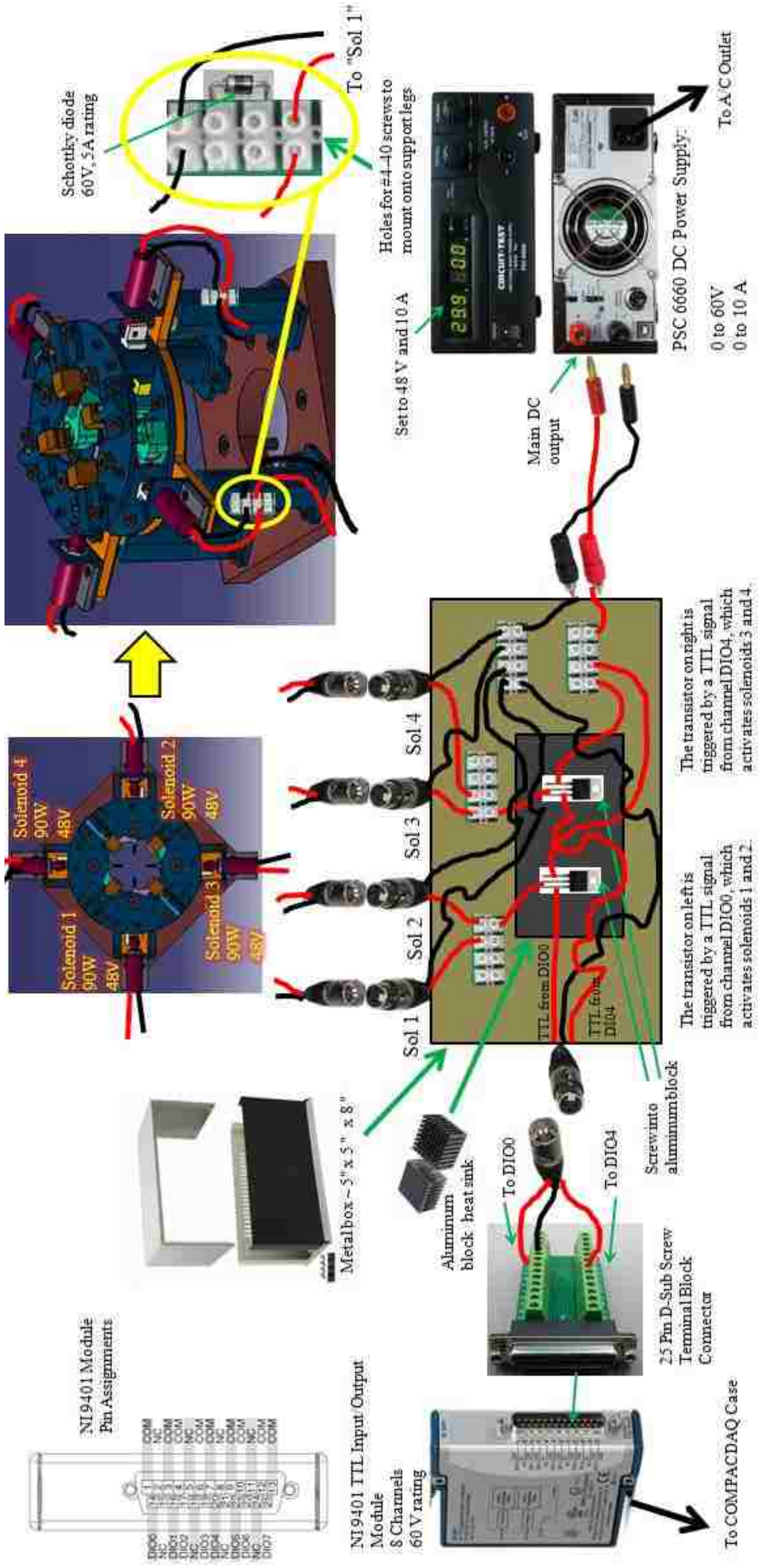

Figure C1: Graphical representation of electronic hardware and connections in solenoid control system.

deformation energy. The computations of the velocities and critical distance are discussed in Chapter 8.0. where the testing plan is developed.

To help comprehend the solenoid control system, a graphical representation of the hardware and connections are shown in Figure C1. The bottom center image shows the internals of the solenoid driver, which is the main gate connecting all the components. From the top four 3-pin output terminals are connected the four solenoids. Note the wires from each solenoid pass through a screw terminal containing a Schottky diode. This Schottky diode is crucial because without it, after the solenoid shaft is retracted and the circuit is open again, the current will attempt to short circuit across the wires of the solenoid. The diode allows the current to circulate through the solenoid coil repeatedly, gradually dissipating the electrical energy in the form of heat. The bottom right image is the PSC 6660 DC power supply which is connected to an AC outlet. Since each SOTUL0230051 solenoid only needs to operate for a fraction of a second, a 10% duty cycle solenoid was selected, requiring an input power of 90 W. The voltage of the solenoid had to be selected as well. To minimize the required current per solenoid, and also not require a DC power supply with an exceedingly high voltage rating, which is more expensive, a 48 V solenoid was found to be the most economical option.

For either the 6-blade or 8-blade configuration, two solenoids are operated simultaneously. Since each solenoid requires 90 W, the DC power unit must be able to supply at least 180 W. Also, since each 48 V solenoid is wired in parallel and each one draws nearly 2 A, to operate two solenoids, the power supply must have at least a 4 A capability. The PSC 6660 power supply is an appropriate choice having a rating of 60 V and 10 A. It is also an economical choice because it does not have any programmable features other than the voltage and current limits which can be manually set with knobs. Banana jack output terminals connect from the DC power supply to the solenoid driver. The bottom left hand image is the National Instruments NI 9401 8-channel input/output module, which is used in this application to output the transistor-transistor logic (TTL) signal to the solenoid driver. The NI 9401 module is connected to a compatible NI Compact DAQ case to which the LabVIEW enabled laptop, the laser displacement transducers, and the load cells, are also connected. A 25 Pin D sub screw terminal block adapts onto the NI 9401 module. The 4-pin connector from the solenoid driver connects to the 25 pin screw terminal via three splayed wires. Two of these wires are fastened into two separate channels, DIO0 and DIO4, and the third wire is fastened to the ground terminal. The solenoid driver consists of a metal box enclosing a pair of transistors screwed onto an aluminum block heat sink, and a few screw terminals to form the circuits. These transistors are referred to as N-channel metal oxide power mosfets having three terminals, one of which is a logic level gate. Only when a TTL signal is sent to the logic level gate terminal of the transistor will a closed circuit exist and will current from the DC power supply flow into the circuit.

Referring to the connection diagram in Figure C1, when a TTL signal is sent to the solenoid driver from channel DIO0 on the NI 9401 output module, the left transistor closes its circuit. Thus, current from the power supply flows to the left transistor and into solenoids 1 and 2 labeled “Sol 1” and “Sol 2”. The 6-blade arrangement would be deployed as a result. Conversely, when a TTL signal is sent to the solenoid driver from channel DIO4 on the NI 9401 output module, the right transistor will close its circuit. Thus, current from the power supply flows to the right transistor and into solenoids 3 and 4 labeled “Sol 3” and “Sol 4”, deploying the 8-blade arrangement.

All of this hardware has been acquired and/or fabricated by a professional technician and ready to implement on the adaptive cutter. The only missing link is the LabVIEW program which has yet to be written, and is not included as part of this thesis. A clearer picture of the available components and wiring is provided in Figures C2(a) though (e): Shown in (a) is the PSC 6660 DC power supply. Shown in (b) is the front view of the solenoid driver with the banana cables for the DC power supply and the 4-pin terminal for the TTL input signal. Shown in (c) are the 25-pin D-sub screw terminal block and the 8-channel NI 9401 TTL Input/Output module. Shown in (d) is the back view of the solenoid driver with the four 3-pin output terminals for the four solenoids. Also shown is a sample wire and screw terminal to which the Schottky diode and solenoid wires fasten. Each of these screw terminals will be fastened with a #4-40 type screw into the back side of each of the adaptive cutter’s support legs, which face away from the flaring AA6061-T6 extrusion petals. Finally, shown in (e) is the linear pull-type solenoid model SOTUL0230051, which has a rating of 48 V, 10% duty cycle, and 90 W.

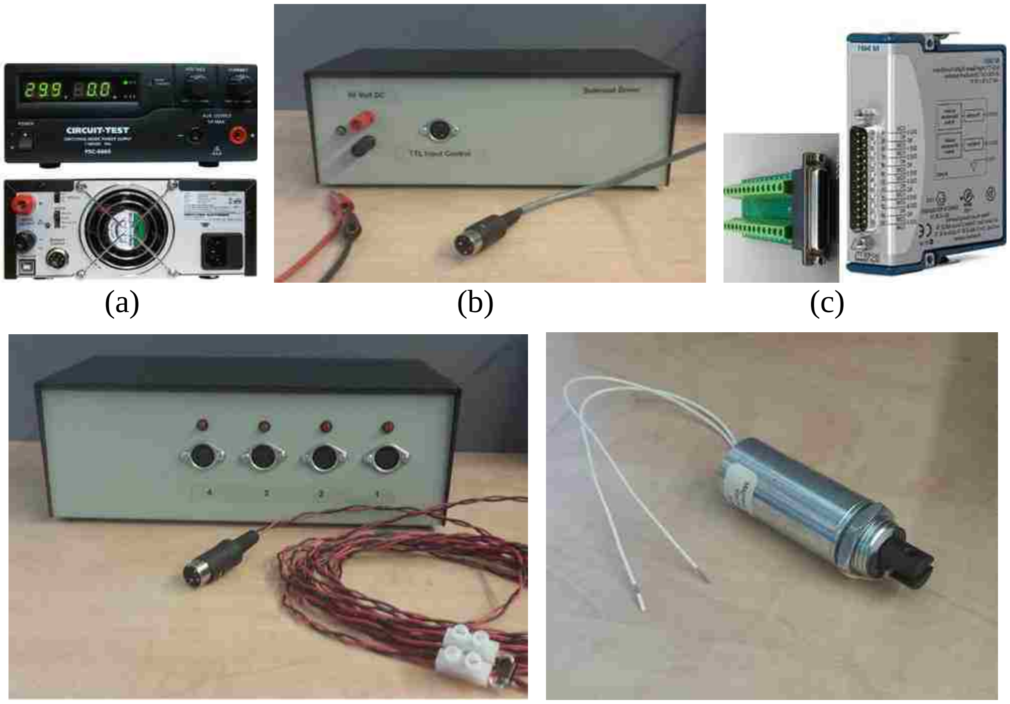

(a) (b) (c)

(d) (e)

Figure C2: Photographs of available hardware for electronic system. (a) DC power supply. (b) Solenoid driver (Front). (c) 25 pin D-sub screw terminal block and 8 channel NI 9401 TTL Input/Output module. (d) Solenoid driver (back). (e) Linear pull type solenoid.

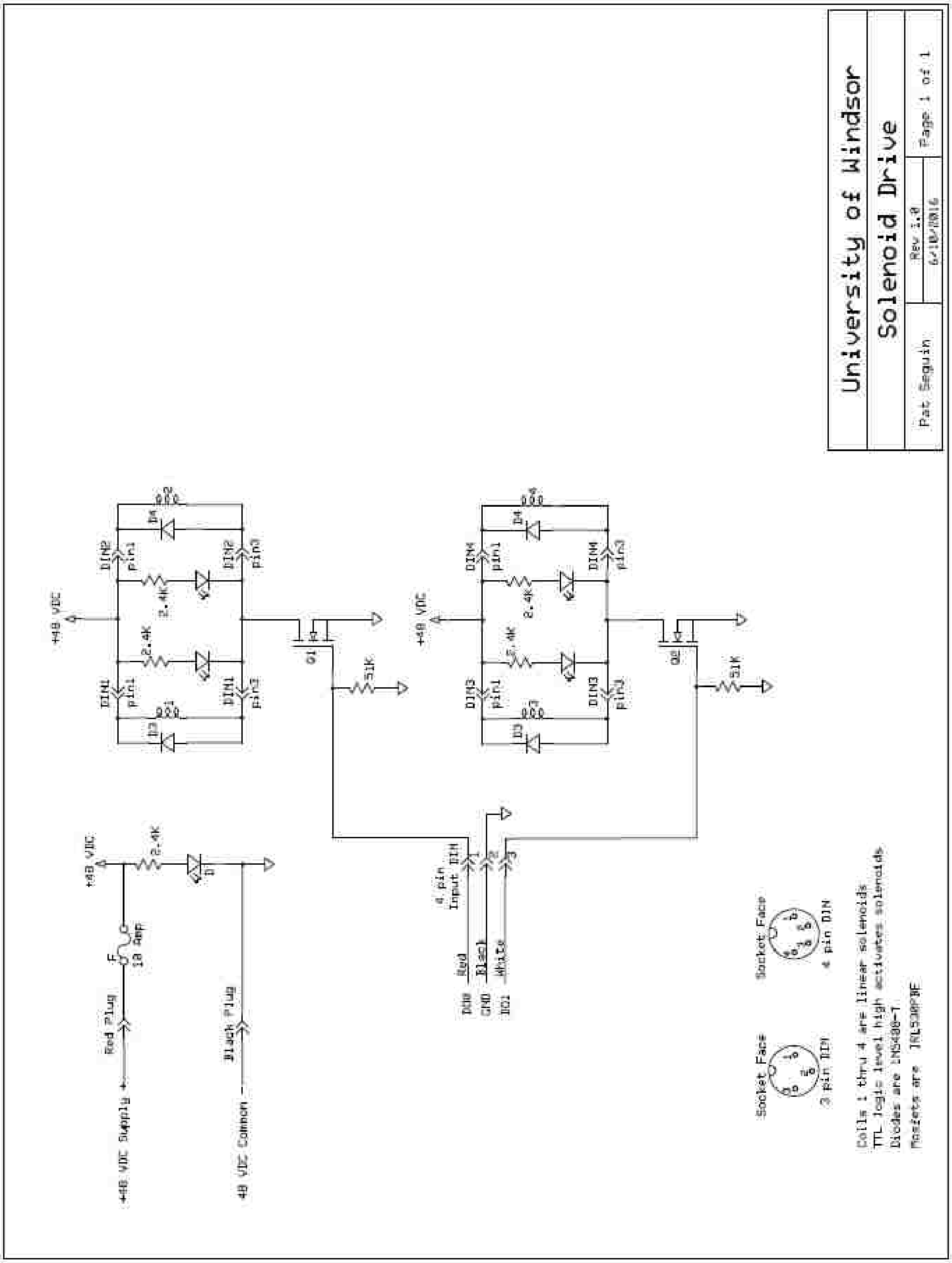

Figure C3: Solenoid Control System Circuit Diagram.

APPENDIX D: ENGINEERING PART DRAWINGS OF CUTTER DEPLOYMENT APPARATUS

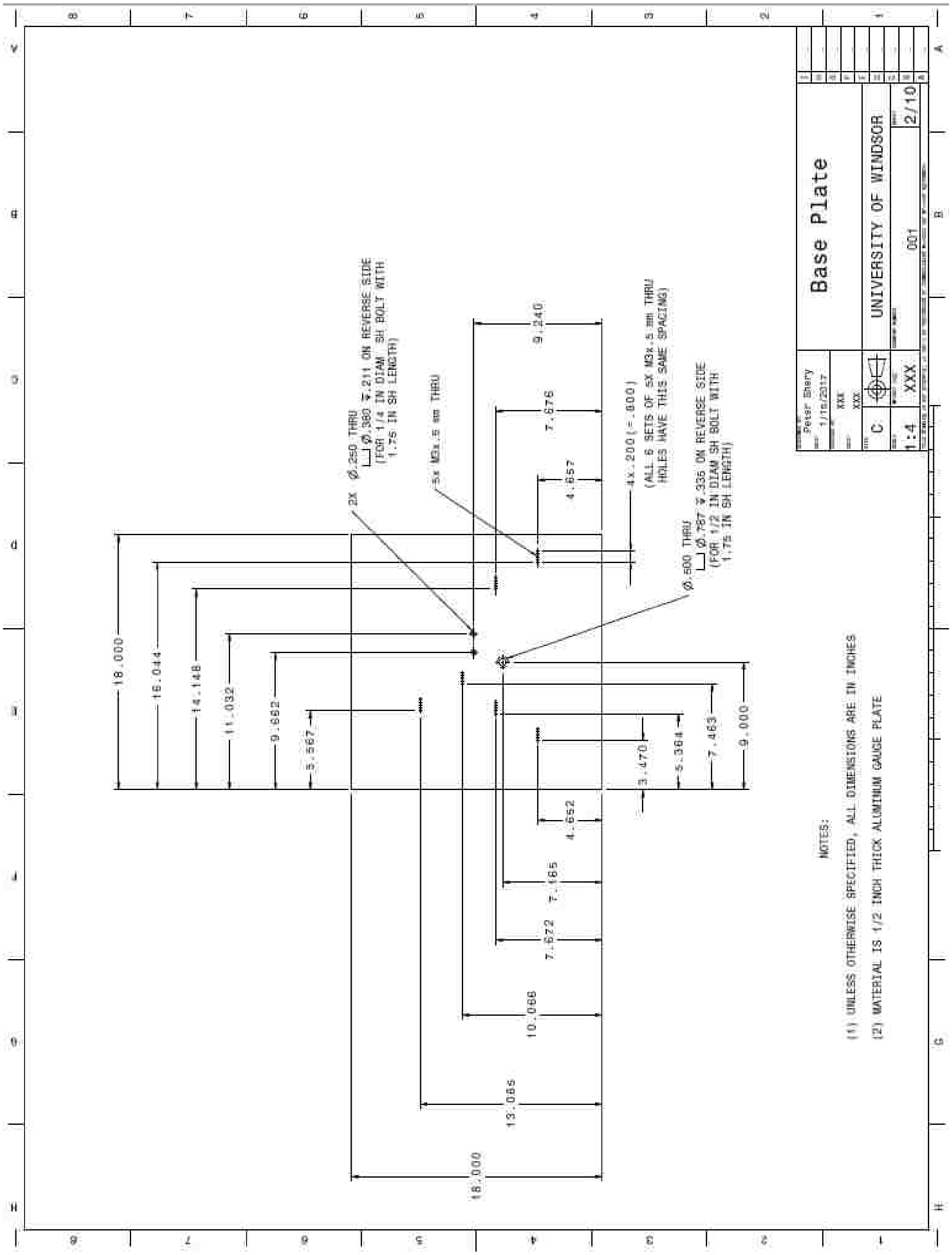

Figure D1: Base Plate.

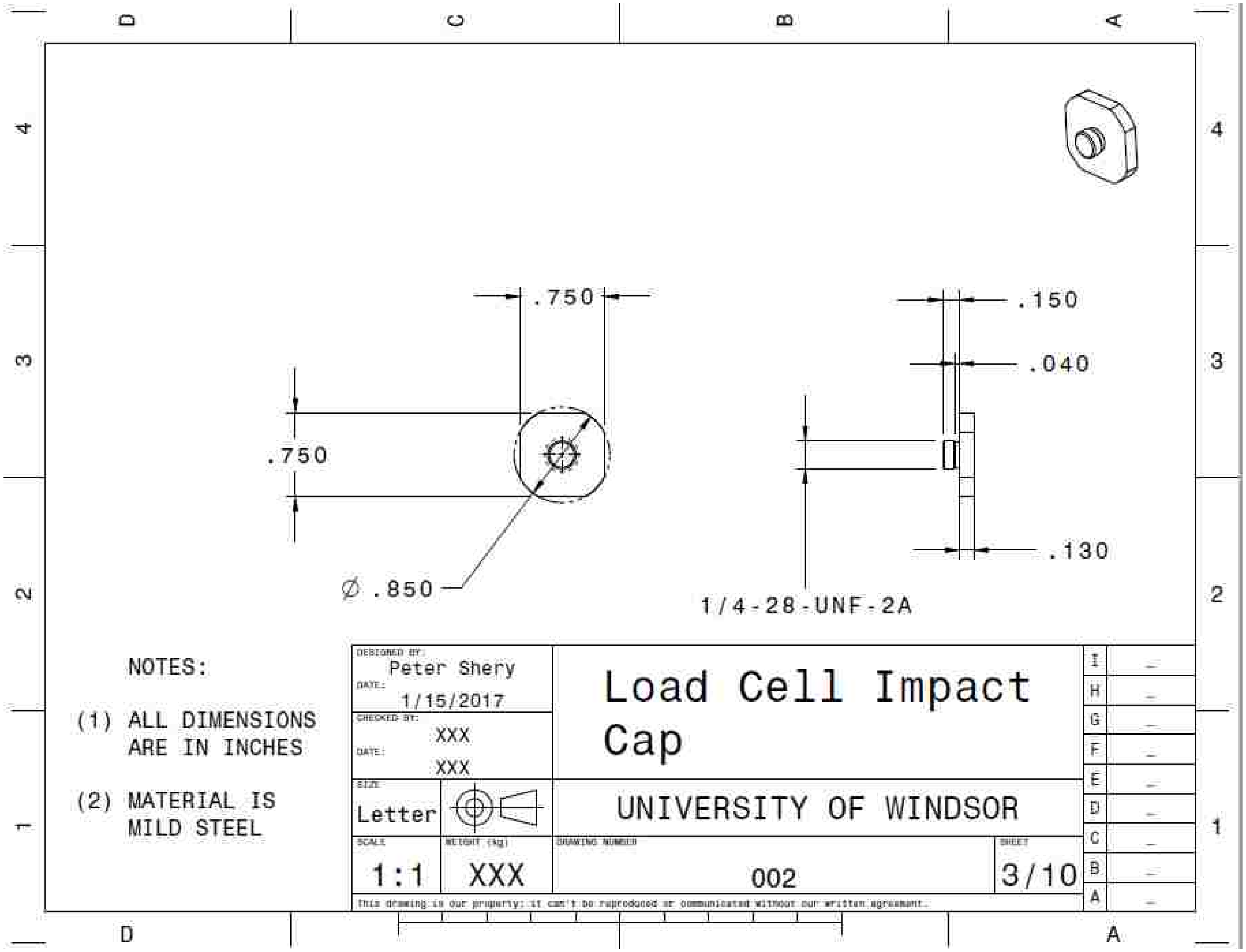

Figure D2: Load Cell Impact Cap.

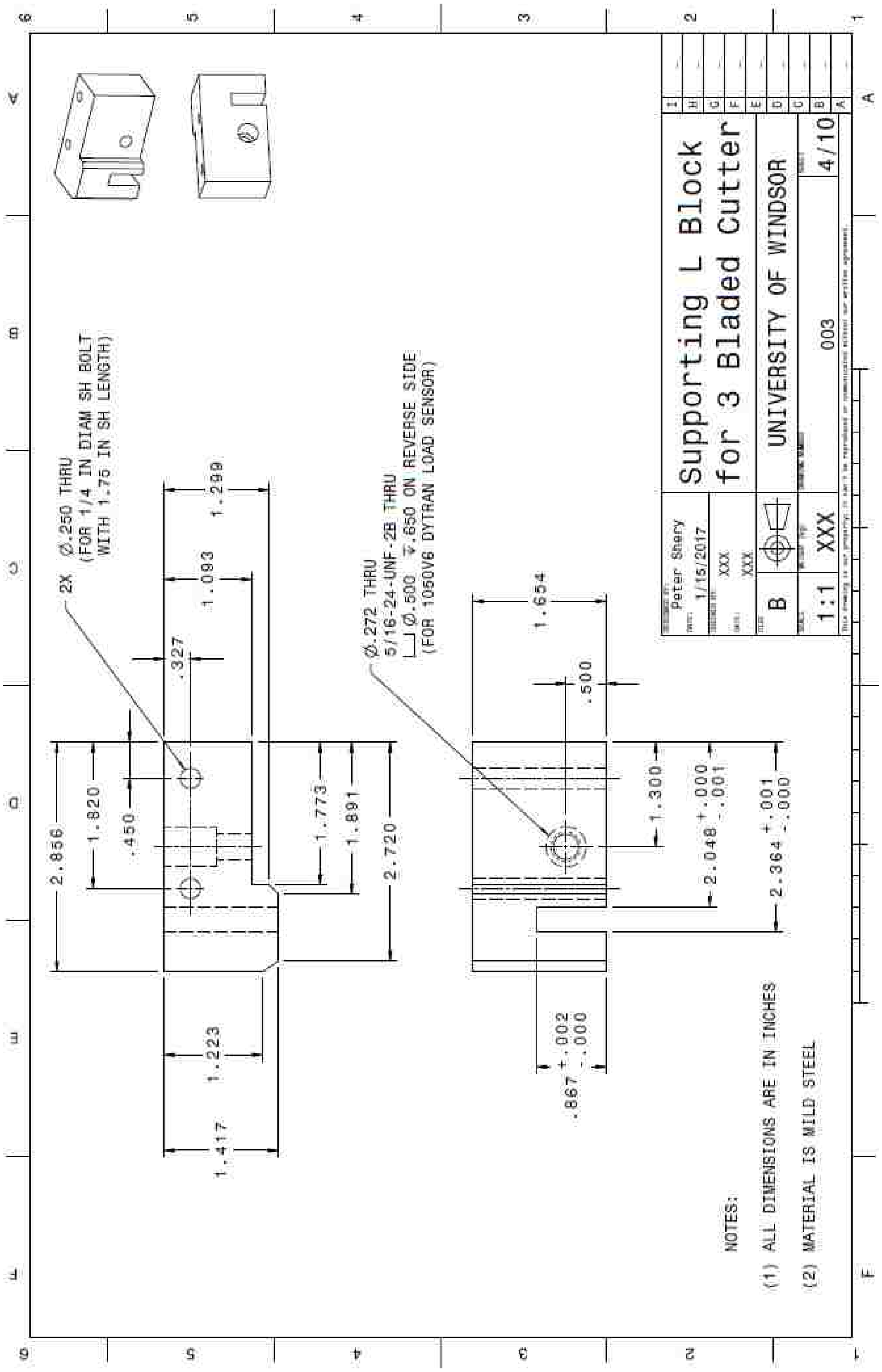

Figure D3: Supporting L-Block for 4-Bladed Cutter.

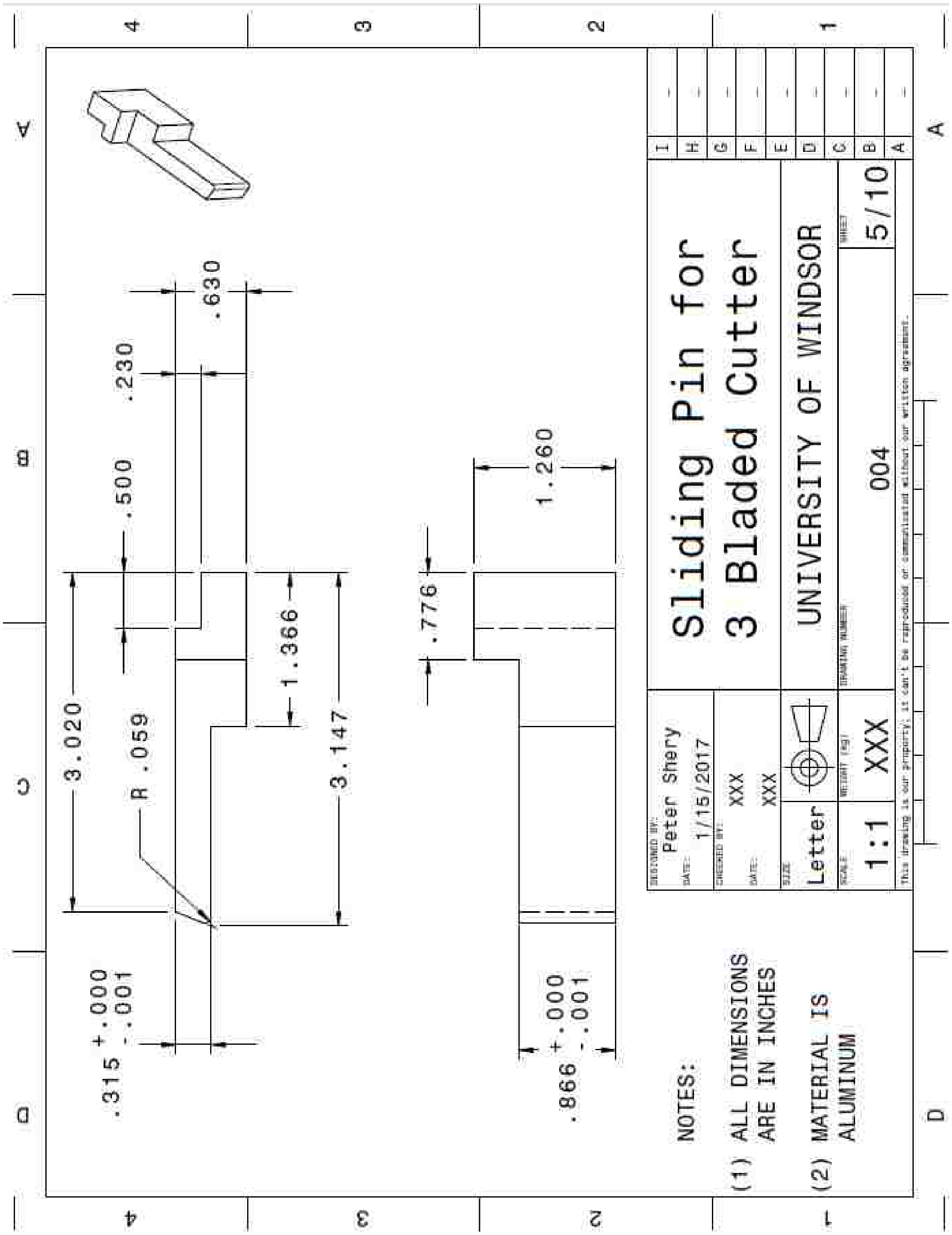

Figure D4: Sliding Pin for 3-Bladed Cutter.

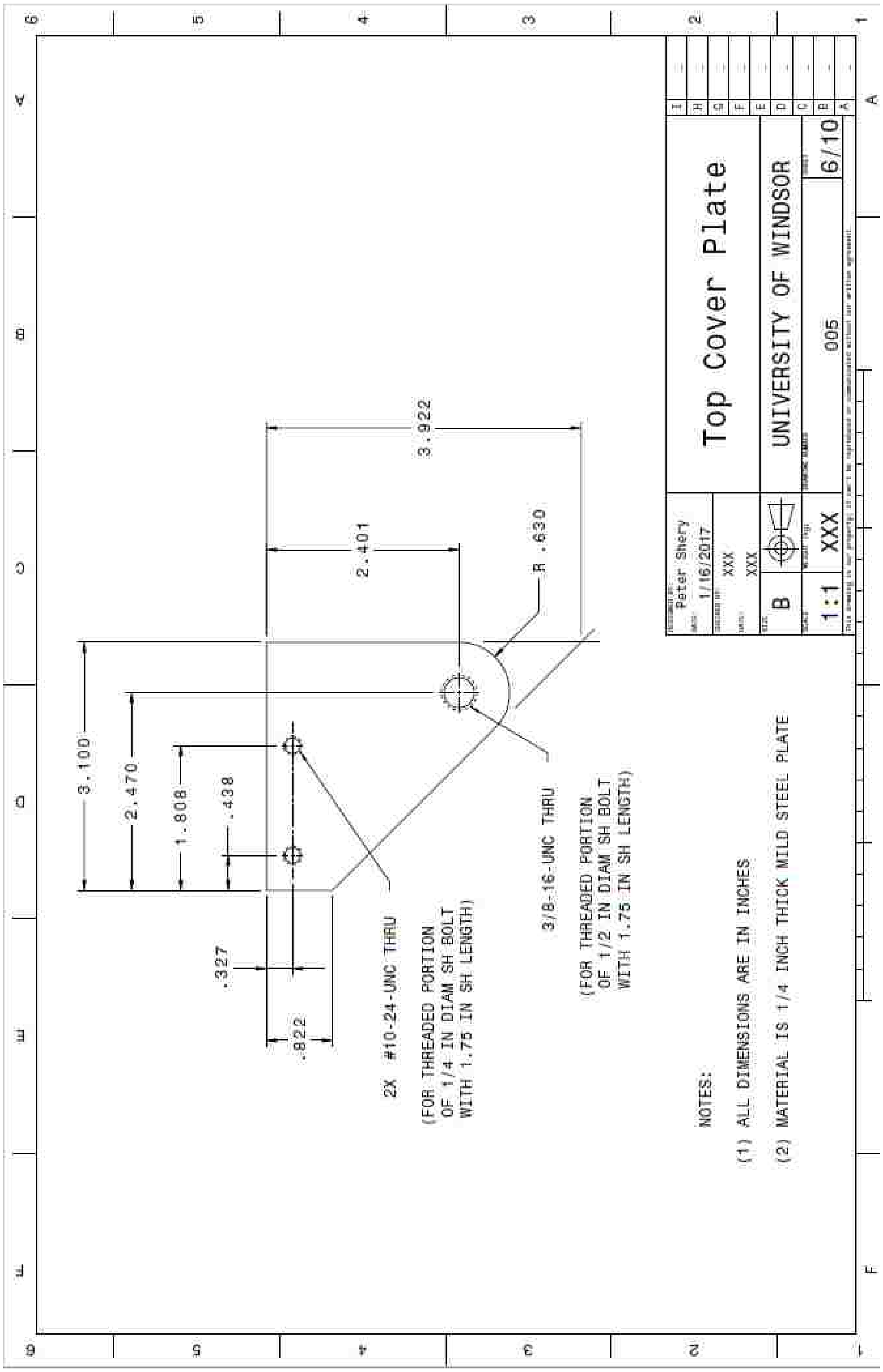

Figure D5: Top Cover Plate.

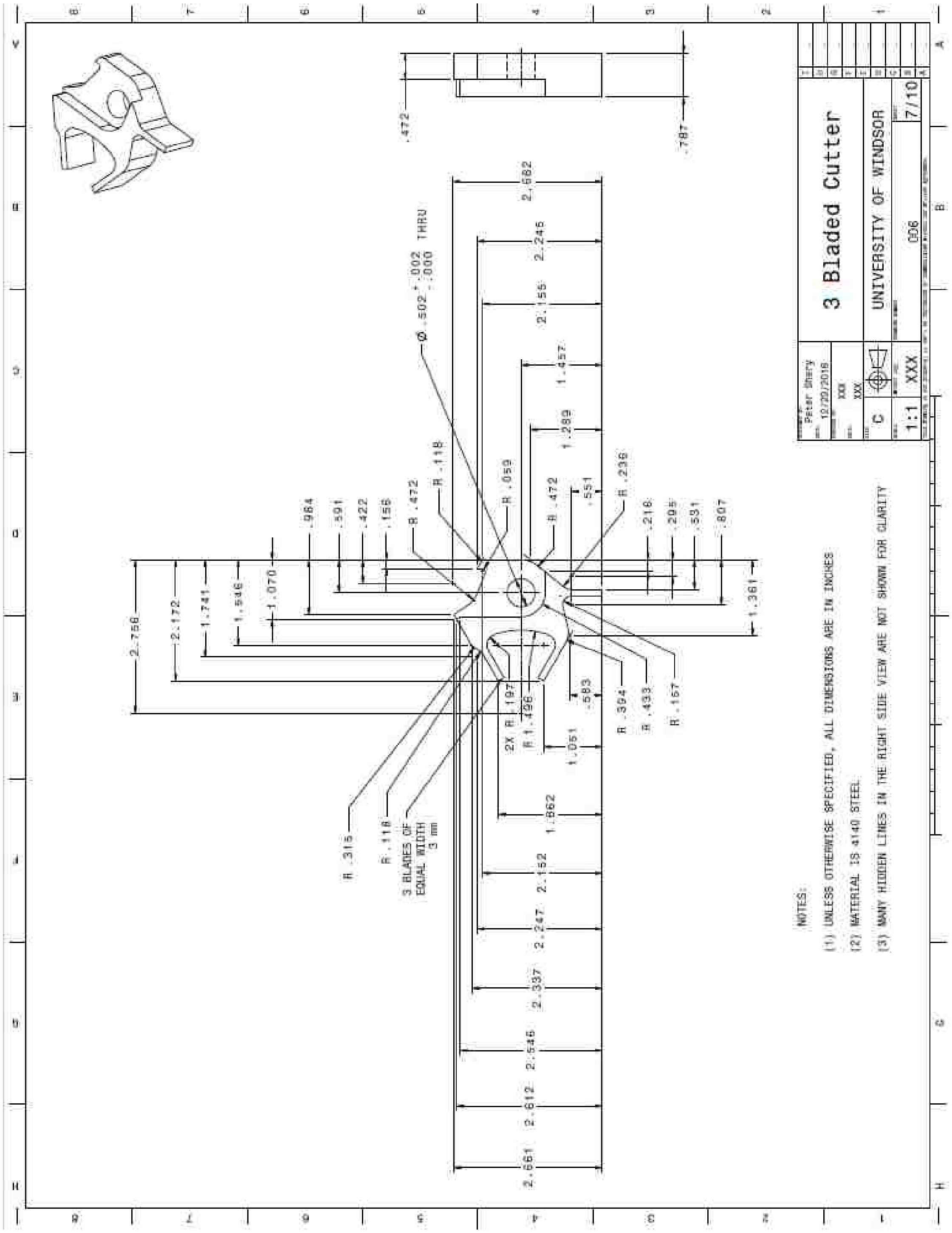

Figure D6: 3-Bladed Cutter.

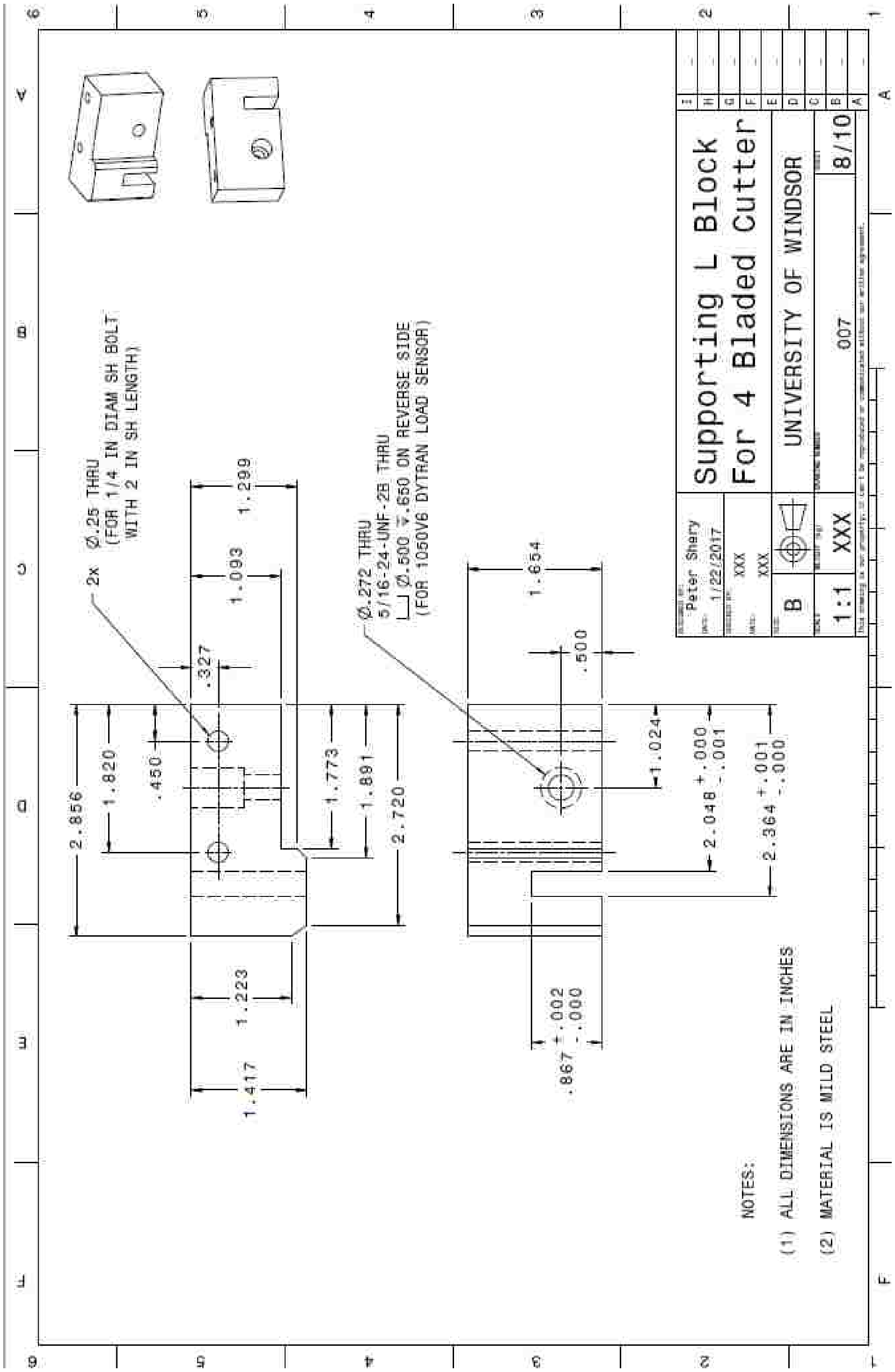

Figure D7: Supporting L-Block for 4-Bladed Cutter.

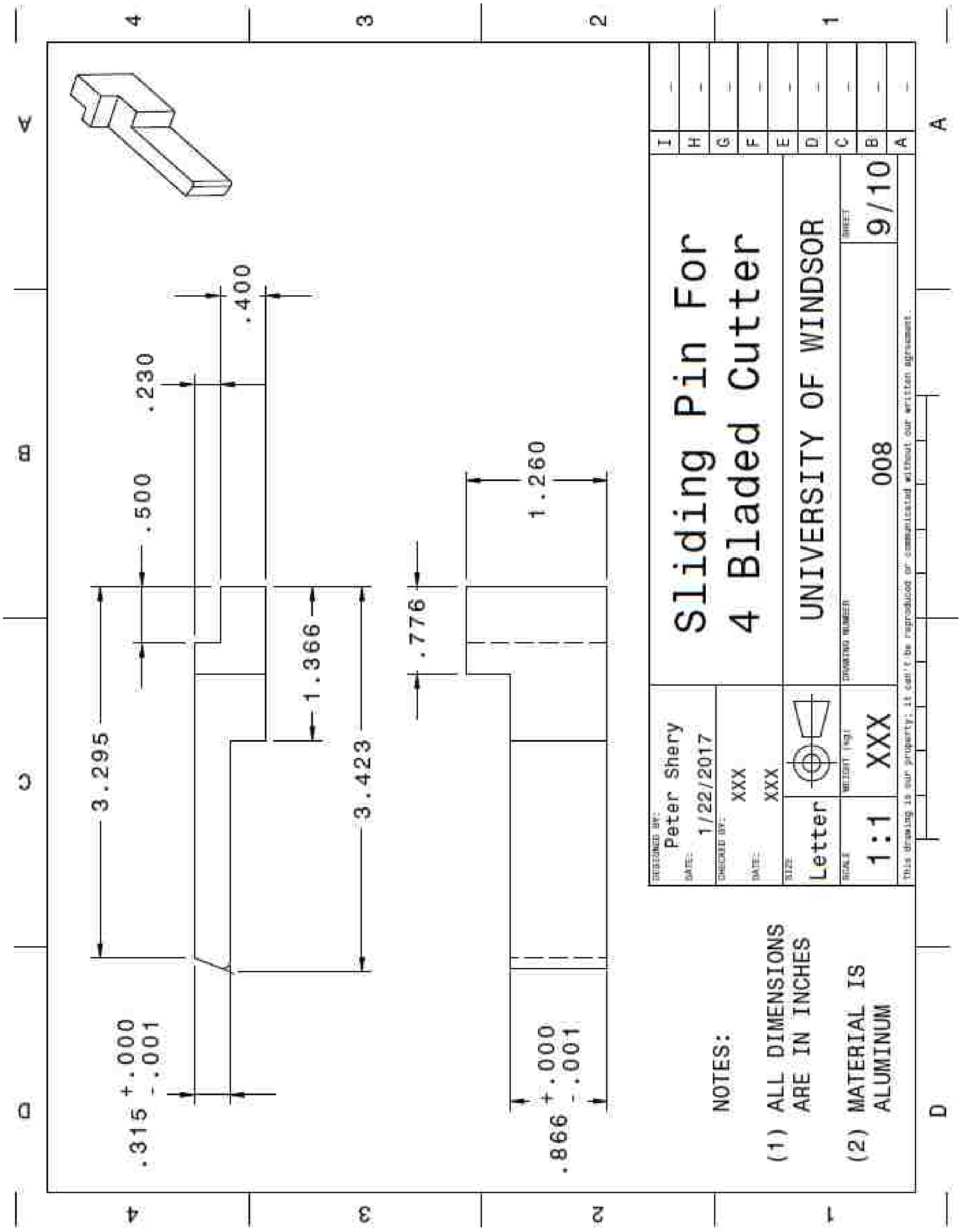

Figure D8: Sliding Pin for 4-Bladed Cutter.

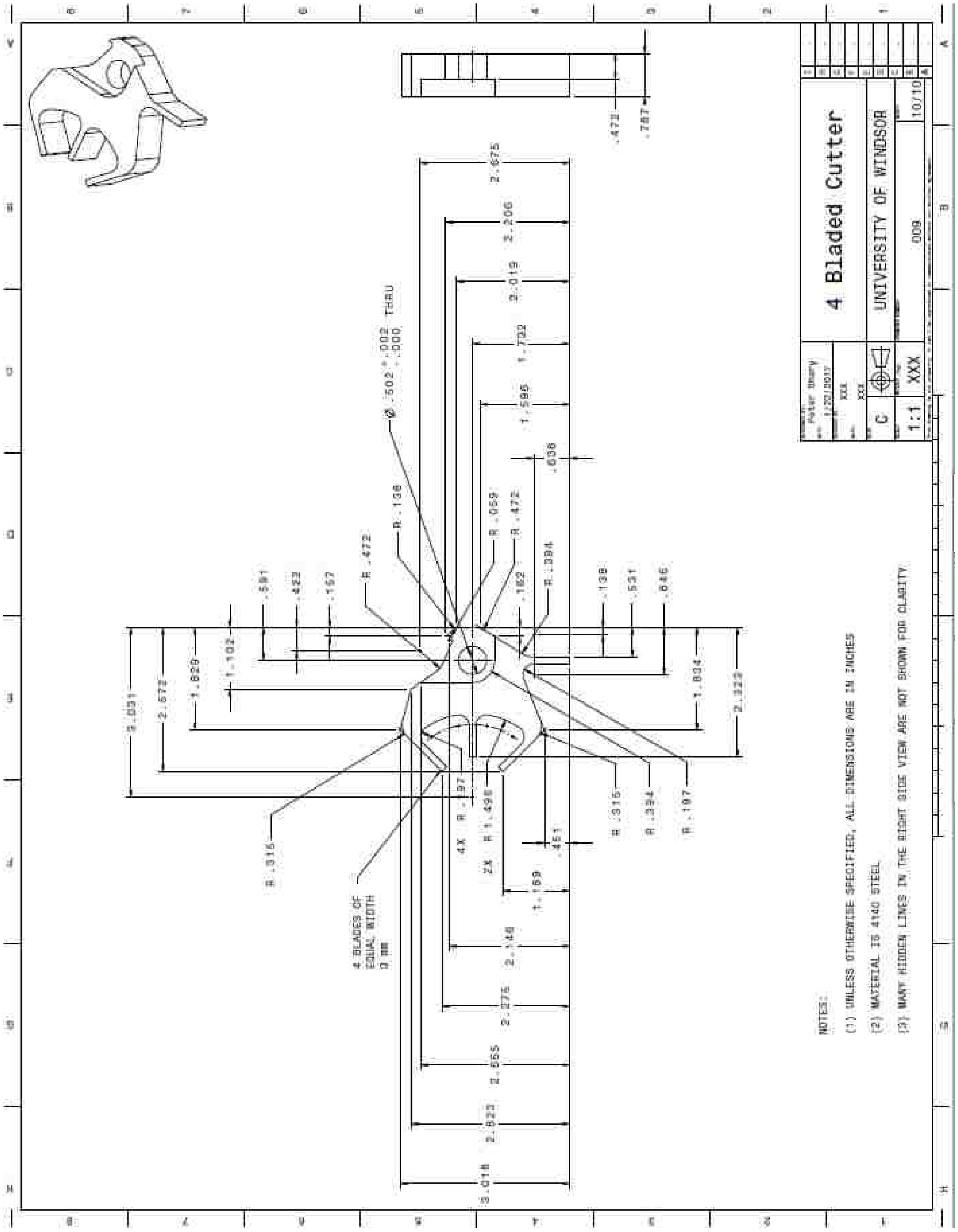

Figure D9: 4-Bladed Cutter.

APPENDIX E: PROPOSED FUTURE ADAPTIVE CUTTER DESIGN TO ACHIEVE FASTER RESPONSE TIME

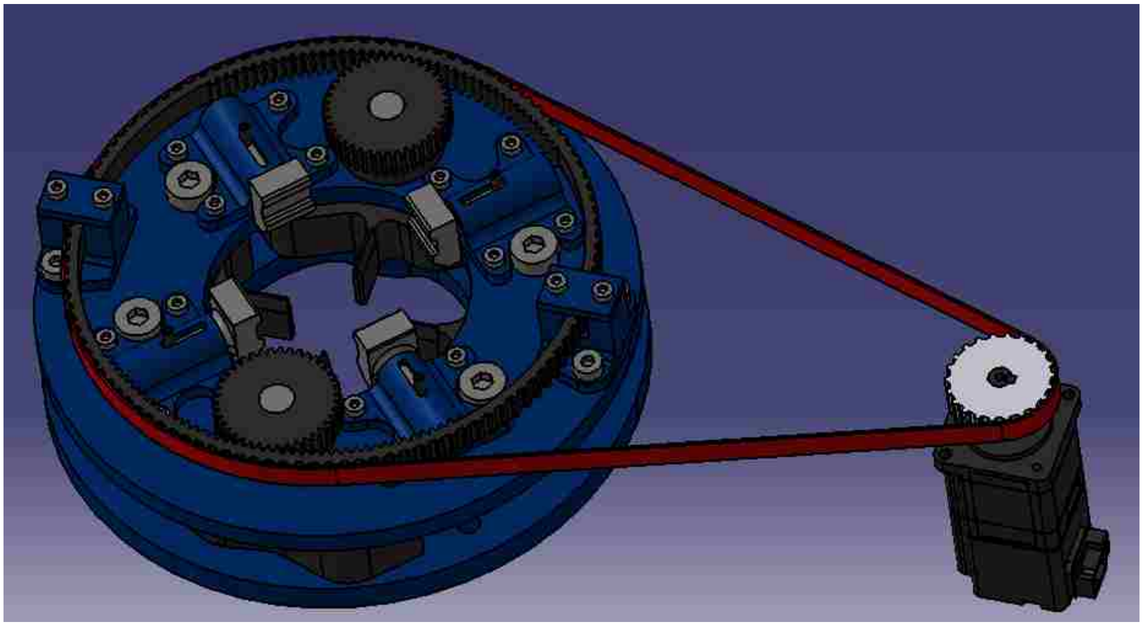

Figure E1: Direct-drive adaptive cutter system with timing belt and servomotor.

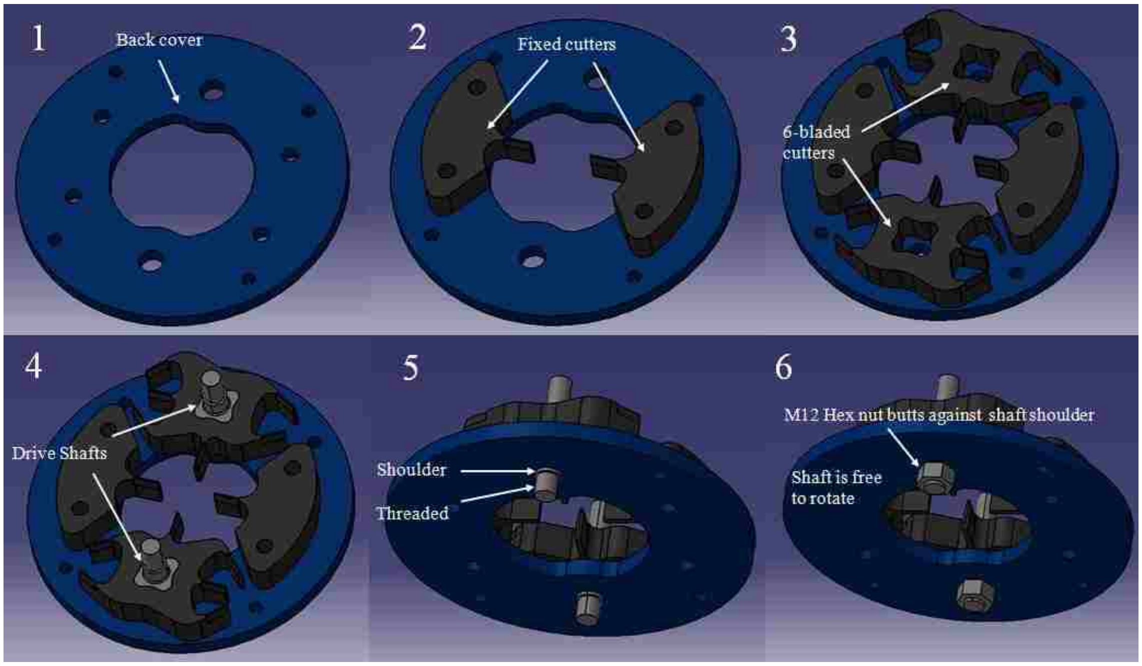

Figure E2: Step-by-step assembly of direct-drive adaptive cutter device.

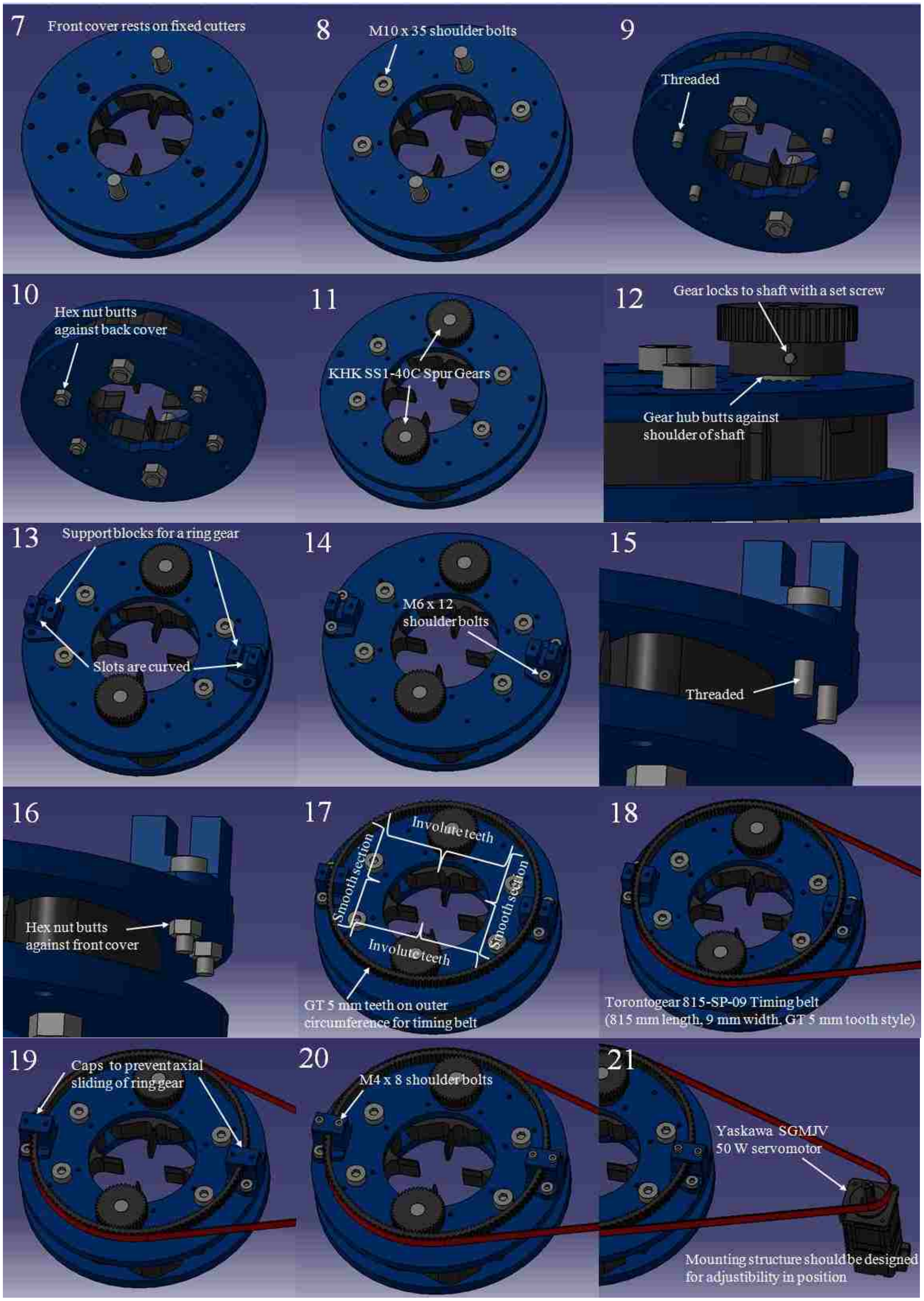

Figure E2: Step-by-step assembly of direct-drive adaptive cutter device (continued).

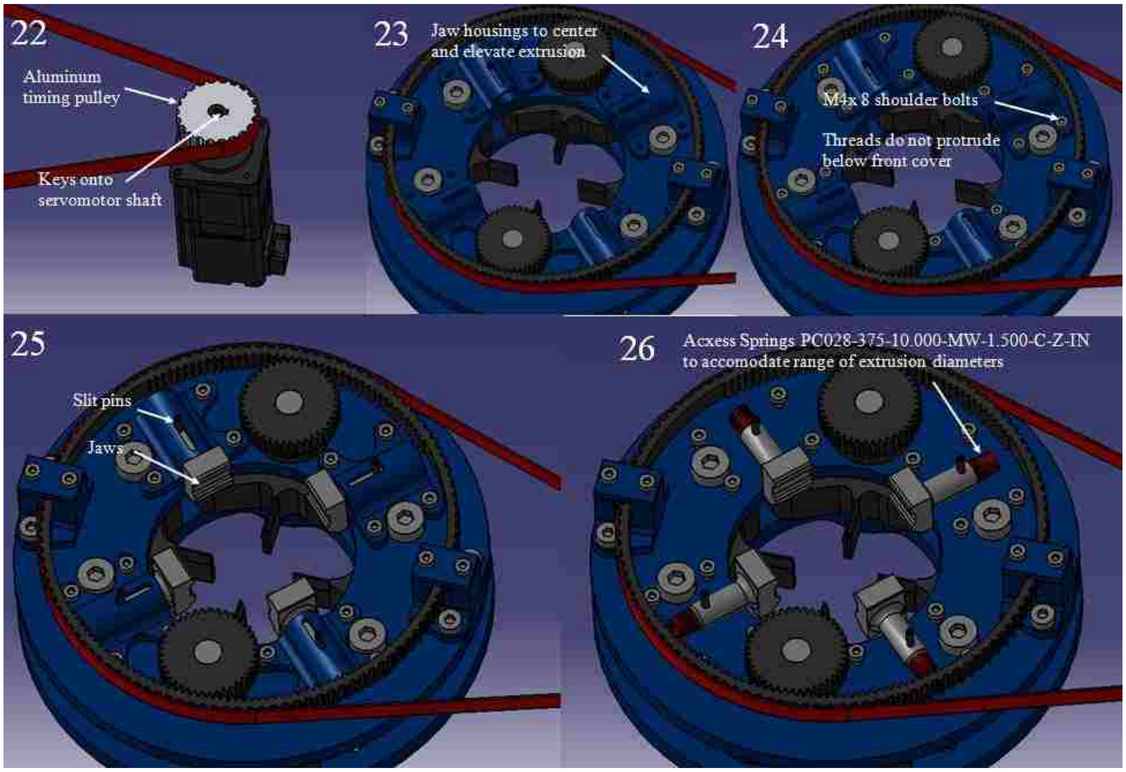

Figure E2: Step-by-step assembly of direct-drive adaptive cutter device (continued).

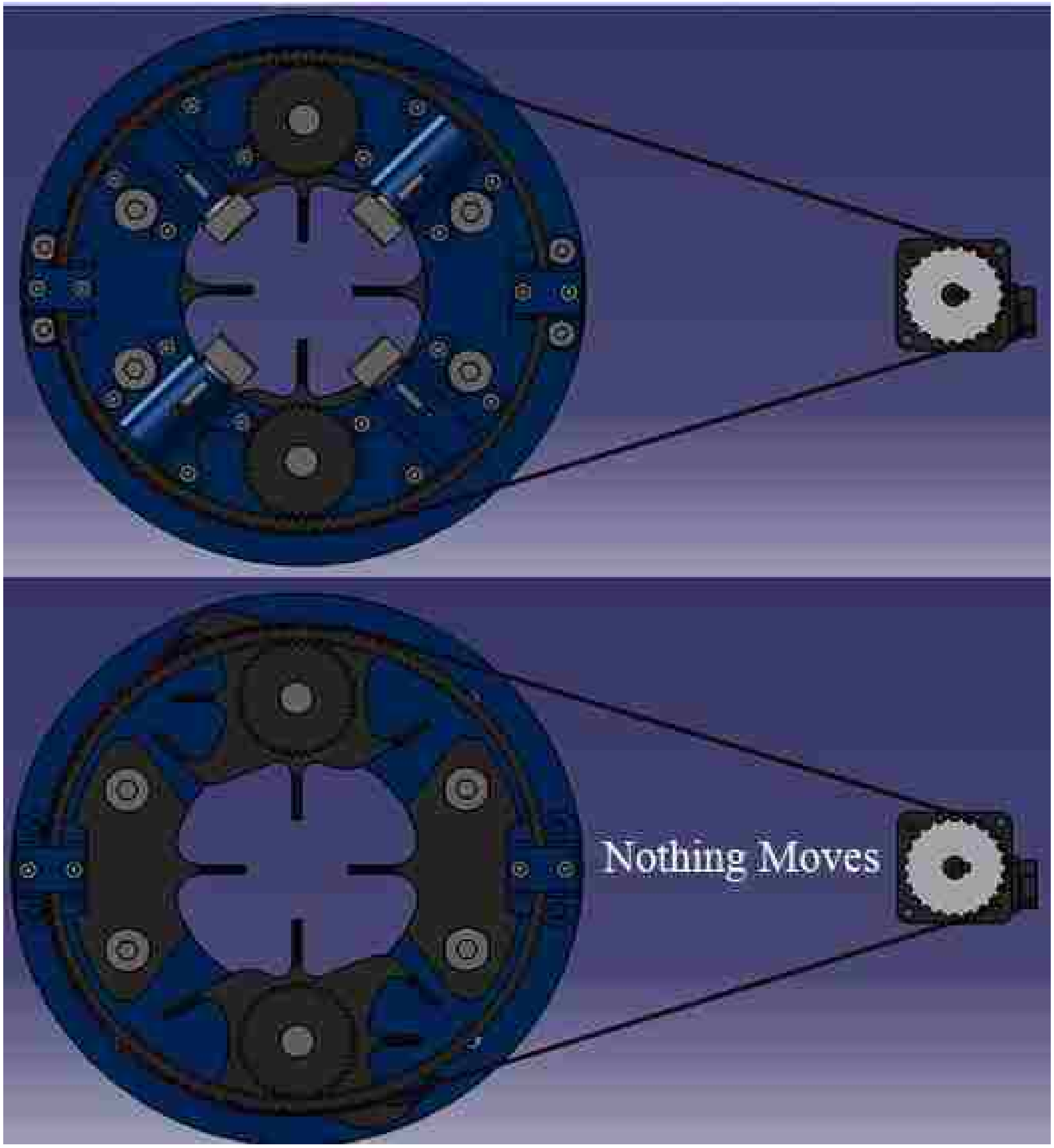

Figure E3: 4-blade configuration of direct-drive adaptive cutter device.

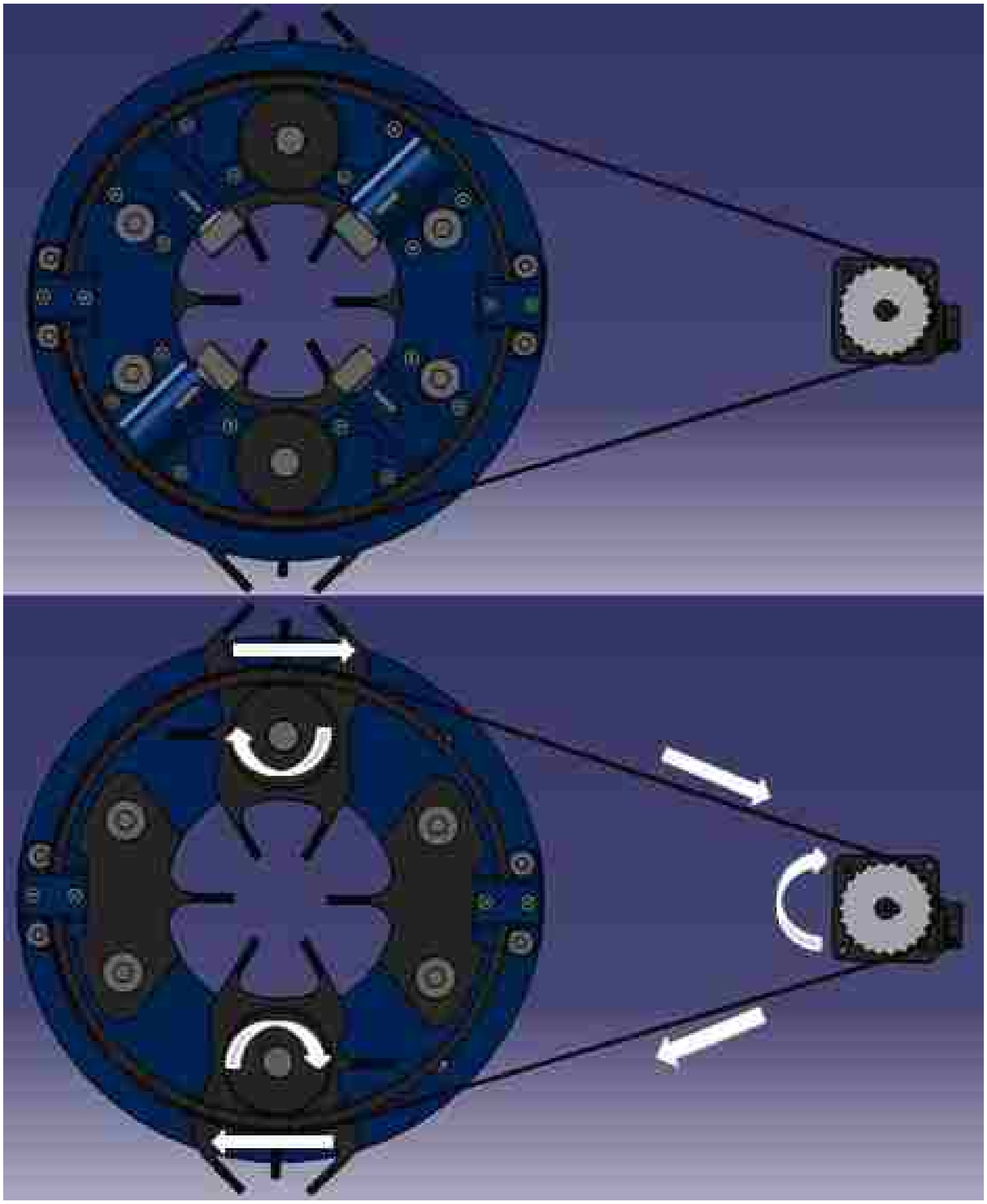

Figure E4: 6-blade configuration of direct-drive adaptive cutter device.

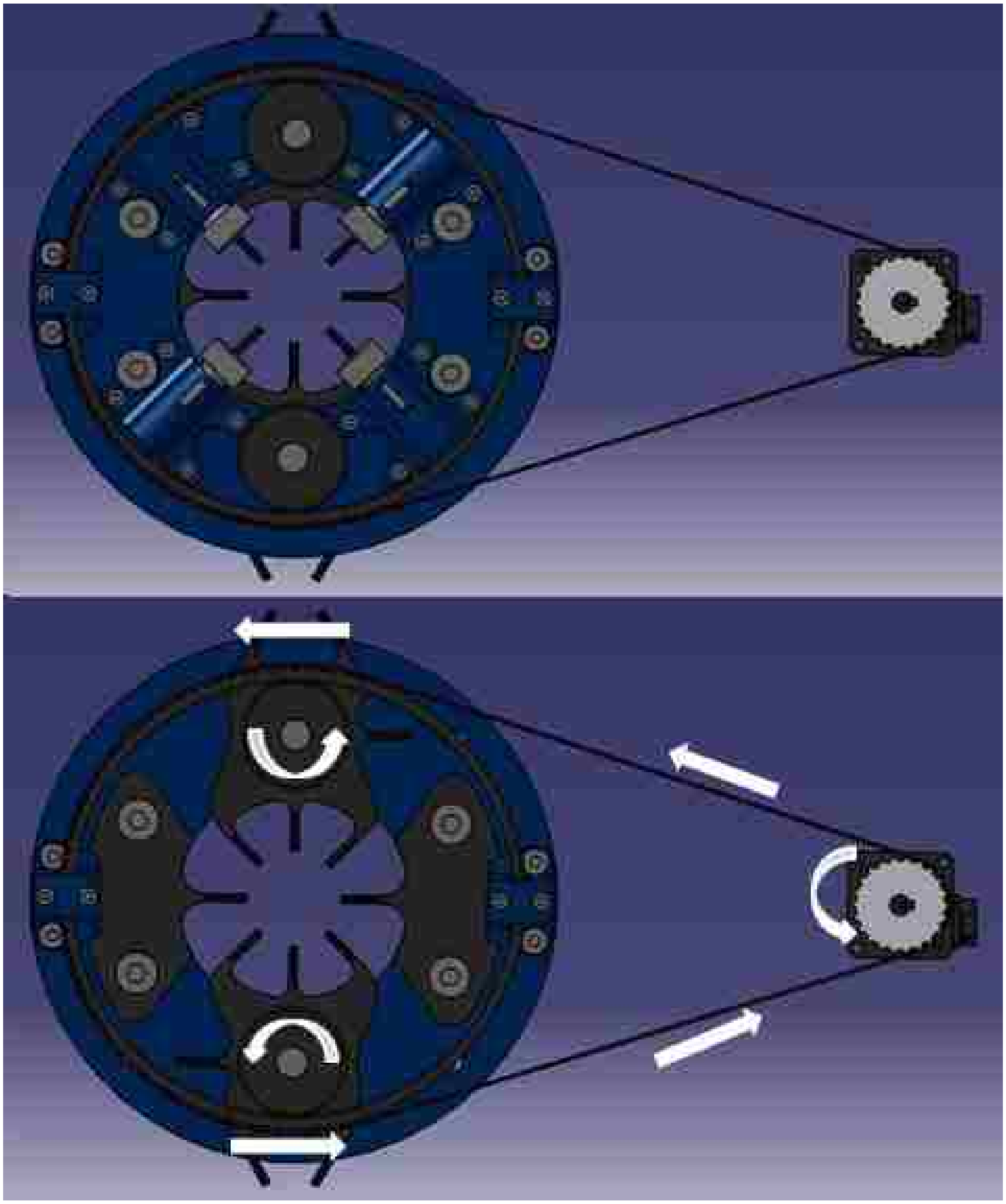

Figure E5: 8-blade configuration of direct-drive adaptive cutter device.

APPENDIX F: FAR-FIELD VIEW OF EXPERIMENTAL SETUP FOR CUTTER DEPLOYMENT APPARATUS

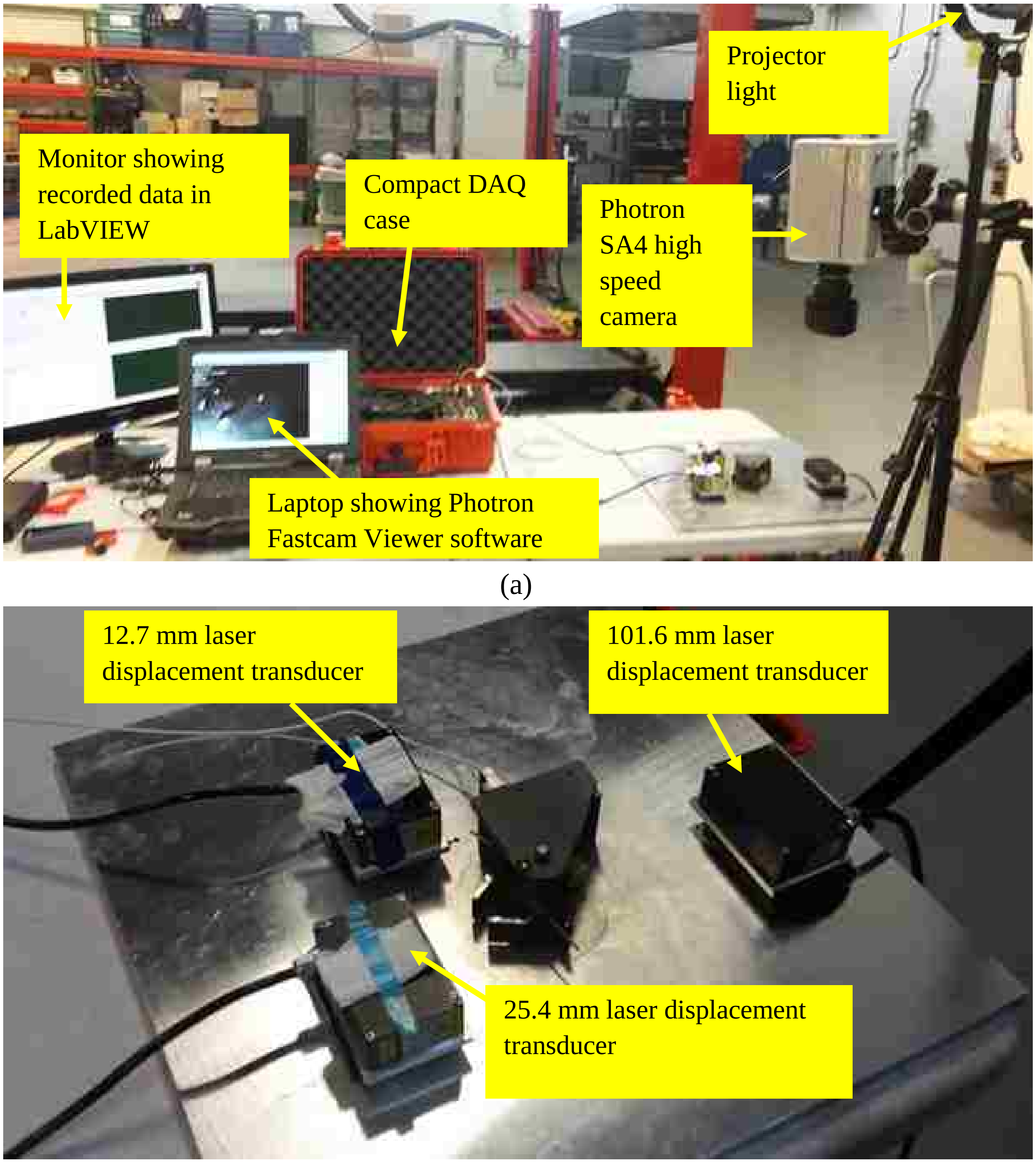

(a)

(b)

Figure F1: (a) Far-field view of experimental setup for cutter deployment apparatus. (b) Close-up view of cutter assembly with laser displacement transducers.

APPENDIX G: FINITE ELEMENT SIMULATIONS OF AXIAL CUTTING FOR THE FIRST ADAPTIVE CUTTER DESIGN

In this appendix, the results of the 3 cutting configurations for the first adaptive cutter that was deemed ready for numerical model development are presented. Details of the model development for axial cutting are not discussed here for brevity. They are instead described in Section 5.4 for the quadrotor adaptive cutter.

G.1 Axial Cutting with the First Adaptive Cutter in the 4-Blade Configuration

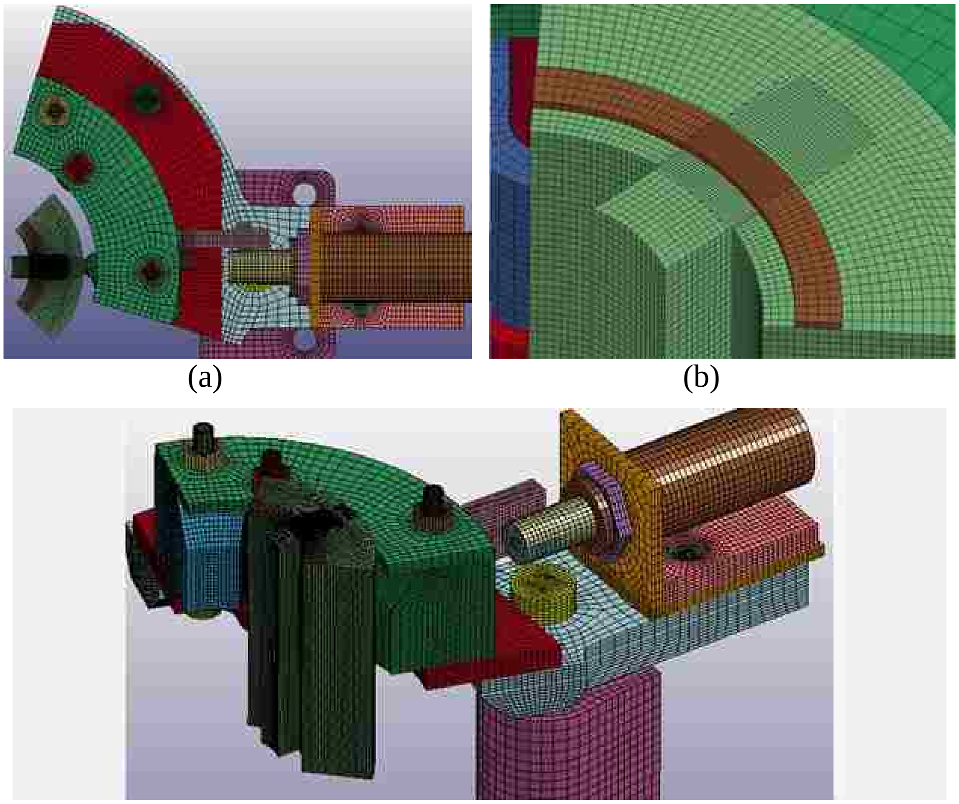

(a) (b)

(c)

Figure G1: Model of cutting simulation for the first adaptive cutter in the 4-blade configuration. (a) Top view. (b) Close-up view of extrusion and airmesh interface. (c) Isometric view of complete model.

An AA6061-T6 aluminum extrusion with 3.175 mm wall thickness and smallest diameter (44.45 mm) was considered in the analysis because the cantilever distance on the blades is longest, resulting in the worst load condition. The extrusion deformation is depicted in Figure G2(a) and (b). As expected, the petals of the extrusion flare only slightly and symmetrically on either side of the fixed blade.

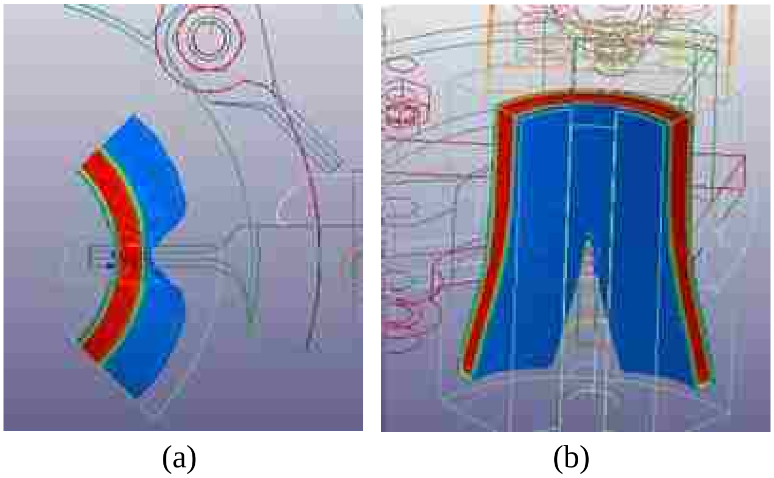

(a) (b)

Figure G2: Numerical simulation of extrusion deformation for the first adaptive cutter in the 4-blade configuration. (a) Top view. (b) Isometric view.

The forces from the extrusion acting on the blade are shown in Figure G3. The bulk of the cutting force is in the axial direction (*z-axis*) being approximately 10 kN. This force equates to 40 kN for 4 blades, which is consistent with experimental measurements in [11] and the prediction from the analytical model in Eq. 2.1 for the same extrusion thickness and diameter. The small *x* and *y* forces derive from the flaring petals rubbing on either side of the fixed blade, exerting outward radial forces.

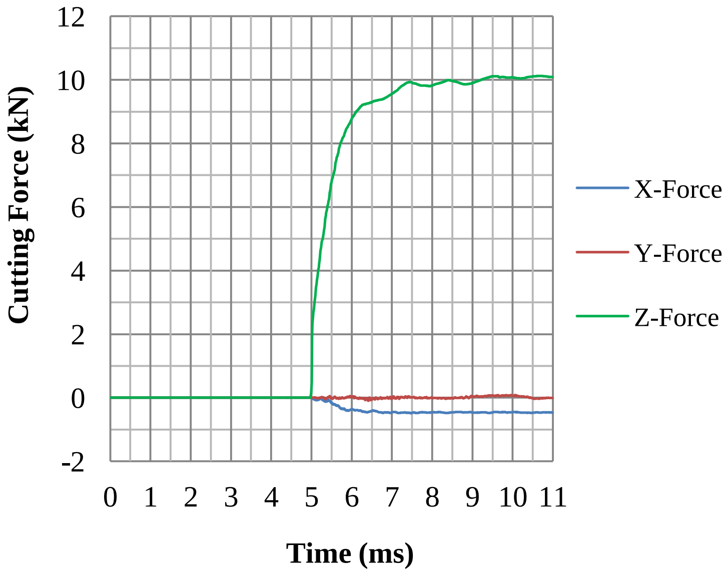

Figure G3: Cutting force for first adaptive cutter in 4-blade configuration.

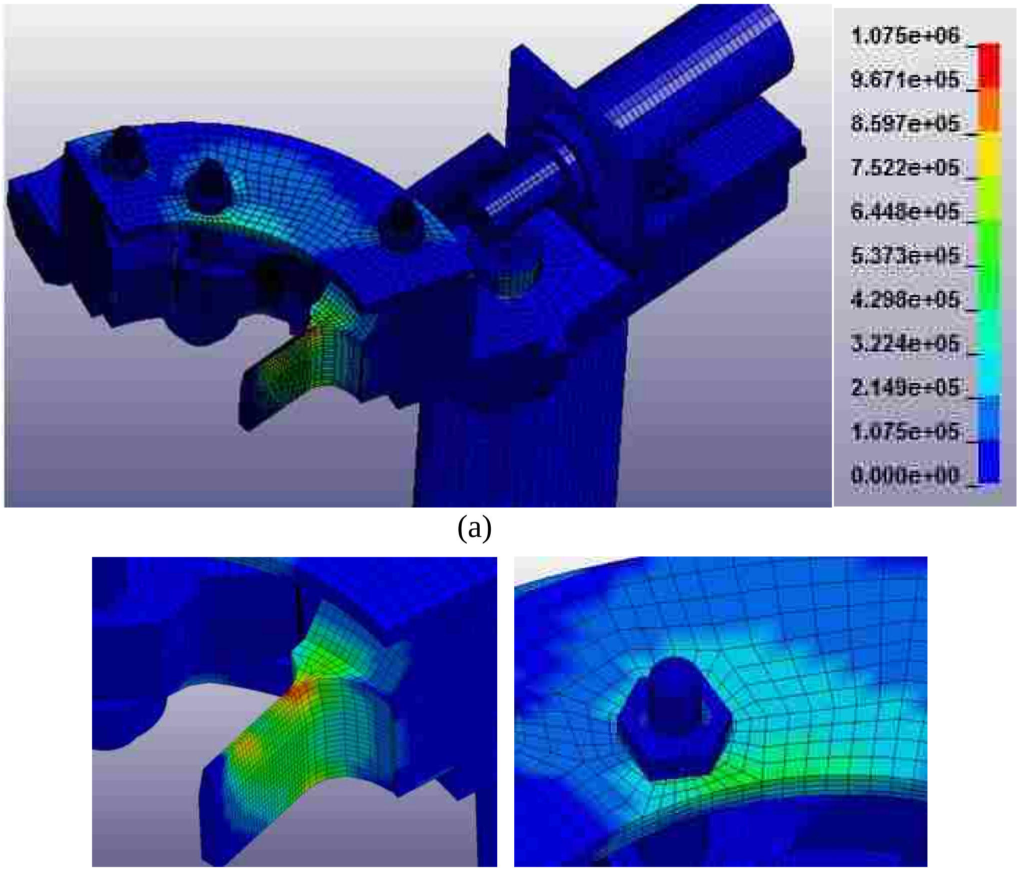

(a)

(b) (c)

Figure G4: von Mises stress contours (kPa) for first adaptive cutter in 4-blade cutting. (a) Complete device. (b) Fixed blade. (c) Front cover.

The effective stresses in the adaptive cutter are illustrated in Figure G4. Globally, as seen in Figure G4(a), the critical region is at the root of the fixed blade being approximately 1100 MPa. The next region of high stress is in the front cover at 430 MPa, depicted in Figure G4(c). Stresses in all other components are far below 400 MPa and are summarized in Table G1 at the end of this appendix.

G.2 Axial Cutting with the First Adaptive Cutter in the 6-Blade Configuration

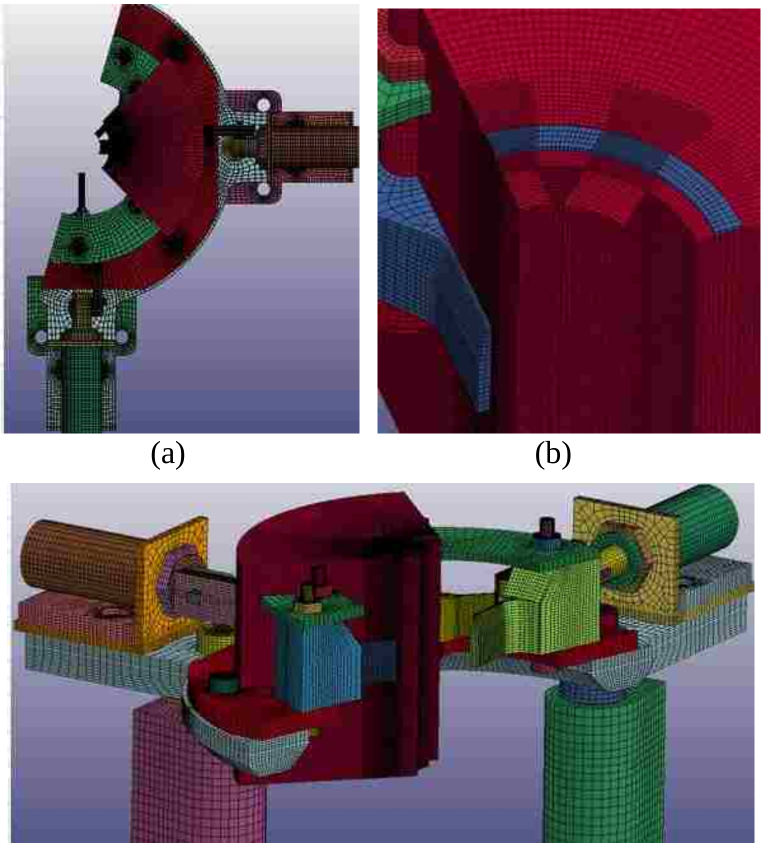
(a) (b)

(c)

Figure G5: Model of cutting simulation of first adaptive cutter in the 6-blade configuration. (a) Top view. (b) Close-up view of extrusion and airmesh interface. (c) Isometric view of complete model.

Note from Figure G5(b), only half of the switchblade (blue entity) is covered by the boundary of the airmesh (red quarter-cylinder entity). Given the geometry of the 6-blade arrangement, half of the switchblade must be covered to correctly apply reflective symmetry at either airmesh boundary. The outer radius of the airmesh is larger than that in the 4-blade cutting model because the degree of petal flaring is expected to be more significant. The discretization and element formulations of the mesh are the same as for the 4-blade cutting simulation.

The cutting deformation of an AA6061-T6 extrusion with wall thickness of 3.175 mm and the smallest diameter (44.45 mm) is depicted in Figure G6. Although the petals do not contact any part of the device other than the blades, slightly more petal flaring occurs on one side of the fixed blade. This asymmetric petal flaring is expected for the fixed blade since the next consecutive blade on either side has inconsistent angular spacing; 45 degrees on one side, but 90 degrees on the other side. However, the slightest difference in flaring causes the fixed blade to be subjected to a resultant side load, which would otherwise be cancelled out if flaring was symmetric. As evidenced in Figure G6(a), the side load bends the fixed blade, and combined with the axial cutting force, causes the fixed blade to twist to certain failure. Another problem is noticed regarding the selected boundary conditions for the airmesh/extrusion: by covering only half of the switchblade, the extrusion forces the switchblade out of alignment with the radial direction. The cutting force on the switchblade is therefore less than half of the true cutting force on the switchblade.

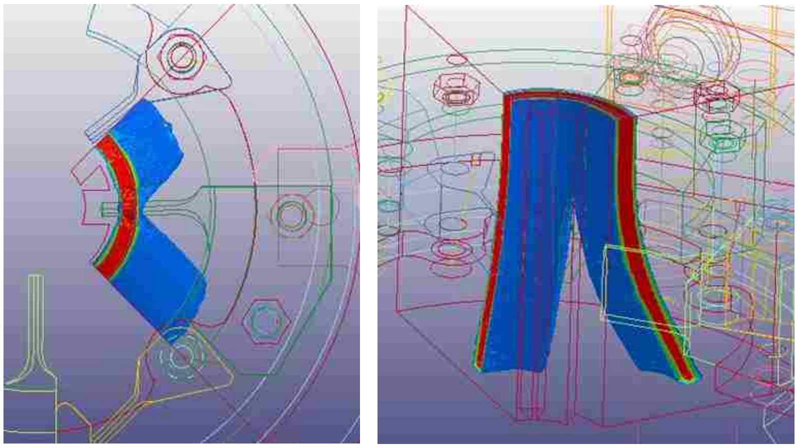
(a) (b)

Figure G6: Numerical simulation of extrusion deformation for first adaptive cutter in the 6- blade configuration using 44.45 mm diameter, 3.175 mm thick extrusion. (a) Top view. (b) Isometric view.

The results shown in Figure G6 alone demonstrate the need to have (1) equal blade spacing about the circumference, and (2) the airmesh and extrusion covering the entire blade to properly represent the externally applied cutting force on the adaptive cutter.

The cutting force along the axial and side directions for the 6-blade arrangement is shown in Figure G7. The axial force (*z axis*) shows a “blip” in the response at 6 ms which is caused by the offset in axial distance between the fixed blade and switchblade. The extrusion contacts the tip of the fixed blade at approximately 5 ms, but only makes contact with the tip of the switchblade, being 4 mm lower than the tip of the fixed blade, 1 ms later. If the fixed blades and switchblades were all in the same plane, the cutting force/time response would not show this discontinuity. On the other hand, the switchblade would not have the needed clearance to deploy below the mounted extrusion. Also, the axial cutting force stabilizes at approximately 11 kN, which is only 1 kN higher than the 4-blade simulation. One expected that since the cutting force for this diameter and thickness extrusion using 4 blades was 10 kN per blade, the cutting force for the 6-blade configuration would be 1.5 times higher. However, the switchblade was pushed out of its radial position, underestimating its axial component of the cutting force. The asymmetric petal flaring is further highlighted by the large *x* and *y* forces acting on the sides of the fixed blade. With symmetric petal flaring, these components of the cutting force would be closer to zero, unless the petals rub against other parts of the device where friction would contribute to *x* and *y* forces.

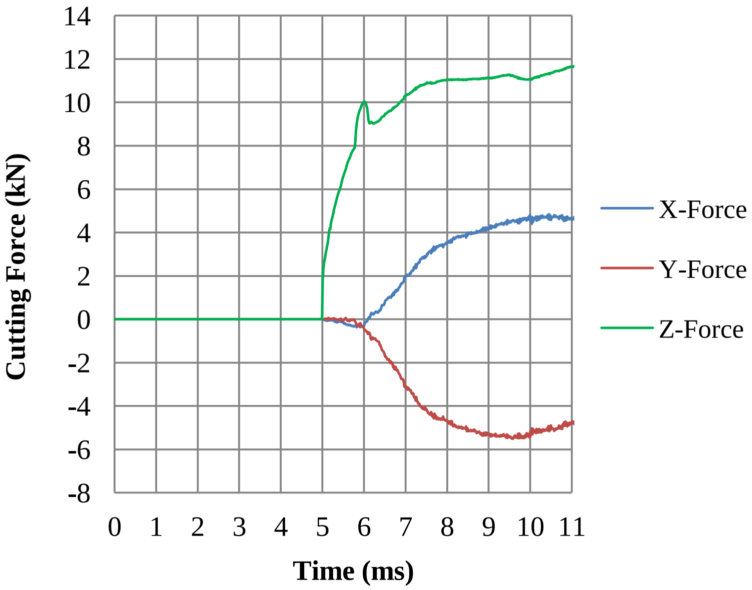

Figure G7: Cutting force for first adaptive cutter in 6-blade configuration using 44.45 mm diameter, 3.175 mm thick extrusion.

The effective stresses in the main components of the adaptive cutter are shown in in Figure G8. Globally, the highest stresses in the device, similar to the 4-blade cutting configuration, are in the blades as evidenced by the predominantly blue regions in Figure G8(a). The twisting of the fixed blade is also clearly seen, inducing excessively high stress of 2200 MPa at the root on the side face, indicated by the yellow zone. This stress approaches the yield strength in tension of the strongest tool steels available. The red zone of 3100 MPa stress is located on the side of the switchblade, but is not realistically represented since the boundaries of the airmesh had caused the switchblade to be pushed out of position. Nonetheless, the unequal blade spacing of the 6-blade configuration should be avoided. The cutting load on the switchblade tends to not only push the switchblade down against the back cover, but also pull the switchblade radially inward, loading the bolt shaft perpendicularly. The resulting stress on this ¼ in bolt

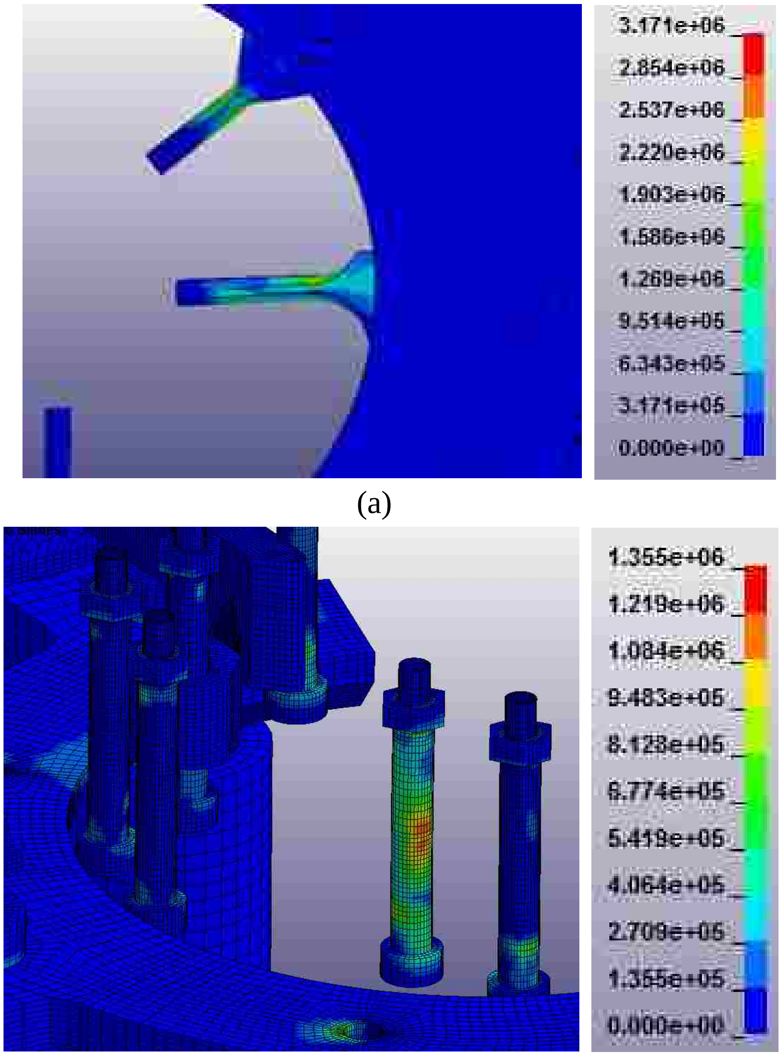

(a)

(b)

Figure G8: von Mises stress contours (kPa) in first adaptive cutter for 6-blade cutting. (a) Top view. (b) Shoulder bolts exposed.

shaft, indicated in orange in Figure G8(b) is 1200 MPa. The yield strength of shoulder bolts are rated at 800 MPa, which indicates that failure would likely occur. Conversely, the stresses in the ¼ in shoulder bolts through the fixed blades are much lower because the shafts are surrounded by a significant amount of material which experience little stress compared to the fixed blades themselves.

G.3 Axial Cutting with the First Adaptive Cutter in the 8-Blade Configuration

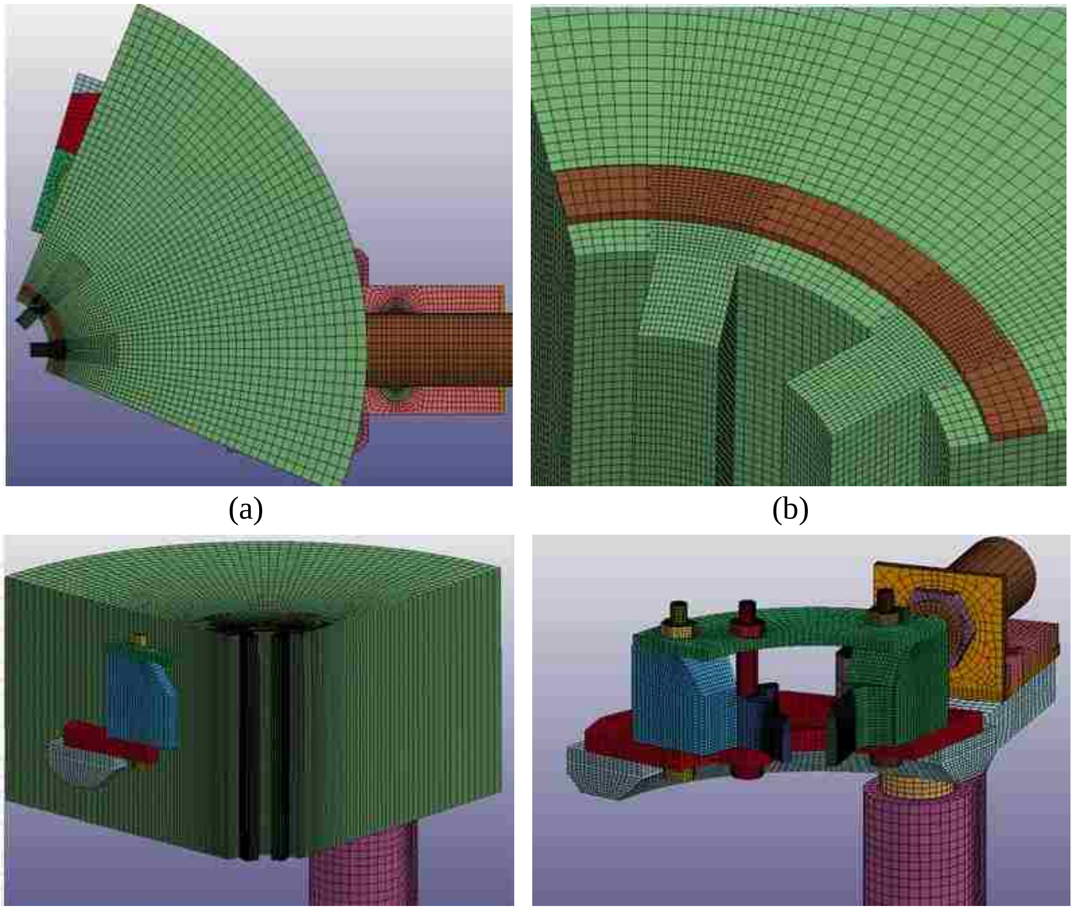

(a) (b)

(c) (d)

Figure G9: Model of first adaptive cutter in 8-blade cutting. (a) Top view. (b) Close-up view of extrusion and airmesh interface. (c) Isometric view of complete model with airmesh. (d) Airmesh removed.

Note the radius of the airmesh in Figure G9 has been extended substantially to ensure the flaring of the petals will be contained within the airmesh walls. The cutting deformation of an AA6061-T6 extrusion with 3.175 mm wall thickness and the smallest diameter (44.45 mm) is depicted in Figure G10. With equal blade spacing, the extrusion petal flaring is symmetric, but very significant. Figure G10(b) clearly shows that the petals will unavoidably rub against the thicker face on the fixed blade, the back cover, and the elevated platform if the simulation continued further in time.

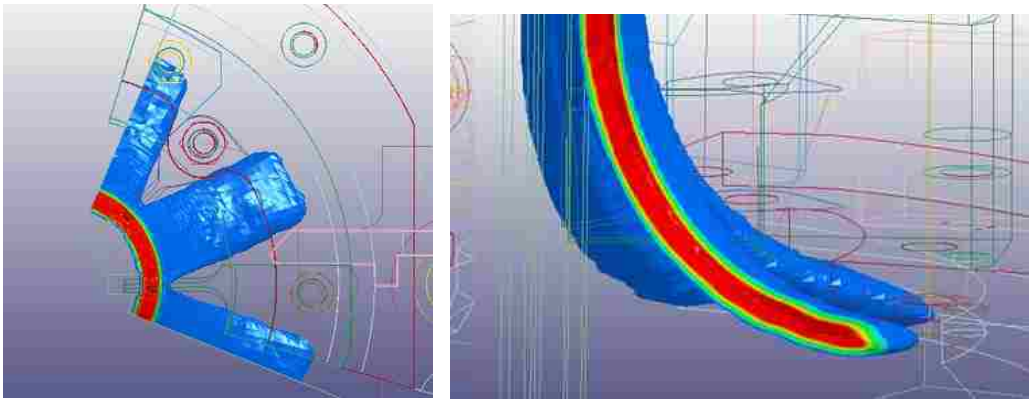

(a) (b)

Figure G10: Numerical simulation of extrusion deformation for first adaptive cutter in the 8-blade configuration using 44.45 mm diameter, 3.175 mm thick extrusion. (a) Top view. (b) Side view of petal flaring contacting back cover.

Similar to the 4-blade cutting configuration, the majority of the cutting force for the 8-blade configuration, as seen in Figure G11, is axial (*z-axis*). The steeper slope beginning at approximately 6 ms and 8 kN is the instant the extrusion makes contact with the switchblade. A steady axial load of 18 kN is reached until a time of 11 ms, when the extrusion petals contact the thicker face on the fixed blade and the load gradually ramps upward. The petals eventually contact the edge of the large central hole in the back cover. The rubbing between the petal exteriors with the sharp edge on the back cover induces an undesired fluctuating load/time response. Although the load is no longer smooth at times beyond 12 ms, the load at least does not fluctuate with significant amplitude. The *x* and *y* components of the cutting force come from the friction between the extrusion walls and blade sides and back cover. Note that these components of the force are not only low compared to the axial load, but approximately equal and opposite which indicates that the petals are deforming symmetrically.

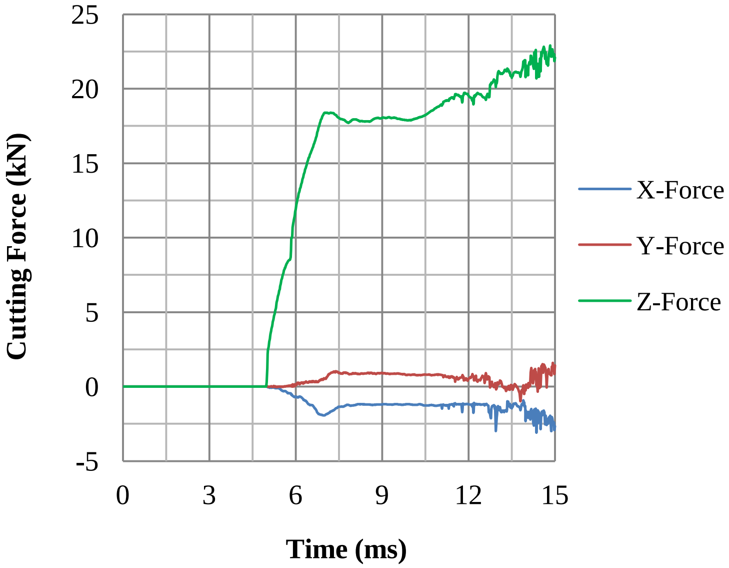

Figure G11: Cutting force for first adaptive cutter in 8-blade configuration using 44.45 mm diameter, 3.175 mm thick extrusion.

Subjected to 8-blade cutting, high stresses are distributed in more components of the device than just the blades, namely the back cover, front cover, and bolts, as noted by Figure G12(a). The fixed blade and switchblade each show critical stresses of 1800 MPa indicated by the yellow zones near the roots. The front cover has a critical stress of 900 MPa, which can be managed by the proper grade of steel. However, the front cover thickness does not contribute to the amount of clearance available for the extrusion petals below the device. So to reduce stresses in the front cover, its thickness can be increased. The switchblade applies significant pressure against the back cover as noted by Figure G12(b), indicating that the back cover would likely need to be made of another tool steel like the blades. The back cover thickness should not be increased though to reduce its stress because its thickness influences the overall height of the device, further limiting the clearance for the extrusion petals to flare underneath. The region in red of 2200 MPa predicts certain failure of the shaft of the ¼ in shoulder bolt passing through the switchblade. This bolt must therefore be larger in diameter if it is to withstand the cutting force in the 6-blade or 8-blade configuration.

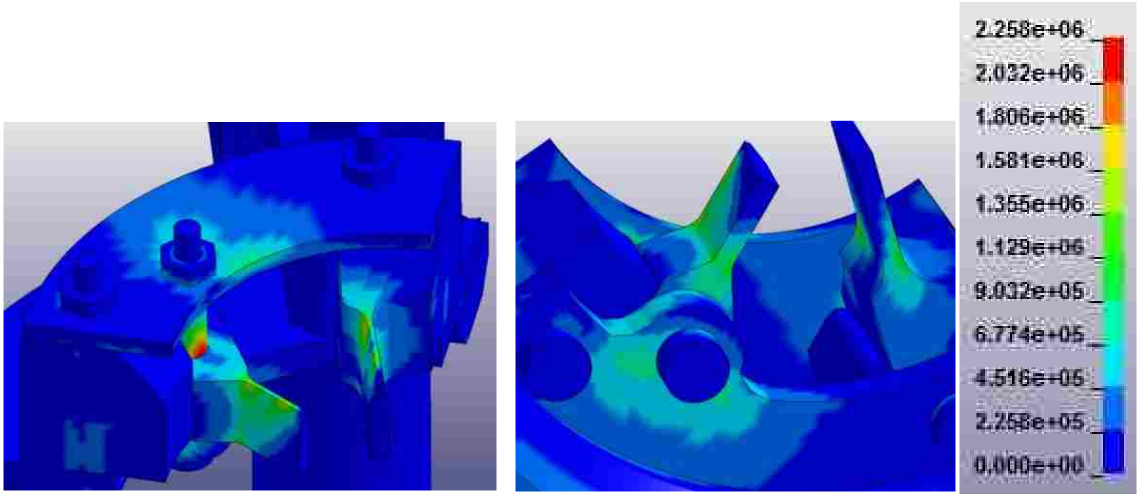

(a) (b)

Figure G12: von Mises stress contours (kPa) for first adaptive cutter in 8-blade cutting using 44.45 mm diameter, 3.175 mm thick extrusion. (a) Blades. (b) Back cover.

The substantial cutting force using 8 blades causes the entire device to flex more than in the 4-blade or 6-blade configurations. During cutting, as the elevated platform near the central hole flexes downward, a rippling effect causes the exterior of the platform, where the angle plate is fastened, to flex upward. Seen in Figures G13(a) and (b), the neoprene pad below the solenoid casing is pressed against the casing as the elevated platform flexes upward and the angle plate flexes inward. Despite this flexing, the effective stresses in the elevated platform, angle plate, and solenoid are not high enough to be of concern and for the sake of brevity are not shown. The effective stress in the neoprene pad as it is compressed, shown in Figure G13(b) is 600 kPa, which is far below the yield strength of neoprene (3 to 4 MPa). The neoprene pad is demonstrated to be an important feature in the adaptive cutter design as it indeed cushions the solenoid casing. Another consequence from the flexing of the elevated platform is axial vibration of the Teflon pin. The pin is unconstrained axially in this adaptive cutter design, which could induce a perpendicular load on the solenoid shaft. Although no significant load was transferred to the shaft, the pin would still be better constrained to pure radial motion if it slid inside a slot.

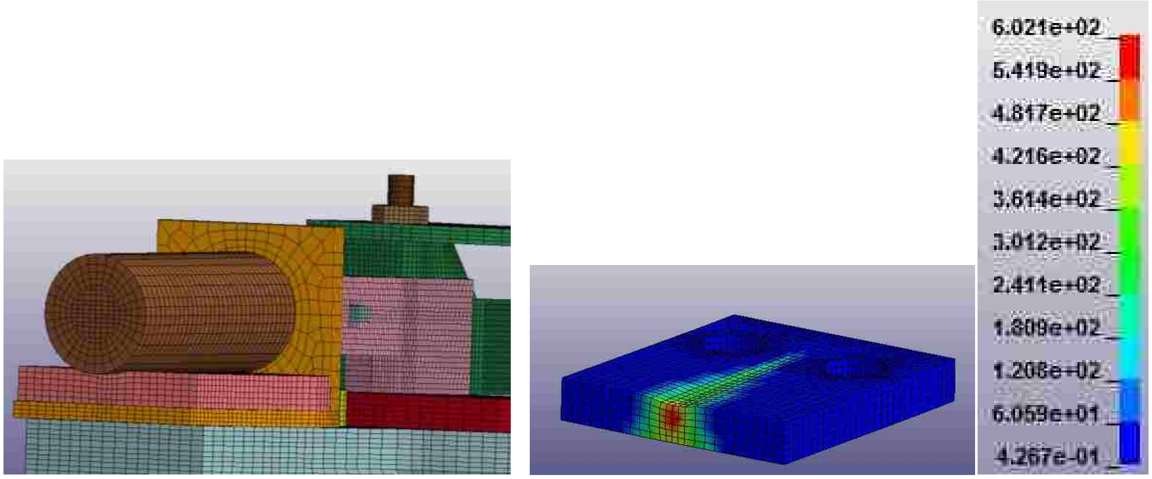

(a) (b)

Figure G13: Flexing of the first adaptive cutter during cutting with 8 blades. (a) Side view of neoprene pad pushing up against solenoid casing. (b) von Mises stresses (kPa) in neoprene pad.

One questions how the adaptive cutter will perform using 8 blades when cutting with the largest diameter extrusion of 63.5 mm. Although a larger diameter extrusion is expected to result in a less severe loading condition on the blades, the lack of space available for petal flaring will likely lead to more rubbing contact. As expected, Figure G14 depicts how the thick face of the fixed blade hinders the extrusion petals from flaring significantly. Although no contact occurs with the back cover, the rubbing contact between the extrusion outer wall and thicker portion of the fixed blade is continuous. The

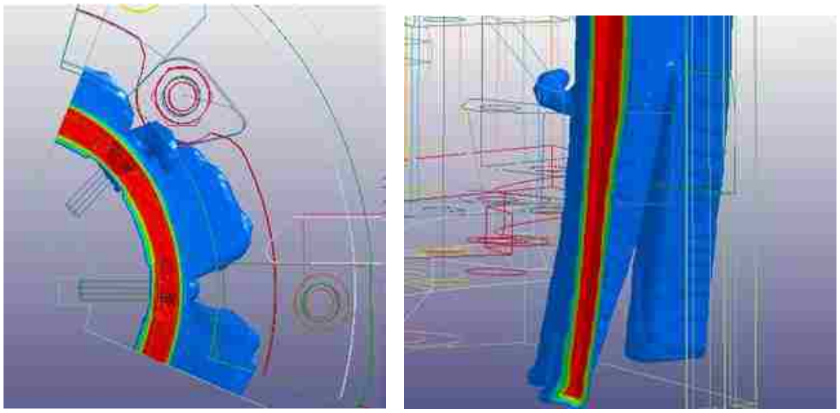

(a) (b)

Figure G14: Numerical simulation of extrusion deformation for first adaptive cutter in the 8-blade configuration using 63.5 mm diameter, 3.175 mm thick extrusion. (a) Top view. (b) Side view with chip formation.

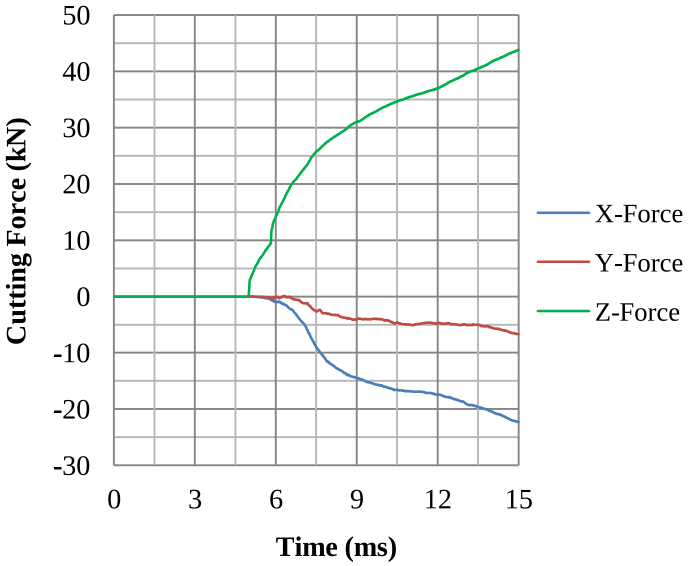

Figure G15: Cutting force for first adaptive cutter in 8-blade configuration using 63.5 mm diameter, 3.175 mm thick extrusion.

thicker portion of the switchblade also promotes the formation of a chip, which shows a clean curling shape.

Note from Figure G15 that the continuous rubbing contact also apparently raises the cutting force in the axial direction (*z-axis*) with no sign of stabilizing. Despite the frictional contact, the force/time response is smooth unlike that for the 44.45 mm diameter extrusion in Figure G11. However, the magnitude of the cutting force for the 63.5 mm diameter extrusion is questionable: the cutting force is expected to approximately double from 4 blades to 8 blades, but the force reaches up to 45 kN (i.e. 180 kN for 8 blades) which is more than four times the cutting force using 4 blades (i.e. 40 kN). In reality, the extrusion may bind with the adaptive cutter if flaring is prevented. However, a cutting experiment using a containing device may be worth investigating with the fixed cutters of [10] to determine whether the cutting force/time response truly behaves as Figure G15 suggests. Finally, the nonzero *x* and *y* force components derive from the friction forces in sliding contact between the extrusion and thick portions of the fixed blades.

Table G1 summarizes the critical effective stresses in each component for the 3 blade configurations in the cutting phase. Note the stress results for the 6-blade configuration have not been presented because cutting using the uneven blade spacing would cause catastrophic failure of the fixed blade and as a result should not be considered. All the other components have the worst stress condition in the 8-blade cutting configuration. Although the blades have high stress and the ¼ in bolts would fail, the remaining components have acceptable stress levels that a suitable grade of steel can manage. Furthermore, the solenoid and its mounting structure did not experience unacceptable stress, and so could be used again in a redesign of the adaptive cutter.

Table G1: Critical von Mises stresses in each component of first adaptive cutter.

		4 Blades	**6 Blades** [a]	**8 Blades**
		Clamp (Cutting)	**Clamp, Set (Cutting)**	**Clamp, Set (Cutting)**
No.	**Component**	**Max Stress (MPa)**	**Max Stress (MPa)**	**Max Stress (MPa)**
1	Support Leg	112	-	330
2	Elevated Platform	126	-	430
3	Angle Plate	98	-	190
4	Neoprene Pad	1.2 kPa	-	725 kPa [b]
5	Solenoid Casing	43	-	100
6	Solenoid Shaft	77	-	44
7	Mounting Hex Nut	30	-	117
8	Solenoid Adaptor	95	-	60
9	Teflon Pin	10	-	11 [c]
10	Back Cover	260	-	830
11	Front Cover	340	-	1000
12	Fixed Blade	1100	-	1800
13	Switchblade	29	-	1800
14	#10 Hex Nut	200	-	430
15	1/4 in Shoulder Bolt	335	-	2260 [d]
16	M6x10 Shoulder Bolt	150	-	420
17	M10x35 Shoulder Bolt	195	-	400
18	M6x6 Shoulder Bolt	124	-	124

a: Uneven petal flaring twists blades to failure, precluding use of this configuration
b: Approximately 20% of yield strength of Neoprene
c: Approximately 50% of yield strength of Teflon
d: Indicates definite failure

The results of the cutting simulations outlined in this appendix indicate two important findings about the first adaptive cutting device:

1. Unequal blade spacing leads to twisting of the fixed blade to definite failure.
2. The ¼ in bolts passing through the switchblade will definitely fail when subjected to the cutting load in the 6-blade or 8-blade configurations.

APPENDIX H: ADDITIONAL ENGINEERING ANALYSES FOR THE QUADROTOR ADAPTIVE CUTTER DESIGN

H.1 Normal Force Acting at Teflon Pin/4-Bladed Cutter Contact Interface

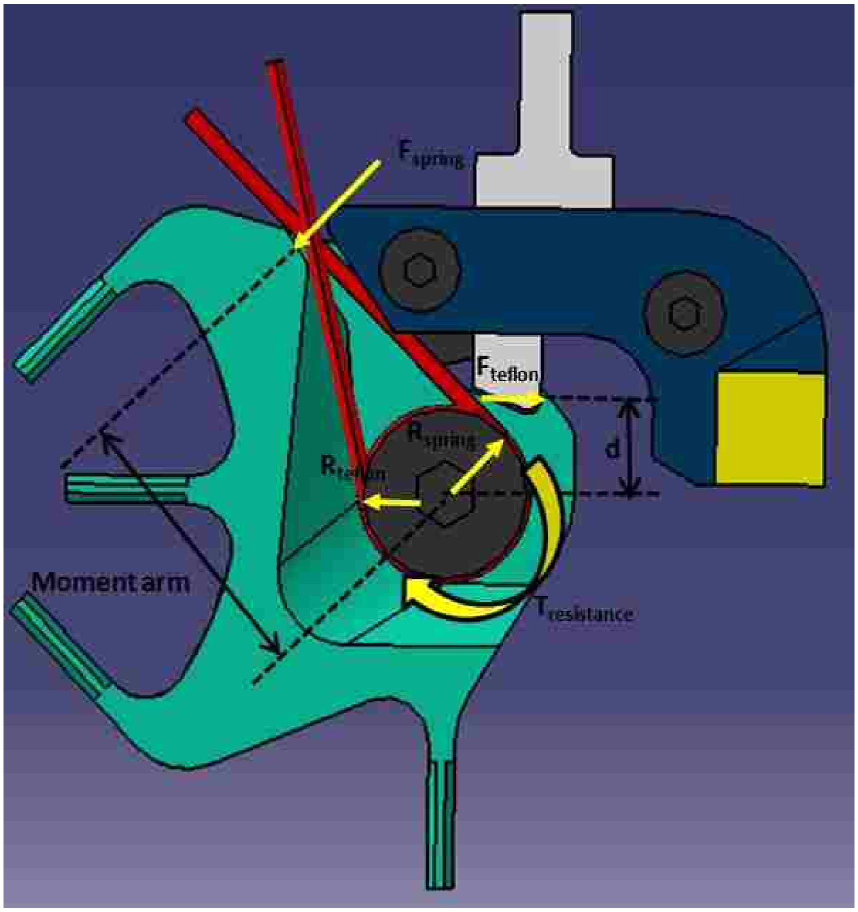

Figure H1: Free body diagram of forces and torques applied to the 4-bladed cutter.

An important check on the quadrotor design is the pull force of the SOTUL0230051 solenoid. The 4-bladed cutter will have a larger force of resistance at the Teflon pin/cutter contact interface than the 3-bladed cutter because the 4-bladed cutter has a shorter distance *d*, depicted in Figure H1. Therefore, only the 4-bladed cutter is considered in this simplified force and torque balance analysis. The angular offset of the torsion spring is 145 degrees, which results in a torque of approximately 952 N·mm. This torque, which is counterclockwise, is produced by the force in the spring, F_{spring}, multiplied by *Moment arm*. F_{spring} must be balanced by a reaction force at the bolt, R_{spring}. The counterclockwise torque produced by F_{spring} must be balanced by a clockwise resistance torque at the bolt plus a clockwise torque equal to F_{Teflon} multiplied by *d*. If the torque at the bolt is assumed to be zero (frictionless), the clockwise counteracting torque depends entirely on the force at the Tefon/cutter interface. Knowing that the perpendicular distance d is 12 mm, the force F_{Teflon} is thus equal to 79 N. Using the coefficient of friction between Teflon and hard steel as 0.16, the friction force that the solenoid must overcome is 12.7 N. With its shaft positioned 6 mm away from the neutral, the solenoid model SOTUL0230051 according to the manufacturer's specifications has a pull force of 18.5 N, which should be able to overcome the force of friction at the Teflon pin/cutter interface. In addition, the resistance torque $T_{resistance}$ at the bolt would not be zero as it was assumed here, so the required force to pull out the Teflon pin would actually be lower. Therefore, the solenoid model used in this adaptive cutter design should be able to overcome friction at the pin/cutter interface when activated.

To double check the analytical calculation, the contact force between the Teflon pin and the 4-bladed was verified from the LS-DYNA simulation of the 6-blade pre-cutting configuration. The 4-blade precutting simulation did not allow enough time to establish a stable normal force between the 3-bladed or 4-bladed cutter and the Teflon pin. However, in the 6-blade pre-cutting simulation, the 30 ms end time is more than

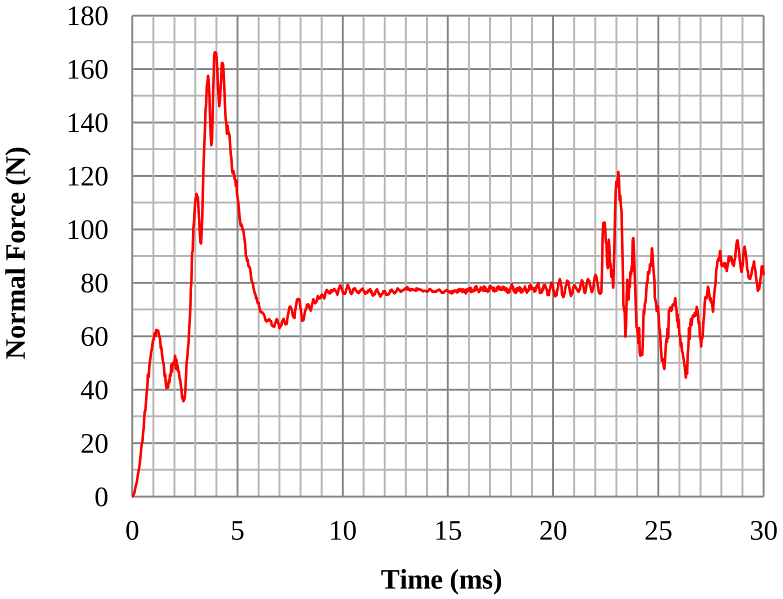

Figure H2: Normal force between Teflon pin and 4-bladed cutter for quadrotor adaptive cutter from pre-cutting model in the 6-blade configuration.

enough for the normal force between the 4-bladed cutter and Teflon pin to stabilize. In Figure H2, note that due to an initial gap (to prevent initial penetrations), the 4-bladed cutter is not immediately in contact with the pin at time=0. In the first few milliseconds, the 4-bladed cutter gently strikes the Teflon pin, causing a “blip” in the contact force. By 10 ms, the normal force has stabilized at approximately 78 N, which is remarkably close to the analytically calculated normal force predicted from the FBD in Figure H1. Seeing that the normal force is not higher than initially predicted, the solenoid should have enough pull force to extract the pin. At 22.5 ms, the time of impact between the 3-bladed cutter and magnet, the slightest shaking of the device causes a dynamic response in the normal force.

H.2 Impact of AA6061-T6 Extrusion Specimen on Jaw Assembly of Quadrotor

The initial impact the extrusion has on the jaw assembly, mounted on the front cover of the quadrotor adaptive cutter, is important to assess. Since all four jaws and jaw housings are geometrically identical, a quarter model considering a single jaw and housing was constructed to economize on CPU cost. The smallest diameter extrusion of 44.45 mm is the worst load case on the jaw because it protrudes out of its housing with the longest cantilevered shaft. The quarter mesh of the extrusion impact on the jaw is shown in Figure H3. All parts are composed of solid, hexahedral elements with single point integration. The impacting crosshead on the low energy droptower in the Structures lab at the University of Windsor has a mass of 60 kg. For this model, the dimensions of the crosshead block were selected such that its volume multiplied by the density of steel (8000 kg/m^3) equals 15 kg; a quarter of the total crosshead mass. The jaw (blue) and jaw teeth (green) would have been difficult to mesh as a single entity. Since the region of concern is not the teeth, but the radius between the jaw body and jaw shaft, this area should be meshed as a single entity. To simplify the meshing process, the jaw body and jaw teeth were meshed separately and joined at their faces using a *CONTACT_ SURFACE_TO_SURFACE_TIED algorithm. Materials for the jaw body, jaw teeth, and housing were modeled using *MAT_ELASTIC with a modulus of elasticity of 200 GPa and density of 8000 kg/m^3, representing mechanical properties of steel. Hourglass control was invoked for these materials with *HOURGLASS setting IHQ=6 and QM=1. The crosshead was modeled as rigid using the same mechanical properties defined for steel.

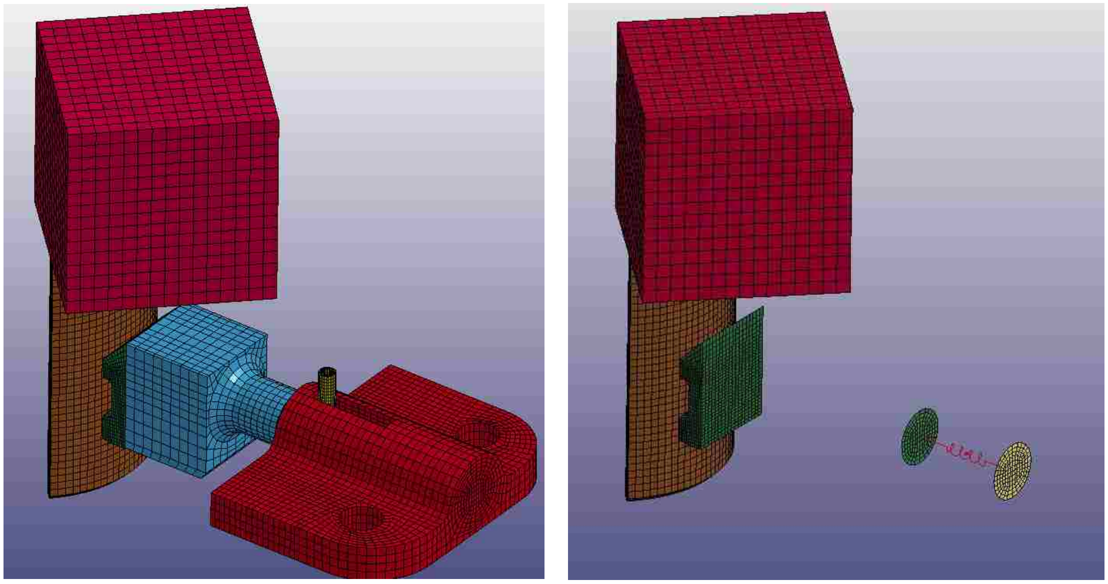

(a) (b)

Figure H3: Numerical model of jaw assembly, extrusion, and impacting crosshead. (a) Isometric view. (b) Discrete spring and rigid shell disks in housing.

The extrusion was also modeled as rigid, but using a modulus of elasticity of 70 GPa and density of 2700 kg/m^3, representing properties of aluminum. The slit pin was modeled as rigid with the same properties of steel and attached to the jaw shaft using a *CONTACT_SURFACE_TO_SURFACE_TIED algorithm. Contact between all other surfaces used *CONTACT_SURFACE_TO_SURFACE with individual segment sets. For steel on steel contact, static and dynamic coefficients of friction were 0.55 and 0.50, respectively. For aluminum on steel contact, static and dynamic coefficients of friction were 0.47 and 0.38, respectively. In all contact algorithms, a decay coefficient of 10^6 was applied. The two hole peripheries in the jaw housing were fully constrained. The crosshead was prescribed a downward velocity of 10 m/s in *BOUNDARY_PRESCRIBED_MOTION_RIGID. An initial gap of 0.05 mm between the base of the crosshead and the top of the extrusion was specified to prevent initial contact penetrations. The compression spring located in the housing was modeled using a discrete linear spring element by specifying DRO=0 in *SECTION_DISCRETE and its stiffness of 0.46 N/mm in *MAT_SPRING_ELASTIC. With the 44.45 mm diameter extrusion, a 16.65 mm offset in the spring is specified in *ELEMENT_DISCRETE as negative to indicate it is compressively preloaded. Seen in Figure H3(b), each end of the spring is attached to a node on a rigid shell disk; one disk shares its nodes with the back face of the jaw shaft and the other disk shares its nodes with the back face inside the jaw housing. This technique of attaching the spring distributes the load on the back of the shaft more effectively and prevents localized hourglassing at the spring attachment points. The jaw teeth and the outer wall of the extrusion had a minimum gap of 0.04 mm to ensure no initial penetrations.

The effective stress contours on the jaw assembly are shown in Figure H4. From Figure H4(a), the friction between the extrusion and jaw teeth causes a downward acting force on the jaw, which places the top side of the shaft in a tensile state of stress. This critical stress, indicated in red, is only 1 MPa. The sliding motion of the jaw inside the housing is so minute, yet the contact between the slit pin and the jaw shaft is still not maintained. However, the stress near the region of the slit pin and housing slot is negligible, indicating that the slit pin is not an important aspect of the model. Later models of the quadrotor adaptive cutter included a key, extruded directly from the shaft mesh, to replace the slit pin. This approach ensured no loss of contact and prevented the spring from pushing the jaw too far out of its housing.

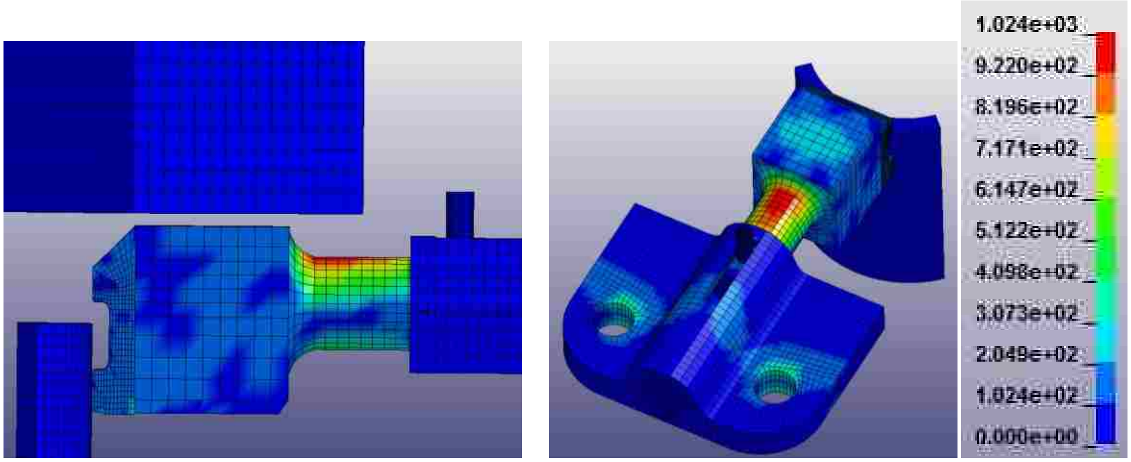

(a) (b)

Figure H4: von Mises stress contours (kPa) of the two-toothed jaw assembly under impact with the extrusion. (a) Side view. (b) Isometric view.

The system energies of the jaw assembly are shown in Figure H5. The total energy, comprised nearly entirely of kinetic energy, is in balance with the external work, thus satisfying the physical law of energy conservation. The internal, spring, hourglass, and sliding energies are negligible by comparison. On this scale, these energy contributions appear to be zero, but they are not, as expected. A zoomed-in scale of the internal, spring, hourglass, and sliding energies is provided in Figure H6. Note the peak sliding energy of 700 mJ is still 1000 times smaller than the kinetic energy of the system. However, Figure H6 illustrates the jaw assembly and extrusion interaction quite well: the spike in sliding energy indicates the initial contact between the crosshead and extrusion. Immediately afterward, the sliding energy remains constant at approximately 70 mJ until 0.94 ms when it jumps to 120 mJ and is held steady. To explain this trend, the period between zero and 0.94 ms is the sliding between the jaw shaft and the housing, without yet any contact between the teeth and extrusion because of the initial 0.04 mm gap. As the spring pushes the jaw outward, the teeth make contact with the extrusion at 0.94 ms, at which time the friction between the extrusion and teeth contributes to the sliding energy of the system. It is at this time the stress in the shaft is highest. The elastic deformation of material is negligible since the internal energy is practically in line with the spring energy; both of which are approximately 70 mJ. Even at the milliJoule scale, hourglass energy is zero.

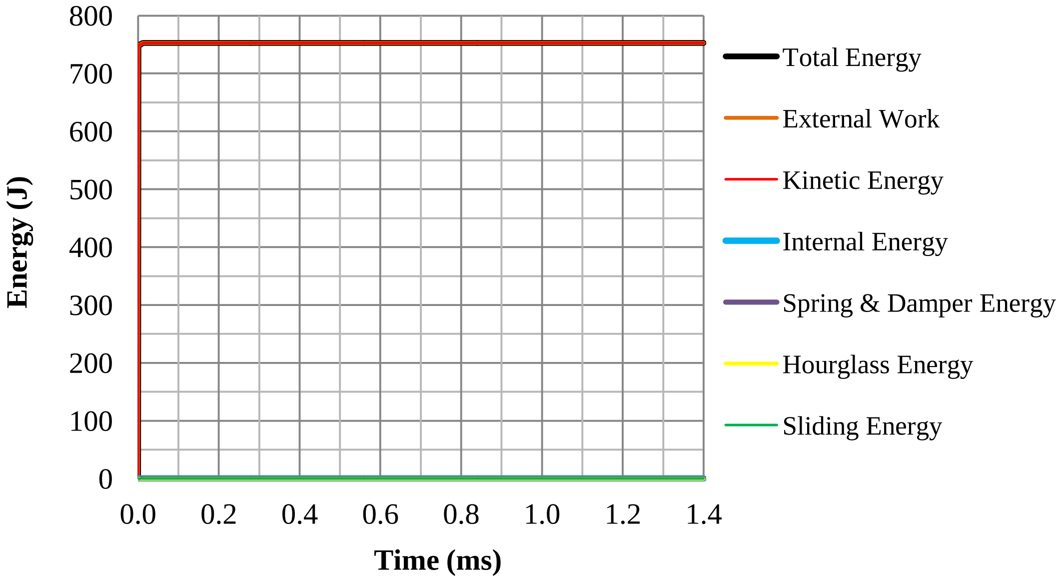

Figure H5: System energies versus time for jaw assembly under impact with extrusion.

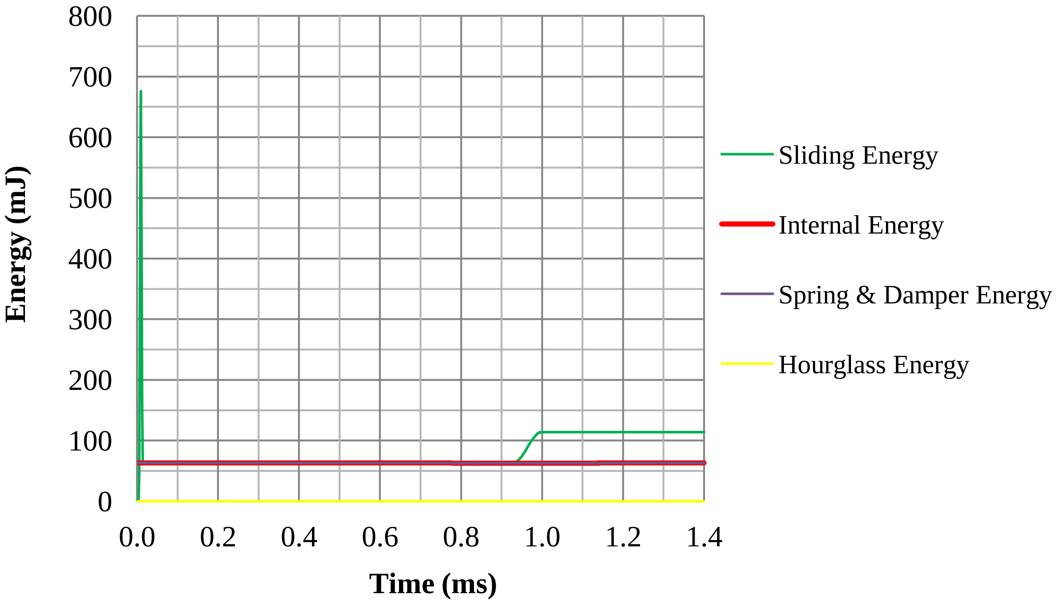

Figure H6: Zoomed-in scale of system energies versus time for jaw assembly under impact with extrusion.

VITA AUCTORIS

NAME: Peter Shery

PLACE OF BIRTH: Longueuil, QC

YEAR OF BIRTH: 1989

EDUCATION: Heritage Regional High School, St-Hubert, QC, 2007

Dawson College, DEC, Montreal, QC, 2009

Concordia University, B.Sc., Montreal, QC, 2014

University of Windsor, M.Sc., Windsor, ON, 2017